takece.com
Continuing Education Simplified!

Course Title: Application of Ultrasound in Diagnostic Imaging

Topic List:-

Chapter 11

Ultrasound

Authors: Dominik Neumann and Eva Kollorz

11.1 Introduction

Acoustic waves with frequencies ξ between 16 Hz and 20 kHz can be sensed by the human hearing and are thus called audible waves or audible sound. If $\xi > 20\,\text{kHz}$, one speaks of ultrasound (Tab. 11.1). Some animal species such as bats can perceive ultrasound and use it for echolocation: by measuring the time between sending and receiving (after partial reflection on a surface) ultrasonic waves, the distance of an object (e. g., a wall or prey) to the sender (bat) can be computed accurately, assuming that the sound velocity is known. In the previous century, modern technology started to make use of this technique with applications ranging from marine distance measurement (1920: SONAR) to medicine (1958: first ultrasound device in clinical use). A typical system is shown in Fig. 11.1.

Today, medical ultrasound often is the first-resort clinical imaging modality due to its cost-effectiveness and lack of ionizing radiation. Typical medical ultrasound frequencies are between $2\,\text{MHz} < \xi < 40\,\text{Mhz}$. Traditionally, medical ultrasound is mainly put to use in diagnostic applications, however, more therapeutic applications are emerging.

A. Maier et al. (Eds.): Medical Imaging Systems, LNCS 11111, pp. 237–249, 2018.
https://doi.org/10.1007/978-3-319-96520-8_11

Figure 11.1: Clinical Ultrasound System in action. Image courtesy of Siemens Healthineers AG.

	f	**Examples**
Infrasound	0 ... 16 Hz	Seismic waves
Audible sound	16 Hz ... 20 kHz	Music Human Speech
Ultrasound	> 20 kHz	Bat, Dolphin, and Whale Sounds Acoustic Microscopy Ultrasound Imaging

Table 11.1: Acoustic spectrum.

11.2 Physics of Sound Waves

This section introduces the basic underlying physics of ultrasound imaging.

11.2.1 Sound Waves

Acoustic signals emerge from organized movement of molecules or atoms, which cause local periodic compression of matter (gas, liquids, solid objects). Such spatially propagating, periodically repeating processes are commonly known as waves. Based on the direction of propagation, a distinction between transverse and longitudinal waves is made, where the nature of sound waves is the one of the latter class.

Sound waves are mainly characterized by *frequency*, *velocity*, *wavelength*, and *intensity*. Frequency ξ is measured in Hertz (Hz) and denotes the oscillation count per second. Sound velocity v within a medium, measured in meters

Medium	v [$\mathrm{m\,s^{-1}}$]	Z [$\mathrm{g\,cm^{-2}\,s^{-1}}$]
Air	331	$4.3 \cdot 10^{1}$
Fat	1470	$1.42 \cdot 10^{5}$
Water	1492	$1.48 \cdot 10^{5}$
Brain tissue	1530	$1.56 \cdot 10^{5}$
Muscles	1568	$1.63 \cdot 10^{5}$
Bones	3600	$6.12 \cdot 10^{5}$

Table 11.2: Sound velocity v and impedance Z of various media occurring in the human body.

per second ($\mathrm{m\,s^{-1}}$), is independent of ξ, but varies with material properties such as elasticity and density. For some prominent examples see Tab. 11.2. The wavelength λ is the distance between two oscillation maxima and measured in meters (m). Recall the *fundamental wave equation* relates wavelength λ with sound velocity c and frequency ξ:

$$\lambda = \frac{c}{\xi} \ . \tag{11.1}$$

Finally, the intensity J of a sound wave is measured in Watts per area ($\mathrm{W\,m^{-2}}$) and denotes the acoustic power density. Typical values for J in ultrasound diagnostics are between 1 and 10 $\mathrm{mW\,cm^{-2}}$.

11.2.2 Sound Wave Characteristics at Boundaries

The human body contains various kinds of boundaries between different materials, for instance, at borders between organs and liquids or other tissues. At such boundaries between two media, sound waves are partially reflected and partially transmitted.

11.2.2.1 Reflection

The well known *law of reflection* states that the angle of incidence equals the angle of reflection. This also holds for reflection of sound waves (cf. Fig. 11.2(b)). For perpendicular incidence (cf. Fig. 11.2(a)), the reflection R and transmission T coefficients write:

$$R = \frac{J_r}{J_0} = \left(\frac{Z_2 - Z_1}{Z_2 + Z_1}\right)^2 \tag{11.2}$$

$$T = \frac{J_t}{J_0} = \frac{4Z_1Z_2}{(Z_1 + Z_2)^2} \ , \tag{11.3}$$

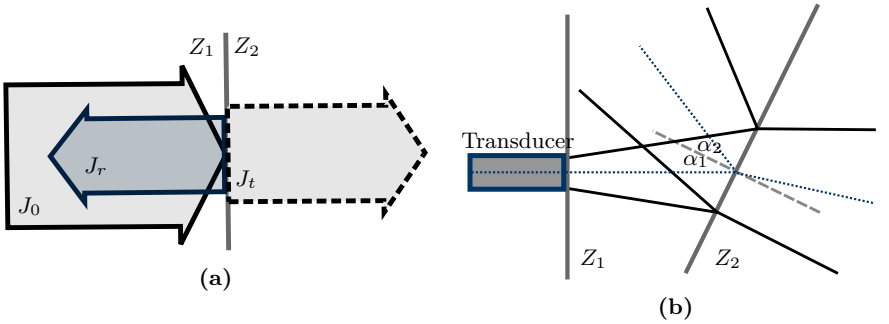

Figure 11.2: (a) Reflected J_r and transmitted J_t wave intensity at border between two different materials with impedance Z_1 and Z_2, respectively. (b) Reflection of sound waves at smooth surfaces ($\alpha_1 = \alpha_2$).

Material 1	**Material 2**	**Reflected**
Brain	Skull bone	43.5%
Fat	Muscle	1%
Fat	Kidney	0.6%
Muscle	Blood	0.1%
Soft tissue	Water	0.25%
Soft tissue	Air	99.9%

Table 11.3: Reflectivity at boundaries between two materials.

where J_r, J_t, and J_0 denote the wave intensity of the reflected, transmitted, and incident sound, respectively. Z_1 and Z_2 denote the acoustic impedance of two different media. Acoustic impedance Z, which is measured in $\mathrm{g\,cm^{-2}\,s^{-1}}$, can be computed from the tensile modulus E (elasticity) and the density D of the given medium:

$$Z = \sqrt{(E \cdot D)} \ . \tag{11.4}$$

For some prominent examples see Tab. 11.2.

From Eq. (11.2), it is interesting to see that for two media with equal impedance $Z_1 = Z_2$, no reflection happens. With similar impedance $Z_1 \approx Z_2$, as often occurring inside the human body at boundaries between similar types of tissue, the reflection coefficient R is rather small, while for $|Z_1 - Z_2| \gg 0$, e. g., at boundaries between air (low impedance) and soft tissue (high impedance), almost the entire wave is reflected (total reflection). The latter immediately leads to the conclusion that organs containing air, such as the lungs, cannot be examined via medical ultrasound. For more details see Tab. 11.3.

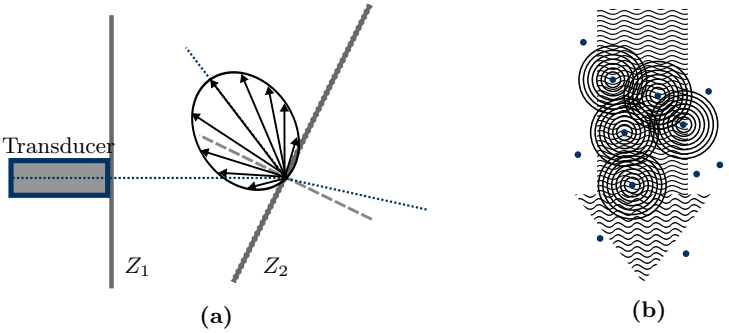

Figure 11.3: Scattering of sound waves at (a) a rough boundary (diffuse reflection) between two different media with impedance Z_1 and Z_2; and scattering at (b) inhomogeneities (depicted as blue dots) in a medium.

11.2.2.2 Scattering

Scattering means diffuse reflection of small portions of a wave in various directions. It should be noted that the law of reflection (see above) holds for each of those portions. Small inhomogeneities in the material cause scattering of sound waves, cf. Fig. 11.3(b). The same holds for boundaries with rough surfaces as shown in Fig. 11.3(a), where the width of the reflection cone increases with decreasing wavelength λ and increasing *roughness* of the surface. Scattering at rough surfaces is highly relevant in medical ultrasound, because in the case of perfectly smooth boundaries, waves are only reflected towards the sender if the direction of the wave is perpendicular to the surface (no diffusion), whereas for rough boundaries, the reflections in various directions enable imaging of tilted boundaries.

11.2.2.3 Diffraction

When sound waves pass barriers, obstacles, or openings on their path, they get diffracted. Diffracion involves a change in direction of the sound wave. Increasing wavelength λ yields an increased amount of diffraction (sharpness of bending), and vice versa. If λ is smaller than the size of the barrier, obstacle, or opening, the occurring diffraction becomes negligible.

11.2.2.4 Refraction

Snell's *law of refraction* known from optics states

ξ [MHz]	$d_{\max}$ [cm]	**Typical Applications**
1.0	50	*n/a*
3.5	15	Fetus, liver, heart, kidney
5.0	10	Brain
7.5	7	Prostate
10	5	Pancreas (intraoperative)
20	1.2	Eye, skin
40	0.6	Intravascular

Table 11.4: Maximum penetration depth $d_{\max}$ for various frequencies f.

$$\frac{v_1}{v_2} = \frac{\sin \alpha_1}{\sin \alpha_2} \ , \tag{11.5}$$

where α_1 and α_2 denote the angle of refraction in two different media, also applies to sound waves. However, since sound velocities (v_1, v_2) in human soft tissue differ only marginally (see Tab. 11.2), the little effects of refraction in medical ultrasound are negligible and therefore not considered further in this chapter.

11.2.3 Attenuation

Attenuation is the reduction in sound wave intensity J that occurs when a wave penetrates a medium. It follows the well-known *exponential law of attenuation*:

$$J(x) = J_0 \exp(-\mu x) \ , \tag{11.6}$$

where J_0 denotes the initial intensity. The attenuation coefficient μ denotes the attenuation that occurs with each cm the sound wave travels inside a medium. It depends on material (tissue type) and ultrasound frequency ξ and is measured in decibel (dB). The attenuation coefficient mainly consists of two additive components $\mu = \mu_a + \mu_s$, namely absorption μ_a and scattering μ_s (see above). Absorption μ_a causes tissue to heat.

From Eq. (11.6), it can be easily seen that the acoustic intensity J decreases with increasing penetration depth x. For a high maximum penetration depth, low frequencies are necessary as shown in Tab. 11.4. However, the resolution of the acquired images decreases with decreasing frequency (cf. Sec. 11.3.3). Thus, the deeper the tissue penetration, the lower the spatial resolution.

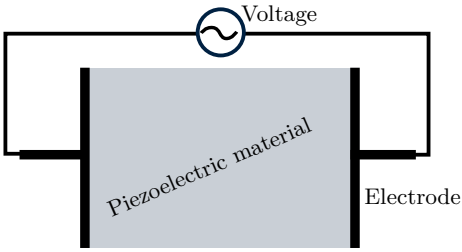

Figure 11.4: Piezoelectric effect.

11.3 Image Acquisition for Diagnostics

11.3.1 Transducers

An ultrasound transducer functions as both: a generator and a detector of ultrasonic waves. It converts mechanical energy into electrical energy and vice versa. When the transducer is pressed against the skin, it directs high-frequency sound waves into the body. Since sound waves produced by the transducer can barely penetrate air (cf. Tab. 11.3), gel is applied to the skin to help to minimize the amount of air between the transducer and the skin. As the waves penetrate the body, sound echoes are generated from the body's fluids and tissues due to (diffuse) reflection and scattering. The strength and character of these sound echoes are recorded by the transducer and, depending on the type of transducer, can be transformed into 1-D, 2-D or 3-D images, which can be rendered and viewed to the user.

11.3.2 Piezoelectric Effect

In order to generate and detect ultrasonic waves, transducers rely on the so-called *piezoelectric effect*. It describes the conversion of electrical energy into mechanical energy and vice versa in piezoelectric materials. On the one hand, mechanical pressure (pressure translates to "piezo" (gr.)) is converted to electric polarization, which generates electric voltage. The electric voltage can be measured using two electrodes, as shown in Fig. 11.4. On the other hand, electrical fields cause contraction or stretching of the piezoelectric material. This contraction and stretching can be used to generate ultrasound waves by applying a high frequency alternating voltage.

Typical piezoelectric materials used in medical ultrasound transducers are barium titanate ($BaTiO_3$) and lead zirconium titanate (PZT).

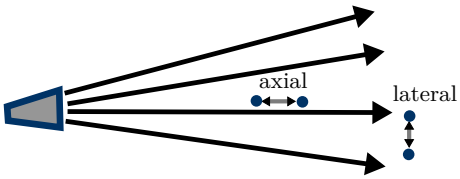

Figure 11.5: Axial and lateral resolution of ultrasound devices. Minimal distance between two structures (blue dots) in axial/lateral direction that allows for distinguishing between them in the ultrasound image.

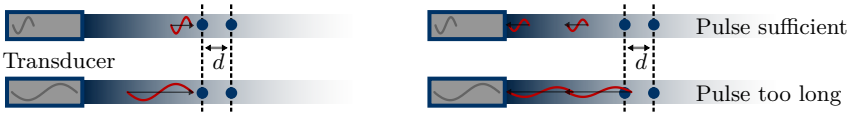

Figure 11.6: Axial resolution: illustration of dependence on wave frequency f. Left and right shows two different timesteps, where d denotes the distance between two structures (blue dots). The high frequency (top) wave allows for distinguishing between the two structures, as clearly separated echoes are sent back to the sender. Using the low frequency wave, the echoes cannot be separated (echoes are merged).

11.3.3 Spatial Resolution

In ultrasound imaging, a distinction is made between two different kinds of spatial resolutions, in particular axial and lateral resolution (cf. Fig. 11.5).

11.3.3.1 Axial Resolution

Axial resolution concerns structures lying behind each other w. r. t. the direction of the ultrasound waves. The better the axial resolution, the smaller the distance between two structures can be such that they can be distinguished by the transducer. Axial resolution is highly dependent on the ultrasound wave frequency f. The illustration in Fig. 11.6 explains that dependency based on a simple example, where an ultrasonic pulse generated by the transducer consists in a single wave only (shortest possible pulse). The distance d between the structures needs to be $d \geq \lambda/2$ in order to be able distinguish between them.

11.3.3.2 Lateral Resolution

Lateral resolution concerns the distinguishability of structures located next to each other in the same lateral distance to the transducer (same penetration depth). Lateral resolution is always inferior to axial resolution.

11.3.3.3 Frequency Trade-off

As described above, axial and lateral transducer resolution depend on the ultrasound frequency ξ, and thus on the wavelength λ. As a rule of thumb:

$$\text{axial:} \quad \Delta z \geq \lambda/2, \tag{11.7}$$

$$\text{lateral:} \quad \Delta x \sim 3 \cdot \lambda \ , \tag{11.8}$$

where Δz and Δx denote the minimum distance between to structures in axial/lateral direction such that the ultrasound echo is distinguishable. Hence, high ξ yields high resolution, whereas low ξ yields low resolution. However, the frequency is also directly related to attenuation (cf. Sec. 11.2.3), where high ξ yields high attenuation and vice versa. Thus, with high frequency f, the penetration depth is low but the images will have high resolution. At low ξ, deeper penetration is possible, but the resolution will be lower. Depending on the application, a trade-off between the desired properties (deep penetration versus high resolution) needs to be found, and the transducer frequency be adjusted accordingly.

11.3.4 Imaging Modes

Ultrasound offers a large variety of different imaging modes. The most common ones include A-mode, B-mode, and M-mode. A- and M-mode generate one-dimensional (1-D) images (signals), whereas B-mode can be used to acquire 2-D or even 3-D images (cf. Geek Box 11.1). Doppler (cf. Geek Box 11.2) can be acquired in 1-D and 2-D, and with the most recent generations of transducers also in 3-D.

11.3.4.1 A-Mode (Amplitude Mode)

A-mode is the simplest scanning mode. The height of the amplitude of the reflected ultrasound is displayed over the sonic runtime in the sonic ray direction. Extractable measurements are: frequency, modulated frequency, height of the impulse/amplitude, runtime, wave phase, phase shift, and attenuation.

However, the major disadvantage is that only very localized information (one single line through the body) is acquired.

The backward scattered ultrasound intensity along a single ray is called *A-mode*. From a continuously running high-frequency generator, a wave packet is cut out with a "gate" and is passed to the transducer. The returning echo is given through a duplexer to a time-dependent amplifier (Time Gain Compensation). Later arriving echoes, which are weaker because of the absorption, are more amplified than the signals from the surface. Signals of high depth (15 cm) are raised up to 120 dB. The signal height of an interface reflected signal is independent of the penetration depth from which the echo comes. The signal-to-noise ratio becomes worse with increasing depth. The next sonic impulse will be emitted if all echoes of the preliminary sonic impulse are decayed. The repeat rate depends on the penetration depth and therewith on the used frequency.

11.3.4.2 B-Mode (Brightness Mode)

B-mode is the most common ultrasound mode. B-mode images are generated by systematically combining a multitude of A-mode (1-D) scans into a single 2-D image, where the intensity of a pixel is defined by the amplitude of the corresponding ultrasonic ray. In brief, in order to acquire 2-D images of the inner body, the ultrasound device has to sample not only on a 1-D ray (as in A-mode), but on a 2-D plane in 3-D space. Hence, various rays are sent in different directions. To achieve this, two techniques are commonly used: the mechanical and the electronic method.

Mechanical scanners The transducer librates in front of the patient, without any external movement of the gaging head. Thus, a slice of the human body is represented in the form of a circle segment. The intensity of the echo is transformed into gray scales and is inserted into an image matrix (*B-Mode*). An image consists of a fan of typically 100 lines.

Electronic scanners (linear/curved arrays) Here, many (60 to 100) and very small (0.5 mm to 1 mm) transducers are used, which are arranged in a row ("array"). A group of transducers is activated simultaneously. For scanning, the whole group of elements is shifted. With a curved arrangement of transducers, an image detail can be represented as a circle segment.

Electronic scanners (phased arrays) Every transducer element of an array can be accessed for both sending and receiving with an individual adjustable delay.

Geek Box 11.1: 3-D Ultrasound

In 3-D ultrasound imaging, several 2-D images (B-mode) at different angles (w. r. t. axial direction) are combined into one 3-D volume. Real-time processing and visualization (rendering) of 3-D ultrasound images (volumes) requires high computational power, where graphics processing units can be used. Arbitrary section planes and "virtual travels through the body" are possible. The first 3-D ultrasound system was reported by Kazunori Baba in 1984. Slowly but steadily, 3-D ultrasound is becoming the standard of care in various medical fields (e. g., echocardiography), where 2-D imaging was traditionally used. One common application is to show their children to parents even before birth. An example is found right below this text.

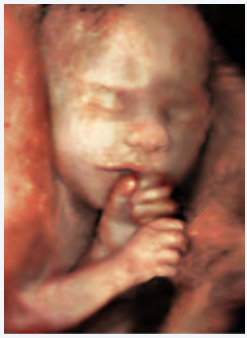

11.3.4.3 M-Mode (Motion Mode)

In motion mode, ultrasonic pulses are emitted from the transducer in quick succession without movement of the transducer. Either an A-mode or a B-mode image is acquired each time. This allows for time-dependent measurement of organ movement relative to the probe. Thus, the velocity of specific organ structures can be obtained. This can be useful, for instance, when the movement of the cardiac wall (myocardium) is to be analyzed (echocardiography).

11.4 Safety Aspects

Ultrasound imaging offers many benefits over other imaging techniques, including:

- Non-invasiveness (no injections or needles in most cases) and mostly painless.

Geek Box 11.2: 3-D Ultrasound

Medical Doppler ultrasonography enables the measuring and visualization of blood flow (blood velocities). Two modes are frequently used: continuous wave (CW) Doppler and pulsed wave (PW) Doppler. In CW Doppler, half of the transducer array emits, and the other half detects pulses. It has the advantage that it allows for continuous imaging due to simultaneous emission and detection. However, no distance information can be measured. In PW Doppler, which is pulse-based, distance information can be obtained using time-gating. However, no continuous imaging is possible.

Doppler ultrasonography exploits the well-known *Doppler effect*. The Doppler effect is named after its discoverer Christian Johann Doppler (1803–1853) and can be observed in various situations, for instance, the noise of the siren of the ambulance when an ambulance passes at high speed. Other examples can be found in astronomy: the astronomical red-shift. Most relevant to medical Doppler ultrasonography, however, is blood flow, i. e., Doppler ultrasonography can visualize blood velocities. The Doppler effect describes the change in wave frequency by a relative movement between *source* and *observer*. A characteristic frequency shift appears, which is proportional to the relative velocity. Doppler ultrasonography aims at measuring the shift in frequency to estimate velocities (e. g., of blood in vessels).

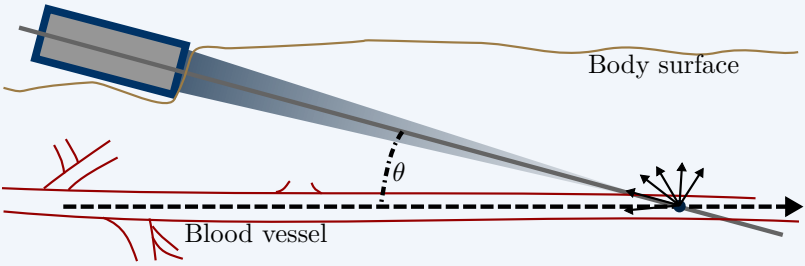

In Doppler blood flow imaging, the *source* are the moving blood cells, at which the waves scatter. The *observer* is the ultrasound transducer. The smaller the angle between the direction of blood flow in the vessel and the ultrasound wave direction, the better the Doppler effect can be exploited.

- Image acquisition is fast and relatively easy to learn.
- No ionizing radiation (contrary to X-ray/CT).
- Large number of potential applications: ultrasound can visualize structure, movement, and function of the body's organs and blood vessels.

However, ultrasound waves can harm the body:

- through heating, proportional to absorbed acoustic intensity, or
- through *cavitation*, which means gas bubbles that emerge in the low pressure phases of sound waves and collapse at high pressure phases.

Since acoustic intensities for medical diagnostics are rather low, the potentially harmful effects described above have proven to be harmless. Medical ultrasound is considered one of the least harmful imaging techniques available today and is even used during pregnancy.

Therapeutical use of ultrasound can be found in gallstone and kidney stone therapies, where high intensity localized ultrasound is used to break up the stones. The heating effect of ultrasound waves can further be used to destroy diseased or cancerous tissue.

Further Reading

[1] Olaf Dössel. *Bildgebende Verfahren in der Medizin: Von der Technik zur medizinischen Anwendung*. Springer, 1999. ISBN: 978-3-540-66014-9.
[2] G Goretzki. *Medizinische Strahlenkunde: physikalisch-technische Grundlagen*. Elsevier, Urban und Fischer, 2004. ISBN: 978-3-437-47200-8.
[3] Paul Suetens. *Fundamentals of Medical Imaging*. Cambridge University Press, 2009. ISBN: 978-0-521-51915-1.

Chapter 9

Strategies for Hardware Reduction on the Design of Portable Ultrasound Imaging Systems

D. Romero-Laorden, J. Villazón-Terrazas,
O. Martínez-Graullera and A. Ibáñez

Additional information is available at the end of the chapter

http://dx.doi.org/10.5772/55910

1. Introduction

In the last decade, ultrasonic imaging systems have been an essential tool for diagnosis in medical and industrial applications, especially in the Non Destructive Testing area (NDT). Conventional ultrasonic imaging devices produce high quality images with good resolution and contrast. However, these machines are usually associated to a high cost in hardware resources, as well as in the time required for the data acquisition and processing stages. This fact hinders the development of good quality, compact and low-power systems that can operate in a wide range of real-time applications.

In this sense, the Synthetic Aperture techniques (SAFT) have demonstrated to be an effective method to achieve these goals, minimizing the size of the systems and accelerating the image acquisition processes. Consequently, both power consumption and overall cost of the systems can be reduced making possible their miniaturization and portability. Conventional SAFT techniques are based on the sequential activation in emission and reception of every transducer element. Once all acoustic signals have been stored in memory, a beamforming process is applied in a post-processing stage in order to focus the image dynamically in emission and reception, obtaining the maximum quality at each image pixel. Despite of this, conventional SAFT techniques present some inconveniences which are summarized in the following points:

1. **Artifacts**. Conventional SAFT techniques produce grating lobes in the images due to the acquisition processes.
2. **Low contrast**. As a consequence of firing only one element at time the received signals have low signal-to-noise ratio, which results in low contrast images that are not feasible for regular imaging visualization (e.g. echography imaging needs very good images in order to reduce the fails in the diagnostic).

3. **Medium penetration**. And for the same reason, the penetration deep of ultrasound in the region of interest is smaller than the achieved using conventional imaging techniques (e.g. needed by cardiac imaging or industrial inspections).

In order to reduce some of these drawbacks, more sophisticated SAFT techniques have been proposed. Total Focusing Method (TFM) [1] is one of them, where each array element is sequentially used as a single emitter and all array elements are used as receivers. Thus, it is possible to obtain a set of $N \times N$ signals (Full Matrix Array capture, FMA) that is used to form the image. According to the description of professors Drinkwater and Wilcox [1–3], its name refers to the possibility of implementing dynamic focusing in emission and reception, which enables to obtain images perfectly focused at all points in the region of interest. However, the complexity of the acquisition process and the computational requirements of the beamforming make this method not appropriate for real-time purposes [1]. Other solutions that use an emission and reception sub-aperture have been also proposed [4–6], although they maintain a certain degree of hardware complexity (focussing is needed in emission and reception) and also require intensive computational capabilities to produce a real-time ultrasonic image.

To overcome the last inconveniences we propose a SAFT methodology based on a new paradigm, known as coarray [5, 6], which allows to use only one element in emission and a limited number of parallel channels in reception at each time. With the proposed solution, a strategy for a hardware reduction in ultrasonic imaging systems is possible, and it involves the following aspects:

- Optimization of the acquisition strategies to achieve the completeness of the coarray with a minimum number of hardware elements. In this sense, our objective is to establish a trade-off between the number of electronic channels, image quality and acquisition velocity [6].
- The use of pulse compression techniques to overcome the reduced capability of penetration when emission is limited to one element [5].
- The development of GPGPU[1] parallel beamforming techniques to achieve real time imaging [7].

This chapter is divided into two main sections. The first one is dedicated to analyse the use of the coarray paradigm as a tool for the design of ultrasonic imaging systems and to present several minimum redundancy coarray techniques. Moreover, Golay codes are presented and their integration within the presented SAFT methods is described. The second section presents the general ultrasonic imaging system's overview, its architecture and the parallel beamforming as a solution for ultrafast beamforming. Finally, we expose our conclusions and future research developments.

[1] General-purpose computing on Graphics Processing Units is the utilization of a graphics processing unit (GPU), which typically handles computation only for computer graphics, to perform computation in applications traditionally handled by the central processing unit (CPU). http://gpgpu.org

http://dx.doi.org/10.5772/55910

2. Coarray: New paradigm for the design of imaging systems

This section is focused on the development of ultrasonic imaging systems based on the pulse/echo aperture model which is known as coarray. In order to clarify this point, we are going to briefly review this mathematical concept and its principal implications.

The coarray is a mathematical tool that is often used by several authors as a way to quickly study the radiation properties of an imaging system [5, 6, 8, 9]. This concept is frequently referred to as *effective aperture* in ultrasound literature, and it basically is the virtual aperture which produces in one way the same beam pattern as the real aperture working in emission and reception as Figure 12 suggests.

Suppose a linear array with N elements. In far-field and assuming very narrow band signals, the radiation pattern could be written as:

$$f(u) = \sum_{n=0}^{N-1} a_n e^{jkx_n u} = \sum_{n=0}^{N-1} a_n e^{jkndu} = \sum_{n=0}^{N-1} a_n (e^{jkdu})^n \tag{1}$$

where a_n are the complex weights of the transducers and $u = sin(\theta)$ being θ the angle measured from the perpendicular to the array. Substituting e^{jkdu} by the complex variable z, the radiation pattern can be expressed as a polynomial, which corresponds with the Z-Transform of the sequence a_n. Thus, considering a pulse-echo system, the complex radiation pattern will be the product of two polynomials with degree $N-1$:

$$f_{total}(z) = Z\{c_n\} = \sum_{n=0}^{2N-2} c_n z^n = \sum_{n=0}^{N-1} a_n z^n \cdot \sum_{n=0}^{N-1} b_n z^n \tag{2}$$

where a_n and b_n are the gains applied to the transducers in emission and reception, and c_n is the coarray ($Z\{c_n\}$ represents the Z-Transform of the sequence c_n). Returning to the unit circle ($|z| = 1$, $z = e^{jkdu}$) and considering equation 1 then the radiation pattern of the system in continuous wave is directly the DFT of the coarray [10].

In synthetic aperture systems, each scanned image is obtained after several firing sequences of the elements. According to this, the coarray can then be expressed as a sum of several sub-coarrays. Each of these sub-coarrays will be obtained as the convolution of two sub-apertures that represent the weights of the active elements used to emit and receive the signals each time.

Figure 1 illustrates the coarray generated by TFM method, which has been applied in ultrasound area since the late 60's and early 70's [11, 12]. As we briefly introduced in Section 1, it consists on the sequential emission with each one of the array elements in turn, and the reception in each shot with the full transducer aperture. As we can see, its coarray is fully populated what ensures a grating-lobe free radiation pattern.

The image quality achieved when TFM is employed is the highest possible, but it has, as its counterpart, the huge volume of data which is necessary to acquire. Thus, it requires more storage resources and processing capability than other techniques, which makes difficult its

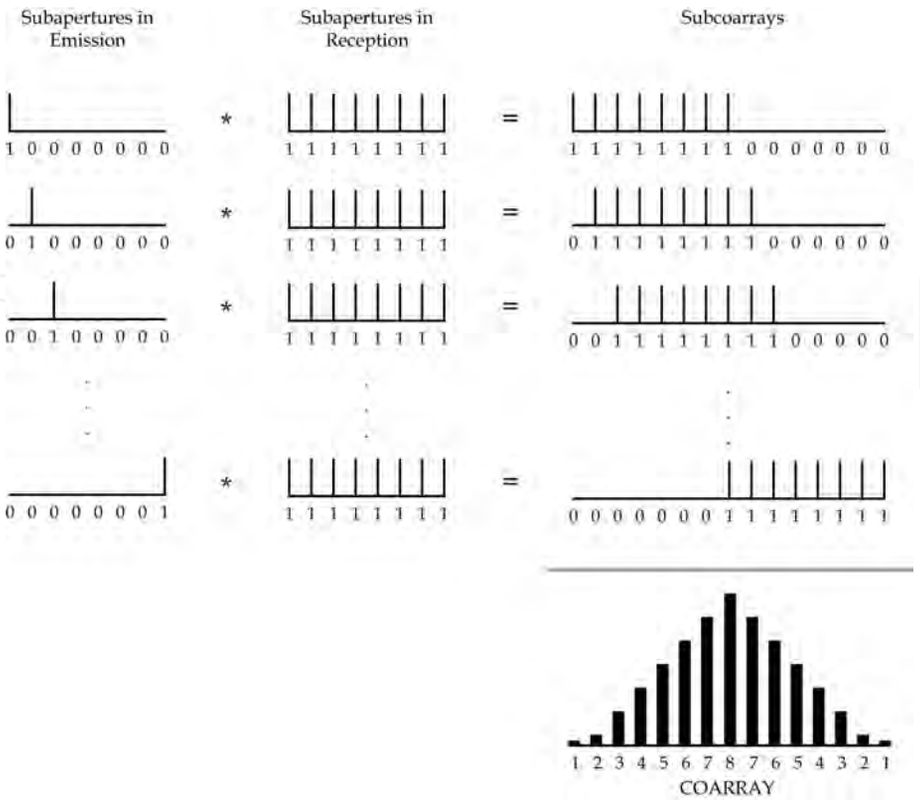

Figure 1. Firing sequences of the elements in TFM, and its corresponding generated coarray

practical implementation with todays' technology. To illustrate this, consider the following example: a 15 cm depth image, 40 MHz sampling rate, 64 channels, 1500 m/s medium velocity and 2 bytes per sample. Each firing generates approximately 1 MB of pulse-echo data, what supposes 64 MB of data to generate a single image frame when TFM is applied. For a frame rate of 20 images per second, it would be necessary to acquire and process 1.2 Gbytes of data per second.

The bandwidth of most I/O standards available today put in evidence that any of current data protocols can not deal with TFM requirements. Supposing a good efficiency and use of the resources (around 80)%, USB 2.0 port (released in April 2000) would be able to transfer less than one image per second (48 MB/s). A similar situation occurs if USB 3.0 (released in November 2008) is employed, being the maximum transmission speed up to 480 MB/s allowing to transfer around 7 images per second, even far respect to the maximum number of images which could be theoretically achieved. Finally, the most recent standard released in February 2011, known as Thunderbolt port and developed by Intel [13], combines PCI Express and DisplayPort into a new serial data interface that can be carried over longer and less costly cables. Thunderbolt has twice the transfer speed of USB 3.0 over copper wire (960 MB/s) giving us transferences of 14 images per second.

Therefore, it is clear that a reduction of data volume is desirable. In this sense, applying the coarray concept permits us to propose system designs that use less channels simultaneously working in emission and reception, but maintaining the same level of image quality. The key point for this is to use the coarray to search for solutions of minimum redundancy. This approach in conjunction with parallel computing techniques will offer an increment of

http://dx.doi.org/10.5772/55910

acquisition velocity maintaining the highest quality and producing high frame rates with low power consumption. This topic will be the main focus of next two sections.

2.1. Minimum redundancy coarray solutions

Coarray analysis identifies which emitter-receiver combination completes each of its elements. In the TFM method seen before, we find that some of the elements are formed by a single signal (in concrete boundary elements) while the others increase progressively until reaching coarray centre with a value of N elements (Figure 1). Thus, we can consider as a minimum redundancy coarray that in which each element is composed of only one signal. Therefore, using the minimum possible number of signals the aperture's diffraction properties can be improved by manipulating the gain of the elements. With this goal in mind, it is possible to establish several strategies which maintain a balance between the number of parallel channels and the number of shots during acquisition processes.

2.1.1. 2R-SAFT acquisition strategy

2R-SAFT technique [14] has some particular advantages that make it very useful for ultrasonic imaging systems. 2R-SAFT uses only one element to transmit and two elements to receive. As it is shown in Figure 2, all elements are consecutively activated as single emitters, without the use of any beamformer in emission. At each shot, two consecutive channels are used as receivers requiring to store two signals per emission.

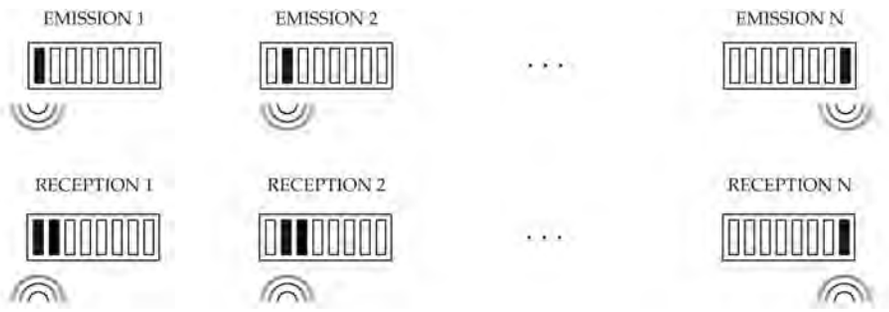

Figure 2. Firing sequences of the elements in 2R-SAFT

Thus, when the i^{th} element is used to emit a waveform, i and $i+1$ elements are used for receiving signals. For the last element of the array, only one signal is recorded. By employing an emitter in each shot all the received signals are completely uncorrelated, containing only information of a single transmitter-receiver pair.

Figure 3 shows the coarray generated when 2R-SAFT is employed. As we can observe, the coarray is fully populated ensuring the suppression of grating lobes in the radiation pattern which produces good quality images [14, 15].

2.1.2. Accelerated-SAFT acquisition strategy

Here we present a minimum-redundancy technique we have denominated Accelerated-SAFT or, in its short form, kA-SAFT. The k subscript refers to the acceleration factor carried out during the acquisition stage which can go from 2x to Nx depending on the number of

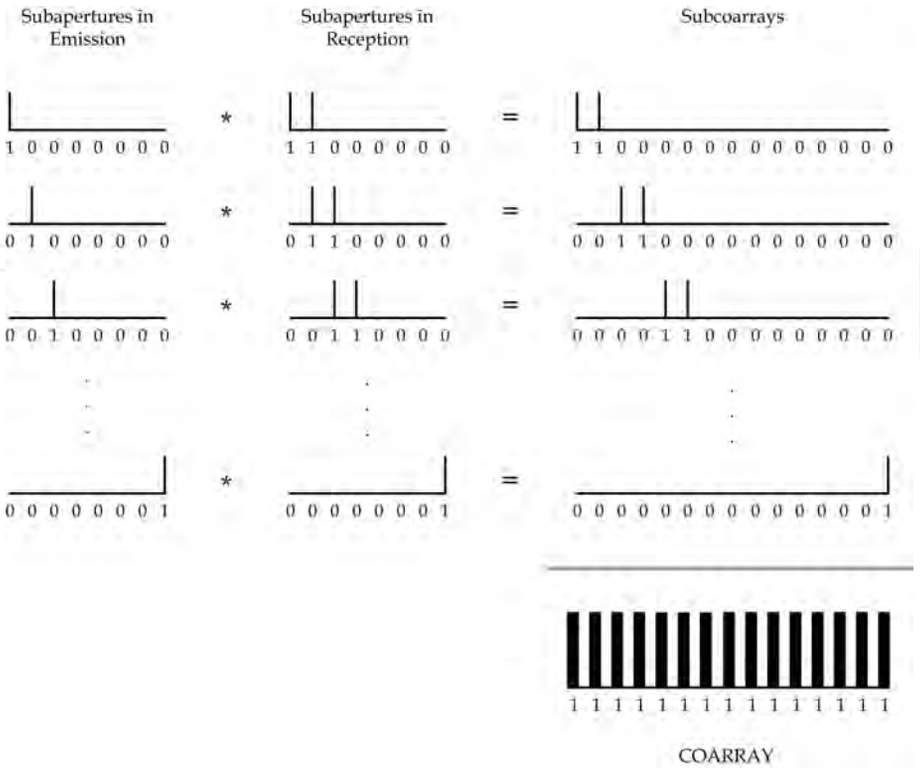

Figure 3. Coarray sequences for 2R-SAFT

channels used for the reception. This strategy increases a little bit the cost involved in the acquisition system respect to 2R-SAFT, but at the same time, reduces the number of shots by k times.

The kA-SAFT uses n_A consecutive elements to receive and a single element to emit which is centred in the active subaperture. As shown in Figure 4, the elements on emission are sequentially activated with a shift of $\frac{n_A}{2}$ elements. At each shot n_A consecutive channels are used as receivers, needing to store n_A signals per emission except for the first and the last array elements where half of the signals is acquired.

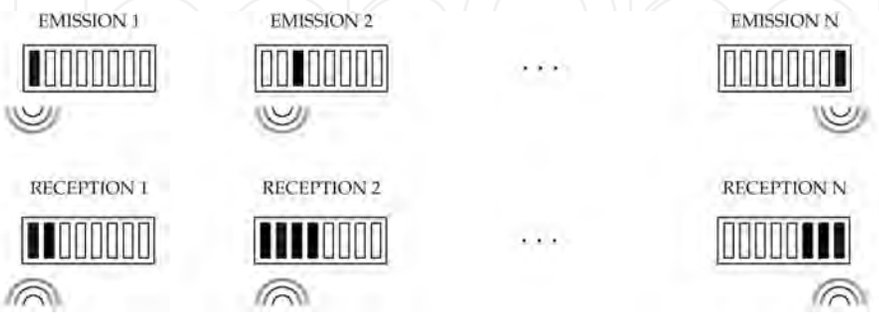

Figure 4. Firing sequences of the elements in kA-SAFT being k = 2x and $n_A = 4$

In this sense, when the i^{th} element is used to emit the elements that are going to use as receivers are given by:

http://dx.doi.org/10.5772/55910

$$Elements_{rx} = \left\{ i - \frac{n_A}{2} + j \right\} \qquad 0 \leq j \leq n_A \tag{3}$$

Figure 5 shows the coarray generated when kA-SAFT is employed for the case of $n_A = 4$. As we can observe, the coarray is identical to that obtained with 2R-SAFT (Figure 3) preserving all its advantages but multiplying by 4 the frame rate in acquisition.

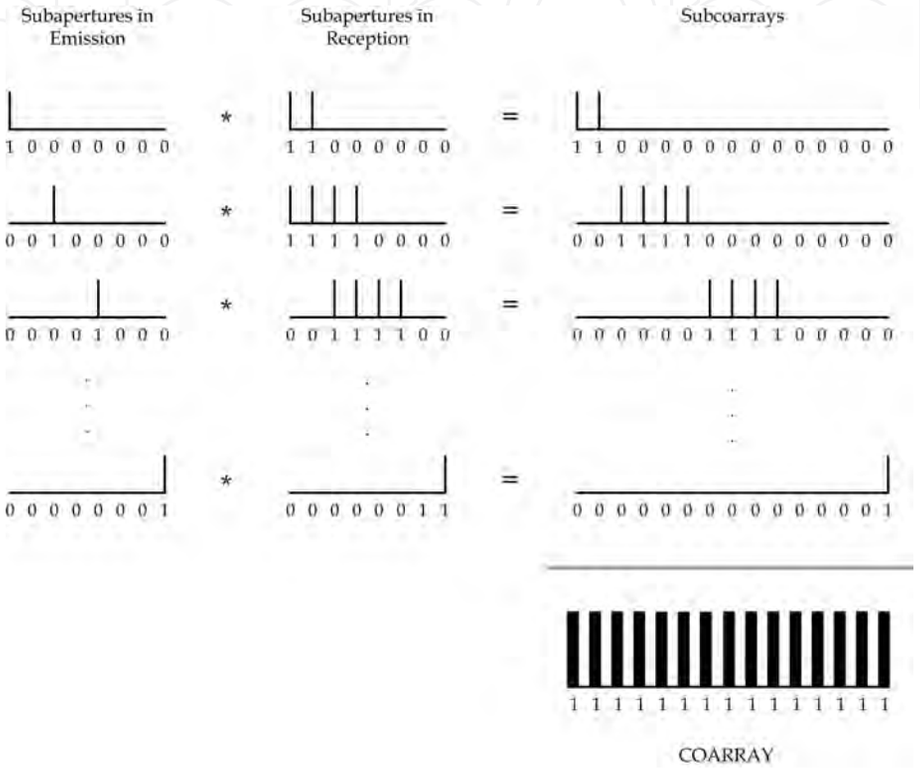

Figure 5. Coarray sequences for kA-SAFT being k = 2x and $n_A = 4$

2.1.3. Experimental results

We present some experimental results that have been done on a tissue phantom (Model 040GSE - CIRS Inc.) with 0.5dB/cm attenuation, where several cysts and wires of 0.1mm diameter are located at different depths (Figure 6). We have used a 2.6MHz phased array transducer with $N = 64$ elements, 0.28mm of pitch (Vermon Inc.) for the measurements. We will use the Total Focusing Method as a reference model to examine the cysts and wires in the tissue covering an area starting from 25mm to 80mm depth, and we will compare it to 2R-SAFT and kA-SAFT techniques. All images have been obtained by applying the DAS algorithm. TFM uses the complete set of signals N^2 = 4096 while 2R-SAFT and kA-SAFT images have been calculated using $2N - 1$ = 127 signals.

In Figure 7, images for all strategies are presented. It is easily observed how Figures 7(a,b,d,e,g) are very similar in terms of quality. Consequently, the strategy to be chosen relies fundamentally on the hardware requisites.

Nevertheless, at a depth greater than 60 mm none reaches the same contrast level as TFM (Figure 7(h)), highlighting the limited signal to noise ratio suffered by all minimum

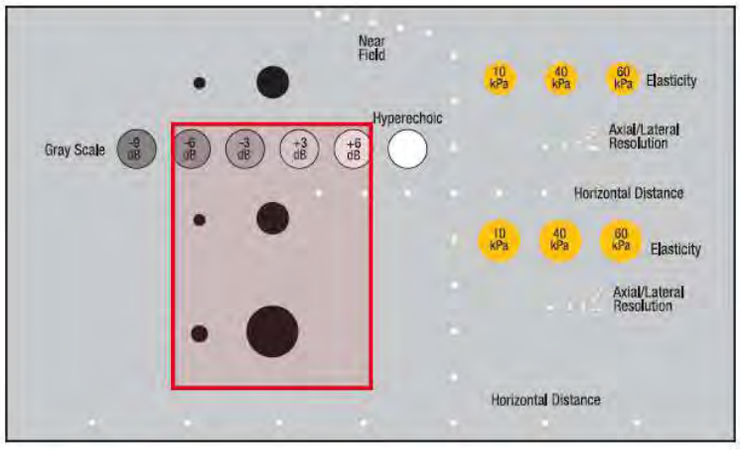

Figure 6. Region of interest analysed from tissue phantom model 040GSE by CIRS Inc.

redundancy techniques. In table 1, a comparison between the number of channels in emission and reception, number of firings, acquisition frame rates and memory buffers needed is performed for the different strategies presented. As we can see, TFM is the technique which more storage as well as more hardware channels needs. By contrast, minimum redundancy techniques requisites are more affordable and suitable for applications where size matters.

Strategy	Channels (tx,rx)	Firings	Framerate	Buffer
2R-SAFT	(1,2)	$N_{firings} = N$	$f_{frame} = \frac{f_{prf}}{N}$	$2N-1 \times L$
2xA-SAFT ($n_A = 4$)	(1,4)	$N_{firings} = \frac{N}{2}$	$f_{frame} = 2\frac{f_{prf}}{N}$	$2N-1 \times L$
4xA-SAFT ($n_A = 8$)	(1,8)	$N_{firings} = \frac{N}{4}$	$f_{frame} = 4\frac{f_{prf}}{N}$	
8xA-SAFT ($n_A = 16$)	(1,16)	$N_{firings} = \frac{N}{8}$	$f_{frame} = 8\frac{f_{prf}}{N}$	
16xA-SAFT ($n_A = 32$)	(1,32)	$N_{firings} = \frac{N}{16}$	$f_{frame} = 16\frac{f_{prf}}{N}$	
TFM	(1,N)	$N_{firings} = N$	$f_{frame} = \frac{f_{prf}}{N}$	$N^2 \times L$

Table 1. Comparison of the several acquisition strategies presented

2.2. Golay Codes

As we have seen, synthetic aperture images have low contrast due to the poor signal to noise ratio (SNR). Along this section, we will study how the use of pulse coding based on Golay codes [16, 17] can help to improve the dynamic range and SNR, in order to achieve an image quality comparable to that of Total Focusing Method.

2.2.1. Golay encoding for ultrasonic excitation

Golay complementary pairs have been widely used for transducer excitation because the sum of its auto-correlation function has a main peak and zero side-lobes [16]. A complementary pair is composed of two binary sequences, $A[n] = [a_0, a_1, \ldots, a_{N-1}]$ and $B[n] = [b_0, b_1, \ldots, b_{N-1}]$, of the same length N such that $a_i, b_i \in \{-1, +1\}$.

http://dx.doi.org/10.5772/55910

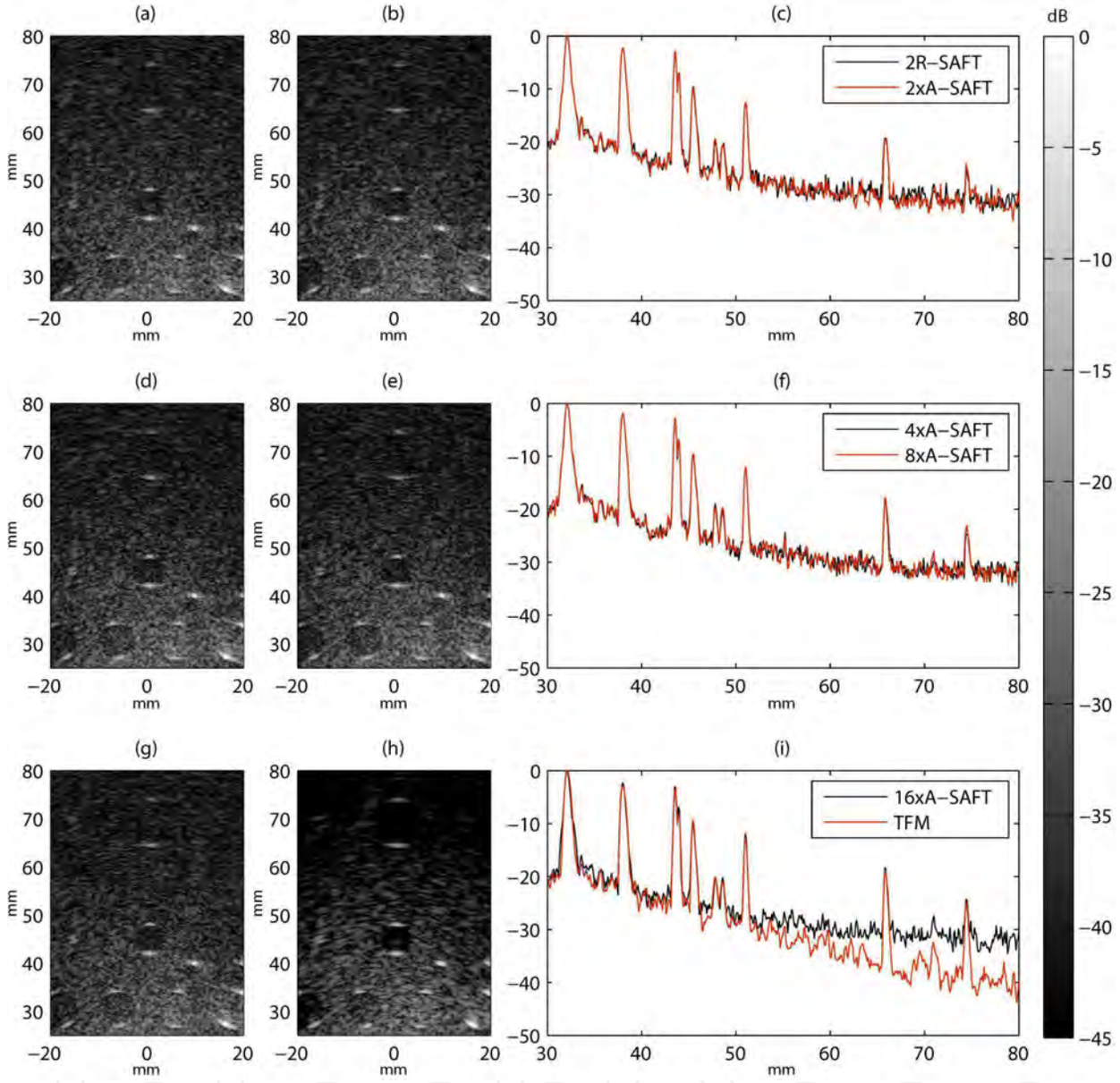

Figure 7. Experimental images from tissue phantom. (a) 2R-SAFT, (b) 2xA-SAFT, (c) Lateral profiles comparison between 2R-SAFT and 2xA-SAFT, (d) 4xA-SAFT, (e) 8xA-SAFT, (f) Lateral profiles comparison between 4xA-SAFT and 8xA-SAFT, (g) 16xA-SAFT, (h) TFM, (i) Lateral profiles comparison between 16xA-SAFT and TFM

The auto-correlation functions of $A[n]$ and $B[n]$ have side lobes with equal magnitude but opposite sign. The sum of these independent auto-correlation functions provides an ideal delta function according to:

$$C_A[n] + C_B[n] = \begin{cases} 0, \, n = 0 \\ 2N, \, otherwise \end{cases} \tag{4}$$

where $C_A[n]$ and $C_B[n]$ are the auto-correlation functions of $A[n]$ and $B[n]$, respectively, for any integer n satisfying the equation 4. The construction of Golay code pairs is done recursively with the *"negate and concatenate"* method, a technique used by Golay [16] to create longer pairs from shorter hand-constructed given pairs. Specifically, if $A[n]$ and $B[n]$ are the N-digit binary representations of a complementary pair of codes, then a new pair of complementary codes $A'[n]$ and $B'[n]$ of length $2N$ can be formed by concatenating $B[n]$ to $A[n]$ and concatenating $\sim B[n]$ to $A[n]$ where $\sim B[n]$ is the complement of $B[n]$. Thus, $A'[n] = A[n] \mid B[n]$, and $B'[n] = A[n] \mid \sim B[n]$.

One of the major drawbacks of Golay codes is that two shots are needed for each emitting element in order to complete both A and B codes respectively. In our work, Golay codes of length equal to 8 bits have been used, being $A[8] = [+1+1+1+1+1-1-1+1]$ and $B[8] = [+1-1+1-1+1+1-1-1]$, producing a gain of 24dB according to equation 4.

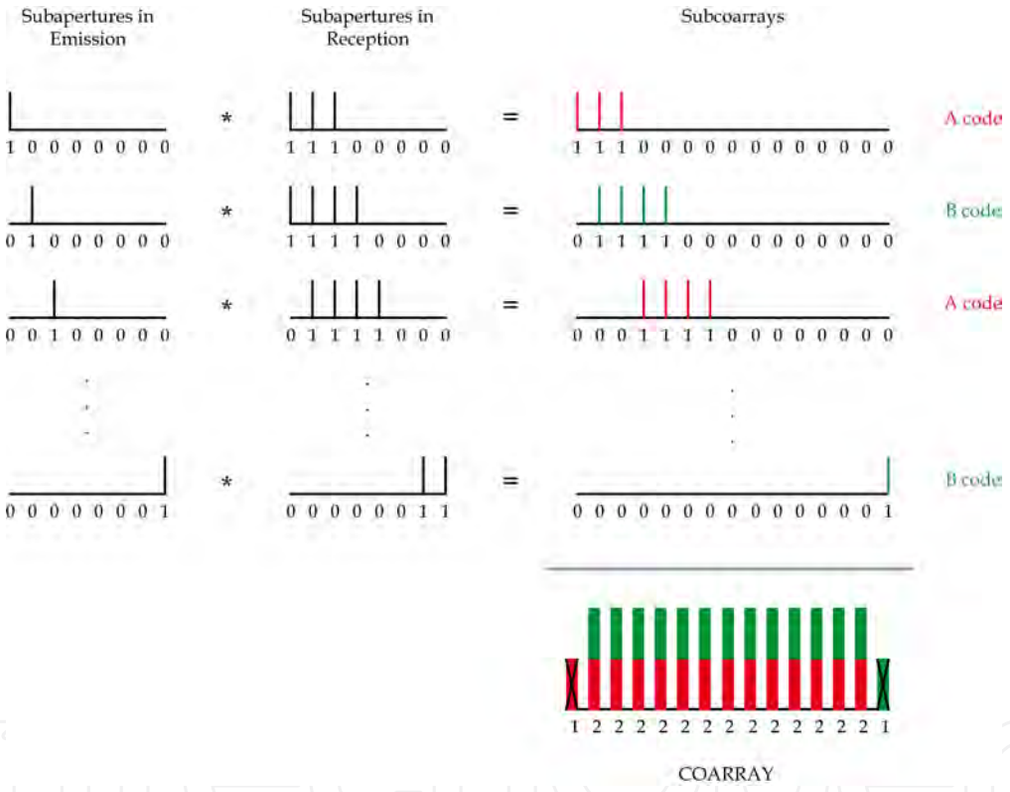

Figure 8. Golay encoding integration example

2.2.2. Coarray for Golay encoding

Golay codes, described previously, and minimum redundancy techniques can be combined. In order to illustrate how this can be done, Figure 8 shows an example using a 4R-SAFT (four receivers) [15] plus Golay codes. Here, two signals per coarray element are acquired and because Golay encoding needs to fire twice, A or B codes are alternated between shots.

This process is mathematically identical for the formerly presented strategies 2R-SAFT and kA-SAFT but with some particularities:

http://dx.doi.org/10.5772/55910

1. The number of channels in reception (sensors) must double the original number, in order to have two signals per coarray element for A and B codes.
2. The amount of acquired data signals also doubles the original, because of the first point.
3. The original firing rate is preserved, which means achieving identical performance at the expense of doubling the hardware involved in the reception process.

2.2.3. Experimental results

With the use of Golay codes to image the same area than in previous results, the panorama has changed. As before, TFM image has been composed from the complete set of signals N^2 = 4096, but now 2R-SAFT and kA-SAFT have been calculated using $4N - 2$ = 254 signals. From Figure 7 in section 2.1.3, where the corresponding images with no encoding were analysed, it can be seen how the reduction in the number of signals employed produces a loss of dynamic range respect to TFM method. Thus, with the use of Golay codes in Figure 9 we can observe how the contrast and level of detection have substantially increased. Now, both 2R-SAFT and kA-SAFT techniques distinguish the complete set of defects. Thus, in relation to TFM the number of signals is drastically reduced from N^2 to $4N - 2$, accelerating acquisition and processing velocities and the system's frame rate.

3. Ultrasonic imaging system

3.1. General system's overview

As we have said, our goal is centred in the design of ultrasonic imaging systems based on solutions which require fewer resources and storage capacity than conventional systems. Thus, in Figure 10 is schematically represented our vision of the system, which is composed by three parts:

1. **The array or probe**. It is usually composed by 64, 96, 128 or even more transducers depending on the type of application.
2. **Acquisition subsystem**. The hardware subsystem used for transducer excitation and data acquisition (represented by the box in the center). Nowadays, several electronic manufacturers have in their catalogues electronic boards and systems, which are small and can be easily used for our purposes. For example, National Instruments has 32-channel digitizer module capable of sampling on all channels at 50 MS/s with 12-bit resolution. The module is optimized for ultrasound applications [18]. Additionally, both multiplexer and bipolar programmable pulser are required. Specific architectures depending on the type of acquisition strategy will be studied in the next section.
3. **Image generation subsystem**. It is the software system which can take place in any computational device (PC, laptop, ...) shown on the right side of Figure 10. These processes include the digital signal pre-processing of the received signals and filtering; beamforming of the image, delaying and adding signals according to emission and reception lenses, post-processing the image and its representation to properly show data on the screen. To achieve these tasks, the use of GPU's great power for parallel computing will allow us to quickly and efficiently accelerate the algorithms.

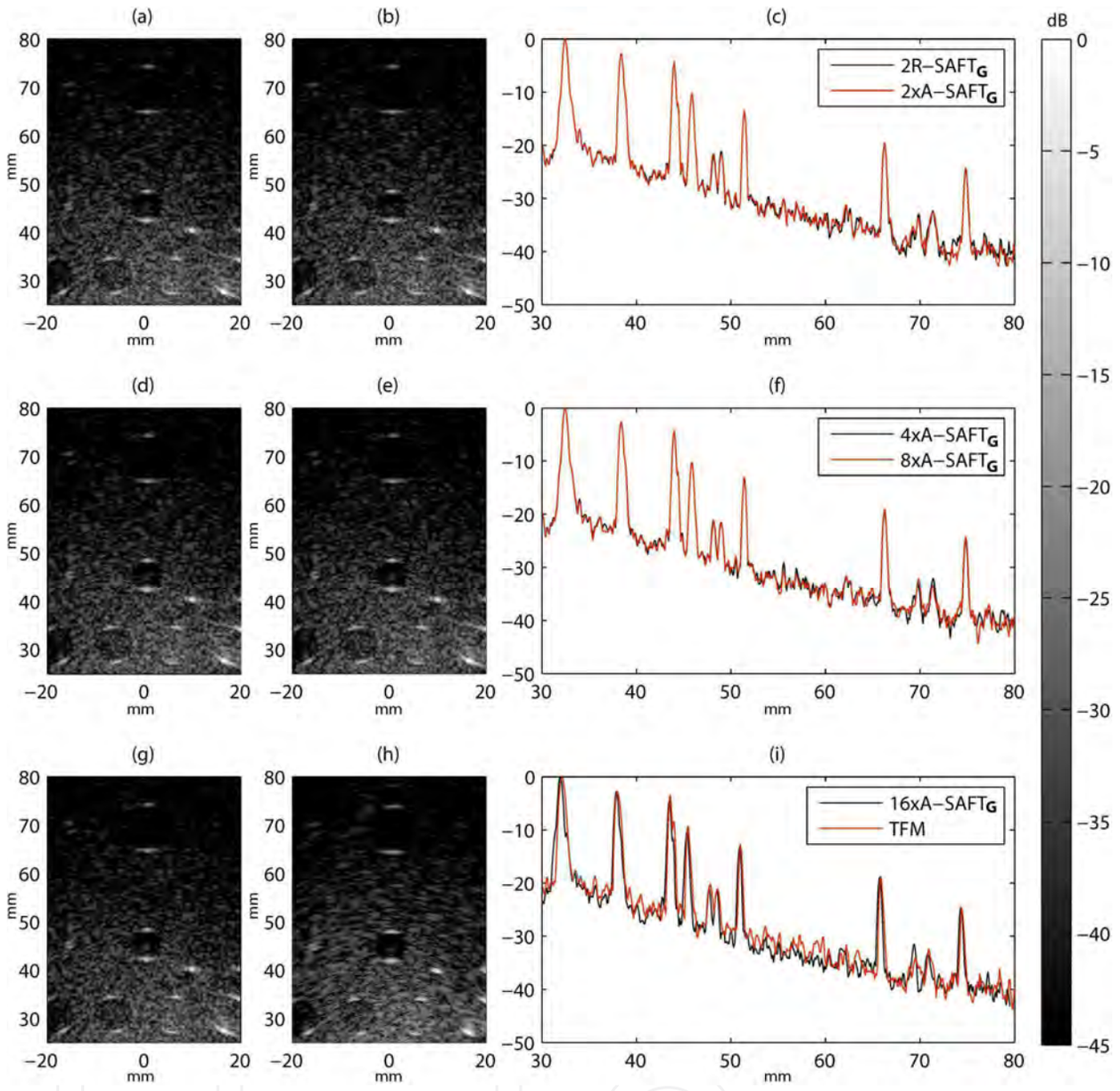

Figure 9. Experimental images from tissue phantom. (a) 2R-SAFT + Golay, (b) 2xA-SAFT + Golay , (c) Lateral profiles comparison between 2R-SAFT + Golay and 2xA-SAFT + Golay, (d) 4xA-SAFT + Golay, (e) 8xA-SAFT + Golay, (f) Lateral profiles comparison between 4xA-SAFT and 8xA-SAFT + Golay , (g) 16xA-SAFT + Golay, (h) TFM , (i) Lateral profiles comparison between 16xA-SAFT and TFM

3.2. Acquisition subsystem

In this section, two acquisition architectures are exposed. On one hand, a minimal system for 2R-SAFT strategy which allows a low-cost and small imaging system and, in the other hand, the architecture which implements 8xA-SAFT plus Golay encoding strategy and uses more hardware but yields better quality images. Which strategy to use depends on the concrete application. Any of these configurations can be carried out using boards systems available in the market.

http://dx.doi.org/10.5772/55910

Figure 10. Hardware/Software system proposed

3.2.1. 2R-SAFT architecture

As we study in section 2.1.1, it is basically composed of one channel in emission and two channels in reception. Figure 11 shows the complete architecture for 2R-SAFT implementation. As we can see, a multiplexer is connected to the transmission channel for sequentially activate each element as an emitter, and a second multiplexer will be on charge of connecting the selected elements to both reception channels.

All the acquisition process is managed by a hardware control system which is located in a field-programmable gate array (FPGA). In addition, a local memory is also used to store every received signal. Finally, the signals are transferred to the imaging system using any communication interface (USB, Ethernet, PCI Express). In the imaging system, raw data is stored in a RAM memory of $2N-1$ signals of capacity to be used for compose and beamform the ultrasonic images using a GPU.

3.2.2. 8xA-SAFT with Golay encoding architecture

As we see in sections 2.1.2 and 2.2, and in order to combine 8xA-SAFT with Golay codes, we will double the number of channels in reception to maintain the number of original firings. Thus, in this case the system is composed of one channel in emission and 32 channels in reception as Figure 12 suggests. A multiplexer connects the transmission channel to elements for sequentially activate one of them, in steps of 8 elements, to transmit an A or B code for odd or even shots respectively. A second multiplexer will be on charge of connecting the 32 reception channels to the receiving aperture ensuring that every coded signal is stored in a local memory. Therefore, two signals per coarray element are overlapped, each one belonging to an A or B code respectively. Additionally, an offset is added to the coarray structure in order to centre its elements, and the boundary coarray elements are removed from it as we illustrated in section 2.2.2.

Now the software imaging system requires a bigger memory and an additional decoding stage, where the complete set of signals is deconvolved, generating a $2N-8$ data set. Later on, as usual, the data will be beamformed using the graphics processing unit.

3.3. Image generation subsystem: Parallel beamforming

In recent years, computing industry has been opened a way to parallel computing. Nowadays, all consumer computers ship with multi-core processors. Dual-core processors (CPUs) were introduced in personal systems at the beginning of 2006, and it is currently common to find them in laptops as well as 8 and 16-core workstation computers, which

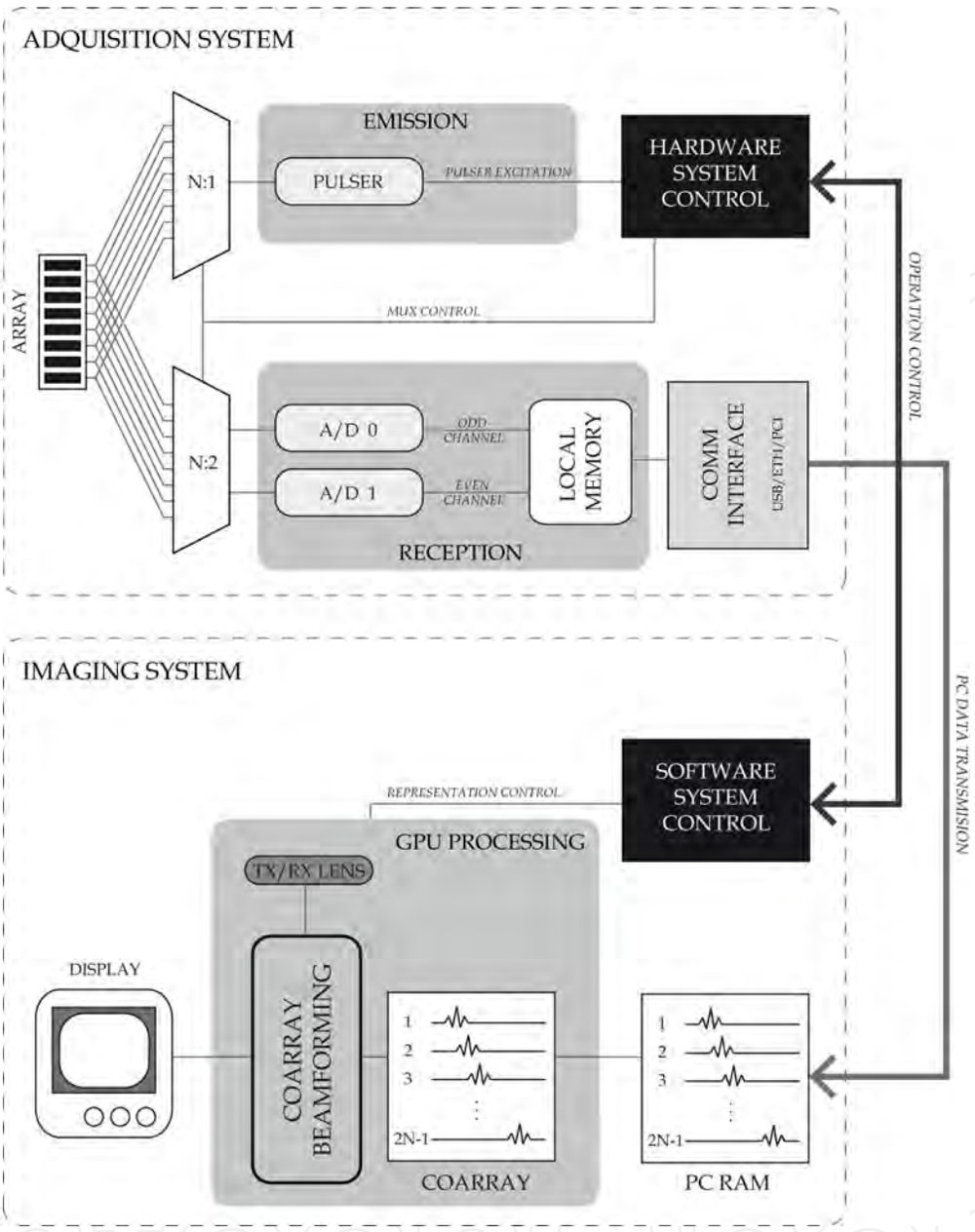

Figure 11. 2R-SAFT Minimal Architecture

means that parallel computing is not relegated to big supercomputers or mainframes computers. However, Graphics Processor Units (GPUs), as their name suggests, came about as accelerators for graphics applications, predominantly those using the OpenGL and DirectX programming interfaces. Although originally they were pure fixed-function devices, the demand for real time and 3D graphics made them evolve into increasingly flexible highly parallel, multithreaded processors with extremely high computational power and very high memory bandwidth converting them into massively parallel machines.

Unlike earlier GPU generations, where computing resources were partitioned into vertex and pixel shaders, nowadays they can be programmed directly in C using CUDA or OpenCL [19], APIs which include a unified shader pipeline, allowing each and every arithmetic logic

http://dx.doi.org/10.5772/55910

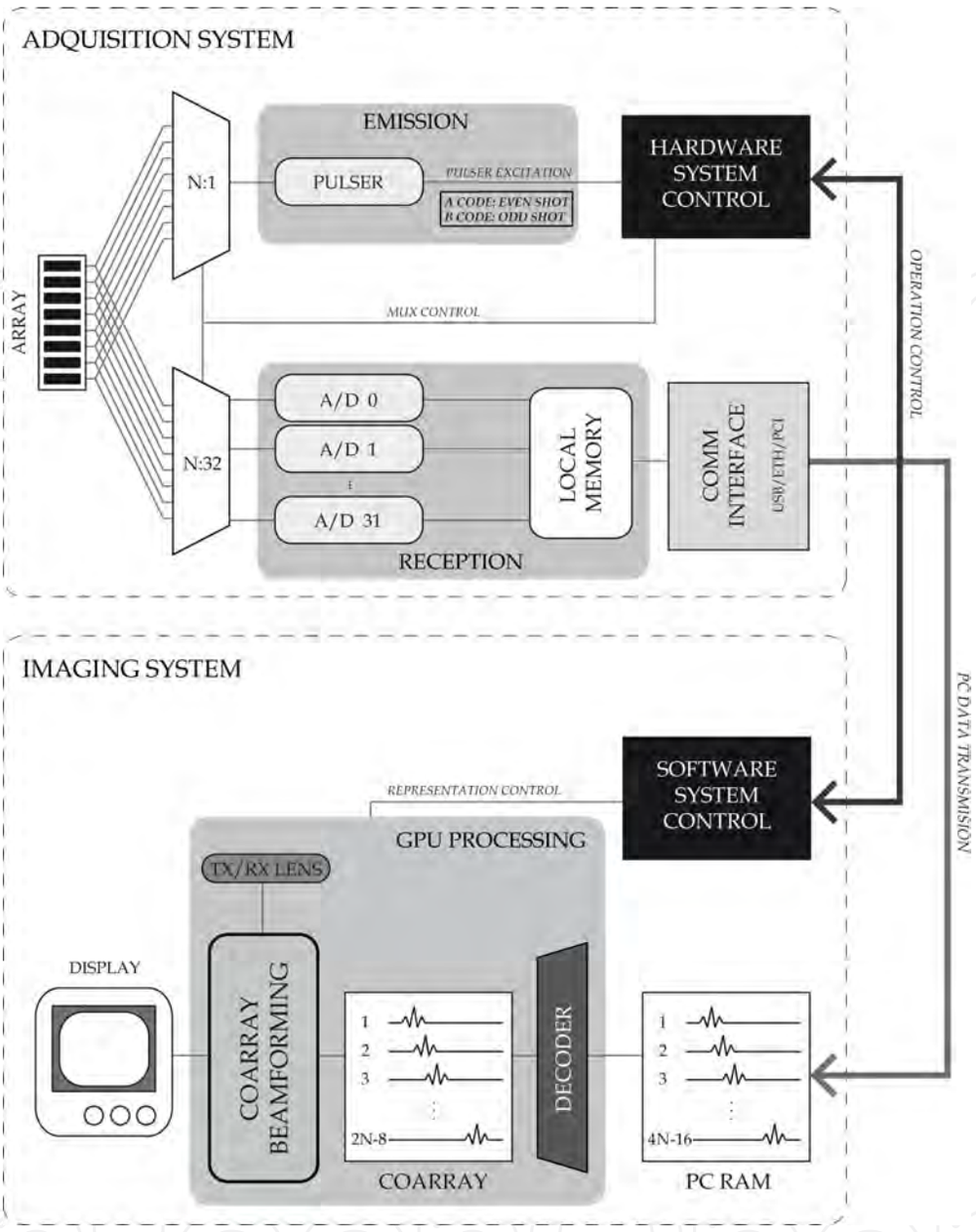

Figure 12. 8xA-SAFT Architecture with 32 channels in reception needed for Golay encoding

unit on the chip to be used by a program intending to perform general-purpose computations (GPGPU). Furthermore, the execution units on the GPU allow arbitrary read and write access to memory as well as access to a software-managed cache known as shared memory. A CUDA program consists of one or more phases that are executed on either the host (CPU) or a device such as a GPU. The phases that exhibit little or no data parallelism are implemented in CPU code. The phases that exhibit rich amount of data parallelism are implemented in the GPU code. The parallel functions (called kernels) typically generate a large number of threads to exploit data parallelism. It is worth noting that CUDA threads are of much lighter weight than the CPU threads. CUDA programmers can assume that these threads take very few cycles to generate and schedule due to efficient hardware support. This differs from

CPU threads which typically require thousands of clock cycles for their generation and their scheduling.

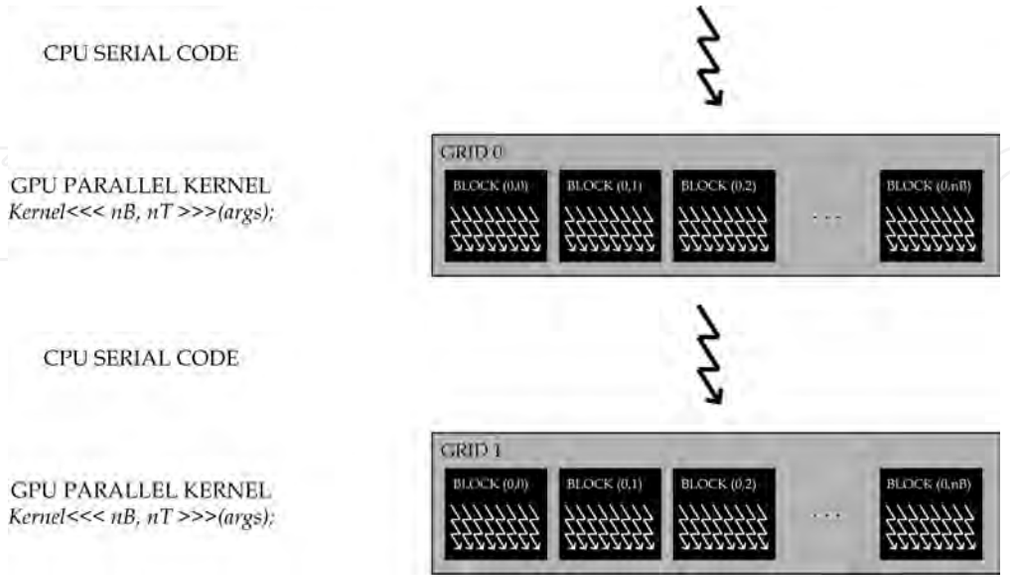

Figure 13. CUDA program execution diagram

The execution of a typical CUDA program is illustrated in Figure 13 where it is observed that the execution starts with host (CPU) execution. When a kernel function is invoked (or launched), the execution is moved to a device (GPU), where a large number of threads are generated to take advantage of huge data parallelism. All the threads generated by a kernel during an invocation are collectively called a grid. Figure 13 shows the execution of two grids of threads. A grid is a 1D, 2D or 3D structure of blocks, and a block is a 1D, 2D or 3D structure of threads. Thus, the program code is composed by classical functions, which run on CPU using only one thread of execution; and kernels, which run on GPU using multiple parallel threads. When all threads of a kernel complete their execution, the corresponding grid terminates, and the execution continues on the host until another kernel is invoked. It is not our purpose to fully cover all the aspects involved in CUDA Architecture. Thus, an extended discussion about the CUDA hardware and programming model is available in multiple sources in the literature [19–21].

Therefore, in this section we will examine different ways to implement the beamforming process on the GPU using the CUDA programming model. From the model, it is extracted that functions which are executed many times independently over different data are the ideal candidates for this kind of computing. In this sense, several algorithms have been implemented to cover the fundamental parts of a conventional Delay-and-Sum Beamformer (DAS) and they have been also evaluated for their performance. This analysis helps to give a better understanding of the GPU architecture and how to write applications for it.

Schematically, Figure 14 show the main stages of a general beamformer. As we can appreciate there are three main operations to be done: pre-processing of signals, beamforming and post-processing. In the software system we propose (Figure 10) all beamforming procedures take place in the GPU.

http://dx.doi.org/10.5772/55910

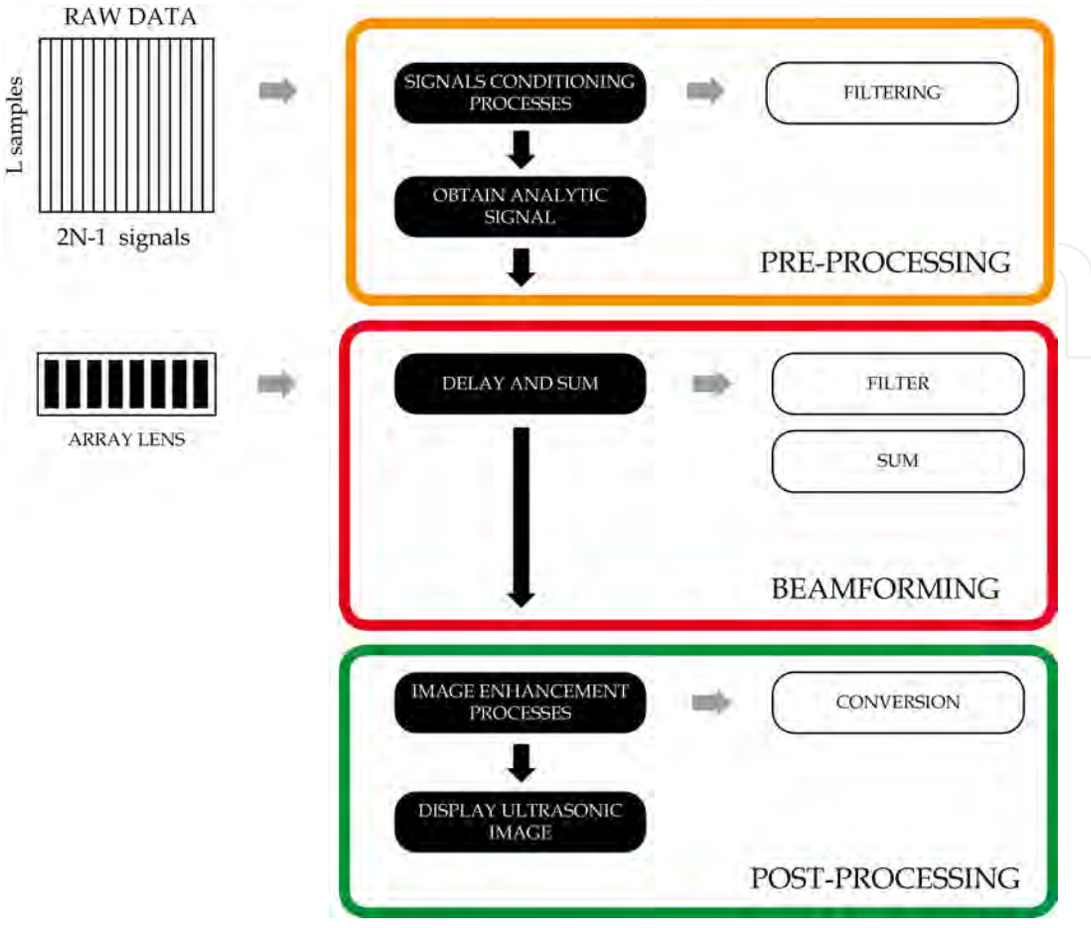

Figure 14. Schematic diagram main parts of a general SAFT beamformer

Implementing the imaging algorithm on GPU systems primarily involves the parallelization of the core algorithm into small independent threads which can be executed by the GPU in runtime. Thus, the imaging process occurs in multiple stages, which follows closely to that has been detailed in Figure 14. Thus, in order to maximize GPUs efficiency and reduce image generation time as much as possible, a specific solution for every different task have been designed. Figure 15 shows how these tasks have been parallelized on the GPU.

The first step consists on copying the complete set of acquired signals from CPU memory to GPU memory. We already know that this transaction is slow, and therefore it is recommended to copy all signals at the same time rather than doing it signal by signal.

3.4. Pre-processing

The pre-processing of the complete set of signals is a fundamental part of the image generation process. Supposing $X_{tx,rx}(t)$ the received signal from any emitter tx and receiver rx pair, a function $H(t)$ is applied to every signal as the following expression suggests:

$$Y_{tx,rx}(t) = X_{tx,rx}(t) \cdot H(t) \tag{5}$$

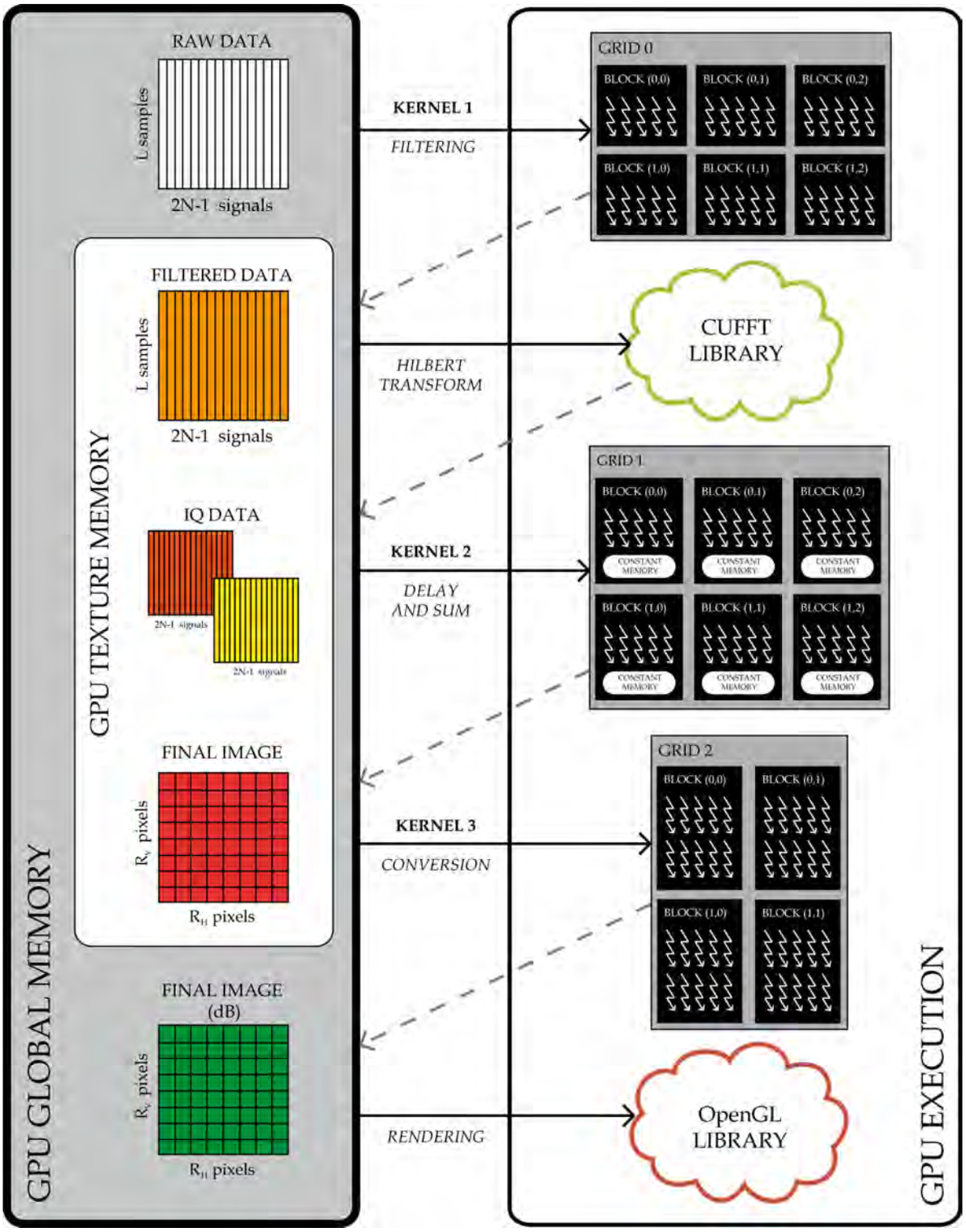

Figure 15. System beamforming loop parallelized on GPU for SAFT implementation

http://dx.doi.org/10.5772/55910

and

$$H(t) = H_F(t) \cdot H_{IQ}(t) \tag{6}$$

where $H_F(t)$ is a signal conditioning process where a filter is applied in order to remove the offset level introduced during the acquisition system and to reduce the noise.

Additionally and for convenience, the acquired signals can be decomposed into their analytic signals form [22] (in-phase I and quadrature components Q) . Thereby, the second function $H_{IQ}(t)$ is the Hilbert Transform in order to reduce errors and artefacts which appear at the envelope detection stage. Then, the signals $X_{tx,rx}(t)$ can now be expressed as:

$$X_{tx,rx}(t) = I_{tx,rx}(t) + jQ_{tx,rx}(t) = \mathbf{X}_{tx,rx}(t)e^{j\phi_{tx,rx}(t)} \tag{7}$$

where $\mathbf{X}_{tx,rx}(t)$ is the modulus and $\phi_{tx,rx}(t)$ its corresponding signal phase.

3.4.1. Parallel implementation

In order to carry out a parallel implementation of these operations, the proposed parallelism strategy lies in a signal-oriented parallelization. This means that a GPU computational thread will be associated to each stored signal sample. Thus, considering signals with L samples, the computational grid of the kernel will be formed as shown in Figure 15 being the number of blocks in x-dimension $BX = \lceil \frac{L}{T_{BX}} \rceil$ and the number of blocks in y-dimension $BY = 2N - 1$. As we know, the number of threads per block T_{BX} is an empirical value and the designer should evaluate what is the best according to the GPU resources. Typical values are 32, 64 or 128 threads per block, generally any power of two, and attending to our tests we have chosen 256 as the optimal value.

There is no limitation on filter length because its coefficients are stored in texture memory, which resides in the device memory and is cached in texture cache to optimize read accesses. Thus, each thread reads from memory the filter coefficients and L samples of a signal, convolving them to obtain a filtered sample.

Later on, the Hilbert Transform is applied to every filtered signal so we can obtain their analytic signals. In this case, FFT algorithms provided by CUDA (CUFFT libraries [20]) are used to compute the IFFT of the product of the corresponding signal and the Hilbert Transformer FFTs, as it is defined in [23]. With these libraries, there is no need to define a new kernel nor specify grid and block dimensions, since they are responsible for properly parallelizing and splitting the algorithm, computing the FFT of the data set directly on the GPU. In our particular case, a total of $2N - 1$ FFTs of L points are calculated in parallel. The whole resultant I/Q (in-phase/quadrature-phase) signals pairs (Figure 15) are stored in texture memory, and they are passed to the next stage via global device memory.

3.4.2. Optional stage: Decoding

When Golay encoding is used during acquisition, it is necessary to first merge and deconvolve the $4N - 16$ received signals, where 50% of signals belong to A and B codes respectively. This can be done very fast making a parallel implementation where the parallelism strategy is also signal-oriented. In this sense, the previous kernel can be modified in order to include the sum of both signals in parallel before the application of the filters coefficients to finally obtain $2N - 8$ signals.

3.5. Beamforming: Delay and Sum

All time-domain imaging algorithms are based on the principle of delay-and-sum beamforming. Typically, these algorithms emulate an acoustic lens by applying appropriate time delays to the array elements in order to focus or steer the beam as desired. SAFT beamformers focus the beam at every point in the image, giving better defect detectability as we mentioned [2, 4, 5, 7]. DAS beamforming is not difficult to implement and permits the use of arbitrary array geometries what makes suitable for a wide range of applications.

According to the Hilbert transformation of the first step, two processing streams have been created where two parallel images will be calculated following these equations:

$$A_I(x,z) = \sum_{i=1}^{N}\sum_{k=1}^{N} I_{tx_i,rx_k}(D(x,z)) \tag{8}$$

$$A_Q(x,z) = \sum_{i=1}^{N}\sum_{k=1}^{N} Q_{tx_i,rx_k}(D(x,z)) \tag{9}$$

where $A_I(x,z)$ and $A_Q(x,z)$ are the in-phase and quadrature images respectively, and $D(x,z)$ is the focussing delay for the spatial point (x_p, z_p) in the grid which is calculated as follows:

$$D(x,z) = \frac{\sqrt{(x_p - x_{tx})^2 + z_p^2} + \sqrt{(x_p - x_{rx})^2 + z_p^2}}{c} \tag{10}$$

being x_{tx} and x_{rx} the coordinates of the transducer elements tx and rx, respectively.

Henceforth, we will focus on the all the operations involved in Delay-and-Sum algorithm, studying the diverse alternatives and their parallel implementation as well as the best way of their optimization.

- **Lens calculation**. A fundamental part of beamforming is calculating the differences in wave arrival time between array elements. Therefore, each signal sample has to be properly delayed according to the distance from the spatial point to the emitter or receiver array elements. The calculation of delays is achieved using equation 10. Although in a conceptual form is a delay, what is actually done is a mapping to the memory buffer (at

http://dx.doi.org/10.5772/55910

the sampling frequency) where the corresponding sample value of the signal is retrieved. Therefore, the number of delays to be calculated is usually large and it is given by:

$$Memory|_{lens} = R_H \times R_V \times 2N - 1 \tag{11}$$

where $R_H \times R_V$ are the dimensions of the desired ultrasonic image. Thus, the lens calculation can be afforded using two different approaches:

- *Load pre-calculated delays*. The delays are pre-calculated before beamforming and they are recovered from a look-up table inside the image generation process. The necessary memory to store all the delays is not a significant problem, but the main drawback is the requirement of high bandwidth to make the process faster as well as the fact of updating the table each time. Thereby, this would be a good solution for no in-vivo inspections, where the scenario is known and the delays are calculated only once for the complete acquisition.
- *Calculate delays on-the-fly*. The delays are dynamically calculated inside the beamforming process. This task, which can be at first computationally more expensive than the first alternative, is however not a heavy computational problem because of the great power of actual systems. In this regard, dynamic calculation of the lenses inside the threads will simplify other operations on images, such as scrolling and zooming.

Which approach to choose relies on the rest of the beamformer implementation. Thus, in order to take full advantage of the GPU it is needed to have a balance between bandwidth use and arithmetic operations. In this regard, it has been proved that it is faster to obtain the values for the lenses inside the kernels instead of having them stored in the device memory. Therefore in our proposal, it makes sense to calculate the delays on-the-fly.

- **Filtering**. In a real implementation, we sample the elements at a rate just above the Nyquist criteria. Although this preserves the frequency content of the signal, this does not give enough steering delay resolution. The solution is to perform a digital interpolation, increasing the steering-delay resolution. In this particular case, linear interpolation and polynomial interpolation can be easily implemented. The results obtained are practically identical, although the cost associated to each solution differs being the polynomial interpolation time the double of linear interpolation. For this reason, we decided to simply interpolate across two consecutive samples. The penultimate operation is the application of a window function which is multiplied with the data from each channel in order to reduce mainly the level of sidelobes.
- **Sum**. The final step in the ultrasonic generation process is to obtain the accumulated sum of all the signals samples which contribute to a given spatial point.

3.5.1. Parallel implementation

The delay-and-sum process is applied to the complex signals obtained in the previous stage. We have identified different strategies to implement the ultrasonic image generation process in a GPU depending on how the algorithm is parallelized with respect to threads and blocks and relative to the use of GPU resources.

As Figure 16 shows, the parallelization is carried out by launching a thread per image pixel. To this end, a computation grid ($GRID_1$) with $BX = \lceil \frac{R_H}{T_{BX}} \rceil$ and $BY = \lceil \frac{R_V}{T_{BY}} \rceil$ blocks of $T_{BX} \times T_{BY}$ threads is defined on the kernel, where R_H and R_V are the desired image resolution in horizontal and vertical directions, respectively. Each thread is responsible then for calculating

the coordinates for the spatial point (x_p, z_p) of a specific image pixel and calculating the lens to focus at this point.

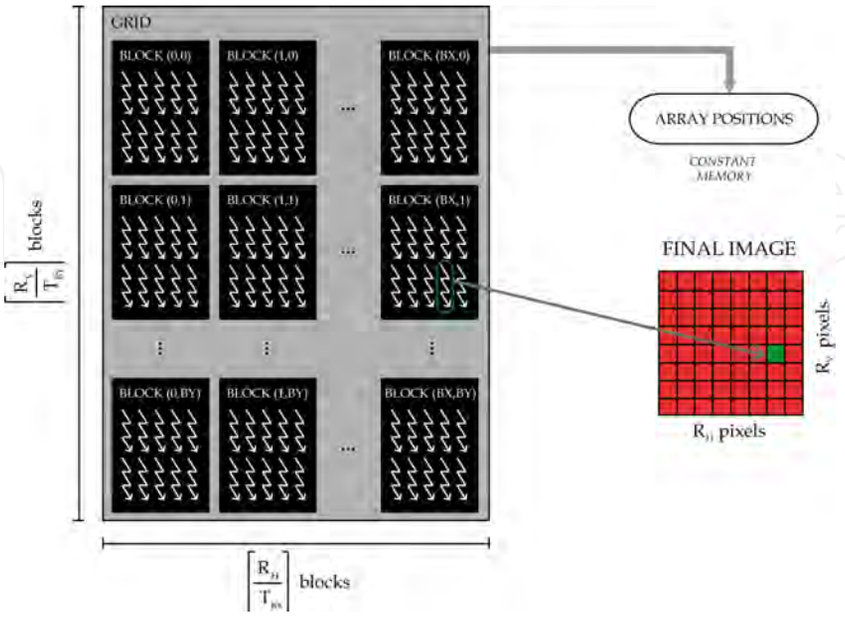

Figure 16. One thread is responsible for a image pixel

In this case, the lens is formed by the $2N-1$ times of flight of each emission-reception pair combination. Thus, in order to accelerate all these calculations, the transducer elements coordinates are stored in constant memory in each GPU multiprocessor. In addition, the computed distances from an array element to an image pixel are reused to save time avoiding duplicate calculations. The lens obtained allow us to index in the complex signals stored in texture memory, and real and imaginary parts are interpolated when needed. To this respect, lineal interpolation was implemented obtaining good performance. Then, the $2N-1$ resultant complex samples are multiplied by the corresponding apodization gains and added together. Finally, the resultant image (final image in Figure 15) is also stored in texture memory, for a quick data access to the post-processing stage.

3.6. Post-processing

The post-processing stage involves firstly calculate the envelope (in essence the modulus) of the beamformed images, according to the following expression:

$$A = \sqrt{{A_I}^2 + {A_Q}^2} \tag{12}$$

where A_I and A_Q are the *In-phase* and *Quadrature* images derived from the beamforming process. This operation prevents the appearance of diverse artefacts associated with the Hilbert Transform.

Likewise, (an optional) stage in the process is in charge of normalizing and converting the image to decibels scale. Although this is not a complex task, it cannot be carried out in the previous stage because we need to know what the maximum value for the image:

http://dx.doi.org/10.5772/55910

$$A|_{decibels} = 20\log_{10}\left(\frac{A}{max(A)}\right) \tag{13}$$

Finally, the generated ultrasonic image (Final image (dB) referenced in Figure 15) is directly displayed on the screen using the OpenGL libraries, which provide specific functionality for graphics representation.

3.6.1. Parallel implementation

The parallel implementation of the envelope calculation is carried out inside the beamforming kernel. This is because at the end of the pixel calculation, we have the final output values for both I and Q components. Thus, we avoid writing twice and we only obtain a single image. For the optional conversion to decibels scale, a new kernel (Kernel 3 in Figure 15) is defined which uses a grid with $\lceil \frac{R_H}{B_x} \rceil$ and $\lceil \frac{R_V}{B_y} \rceil$ blocks of T_{BX} threads having a thread per image pixel as before.

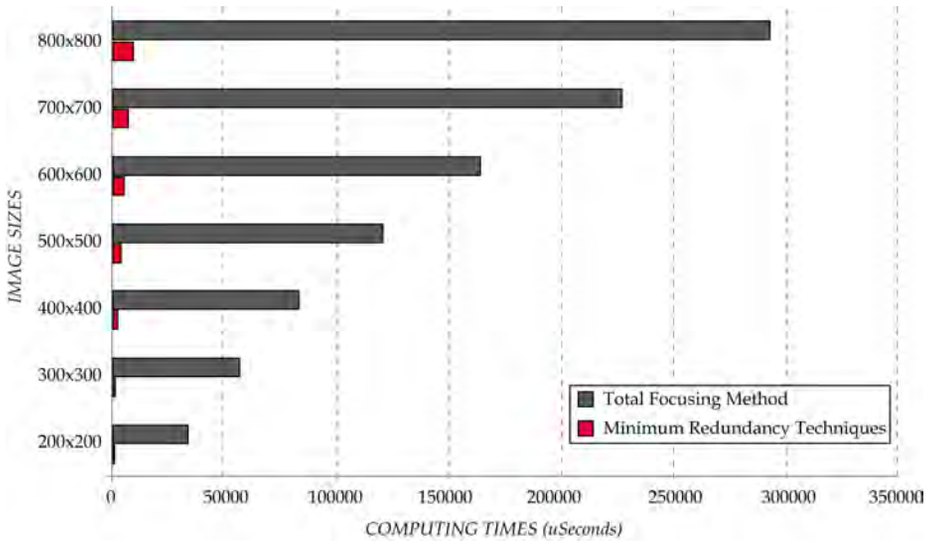

Figure 17. Computing times for TFM and MR solutions using GPU in μseconds

3.7. Performance

A NVIDIA Quadro 4000 graphics card was used to test the beamforming time achieved with the system proposed here. This card has 256 cores and 1GB global memory. It was installed in a computer with a four-core 2.66GHz Intel Q9450 processor and 4GB RAM. GPU-based implementation of the beamformer was done and tested for all acquisition strategies exposed along this chapter. In Figure 17 computing times considering image sizes starting from 200×200 to big size 800×800 for both TFM and minimum redundancy solutions are presented where it is evident than despite using the great power of GPU's the TFM solution is a very intensive procedure.

In Figure 18, the frame rate obtained for different image sizes when 2R-SAFT and kA-SAFT are employed is presented. In particular, attending to the case of an image with 500×500

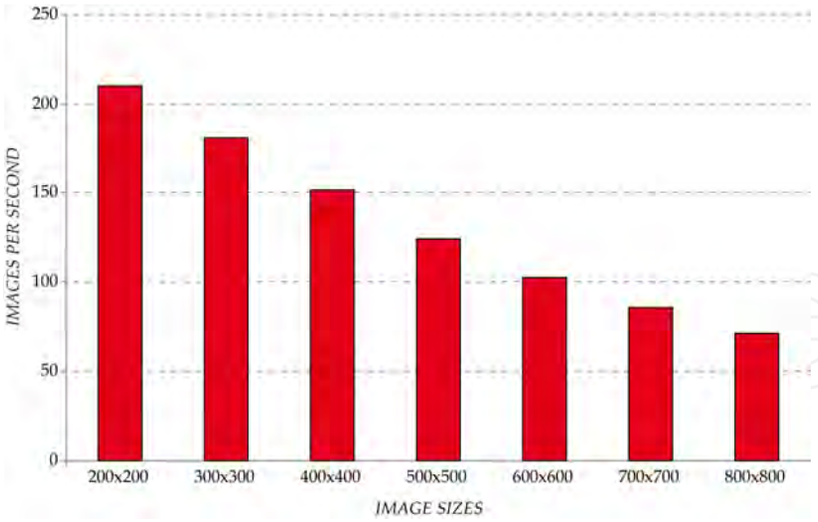

Figure 18. Images per second achieved using GPU for different image sizes for 2R-SAFT and kA-SAFT

pixels, the GPU is able to get 135 images per second, which is in nearly to the acquisition system's rate. The evidence here is that we are using a smaller dataset than that obtained with TFM method but preserving the image quality with all GPU cores completely dedicated to fast computation.

4. Conclusion and future developments

This work has presented how the use of coarray paradigm makes possible the design of ultrasonic imaging systems with reduced hardware requirements. The system is divided into two subsystems, hardware and software respectively. The first one is focused on the development of the data acquisition system, whose design is done analysing the compromise between parallel electronic resources and acquisition time. The second one exploits GPU technology to implement the beamformer via software, compensating the emission and reception distances to each image point, providing the maximum possible quality at each image pixel.

Two solutions, based on the availability of instrumentation in the market, are presented attending to this design following the minimum redundancy coarray model. In one case, it has been emphasized the miniaturization of the hardware (with only two channels in reception), and in the second case the focus has been the reduction of the acquisition time at the expense of increasing and parallelize reception channels (up to a maximum of 32). From the point of view of image quality, both beamforming techniques present similar results. Consequently it is possible to adapt the design of our system to several implementation models depending on the final application requirements.

The problems associated to the low level of the transmitted signals and the signal losses through the material have been analysed. As a solution, we have introduced pulse compression techniques in order to increase the signal to noise ratio. In addition, we have studied the implementation cost of this technique and it has been compared with the TFM technique (based on the FMA capture), verifying that the results are very similar.

Finally, we have made a detailed description of the beamforming process in GPU and it has been quantified the advantage of using the GPU as a processing tool from the image

frame rate point of view. So by using a simple graphics card equipped with NVIDIA CUDA technology, rates that go up to 200 images per second were obtained depending on the image size chosen. Therefore, this solution allows the development of high quality imaging systems with low requirements and excellent capabilities in a compact architecture.

Acknowledgments

This work has been supported by the Spanish Ministry of Science and Competitiveness under the project DPI2010-19376.

Author details

References

[1] Caroline Holmes, Bruce W. Drinkwater, and Paul D. Wilcox. Post-processing of the full matrix of ultrasonic transmit–receive array data for non-destructive evaluation. *NDT & E International*, 38(8):701–711, December 2005.

[2] Caroline Holmes, Bruce W. Drinkwater, and Paul D. Wilcox. Advanced post-processing for scanned ultrasonic arrays: application to defect detection and classification in non-destructive evaluation. *Ultrasonics*, 48(6-7):636–42, November 2008.

[3] Alan J. Hunter, Bruce W. Drinkwater, and Paul D. Wilcox. The wavenumber algorithm for full-matrix imaging using an ultrasonic array. *IEEE transactions on ultrasonics, ferroelectrics, and frequency control*, 55(11):2450–62, November 2008.

[4] Mustafa Karaman, Pai-Chi Li, and Matthew O'Donnell. Synthetic aperture imaging for small scale systems. *IEEE Transactions on Ultrasonics, Ferroelectrics and Frequency Control*, 42(3):429–442, May 1995.

[5] Jørgen Arendt Jensen, Svetoslav Ivanov Nikolov, Kim Lø kke Gammelmark, and Morten Hø gholm Pedersen. Synthetic aperture ultrasound imaging. *Ultrasonics*, 44:5–15, December 2006.

[6] Carlos J. Martín-Arguedas, O. Martínez-Graullera, G. Godoy, and L. Gómez-Ullate. Coarray synthesis based on polynomial decomposition. *IEEE transactions on image processing*, 19(4):1102–1107, 2010.

[7] Carlos J. Martín-Arguedas, D. Romero-Laorden, O. Martínez-Graullera, M. Pérez-Lopez, and L. Gómez-Ullate. An Ultrasonic Imaging System Based on a New SAFT Approach and a GPU Beamformer. *IEEE Transactions on Ultrasonics, Ferroelectrics and Frequency Control*, 59(7):1402–1412, 2012.

[8] Geoffrey R Lockwood, Pai-chi Li, Matthew O'Donnell, and F. Stuart Foster. Optimizing the Radiation Pattern of Sparse Periodic Linear Arrays. *IEEE Transactions on Ultrasonics, Ferroelectrics and Frequency Control*, 43(1):7–14, 1996.

[9] Svetoslav Ivanov Nikolov. *Synthetic aperture tissue and flow ultrasound imaging*. PhD thesis, Technical University of Denmark, 2001.

[10] Bernard D. Steinberg. *Principles of Aperture and Array System Design*. Wiley, New York, 1976.

[11] John J. Flaherty, Kenneth R. Erikson, and Van Metre Lund. Synthetic aperture ultrasonic imaging systems, Patent number 3548642, 1967.

[12] Christoph B. Burckhardt, Pierre-André Grandchamp, and Heinz Hoffman. An Experimental 2 MHz Synthetic Aperture Sonar System Intended for Medical Use. *IEEE Transactions on Sonics and Ultrasonics*, 21(1):1–6, 1974.

[13] Intel Corporation. Thunderbolt™ technology. http://www.intel.com/thunderbolt, (accessed 6 July 2012).

[14] Carlos J. Martín-Arguedas, O. Martínez-Graullera, and L. G. Reduction of grating lobes in SAFT Images. In *IEEE International Ultrasonics Symposium*, number 1, pages 721–724, Beijing, China, 2008.

[15] Carlos J. Martín-Arguedas. *Técnicas de apertura sintética para la generación de imagen ultrasónica*. PhD thesis, Universidad de Alcalá, 2010.

[16] M. Golay. Golay's complementary series. *IRE Transactions on Information Theory*, pages 273–276, 1961.

[17] Andrzej Nowicki, Igor Trots, Wojciech Secomski, and Jerzy Litniewski. Golay's codes sequences in ultrasonography. *Archives of Acoustics*, 28:313–324, 2003.

[18] National Instruments. 32-channel digitizer module for ultrasound applications. http://sine.ni.com/nips/cds/view/p/lang/en/nid/208657, (accessed 1 October 2012).

[19] Wen-Mei W. Hwu and David B. Kirk. *Programming Massively Parallel Processors : A Hands-on Approach*. Morgan Kaufmann, 2010.

[20] NVIDIA Developer Zone. Software development kit 4.2 version, https://developer.nvidia.com/cuda-education-training, (accessed 1 October 2012).

[21] Jason Sanders and Edward Kandrot. *CUDA by Example*. Addison-Wesley, 2010.

[22] A. V. Oppenheim and W. R. Schafer. *Discrete-Time Signal Processing*. Prentice-Hall, Englewoods Cliffs (NJ), 1989.

[23] S. Lawrence Marple. Computing the Discrete-Time "Analytic" Signal via FFT. *IEEE Transactions on Signal Processing*, 47(9):2600–2603, 1999.

Chapter 8

Speckle Noise Reduction in Medical Ultrasound Images

P.S. Hiremath, Prema T. Akkasaligar and
Sharan Badiger

Additional information is available at the end of the chapter

http://dx.doi.org/10.5772/56519

1. Introduction

The use of ultrasound imaging in medical diagnosis is well established because of its non-invasive nature, low cost, capability of forming real time imaging and continuing improvement in image quality. However, it suffers from a number of shortcomings and these include: acquisition noise from the equipment, ambient noise from the environment, the presence of background tissue, other organs and anatomical influences such as body fat, and breathing motion. Therefore, noise reduction is very important, as various types of noise generated limits the effectiveness of medical image diagnosis.

Ultrasound is a sound wave with a frequency that exceeds 20 kHz. It transports energy and propagates through several means as a pulsating pressure wave [1]. It is described by a number of wave parameters such as pressure density, propagation direction, and particle displacement. If the particle displacement is parallel to the propagation direction, then the wave is called a longitudinal or compression wave. If the particle displacement is perpendicular to the propagation direction, it is a shear or transverse wave. The interaction of ultrasound waves with tissue is subject to the laws of geometrical optics. It includes reflection, refraction, scattering, diffraction, interference, and absorption. Except from interference, all other interactions reduce the intensity of the ultrasound beam.

Ultrasound technique is mainly based on measuring the echoes transmitted back from a medium when sending an ultrasound wave to it. In the echo impulse ultrasound technique, the ultrasound wave interacts with tissue and some of the transmitted energy returns to the transducer to be detected by the instrument [2]. Further, the reflected waves are picked up by the transducer probe and relayed to the machine. The machine calculates the distance from the transducer probe to the tissue or organ (boundaries) using the speed of sound in tissue (1,540 m/s) and the time of the each echo's return (millionths of a second). The machine displays

the distances and intensities of the echoes on the screen, forming a two dimensional image. Superficial structures such as muscles, tendons, testes, breast and the neonatal brain are imaged at a higher frequency (7- 18 MHz), which provides better axial and lateral resolution. Deeper structures such as liver and kidney are imaged at a lower frequency 1-6 MHz with lower axial and lateral resolution but greater penetration.

The usefulness of ultrasound imaging is degraded by the presence of signal dependent noise known as speckle. Speckle noise is multiplicative in nature. This type of noise is an inherent property of medical ultrasound imaging and because of this noise the image resolution and contrast become reduced, which effects the diagnostic value of this imaging modality [3]. So, speckle noise reduction is an essential pre processing step, whenever ultrasound imaging is used for medical imaging. Therefore, image despeckling is a very important task, and should be filtered out [4-6], without affecting important features of the image.

In ultrasound images, the noise content is multiplicative and non Gaussian. Such noise is generally more difficult to remove than additive noise, because the intensity of the noise varies with the image intensity. A model of multiplicative noise is given by

$$y_{ij} = X_{ij} n_i \tag{1}$$

where the speckle image y_{ij} is the product of the original image $X_{ij,}$ and the non-Gaussian noise $n_{ij.}$ The indices i, j represent the spatial position over the image. In most applications involving multiplicative noise, the noise content is assumed to be stationary with unitary mean and unknown noise variance σ^2. To convert multiplicative noise into an additive noise, as given in the Eq.(2), a logarithmic transformation is applied to the speckle image y_{ij} [7]. The noise component n_{ij} is then approximated as an additive zero mean gaussian noise.

$$\ln y_{ij} = \ln X_{ij} + \ln n_{ij} \tag{2}$$

The Discrete Wavelet Transform (DWT) is then applied to $\ln y_{ij}$ and the wavelet transformed image is subjected to thresholding. After applying the inverse DWT, the processed image is subjected to an exponential transformation, which is the inverse logarithmic operation,that yields a denoised image.

1.1. Image quality assessment

Image quality is important when evaluating or segmenting ultrasound images, where speckle obscures subtle details in the image [8]. In a recent study [9] it is shown that speckle reduction improves the visual perception of the expert in the assessment of ultrasound imaging of the human organs. The statistical parameters like Signal to Noise Ratio (SNR), Correlation Coefficient (CC), variance, Mean Square Error (MSE) and Peak Signal to Noise Ratio (PSNR) for image quality assessment are described below. The following metrics are calculated using the original image X and the despeckled image Y.

Variance: It determines the average dispersion of the speckle in the image. A lower variance gives a cleaner image as more speckles are reduced. The formula for calculating the variance is

$$\sigma^2 = \frac{1}{N^2} \sum_{i,j=0}^{N-1} \left(X_{ij} - \bar{X} \right)^2 \tag{3}$$

where $\bar{X}$ is the mean intensity value of the image X of size N×N.

Mean Square Error: The MSE measures the quality change between the original image (X) and denoised image (Y) of size N×N. It is given by

$$MSE = \frac{1}{N^2} \sum_{i,j=0}^{N-1} \left(X_{ij} - Y_{ij} \right)^2 \tag{4}$$

The MSE has been widely used to quantify image quality and, when used alone, it does not correlate strongly enough with perceptual quality. It should be used, therefore, together with other quality metrics and visual perception.

Signal to Noise Ratio: The SNR compares the level of desired signal to the level of background noise. The higher the ratio, the less obtrusive the background noise is. It is expressed in decibels (dB) as

$$SNR = 10 \log_{10} \left(\frac{\sigma^2}{\sigma_e^2} \right) \tag{5}$$

where, σ^2 is the variance of the original image and σ_e^2 is the variance of error (Difference between the original and denoised image i.e. $|X - Y|$).

Peak Signal-to-Noise Ratio: The PSNR is computed as

$$PSNR = 10 \log_{10} \left(\frac{S^2}{MSE} \right) \tag{6}$$

where S is the maximum intensity in the original image. The PSNR is higher for a good quality image and lower for a poor quality image. It measures image fidelity, that is, how closely the transformed image resembles the original image.

Correlation Coefficient: It represents the strength and direction of a linear relationship between two variates. The best known is the Pearson product moment correlation coefficient, which is obtained by dividing the covariance of the two variables by the product of their standard deviations, and it is given by

$$CC = \frac{N^2 \sum X_{ij}\ Y_{ij} - \sum X_{ij} \sum Y_{ij}}{\sqrt{N^2 \sum X_{ij}^2 - \left(\sum X_{ij}\right)^2} \sqrt{N^2 \sum Y_{ij}^2 - \left(Y_{ij}\right)^2}} \quad (7)$$

where the summations are done over both the indices i and j from 0 to N-1. If the correlation coefficient is near to +1, then there exists stronger positive correlation between the original image and despeckled image.

Computational time: The computational time (T_c) of a filter is defined as the time taken by a digital computing platform to execute the filtering algorithm when no other software, except the operating system, runs on it. Normally, T_c depends on the computing system's clock time period. But, in addition to the clock period, it depends on the memory size, the input data size, and the memory access time, etc. The computational time taken by a filter should be low for online and real time image processing applications. Hence, a filter with lower T_c is better than a filter having higher T_c value while all other performance measures remain identical.

1.2. Image data set

For the purpose of experimentation, a medical ultrasound image database is prepared in consultation with a medical expert for the present study. The images are acquired using the instrument GE LOGIQ 3 Expert system with 5 MHz transducer frequency, in JPEG format. The data set consists of 70 ultrasound images of size 512x512, of kidney and liver.

In the present Chapter, the aim of the study is to address, novel issues related to despeckling medical ultrasound images. It is envisaged that the results of this investigation would be used as a pre processing step for effective image segmentation or image registration techniques in other applications also.

The remaining part of this Chapter is organised into five sections. The section 2 deals with common speckle filters. The section 3 examines wavelet transform methods, while the section 4 investigates contourlet transform methods. The section 5 describes the Gaussian model of speckle noise. Finally, the section 6 gives the conclusions.

2. Common speckle filters

Speckle reducing filters are originated from the synthetic aperture radar community [10]. Later these filters are applied to ultrasound imaging since the early 1980s [11]. There are two major classifications of speckle reduction filters, viz. single scale spatial filters and transform domain multiscale filters. The spatial filter acts on an image by smoothing it; that is, it reduces the intensity variation between adjacent pixels. The simple sliding window spatial filter replaces the center value in the window with the average of all the neighboring pixel values including itself. By doing this, it replaces pixels, that are unrepresentative of their surroundings. It is implemented with a convolution mask, which provides a result that is a weighted sum of the values of a pixel and its neighbors. It is also called a linear filter. The mask or kernel is a square.

http://dx.doi.org/10.5772/56519

Often a 3× 3 square kernel is used. If the coefficients of the mask sum up to one, then the average brightness of the image is not changed. If the coefficients sum to zero, the average brightness is lost, and it returns a dark image.

The common speckle filters such as Lee, Kuan and Wiener filters are considered for the study. The brief definition and mathematical description of the standard spatial filters are discussed below:

Lee filter:

The Lee filter [12] is based on the approach that the smoothing is performed on the area having low variance. However, smoothing will not be performed on area of high variance, which is near edges. The Lee filter assumes that the image can be approximated by a linear model represented by Eq.(8)

$$Y_{ij} = \bar{K} + W^{*}(C - \bar{K}) \tag{8}$$

where Y_{ij} is the gray scale value of the pixel at (i, j) after filtering. If there is no smoothing, the filter will output, only the mean intensity value $\bar{K}$ of the kernel K, otherwise, the difference between the centre pixel C and $\bar{K}$ is calculated and multiplied with a weighting function W given in Eq.(9) :

$$W = \frac{\sigma_k^2}{(\sigma_k^2 + \sigma^2)} \tag{9}$$

and then summed with $\bar{K}$, where σ_k^2 is the variance of the pixel values within the kernel given by the Eq. (10):

$$\sigma_k^2 = \frac{1}{M^2} \sum_{u,v=0}^{M-1} (K_{uv} - \bar{K})^2 \tag{10}$$

where MxM is the size of the kernel and K_{uv} is the pixel value within the kernel at indices u and v, $\bar{K}$ is the mean intensity value of kernel. The parameter σ^2 is the variance of the image X, which is given by the Eq.(3). The main disadvantage of Lee filter is that it tends to ignore speckle noise in the areas closest to edges and lines.

Kuan filter:

The Kuan filter [13] is a generalization of the Lee filter. The Kuan filter converts the multiplicative model of speckle into an additive linear form. However, it is based on the equivalent number of looks (ENL), which is computed from an ultrasound image to determine a different weighting function W given by the Eq.(11):

$$W = \frac{(1 - C_u / C_i)}{(1 + C_u)}. \tag{11}$$

The weighting function is computed from estimated noise variation coefficient of the image, C_u given by the Eq.(12):

$$C_u = (ENL)^{-\frac{1}{2}} \tag{12}$$

and the variation coefficient C_i of the image given by the Eq. (13):

$$C_i = \sigma_k / \bar{K} \tag{13}$$

where ENL is given by the Eq.(14) :

$$ENL = \left(\frac{\bar{K}}{\sigma_k} \right)^2 \tag{14}$$

In the Eq.(14), the σ_k is the standard deviation of the kernel and $\bar{K}$ is the mean intensity value of the kernel. The only disadvantage of the Kuan filter is that the ENL parameter needs to be computed.

Wiener filter:

The Wiener filter [14] is a linear spatial domain filter. There are two alternatives : (i) Fourier transform method (frequency domain) (ii) mean squared method (spatial domain), for implementing the Wiener filter. The first alternative is used for denoising and deblurring, whereas the second alternative is used for denoising only. The frequency domain alternative of Wiener filtering requires a prior knowledge of noise power spectra and the original image. But, in the spatial domain alternative, no such prior knowledge is required. It is based on statistical least squared principle and minimizes the mean squared error between actual signal sequence and desired signal sequence.

In an image, the statistical properties differ too much from one region to another region. Thus, both global statistics (mean, variance, and higher order moments of entire image) and local statistics (mean, variance, and higher order moments of kernel) are important. Wiener filtering is based on both, global and local statistics and is given by

$$Y_{ij} = \bar{K} + \frac{\sigma_k^2}{\sigma_k^2 + \sigma^2} \left(K_{uv} - \bar{K} \right) \tag{15}$$

where Y_{ij} denotes the despeckled image, $\bar{K}$ is the local mean, σ_k^2 is the local variance, K_{uv} is $(u, v)^{th}$ pixel in the kernel K and σ^2 is the global variance. Let us consider kernel of size MxM, then local variance σ_k^2 is defined by Eq.(10). From the Eq.(15), it is observed that the filter output is equal to local mean if the centre pixel value equals local mean, or else it outputs the modified value different from local mean. Thus, filter output varies from the local mean

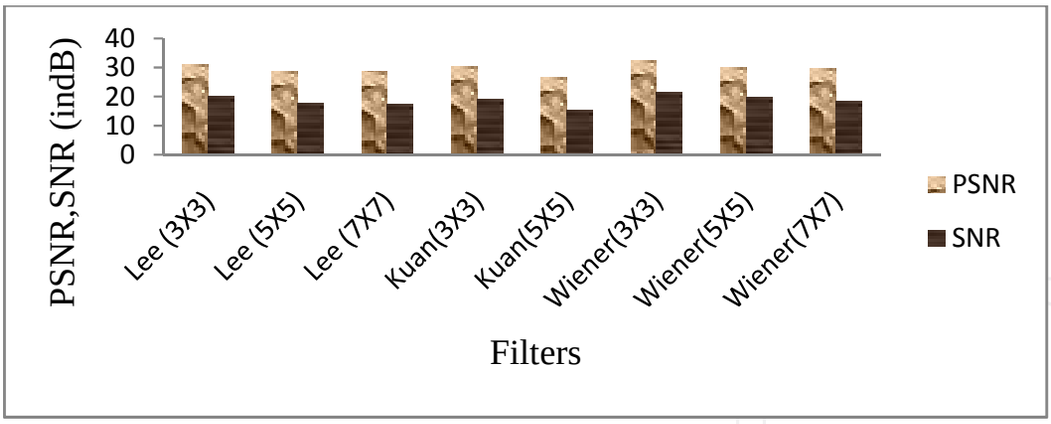

Figure 1. Performance of various despeckling filters, in terms of PSNR, SNR.

depending upon the local variance and thus tries to hold the true original value as far as possible.

The Lee filter and Wiener filter are implemented using kernel size 3x3, 5x5, 7x7 and Kuan filter using kernel size 3x3 and 5x5.The classical Wiener filter, is not adequate for removing speckle, since it is designed mainly for additive noise suppression. To address the multiplicative nature of speckle noise, a homomorphic approach is developed in [15], which converts the multiplicative noise into additive noise, by taking the logarithm of image and then applies the Wiener filter. The PSNR, SNR, CC, variance and MSE are considered as filter performance measures. The Figures 1.-4. show the average results obtained for 70 ultrasound images, which are despeckled using Kuan, Lee and Wiener filter. The optimality is determined by the criteria, namely (i) higher SNR and PSNR values, (ii) lower variance, MSE values and (iii) Correlation Coefficient is nearly equal to one. From the Figures 1.-4., it is observed that Wiener filter with kernel size 3x3 gives better results than other despeckling filters. The computational time of different filters are given in the Table 1. The filter having less computational time is usually required for online and real time applications. The least value of computation is highlighted. From the Table 1, it is observed that Wiener filter with kernel size 3x3 is better among all the filters compared here, for despeckling medical ultrasound images.

For proper judgement of performance of filters, the subjective evaluation should be taken into consideration. For subjective evaluation, the despeckled images of various filters are shown in the Figure 5. From the Figure 5, it is observed from visual inspection that all the three methods achieved good speckle suppression performance. However, Lee and Kuan filters lost many of the signal details and the resulting images are blurred. Further, Wiener filter with kernel size 3x3 yielded better visual enhancement of medical ultrasound images. However, the Lee filter smoothes away noise in flat regions, but leaves the fine details such as lines and texture unchanged.

Thus the main disadvantage of Lee filter is that, it tends to ignore speckle noise in the area closest to edges and lines. The Kuan filter is considered to be more superior to the Lee filter. It does not make an approximation on the noise variance within the filter window. The only

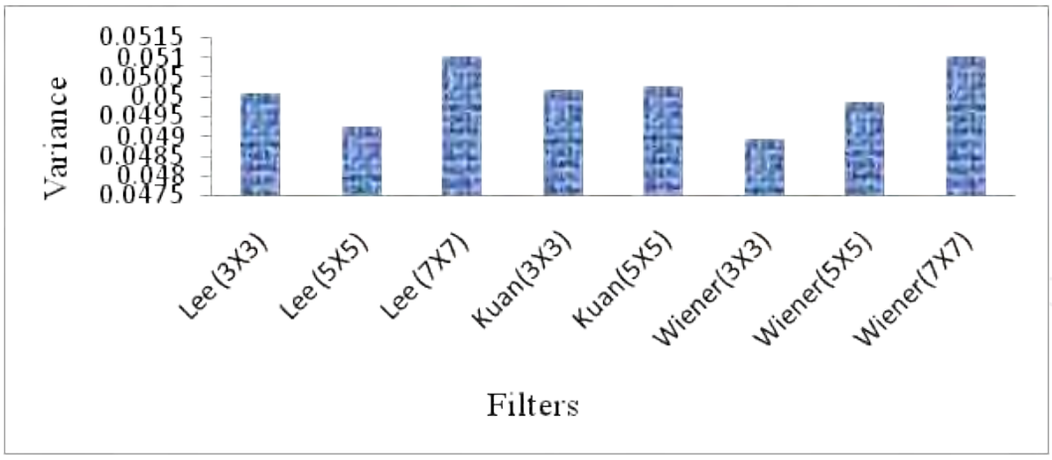

Figure 2. Performance of various despeckling filters, in terms of variance

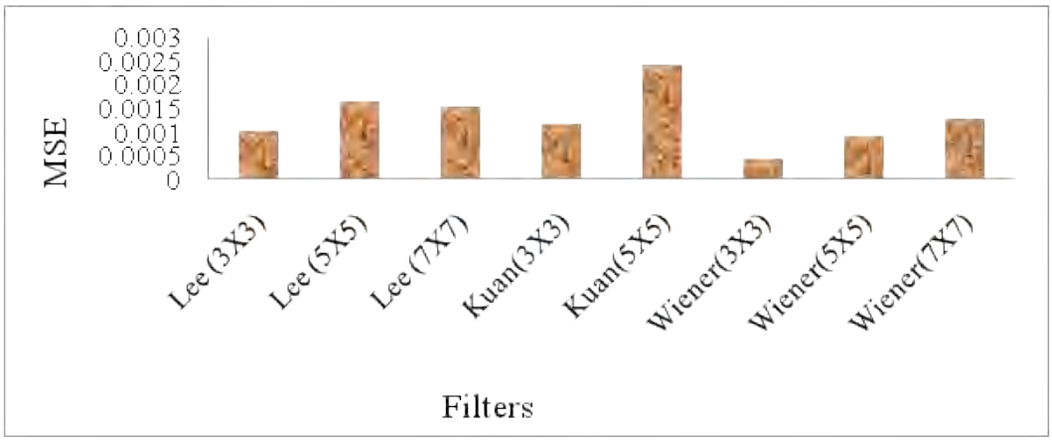

Figure 3. Performance of various despeckling filters, in terms of MSE.

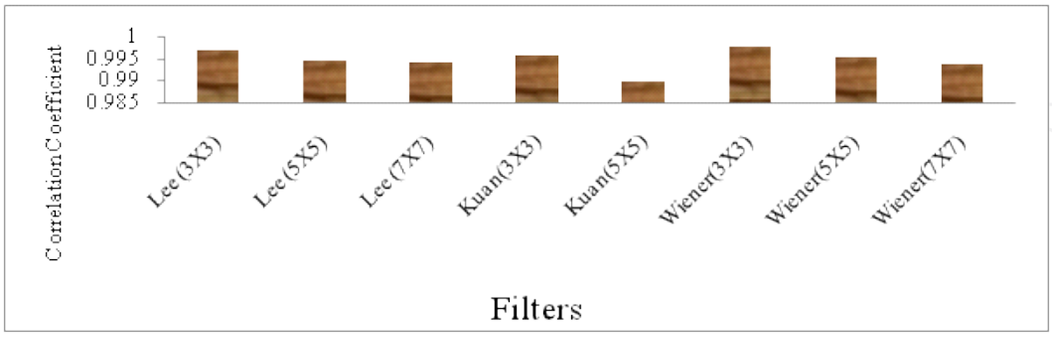

Figure 4. Performance of various despeckling filters, in terms of Correlation Coefficient

limitation of Kuan filter is the high computational time due to estimation of ENL parameter. The Wiener filter with kernel size 3×3 is effective in preserving the edges and other detailed information upto some extent. Further, when the various spatial domain filters are compared by visual inspection, it is observed that Wiener filter with kernel size 3×3 yielded better visual

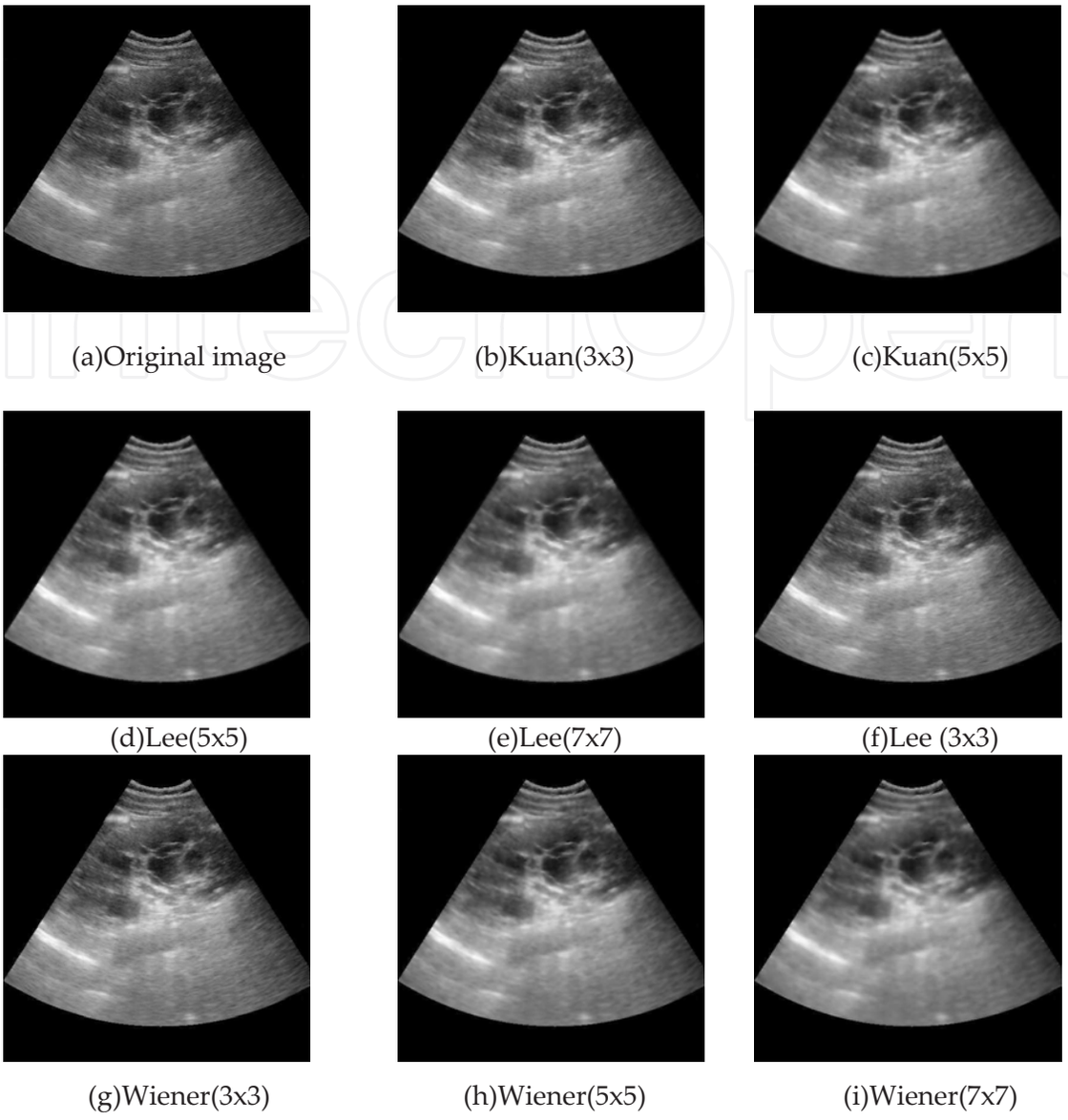

Figure 5. Performance comparison of various despeckling filters by visual inspection of an ultrasound image of kidney.

enhancement of medical ultrasound images. Further, for the complete removal of speckle without losing any data is not possible at the moment. This is because all of these filters rely on local statistical data related to the filtered pixel. An alternative approach is to use wavelet transform.

3. Wavelet transform method

The primary goal of speckle reduction is to remove the speckle without losing much detail contained in an image. To achieve this goal, we make use of the wavelet transform and apply multiresolution analysis to localize an image into different frequency components or useful

Despeckling filters	Computational Time (in Secs.)
Lee (3x3)	25.60
Lee (5x5)	25.63
Lee (7x7)	25.64
Kuan(3x3)	40.89
Kuan(5x5)	41.57
Wiener(3x3)	**4.14**
Wiener(5x5)	5.14
Wiener(7x7)	6.15

Table 1. Performance comparison of various despeckling filters based on computational time.

subbands and then effectively reduce the speckle in the subbands according to the local statistics within the bands. The main advantage of the wavelet transform is that the image fidelity after reconstruction is visually lossless.

A wavelet is a mathematical function used to decompose a given function or continuous-time signal into different frequency components and study each component with a resolution that matches its scale. A wavelet transform is the representation of a function by wavelets. The wavelets are scaled and translated copies (known as daughter wavelets) of a finite length or fast decaying oscillating waveform (known as mother wavelet). Wavelet transforms are classified into continuous wavelet transform (CWT) and discrete wavelet transform. The CWT analyzes the signal through the continuous shifts of a scalable function over a time plane. Because of computers discrete nature, computer programs use the discrete wavelet transform. The discrete transform is very efficient from computational point of view.

Image denoising using wavelet techniques is effective because of its ability to capture most of the energy of a signal in a few significant transform coefficients. Another reason of using wavelet transform is due to development of efficient algorithms for signal decomposition and reconstruction [16] for image processing applications such as denoising and compression. A survey of despeckling techniques is discussed in [17, 18] and many wavelet domain techniques are already available in the literature. In [19], the authors have presented a novel speckle suppression method for medical ultrasound images, in which it is shown that the subband decompositions of ultrasound images have significantly non Gaussian statistics that are best described by families of heavy tailed distributions such as the alpha stable. Then, a Bayesian estimator is designed to exploit these statistics. Alpha stable model is used to develop a blind noise removal processor that performs a nonlinear operation on the data. In [20], the authors have proposed a novel technique for despeckling the medical ultrasound images using lossy compression. In [21], authors have proposed a new wavelet based image denoising technique, in which the different threshold functions, namely universal threshold, Visu shrink, sure shrink, Bayes shrink and normal shrink are considered for the study. The threshold value is

calculated using circular kernel, mean max threshold, nearest neighbour and new threshold function.

Any decomposition of an image into wavelets involves a pair of waveforms, one to represent the high frequencies corresponding to the detailed parts of an image (wavelet function ψ) and one for high frequencies are transformed with short functions (low scale). The result of WT is a set of wavelet the low frequencies or smooth parts of an image (scaling function ϕ) coefficients, which measure the contribution of the wavelets at different locations and scales. The WT performs multiresolution image analysis [22]. The scaling function for multiresolution approximation can be obtained as the solution to a two scale dilatational Eq.(16):

$$\phi(x) = \sum_k a_L(k)\phi(2x-k) \tag{16}$$

for some suitable sequence of coefficients $a_L(k)$. Once ϕ has been found, an associated mother wavelet is given by a similar looking Eq.(17):

$$\psi(x) = \sum_k a_H(k)\phi(2x-k). \tag{17}$$

Wavelet analysis leads to perfect reconstruction filter banks using the coefficient sequences $a_L(k)$ and $a_H(k)$. The input sequence X is convolved with high pass (HPF) and low pass (LPF) filters $a_H(k)$, $a_L(k)$ respectively. Further, each result is down sampled by two, yielding the transform signals x_H and x_L. The signal is reconstructed through upsampling and convolution with high and low synthesis filters s_H (k) and s_L (k). By cascading the analysis filter bank with itself a number of times, digital signal decomposition with dyadic frequency scaling known as DWT can be formed. The DWT for an image as a 2D signal can be derived from 1D DWT. The easiest way for obtaining scaling and wavelet functions for two dimensions is by multiplying two 1D functions. The scaling function for 2D DWT can be obtained by multiplying two 1D scaling functions: $\phi(x,y)=\phi(x)\phi(y)$representing the approximation subband image (LL). The analysis filter bank for a single level 2D DWT structure produces three detail subband images (HL, LH, HH) corresponding to three different directional orientations (Horizontal, Vertical and Diagonal) and a lower resolution subband image LL. The filter bank structure can be iterated in a similar manner on the LL channel to provide multilevel decomposition. The separable wavelets are also viewed as tensor products of one dimensional wavelets and scaling functions. If $\psi(x)$ is the one dimensional wavelet associated with one dimensional scaling function $\phi(x)$, then three 2D wavelets associated with three subband images, called as vertical, horizontal and diagonal details, are given by

$$\psi^V(x,y) = \varphi(x)\psi(y) \tag{18}$$

$$\psi^H(x,y) = \psi(x)\varphi(y) \tag{19}$$

$$\psi^{D}(x,y) = \psi(x)\psi(y) \tag{20}$$

which correspond to the three subbands LH, HL and HH, respectively [23]. The wavelet equation produces different types of wavelet families like Daubenchies, Haar, Symlets, Coiflets and Biorthogonal wavelets [24].

3.1. Thresholding techniques

There are two approaches to perform the thresholding after computation of the wavelet coefficients, namely, subband thresholding and global thresholding [25]. In subband thresholding, we compute the noise variance of the horizontal, vertical and diagonal sub bands of each decomposition level, starting from the outer spectral bands and moving towards inner spectral bands (decomposition from higher levels towards lower levels) and calculate threshold value using Bayes shrinkage or Visu shrinkage rule. In global thresholding, we determine the threshold value from only the diagonal band but we apply this threshold to the horizontal, vertical and diagonal sub bands. This approach assumes that the diagonal band contains most of the high frequencies components; hence the noise content in diagonal band should be higher than the other bands. Thresholding at the coarsest level is not done, because it contains the approximation coefficients that represent the translated and scaled down version of the original image. Thresholding at this level will cause the reconstruction image to be distorted.

Shrinkage scheme:

The thresholding approach is to shrink the detail coefficients (high frequency components) whose amplitudes are smaller than a certain statistical threshold value to zero while retaining the smoother detail coefficients to reconstruct the ideal image without much loss in its details. This process is sometimes called wavelet shrinkage, since the detail coefficients are shrunk towards zero. There are three schemes to shrink the wavelet coefficients, namely, the keep-or-kill hard thresholding, shrink-or-kill soft thresholding introduced by [26] and the recent semi soft or firm thresholding. Shrinking of the wavelet coefficient is most efficient if the coefficients are sparse, that is, the majority of the coefficients are zero and a minority of coefficients with greater magnitude that can represent the image [27]. The criterion of each scheme is described as follows. Given that λ denotes the threshold limit, X_w denotes the input wavelet coefficients and Y_t denotes the output wavelet coefficients after thresholding, we define the following thresholding functions:

Hard thresholding:

$$\begin{aligned} Y_t &= T_{hard}(X_w) \\ &= \begin{cases} X_w & \text{, for } |X_w| \geq \lambda \\ 0 & \text{, for } |X_w| < \lambda \end{cases} \end{aligned} \tag{21}$$

Soft thresholding:

http://dx.doi.org/10.5772/56519

$$Y_t = T_{soft}(X_w) = \begin{cases} \text{sign}\{X_w\}(|X_w| - \lambda) & \text{, for } |X_w| \geq \lambda \\ 0 & \text{, for } |X_w| < \lambda \end{cases} \quad (22)$$

Semi soft thresholding:

$$Y_t = T_{semisoft}(X_w) = \begin{cases} 0 & \text{, for } |X_w| \leq \lambda \\ \text{sign}\{X_w\}\dfrac{\lambda_1(|X_w| - \lambda)}{\lambda_1 - \lambda} & \text{, for } \lambda < |X_w| \leq \lambda_1 \\ X_w & \text{, for } |X_w| > \lambda_1 \end{cases} \quad (23)$$

where $\lambda_1 = 2\lambda$.

The hard thresholding procedure removes the noise by thresholding only the wavelet coefficients of the detail sub bands, while keeping the low resolution coefficients unaltered. The soft thresholding scheme shown in Eq. (22) is an extension of the hard thresholding. It avoids discontinuities and is, therefore, more stable than hard thresholding. In practice, soft thresholding is more popular than hard thresholding, because it reduces the abrupt sharp changes that occurs in hard thresholding and provides more visually pleasant recovered images. The aim of semi soft threshold is to offer a compromise between hard and soft thresholding by changing the gradient of the slope. This scheme requires two thresholds, a lower threshold λ and an upper threshold λ_1 where λ_1 is estimated to be twice the value of lower threshold λ.

3.2. Shrinkage rule

A very large threshold λ will shrink almost all the coefficients to zero and may result in over smoothing the image, while a small value of λ will lead to the sharp edges with details being retained but may fail to suppress the speckle. We use the shrinkage rules, namely, the Visu shrinkage rule and Bayes shrinkage rule for thresholding which are explained in the following:

3.2.1. Visu shrinkage rule

Visu shrinkage rule [28] is thresholding by applying universal threshold. The idea is to find

each threshold λ_i to be proportional to the square root of the local noise variance σ^2 in each subband of the ultrasound image after decomposition. If N_k is the size of the subband in the wavelet domain, then λ_i

$$\lambda_i = \sigma\sqrt{2\log(N_k)} \quad (24)$$

The estimated local noise variance, σ^2, in each subband is obtained by averaging the squares of the empirical wavelet coefficients at the highest resolution scale as

$$\sigma^2 = \frac{1}{N_k^2} \sum_{i,j=0}^{N_k-1} W_{ij}^2 \tag{25}$$

The threshold of Eq.(24) is based on the fact that, for a zero mean independent identically distributed (i.i.d.) Gaussian process with variance σ^2, there is a high probability that a sample value of this process will not exceed λ. Thus, the Visu shrink is suitable for applications with white Gaussian noise and in which most of the coefficients are zero. In such cases, there is a high probability that the combination of (zero) coefficients plus noise will not exceed the threshold level λ.

3.2.2. Bayes shrinkage rule

In Bayes shrink [29], an adaptive data driven threshold is used for image denoising. The threshold on a given subband W_k of the image X, is given by

$$\lambda_K = \frac{\sigma_n^2}{\sigma_x} \tag{26}$$

where σ_n, the estimated noise variance found as the median of the absolute deviation of the diagonal detail coefficients on the finest level (sub band HH_1), is given by

$$\sigma_n = \frac{\text{median}\left(\left\{W_{ij} \in HH_1\right\}\right)}{0.67452} \tag{27}$$

This estimator is used when there is no a priori knowledge about the noise variance. The σ_x, which is the estimated signal variance in the wavelet domain, is given by

$$\sigma_X = \sqrt{\max\left(\sigma_y^2 - \sigma_n^2, 0\right)} \tag{28}$$

and σ_y^2, an estimate of the variance of the W_k, Since W_k is modeled as zero mean, σ_y^2 can be found empirically by,

$$\sigma_y^2 = \frac{1}{N_k^2} \sum_{i,j=0}^{N_k-1} W_{ij}^2 \tag{29}$$

in which N_k is the number of the wavelet coefficients W_k on the subband considered. In the Eq. (27), the value 0.67452 is the median absolute deviation of normal distribution with zero

mean and unit variance. In the Eq.(26), if $(\sigma_n / \sigma_x) << 1$, the signal is much stronger than the noise. The normalized threshold is chosen to be small in order to preserve most of the signal and remove the noise. If $(\sigma_n / \sigma_x) >> 1$, the noise dominates the signal. The normalized threshold is chosen to be large to remove the noise more aggressively. In the Eq.(28), if $\sigma_n^2 \geq \sigma_y^2$, σ_x will become zero i.e. λ becomes infinity. Hence, for this case, $\lambda = \max(\{| W_{ij} |\})$.

The experimentation is carried out for each filter order, for each family and the decompositions are performed upto 4 levels. The statistical features: variance, PSNR, MSE, SNR and correlation coefficient, computed for different wavelets: DW (db1, db5), CW (coif1, coif2, and coif5), SW (sym1, sym3, sym5) and BW (bior2.2, bior6.8). The BW family, where filters are of order 6 in decomposition and order 8 in reconstruction (BW6.8), gives the better results among all the filter types. The PSNR is calculated for bior 6.8 filter up to 4 decompositions. The PSNR value increases up to 3 decompositions and thereafter reduces. Hence, the optimal level of decomposition is 3. The results obtained for the different thresholding schemes are given in the Table 2 [27]. From Table 2, it is found that, there is significant improvement of the subband threshold approach in terms of image quality assessment parameters over the global threshold approach. This is because subband thresholding approach employs an adaptive thresholding approach to respond to the changes in the noise content of the different subbands. In contrast, the global thresholding relies on a Visu threshold to threshold all subbands. The label (written in the parenthesis) in the Table 2. indicates the global(I) and subband thresholding (II), Bayes' (1) or Visu (2) shrinkage rule and the hard (i), soft (ii) or semi soft (iii) thresholding function employed to generate that image. The optimal thresholding scheme with shrinkage rule and shrinkage function are determined by the criteria, namely, higher SNR and PSNR values, lower Variance, MSE values and Correlation Coefficient is nearly equal to one. From Table 2, it is observed that subband decomposition (II) with soft thresholding (ii) using Bayes shrinkage rule (1) gives better results than other techniques. Bayes shrinkage is better than the universal threshold because the universal threshold tends to be high, killing many signal coefficients along with the noise. The Figure 6. shows the visual quality of proposed method based on wavelet filter with Wiener filter. It is observed that the wavelet filter (bior6.8 with level 3(L3)) yields better visualization effect and denoised image than the Wiener filter. The Table 3. shows the performance comparison of proposed method based on wavelet filter with despeckle filter, namely Wiener filter. From Table 3, it is observed that the wavelet filter (bior6.8 with level 3) yields better visualization effect and denoised image than the wiener filter in terms of variance and computational time. But the method based on despeckling using wavelet transforms needs to be improved interms of image quality assessment parameters.

3.3. Laplacian pyramid transform

Several speckle reduction techniques based on multi scale methods (e.g. Wavelet transform, Laplacian pyramid (LP) transform) have been proposed [30-33]. The LP has the distinguishing feature that each pyramid level generates only one bandpass image (even for multidimensional cases), which does not have "scrambled" frequencies. This frequency scrambling happens in the wavelet filter bank when a high pass channel, after down sampling, is folded back into the low frequency band, and thus its spectrum is reflected. In the LP, this effect is avoided by down sampling the low pass channel only.

Bayes' Shrinkage rule(1)	Global thresholding (I)					Subband thresholding (II)				
	Variance	MSE	SNR	CC	PSNR	Variance	MSE	SNR	CC	PSNR
Hard (i)	0.0396	0.0023	16.89	0.991	26.38	0.0482	0.0015	18.94	0.994	28.48
Soft (ii)	0.0396	0.0025	14.83	0.992	26.02	0.0368	0.0012	19.06	0.995	29.94
Semi soft (iii)	0.0370	0.0024	16.04	0.992	26.17	0.0456	0.0016	17.94	0.993	28.56
Visu shrinkage rule (2)	**Global thresholding (I)**					**Subband thresholding (II)**				
Hard (i)	0.0431	0.0028	15.94	0.993	25.52	0.0392	0.0029	16.15	0.992	27.33
Soft (ii)	0.0461	0.0032	14.12	0.992	24.92	0.0372	0.0023	17.79	0.994	28.78
Semi soft (iii)	0.0481	0.0031	14.15	0.992	25.00	0.0385	0.0032	16.17	0.993	27.51

Table 2. Performance evaluation of different thresholding methods interms of variance, MSE,PSNR,SNR and CC values.

Denoising methods	PSNR	SNR	MSE	Variance	CC	Computational time (in Secs.)
WT-L3-ST (bior 6.8)	29.94	19.06	0.00121	0.0368	0.9954	2.80
Wiener (3x3)	32.34	21.53	0.00058	0.0489	0.9977	4.14

Table 3. Performance comparison of wavelet based despeckling method and Wiener filter.

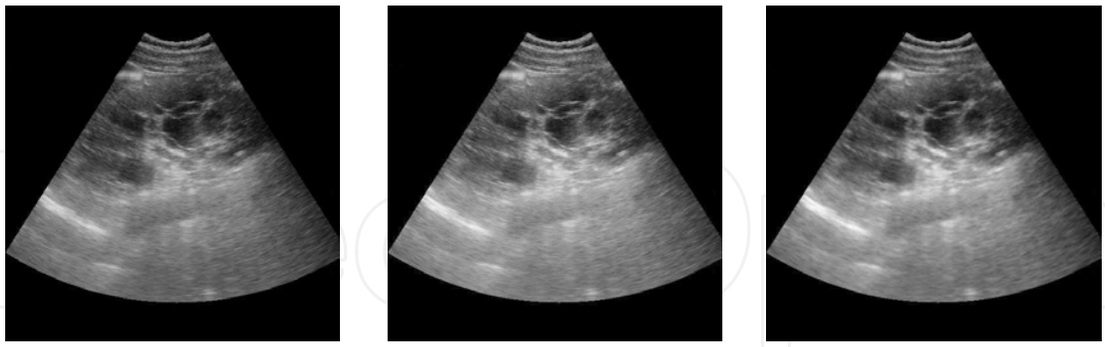

(a) Original ultrasound image (b) Wavelet filter(Bior 6.8,L3) (c) Wiener(3x3)

Figure 6. Despeckled images using Wiener filter and Wavelet filter

A speckle reduction method based on non linear diffusion filtering of band pass ultrasound images in the Laplacian pyramid domain has been proposed in [34], which effectively suppresses the speckle while preserving edges and detailed features. In [31], the authors have implemented a nonlinear multiscale pyramidal transform, based on non overlapping block

http://dx.doi.org/10.5772/56519

decompositions using the median operation and a polynomial approximation. It is shown that this structure can be useful for denoising of one and two dimensional (1-D and 2-D) signals. It can be used for the selection of thresholds for denoising applications.

In [33] the comparison of two multiresolution methods: Wavelet transform and Laplacian pyramid transform, for simultaneous speckle reduction and contrast enhancement for ultrasound images is given. As a lot of variability exists in ultrasound images, the wavelet method proves to be a much better method than the Laplacian one for an overall improvement. However, the Laplacian pyramid scheme need to be explored for achieving better despeckling results.

3.3.1. Laplacian pyramid scheme

One way of achieving a multiscale decomposition is to use a Laplacian pyramid (LP) transform [35]. In the first stage of the decomposition, the original image is transformed into a coarse signal and a difference signal. The coarse signal has fewer samples than the original image but the difference signal has the same number of samples as the original image. The coarse signal is a filtered and down sampled version of the original image. It is then up sampled and filtered to predict the original image. The prediction residual constitutes the detail signal. The coarse signal can be decomposed further and this process can be repeated a few times iteratively. Assuming the filters in LP are orthogonal filters, an image X is decomposed into J detail images d_j, j=1, 2,...,J and a coarse approximation image c_J. Then, we have

$$\|X\|^2 = \sum_{j=1}^{J} \|d_j\|^2 + \|c_J\|^2 \tag{30}$$

The Laplacian is then computed as the difference between the original image and the low pass filtered image. This process is continued to obtain a set of detail filtered images (since each one is the difference between two levels of the Gaussian pyramid). Thus the Laplacian pyramid is a set of detail filters. By repeating these steps several times, a sequence of images are obtained. If these images are stacked one above another, the result is a tapering pyramid data structure and, hence the name the Laplacian pyramid.

A speckle reduction method based on Laplacian pyramid transform for medical ultrasound image is illustrated using the block diagram shown in the Figure 7. In the Figure 7, a homomorphic approach such as the log transformation of the speckle corrupted image, converts the multiplicative noise of the original image into additive noise. Homomorphic operation simultaneously normalizes the brightness across an image and increases contrast. For every difference signal of N-level of Laplacian pyramidal decomposition a threshold value is calculated using Bayes' shrinkage rule. Further, thresholding is performed to reduce speckle. The exponential operation is performed on the filtered output to obtain the despeckled image.

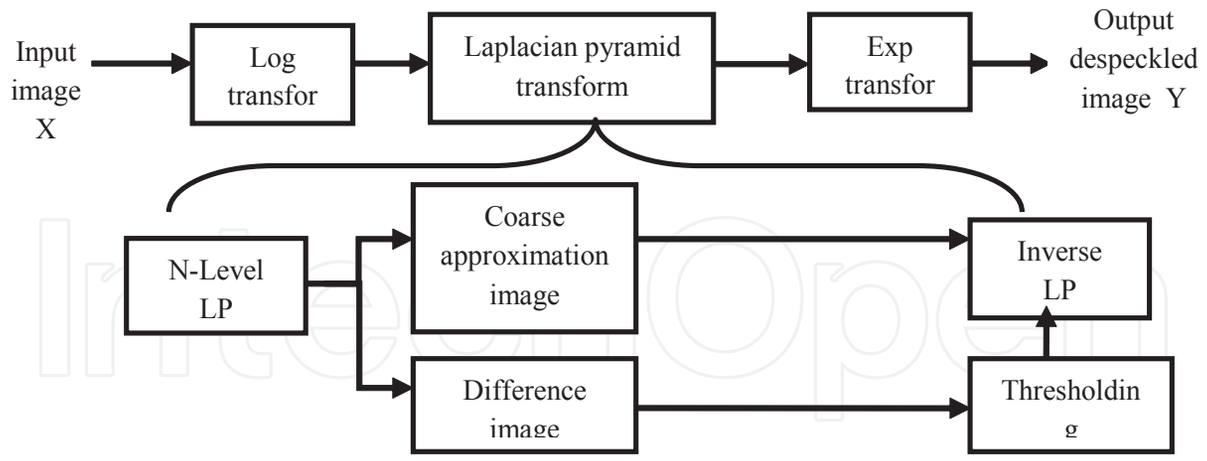

Figure 7. Block diagram of speckle noise suppression using Laplacian pyramid transform

The Laplacian pyramid transform is performed on the log transformed image. The Laplacian pyramidal decompositions up to six levels are obtained using biorthogonal filters with sufficient accuracy numbers such as the "9/7" and "5/3". Further, thresholding schemes such as hard thresholding, soft thresholding and semi soft thresholding is performed to reduce speckle. The threshold value is calculated using Bayes' shrinkage rule. The experimentation is carried out on 70 ultrasound images of liver and kidney. The performance evaluation of the proposed method is done in terms of variance, MSE, SNR, PSNR, CC values that are computed from despeckled image. The Laplacian pyramid transform with 1 level decomposition and hard thresholding is observed to be better than other thresholding methods.

The Table 4. shows the performance comparison of the proposed LP transform based despeckling method with the wavelet transform based despeckling method [36]. It is noticed that, in comparison with the despeckling medical ultrasound images based on WT, the despeckling based on LP method yields poor results. Because multiplicative noise is a particular type of signal dependent noise, in which the amplitude of the noise term is proportional to the value of the noise free signal having nonzero mean. Therefore, a band pass representation like LP is not suitable for multiplicative noise model, So the method needs to be improved.

In order to capture smooth contours in the images, the contourlet transforms, which allow directional decompositions, are employed for despeckling medical ultrasound images in the next section.

4. Contourlet transform method

The contourlet transform (CT) is a multiscale and multidirectional framework of discrete image. It is the simple directional extension for wavelet that fixes its subband mixing problem and improves its directionality. Among the "beyond wavelet" techniques, contourlet allows for different and flexible number of directions at each scale, while achieving nearly critical sampling. The desirable properties of CT for image representation includes multiresolution,

Despeckling methods	PSNR	SNR	MSE	Variance	CC	Computational time (in Secs.)
LP transform based despeckling method (LP-HT-L1)	28.44	18.23	0.00141	0.0416	0.9972	2.24
Wavelet transform based despeckling method (WT-L3-ST)	29.94	19.06	0.00121	0.0368	0.9954	2.80

Table 4. Performance comparison of the LP transform method and the wavelet transform based despeckling method

allowing images to be approximated in a coarse to fine fashion; localization of the basis vectors in both space and frequency; low redundancy, so as not to increase the amount of data to be stored; directionality, allowing representation with basis elements oriented in a variety of directions; and anisotropy, the ability to capture smooth contours in images, using basis elements that are a variety of elongated shapes with different aspect ratios [37].

The contourlet transform has been developed to overcome the limitations of the wavelets, and hence, the new algorithms based on the contourlet transform are more efficient than wavelet methods. In [38], the authors have presented a contourlet based speckle reduction method for denoising ultrasound images of breast. The double iterated filter bank structure and a small redundancy at most 4/3 using two thresholding methods shows a great promise for speckle reduction. In [39], the despeckling medical ultrasound images using contourlet transform using Bayes' shrinkage rule is investigated. The algorithm is also tested on ovarian ultrasound images to demonstrate improvements in the segmentation that yields good classification for follicle detection in an ovarian image [40].

In [41], speckle reduction based on contourlet transform using scale adaptive threshold for medical ultrasound image has been examined, where in the subband contourlet coefficients of the ultrasound images after logarithmic transform are modelled as generalized Gaussian distribution. The scale adaptive threshold in Bayesian framework is applied. The method is tested on both synthetic and clinical ultrasound images interms of S/MSE and edge preservation parameter. The proposed method exhibits better performance on speckle suppression than the wavelet based method, while it does well preserve the feature details of the image.

The contourlet transform can be divided into two main steps: Laplacian pyramid decomposition and directional filter banks. Contourlet transform is a multi scale and directional image representation that uses first a wavelet like structure for edge detection, and then a local directional transform for contour segment detection. A double filter bank structure of the contourlet obtains sparse expansions for typical images having smooth contours. In the double filter bank structure, the Laplacian pyramid is used to decompose an image into a number of radial subbands, and the directional filter banks decompose each LP detail subband into a number of directional subbands. The band pass images (d_j [n]) from the LP are fed into a DFB so that directional information can be captured. The scheme can be iterated on the coarse image

(c_j [n]). The combined result is a double iterated filter bank structure, named pyramidal directional filter bank (PDFB), which decomposes images into directional subbands at multiple scales. The general model for despeckling an image using contourlet transform is shown in the Figure 8.

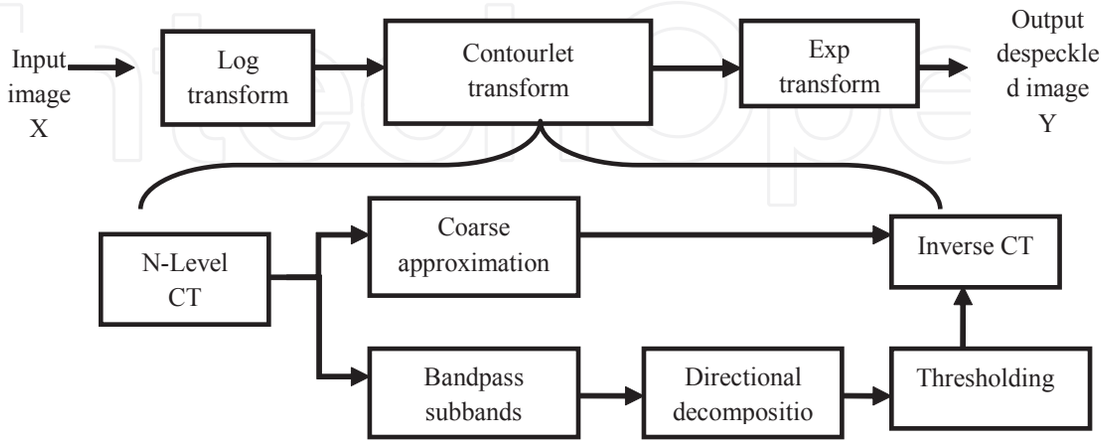

Figure 8. The general model for speckle reduction using contourlet transform.

In the Figure 8, the CT based despeckling method consists of the log transformed original ultrasound image being subjected to contourlet transform, to obtain contourlet coefficients. The transformed image is denoised by applying thresholding techniques on individual band pass sub bands using a Bayes shrinkage rule, derived from the local statistics of the signal in the transform domain. Bayes' shrink was proposed by [29]. The goal of Bayes' shrinkage method is to minimize the Bayesian risk, and hence its name, Bayes' shrink. Further, thresholding schemes such as hard thresholding, soft thresholding or semi soft thresholding is performed to reduce speckle. The exponential operation is performed on the filtered output to obtain the despeckled image.

The experimentation is carried out on 70 ultrasound images of liver and kidney. The six levels of Laplacian pyramidal decompositions are performed using biorthogonal filters with sufficient accuracy numbers such as the "9/7". The directional decompositions up to eight are performed in all the pyramidal levels, using two dimensional ladder filters. The contourlet transform uses the "9/7" filters in LP stage because, in the multiscale decomposition stage, it significantly reduces all inter scale, inter location and inter direction mutual information of contourlet coefficients. Similarly, in directional decomposition stage, the ladder structure PKVA filters [42] are more effective in localizing edge direction as these filters reduce the inter direction mutual information. Further, thresholding schemes such as hard thresholding, soft thresholding or semi soft thresholding is performed to reduce speckle. The threshold value is calculated using Bayes' shrinkage rule. The PSNR is calculated up to 6 LP decompositions. The PSNR value increases up to 2 decompositions using HT, ST and SST, and thereafter reduces. Hence, the optimal level of LP decomposition is 2. Further, it is observed from Table 5, that the 2-level Laplacian pyramidal decomposition and 4 directional bandpass subbands (2 at level 1, 2 at level 2) using hard thresholding yield better results than soft thresholding and semi soft thresholding techniques.

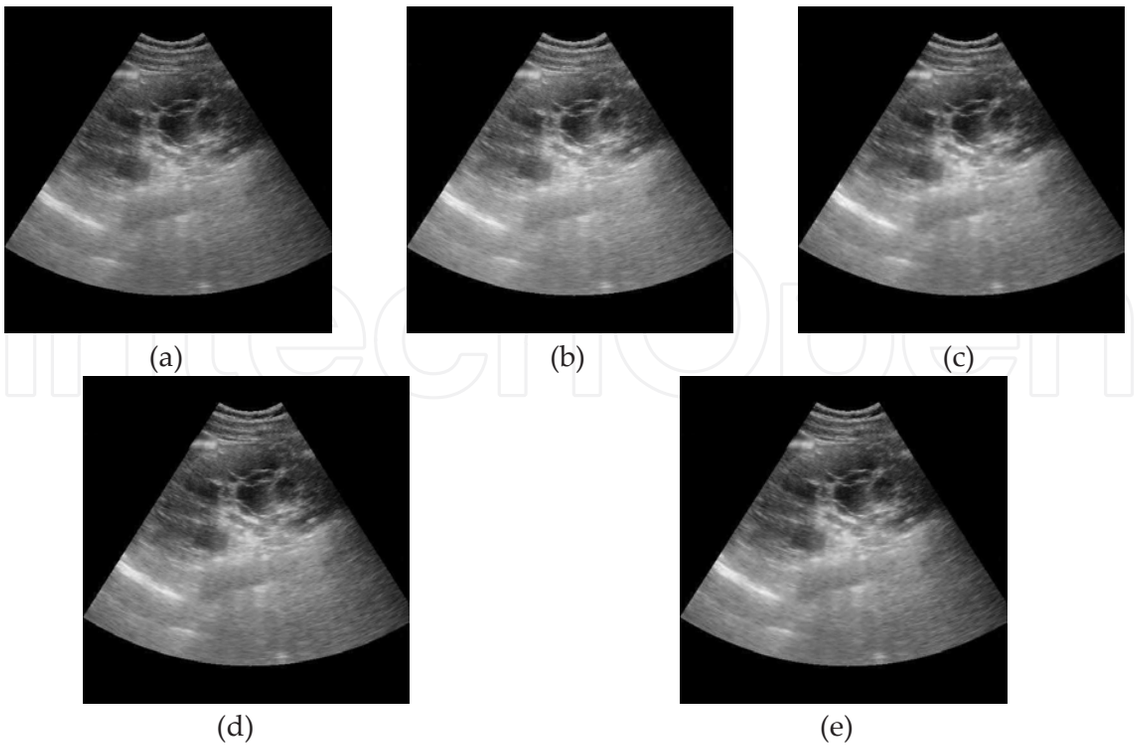

Figure 9. a) Original ultrasound image. (b) Despeckled image using wavelet transform using subband Bayes soft thresholding (level 3). (c) Despeckled image using contourlet transform using soft thresholding. (d) Despeckled image using contourlet transform using hard thresholding. (e) Despeckled image using contourlet transform using semi soft thresholding.

Thresholding methods	Levels	PSNR	Variance	MSE	CC	SNR	Computational time(in Secs.)
Hard thresholding	L2-11	34.21	0.0203	0.00037	0.9990	27.74	1.64
Soft thresholding	L2-31	32.49	0.0382	0.00056	0.9983	24.14	1.68
Semi-soft thresholding	L2-11	33.31	0.0292	0.00046	0.9987	25.91	1.74

Table 5. The results obtained for the optimal optimal decomposition of LP levels and directional decompositions in terms of image quality assessment parameters using contourlet method based on different thresholding techniques with Bayes' shrinkage rule.

The frequency bands obtained by using optimal level L2-11 of contourlet decomposition are as follows: the 2nd level has 1 approximation band of size 128 x128 and 4 detail components (2 of 128 x 256, 2 of 256 x 512). The reconstructed image is the despeckled image. The hard thresholding is better than other thresholding methods, because small coefficients are removed while others are left untouched in HT, while in ST or SST coefficients above the threshold are shrunk by absolute value of threshold. Further, it is found that the despeckling based on contourlet transform gives better results than the speckle reduction method based on wavelet transform in particular. The wavelet based Bayes' shrink thresholding method is based on

separable 2D wavelet transform that has limited directions (Horizontal, Vertical and Directional). Speckle noise in medical ultrasound images will generate significant coefficients in wavelet domain just like true detail features, such as edges. However, the speckle noise is less likely to generate significant coefficients in the contourlet method, and thus, it directly leads to better performance in suppressing noise than the wavelet based Bayes' shrink thresholding scheme.

Another way to analyze the effects of despeckling techniques is to study the despeckled images. In the Figure 9., the resultant images of a sample medical ultrasound image are presented to compare the results of different despeckling techniques by visual inspection. In the Figure 9(b) and (c), the speckle is reduced considerably, but the structures are blurred and some visible artifacts are introduced. However, in Figure 9(e), the speckle is reduced well and structures are enhanced. But some details are lost and some are over enhanced. It is encouraging to note that in the Figure 9(d), the speckle is effectively reduced and also structures are enhanced with almost no loss or noticeable artifact.

4.1. Cycle spinning based contourlet transform

The CT is not translation invariant. This means that the errors after denoising will be sensitive to the positions of discontinuities in the data. In order to avoid such effects, it is necessary to build translation invariant version of the transform. Translation invariance is achieved through several ways. For example, in [43], the time invariant schemes of wavelet based decompositions have been proposed and have been often referred to as cycle spinning. Unfortunately, due to the downsamplers and upsamplers present in the directional filter banks of CT, the CT is not shift invariant, which is important in image denoising by thresholding and normally causes pseudo-Gibbs phenomenon. In [44], the cycle spinning algorithm is utilized in developing a translation invariant contourlet based denoising technique. The experimental results clearly demonstrate the capability of the proposed scheme in image denoising, especially for detailed texture images. It is shown that most of the visual artifacts resulting from the contourlet transform denoising process are eliminated. In [45], a cycle spinning method is used to compensate for the lack of translation invariance property of sharp frequency localized contourlet. Experimental results demonstrate that cycle spinning is a simple and efficient way to average out the pseudo-Gibbs phenomena, which are around singularities and produced by the down sampling and up sampling of directional filter banks, and improve the denoising performance interms of visual quality and PSNR.

To compensate for the lack of translation invariance property of the contourlet transform, we apply the principle of cycle spinning to contourlets. Suppose X and Y are original and despeckled images, F and F^{-1} are forward and inverse contourlet transform, $S_{i,j}$ is the 2D circular shift in i^{th} row and j^{th} column directions, λ is the threshold operator in contourlet transform domain. The cycle spinning based contourlet transform for image denoising could be described as

$$Y = \frac{1}{B^2}\sum_{i,j=1}^{B} CS_{-i,-j}\left(F^{-1}\left(\lambda\left(F\left(CS_{i,j}(X)\right)\right)\right)\right) \tag{31}$$

where B is the series of bit shifts in the i^{th} row and j^{th} column directions. If one decomposes an image of size (N, N) using the contourlet transform, the maximum number of decomposition levels in the LP stage will be B, and therefore, the maximum number of shifts are (B, B) in the row and column directions. After a B number of bit shifts, which depends on the level of decomposition, the transform output degrades. Hence, the cycle spinning has to be stopped after a certain number of bit shifts. The Figure 10. shows the block diagram for speckle reduction method based on contourlet transform with cycle spinning. The cycle spinning is applied to the log transformed image. It performs two dimensional circular shift in i^{th} row and j^{th} column directions. The circular shifting is performed up to B number of bit shifts, where B depends on the level of decomposition. The transform output degrades as B increases. Hence, the cycle spinning has to be stopped after a certain number of bit shifts. Then contourlet transform is performed using double filter bank structure. The six levels of Laplacian pyramidal decompositions are performed using biorthogonal filters with sufficient accuracy numbers such as the ”9-7”.The directional decompositions up to six is performed in the lowest pyramidal level, using two dimensional ladder filters designed in [42]. Further, a thresholding scheme either hard thresholding, soft thresholding or semi soft thresholding, is performed to reduce speckle. The threshold value is calculated using Bayes' shrinkage rule. The results obtained for the optimal bit shifts of cycle spinning using contourlet method based on hard thresholding, soft thresholding and semi soft thresholding using Bayes' rule are presented. The results obtained for different reconstruction methods are shown in Figures 11-15, which exhibit graphs of statistical features PSNR, SNR, variance, MSE and CC, respectively, for different levels of Laplacian pyramid decompositions and directional decompositions corresponding to optimal results of contourlet transform with cycle spinning based despeckling method [46]. The optimal reconstruction method is determined by the criteria, namely, lower variance and MSE, higher SNR and PSNR values, Correlation Coefficient is nearly equal to one. The contourlet transform with 2 level of pyramidal decomposition and two directional decompositions in the finest scale and hard thresholding technique with Bayes' shrinkage rule has yielded better results in comparison contourlet transform based methods [47]. In the Figures 11-15, the horizontal axis label CYC-HT-Bn indicates cycle spin (CYC), thresholding (HT,ST,SST), n number of bit shifts in cycle spinning. From Figures 11-15, it is observed that, 4 bit cycle spinning, having the 2-level of Laplacian pyramidal decomposition with 4 directional bandpass sub bands (2 at level 1, 2 at level 2) subject to soft thresholding, yields optimal results for speckle reduction. The computational time (in Secs.) of the cycle spinning based CT method is shown in Figure 15. The CT based despeckling method takes less computational time as compared to cycle spinning based CT method.

The Figure 16. illustrates the resultant despeckled images of an ultrasound image obtained by the cycle spinning based CT method using hard, soft and semi soft thresholding with Bayes' shrinkage rule, and also that obtained by the CT method [47], for comparison by visual inspection The despeckling method based on cycle spinning using contourlet coefficient shrinkage (Figure16.(b)) performs better and appears to be an improvement over direct contourlet transform based despeckling method.

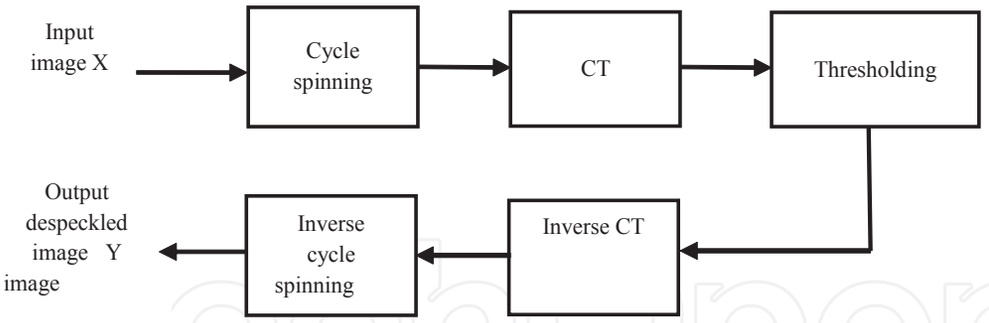

Figure 10. The block diagram of despeckling method based on contourlet transform with cycle spinning.

Among the transform domain filters developed in the previous sections, the contourlet transform with cycle spinning yields better visual quality enhancement of the despeckled images. However, there is still a need to remove Gaussian noise inherent in the medical ultrasound images, which is addressed in the next section.

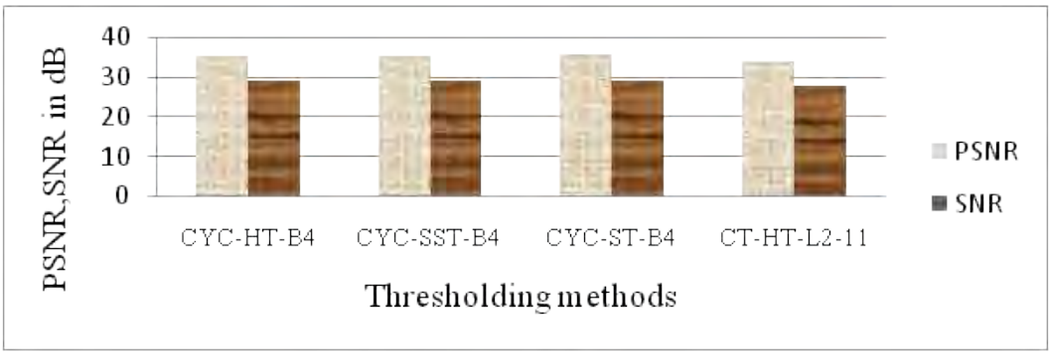

Figure 11. The values of PSNR and SNR for various thresholding methods obtained by cycle spinning based CT method and that by direct CT based method.

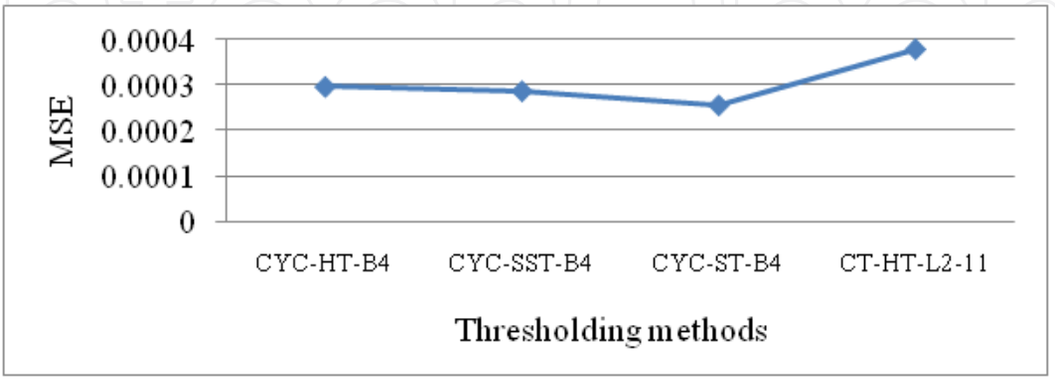

Figure 12. The values of MSE for various thresholding methods obtained by cycle spinning based CT method and that by direct CT based method.

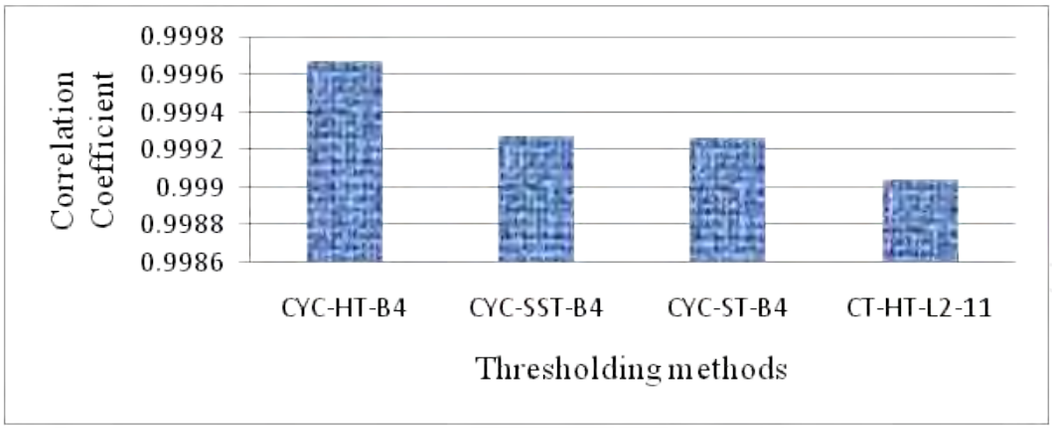

Figure 13. The values of Correlation Coefficient for various thresholding methods obtained by cycle spinning based CT method and that by direct CT based method.

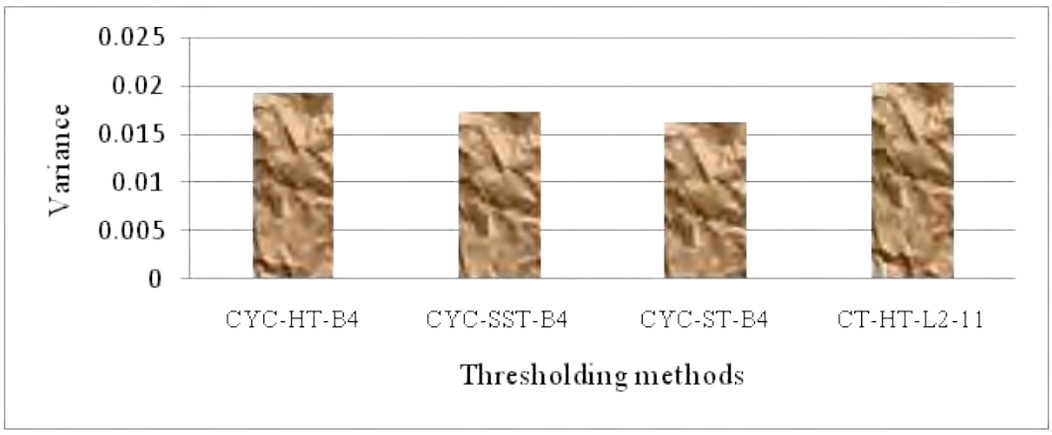

Figure 14. The values of variance for various thresholding methods obtained by cycle spinning based CT method and that by CT based method.

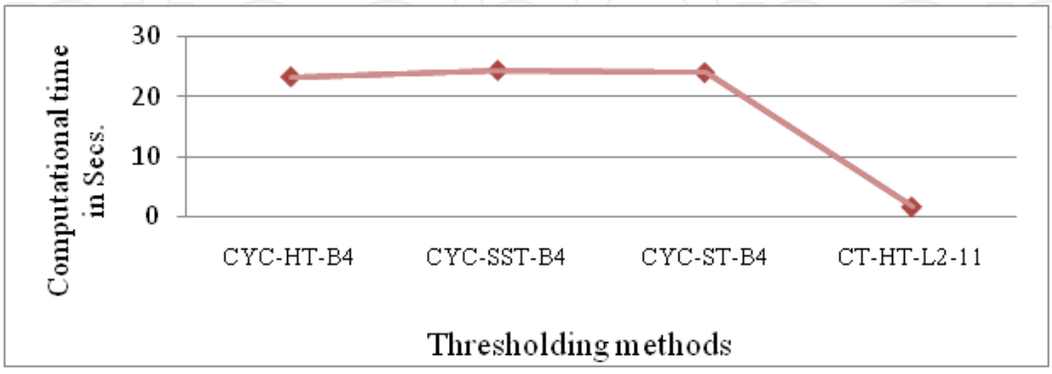

Figure 15. The values of computational time for various thresholding methods obtained by cycle spinning based CT method and that by CT based method.

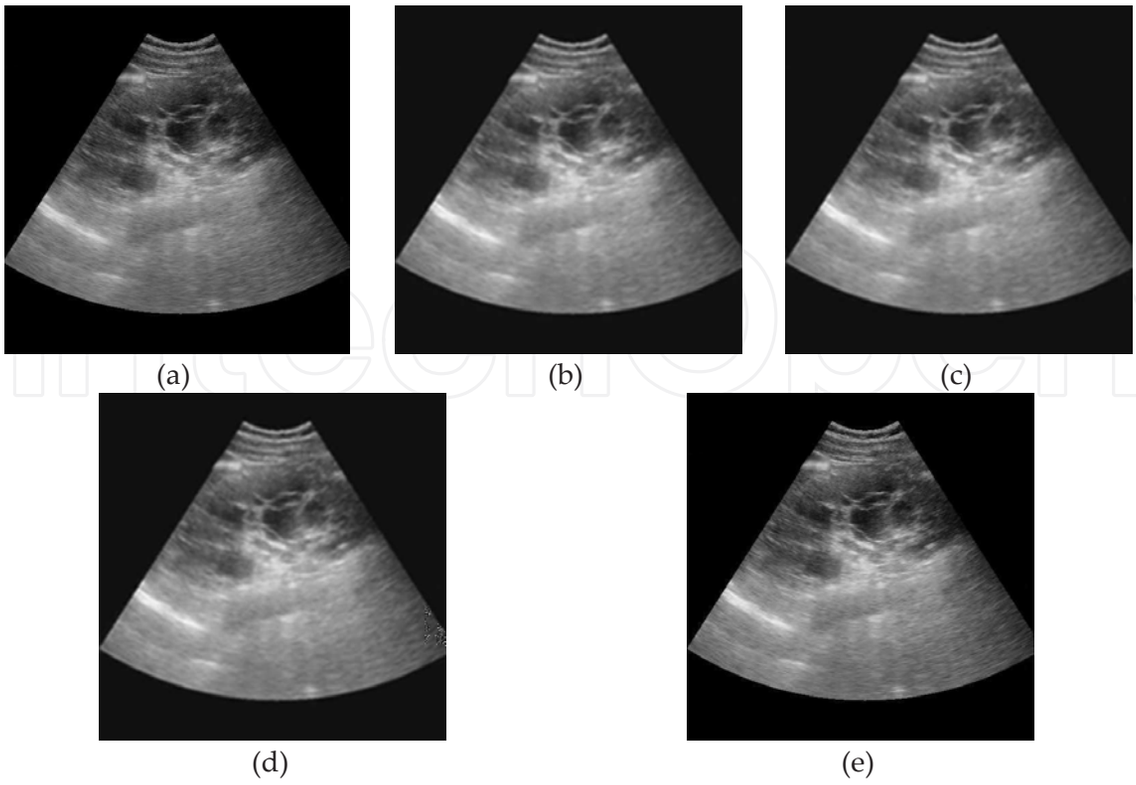

Figure 16. a) Original ultrasound image (b) Despeckled image using cycle spinning based CT using ST method. (c)Despeckled image using cycle spinning based CT using HT method. (d)Despeckled image using cycle spinning based CT using SST method. (e) Despeckled image using direct CT method.

5. Gaussian model for speckle noise

Gaussian probability density is often used in image filtering. The Gaussian has the unique ability not to create new edges as its scale (standard deviation) is increased. This property enables the extraction of edges that represent different levels of detail in an image. As the scale is increased, the number of extracted weak and false edges reduces. However, at the same time edges shift from their true positions. The amount of shift an edge makes not only depends upon the scale of the Gaussian filter, but also on the intensity distributions of the underlying image [48]. Mathematically, a Gaussian filter modifies the input signal by convolution with a Gaussian function. Smoothing is commonly undertaken using linear filters such as the Gaussian function (the kernel is based on the normal distribution curve), which tends to produce good results in reducing the influence of noise with respect to the image. The 2D Gaussian distributions, with standard deviation σ for image X, is given by Eq. (32) [49].

$$G(X, m, \sigma) = \frac{1}{\sigma\sqrt{2\pi}} e^{-\frac{1}{2}\left(\frac{X-m}{\sigma}\right)^2} \tag{32}$$

5.1. Pre- or post –processing

Usually, medical ultrasound images are affected by the mixed noise, which is the combination of speckle noise and Gaussian noise. There are two factors that influence the usefulness of a smoothing filter. The first reduces the range of resolutions over which variations in the output appear by the filter variation Δw, in the frequency domain be small and second factor is increase in spatial localization by a small spatial variance Δx. These localization requirements in the spatial and frequency domain are conflicting and related by the uncertainty principle given in Eq. (33)

$$\Delta w \, \Delta x \geq \frac{1}{4\pi} \tag{33}$$

It has been shown that Gaussian functions are the only ones that provide the optimal trade off between these conflicting requirements constrained by the Eq. (34) [50]..

$$\Delta w \, \Delta x = \frac{1}{4\pi} \tag{34}$$

So Gaussian filters are widely used in image filtering. In [51], the removal of mixed noise using order statistic filter and wavelet domain Wiener filter is proposed. Authors have evaluated two methods. The first method comprises, order statistic prefilter and empirical Wiener filter, which is used to reduce the Gaussian noise. The disadvantage of this method is the higher time consumption. The second method is, order statistic filter for each decomposition level, where decomposition is carried out by the wavelet transform, followed by thresholding. The drawback of this method is that its efficiency is less than that of the first method (about 1dB) in removing the mixed noise. In [52], denoising of mixed noise in ultrasound images is presented. Combined Bayesian maximum a posterior (MAP) estimator and ST-PCNN (Soft threshold pulse coupled neural networks) method has been used for mixed noise reduction. The method removes the speckle noise considerably than the Gaussian noise that degrades the ultrasound images. The drawback of the method is either Gaussian noise or speckle noise is removed. Hence we present a method to remove residual Gaussian noise from despeckled image.

Two alternative algorithms are developed for reducing mixed noise in medical ultrasound images [53]. In the first alternative, the denoising method reduces the Gaussian noise by applying Gaussian filter in pre processing stage, then despeckling is performed using either wavelet transform, Laplacian pyramid transform or contourlet transform. The noise model for the first alternative (i.e. Gaussian noise removal in pre processing followed by despeckling) is given by the Eq.(35).

$$X_{ij} = f_{ij} n_{ij} + g_{ij} \tag{35}$$

where X_{ij} represents the noisy pixel in the image X, f_{ij} represents the noise free pixel, n_{ij} and g_{ij} represent the multiplicative speckle noise and additive Gaussian noise, respectively. The

indices i, j represent the spatial position over the image. We use transform domain filtering techniques [36,54,47] for despeckling along with Gaussian filter in pre processing stage for removal of Gaussian noise.

In the second alternative, the despeckling of medical ultrasound images is performed either using wavelet transform, Laplacian pyramid transform or contourlet transform and, then, it is followed by postprocessing stage in which Gaussian filter removes Gaussian noise from the despeckled image. However, the second alternative assumes the noise model given by the Eq.(36)

$$X_{ij} = (f_{ij} + g_{ij})\, n_{ij} \tag{36}$$

The second alternative is investigated for image quality enhancement, due to noise removal, in an ultrasound image.

The experimentation is carried out using various kernel sizes and different values of σ. Larger values of σ produce a wider peak influencing the greater blurring. Kernel size is increased with increasing σ to maintain the Gaussian nature of the filter. Gaussian kernel coefficients depend on the value of σ. The Figure 17. shows different convolution kernels that approximate a Gaussian with σ. Gaussians are locally sensitive and can be made more spatially localized by decreasing parameter σ. It is observed that the kernel size 3×3 with σ = 0.5 yields better results than other kernels. It is found that larger kernels of size 5×5 or 7×7 produce better denoising effect but make the image more blurred. Thus, the empirically determined kernel size 3×3 and σ=0.5 are used in two alternative methods (Gaussian filter in Pre or Post processing).The two alternative methods are evaluated in terms of filter assessment parameters, namely, PSNR, SNR, MSE, variance and CC. The comparisons of the performance of the both alternatives with the despeckling methods discussed in [36,54, 47] are given in the Table 6. From the Table 6, it is observed that the Gaussian filter in pre processing stage is found to be more effective than that in despeckling based on Laplacian pyramid transform and contourlet transform. However, the Gaussian filter in postprocessing stage is found to be more effective in despeckling based on wavelet transform. Thus, the Gaussian filter improves the performance of despeckling methods, because Gaussian noise is characterized by adding to each image pixel a value from a zero mean Gaussian distribution. The zero mean property of the distribution allows such noise to be removed by locally averaging pixel values [55]. Further, it is observed that, the Gaussian filter in pre processing stage followed by contourlet transform based despeckling method yields better visual enhancement than the other denoising methods, which is illustrated in the Figure 18. The denoising and visual enhancement techniques developed in this study lead to improvement in the accuracy and reliability of automatic methods for medical ultrasound imaging systems.

5.2. Linear regression model

We present a linear regression based approach for clinical ultrasound image despeckling in the spatial domain. We propose a linear regression model for Gaussian noise representation of speckle noise for medical ultrasound images. This approach introduces an adaptive filter,

0.0128	0.0876	0.0128
0.0876	0.5986	0.0876
0.0128	0.0876	0.0128

(a)

0.075	0.124	0.075
0.124	0.204	0.124
0.075	0.124	0.075

(b)

Figure 17. The 3×3 kernel with (a) σ = 0.5, (b) σ = 1.

Denoising methods	SNR	PSNR	CC	MSE	Variance	Computational time (in Secs.)
First alternative with wavelet transform	25.22	30.23	0.9992	0.00050	0.0128	0.91
First alternative with LP transform	20.07	31.66	0.9965	0.00106	0.0426	0.38
First alternative with CT transform	29.99	35.15	0.9998	0.00031	0.0071	1.62
Second alternative with WT transform	26.32	32.54	0.9995	0.00050	0.0120	0.89
Second alternative with LP transform	19.76	30.12	0.9959	0.00133	0.0440	0.76
Second alternative with CT transform	28.89	34.35	0.9996	0.00036	0.0088	2.25
Despeckling method (WT transform) [36]	19.06	29.94	0.9954	0.00121	0.0368	2.80
Despeckling method (LP transform) [54]	18.23	28.44	0.9972	0.00141	0.0416	2.24
Despeckling method (CT transform) [47]	27.74	34.21	0.9990	0.00037	0.0203	1.64

Table 6. Comparison of performance of denoising methods based on Gaussian filtering with despeckling methods.

well preserving edges and structures in the image. The parameters in the model are estimated through an efficient iterative scheme.

In [56], the authors have developed the adaptive weights smoothing algorithm, which is an iterative procedure in which the size of a neighbourhood is adaptive to the surface smoothness. In [57], the estimation of jump surfaces by local piecewise linear kernel smoothing is examined.

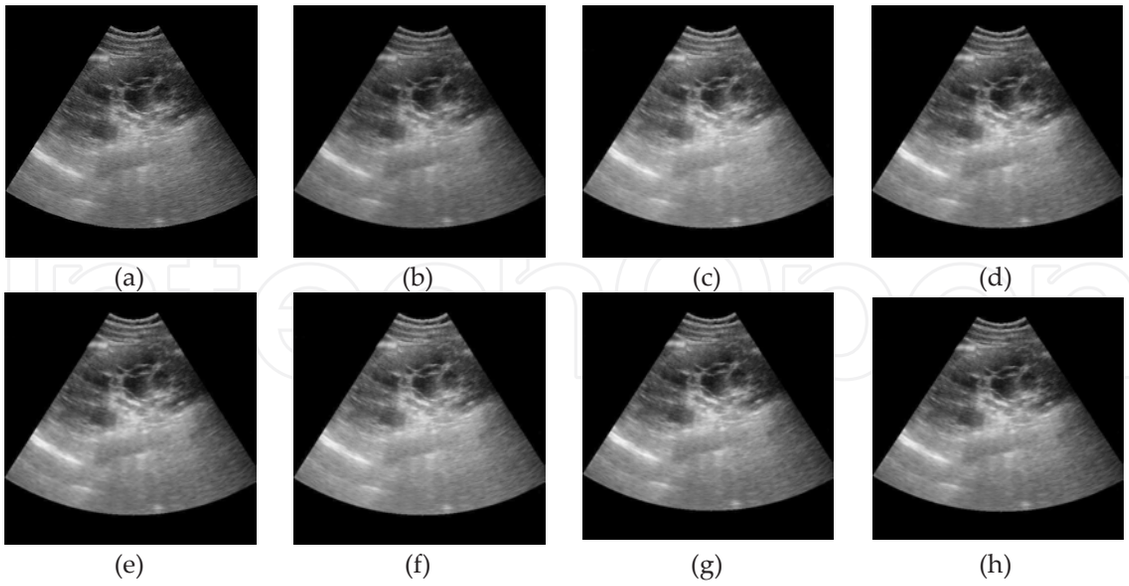

Figure 18. a) Original ultrasound image,(b) Denoised image using Gaussian filter, (c) Denoised image using 1st alternative with WT method (d) Denoised image using 1st alternative with LP method. (e) Denoised image using 1st alternative with CT method. (f) Denoised image using 2nd alternative with WT method. (g) Denoised image using 2nd alternative with LP method. (h) Denoised image using 2nd alternative with CT method.

In [58, 59], an anisotropic diffusion algorithm has been proposed for Gaussian noise removal. In [60], a bilateral filter to remove Gaussian noise is developed. In [61], a window based linear regression filter for echo cardiographic image denoising is proposed. The main draw backs of the above algorithms are that they need more computational time and complex circuit to implement them.

We consider a medical ultrasound image X and the corresponding despeckled image Y obtained by using the contourlet transform with cycle spinning [46]. The subtracted image Z=X-Y is the error image containing speckle noise. We find the mean m and standard deviation σ of Z and then simulate Gaussian noise G with these values of m and σ. The removal of this Gaussian noise G from despeckled image Y yields the new despeckled image $\hat{Y}$, i.e. $\hat{Y}$ =Y-G, which is further subtracted from the original image X to obtain the new error image Z containing the residual speckle noise. This procedure is repeated until the percentage of black pixels in error image Z reaches 99.9. We determine the maximum value of PSNR and the corresponding values of mean m and standard deviation σ using the iterated despeckled images $\hat{Y}$. This procedure is applied for all the medical ultrasound images X_i, i=1,..., 63, in the dataset, yielding the two sets of data points ($PSNR_i, m_i$) and ($PSNR_i, \sigma_i$), i=1,...,n_1 exhibits linear correlation. Using the method of least square errors, we obtain the lines of best fit for these data, namely:

$$m=a * PSNR + b \tag{37}$$

$$\sigma =c * PSNR + d \tag{38}$$

where a, b, c and d are the constants, which are the linear regression model parameters for Gaussian representation G(m, σ) of speckle noise in the medical ultrasound images. The Eqs. (37) and (38) represent the linear regression model for Gaussian representation G(m, σ) of speckle noise in a medical ultrasound image with its PSNR value determined already [62]. The steps involved in this procedure are given in the Algorithm 1.

Algorithm 1. Linear regression model for Gaussian representation G (m, σ) of speckle noise.

Input : Medical ultrasound image.

Output: Linear regression model parameters for Gaussian representation G (m, σ) of speckle noise.

Start

Step 1: Input medical ultrasound image X.

Step 2: Input despeckled ultrasound image Y obtained by using contourlet transform with cycle spinning.

Step 3: Find the error image Z as difference between X and Y
(i.e. Z = X – Y).

Step 4: Find the percentage of black pixels in Z.

Step 5: Find the mean (m) and standard deviation (σ) of Z.

Step 6: Simulate the Gaussian noise G with mean m and standard deviation σ
obtained in the Step 5.

Step 7: Subtract the simulated Gaussian noise G from despeckled image Y to obtain the resultant image ($\hat{Y}$), i. e. $\hat{Y}$ =Y-G.

Step 8: Find the PSNR, mean and standard deviation of the resultant image
($\hat{Y}$) obtained in the Step 7. Set Y = $\hat{Y}$.

Step 9: Repeat the Steps 3-8 until the percentage of black pixels in Z reach 99.9%.

Step 10: Find the maximum of the PSNR values obtained for the iterated despeckled images
($\hat{Y}$) and the corresponding values of m and σ. Store the values of maximum PSNR and corresponding values of m and σ.

Step 11: The Gaussian noise with mean m and standard deviation σ determined in the Step 10 is the modelled Gaussian noise for the image X.

Step 12: Repeat the Steps 1-11 for all the ultrasound images X and their corresponding despeckled images Y in the data set.

Step 13: Obtain the lines of best fit for the both PSNR vs. m and PSNR vs. σ obtained for all the ultrasound images (n_1) in the Step 12 using the method of least square errors. i. e. determine the constants a, b, c and d of the Eqs.(37) and (38), which are the lines of best fit that form the linear regression model for representing the speckle noise in ultrasound image as Gaussian noise. The lines of best fit are found using goodness of fit static.

Step 14: Output linear regression model parameters a, b, c and d of Eqs.(37) and (38).

Stop

The data points ($PSNR_i, m_i$) and ($PSNR_i, \sigma_i$), i=1,...,63 obtained for 63 typical ultrasound images of the image data set are stored and then used for regression of PSNR on m and also PSNR on σ. In the ultrasound image data set used for building regression model for Gaussian representation of speckle noise, we select a reference image X_{ref} for which the PSNR value is minimum. Given an arbitrary input medical ultrasound image X, we compute the PSNR of X with respect to the reference image X_{ref}. Using linear regression model (Eqs. (37) and (38)), we estimate the values of mean m and standard deviation σ of the Gaussian noise, which is removed from the input original image. The resultant image is the despeckled image (Y). The 'goodness of fit' statistic for the lines of regression is given by two quantities, namely, the sum of squares due to error of the fit (SSE) and root mean squared error (RMSE).The SSE is given by Eq. (39) :

$$SSE = \sum_{i=1}^{n} \left(Y_i - \hat{Y}_i \right)^2 \tag{39}$$

where Y_i=actual mean value of Gaussian noise, $\hat{Y}_i$= estimated mean value of Gaussian noise, and

n_1= total number of ultrasound images in the dataset.

The RMSE is given by Eq. (40) :

$$RMSE = \sqrt{\frac{SSE}{n_1}} \tag{40}$$

If the SSE and RMSE values are closer to zero, they indicate better fit. The general model for Gaussian noise estimation and removal in despeckling ultrasound image is shown in the Figure 19.

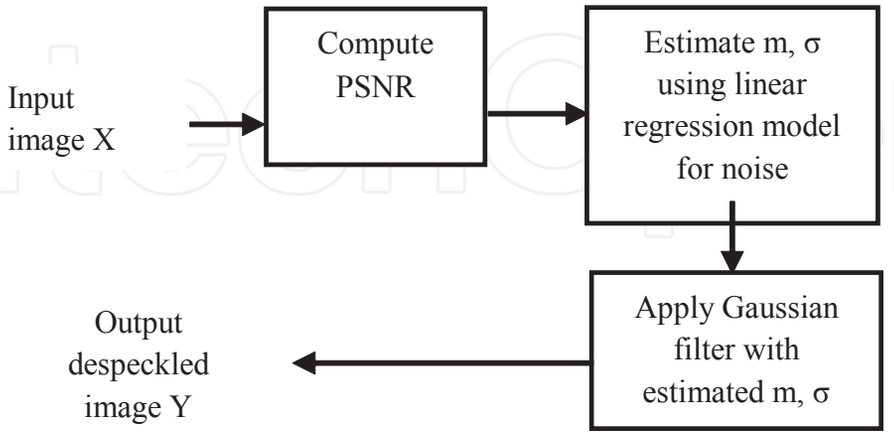

Figure 19. The general model for Gaussian representation of speckle noise.

The steps involved in the denoising process, shown in Figure 19 are given in the Algorithm 2.

Algorithm 2. Despeckling based on linear regression model for Gaussian noise estimation.

Input: Medical ultrasound image.

Output: Despeckled image.

Start

Step 1: Input medical ultrasound image X.

Step 2: Compute PSNR of image X with respect to the reference image X_{ref} prescribed by the regression model.

Step 3: Obtain Gaussian noise estimation G(m, σ) corresponding to the PSNR computed in the Step 2 using the regression model (Eqs.(37) and (38))

Step 4: Apply Gaussian filter with estimated mean (m) and standard deviation (σ), obtained n the Step 3, to the input image X, which yields the despeckled image Y.

Step 4: Apply Gaussian filter with estimated mean (m) and standard deviation (σ), obtained in the Step 3, to the input image X, which yields the despeckled image Y.

Step 5: Output the despeckled image Y.

Stop.

The linear regression model parameters a, b, c and d for Gaussian representation of speckle noise are computed for the dataset of 63 ultrasound images and the linear regression model equations are (Eqs.(37) and (38)),where a=-6.129e-007, b=2.742e-005, c=-0.0002192, d=0.01004, with the measures of 'best fit' are SSE=4.682e-009, RMSE=8.833e-006 for mean vs. PSNR and SSE=0.0006471, RMSE=0.003284 for standard deviation vs. PSNR. The Figures(20 and 21) show the lines of best fit for mean vs. PSNR and standard deviation vs. PSNR, respectively, which are used for Gaussian noise estimation and removal.

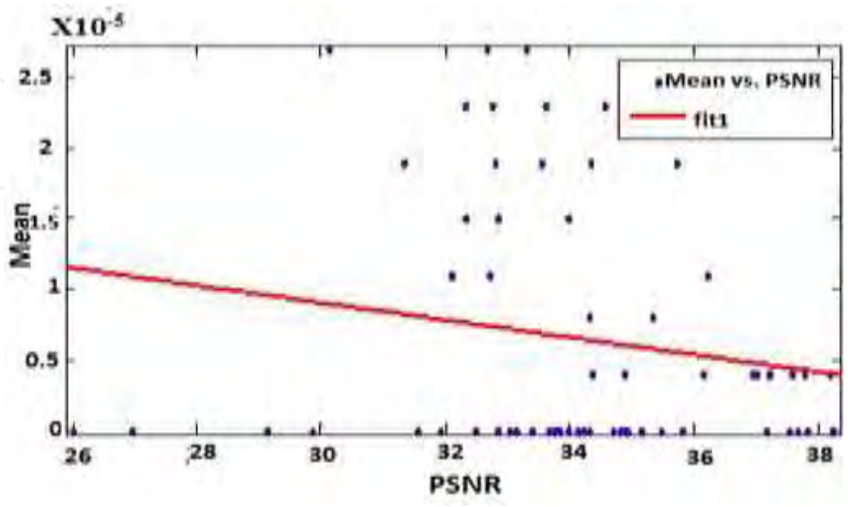

Figure 20. Linear regression of mean on PSNR

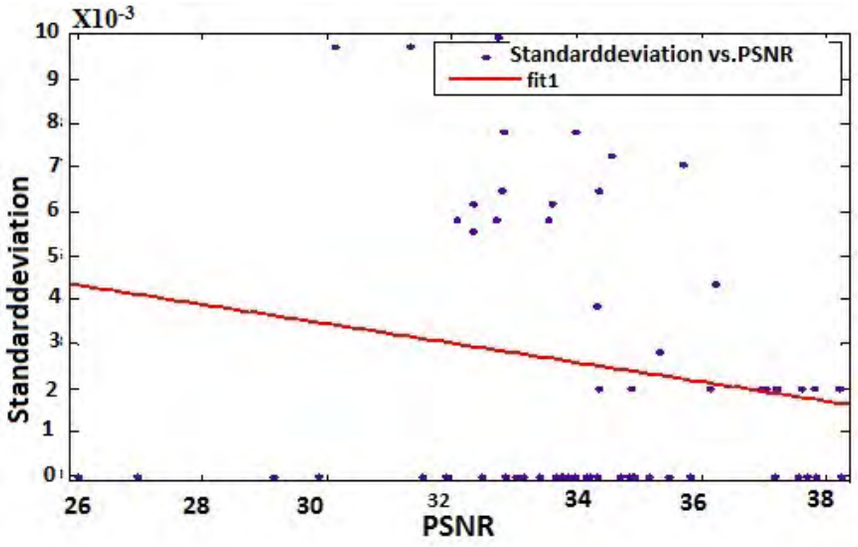

Figure 21. Linear regression of standard deviation on PSNR

The comparison of the results of the proposed method with the contourlet transform method (with cycle spinning) is given in the Table 7. It is observed that the image quality enhancement obtained by the despeckling method based on linear regression model is better than that obtained by the contourlet transform method in terms of PSNR and computational time required for denoising.

Denoising methods	PSNR (in dB)	Computational Time (in Secs.)
Contourlet transform using cycle spinning	35.91	24.09
Proposed method based on linear regression model	36.98	0.34

Table 7. Comparison of performance of despeckling based on contourlet transform and proposed method based on linear regression model.

The Figure 22. shows a sample medical ultrasound image, its despeckled image using contourlet transform with cycle spinning and the denoised image using the linear regression model respectively. The visual quality of image enhancement can also be observed from the sample image and its denoised image. The anatomical structures are more clearly visible in the Figure 22.(c) than that in Figure 22.(b). The box indicates the region of image in (b) and (c) showing prominent visual enhancement due despeckling methods.

The Figure 23 shows the visual enhancement due to various despeckling methods for comparison. (a) shows the sub image of original image, The Figure 23 (b)-(f) indicates the sub image showing visual enhancement due to different despeckling methods namely, Wiener filter with (3X3),wavelet transform method, contourlet transform method, cycle spinning based contour-

http://dx.doi.org/10.5772/56519

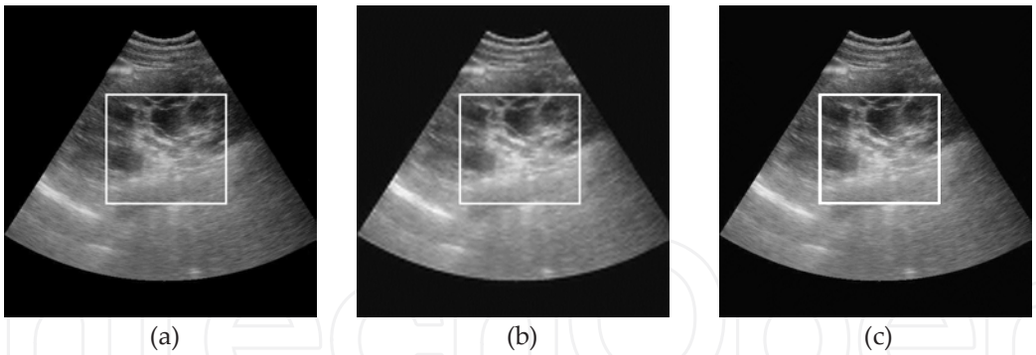

Figure 22. a) Original ultrasound image (b) Despeckled image using the contourlet transform with cycle spinning (c) Denoised image using the proposed linear regression model. The box Indicates the region of image in (b) and (c) showing prominent visual enhancement due to the despeckling.

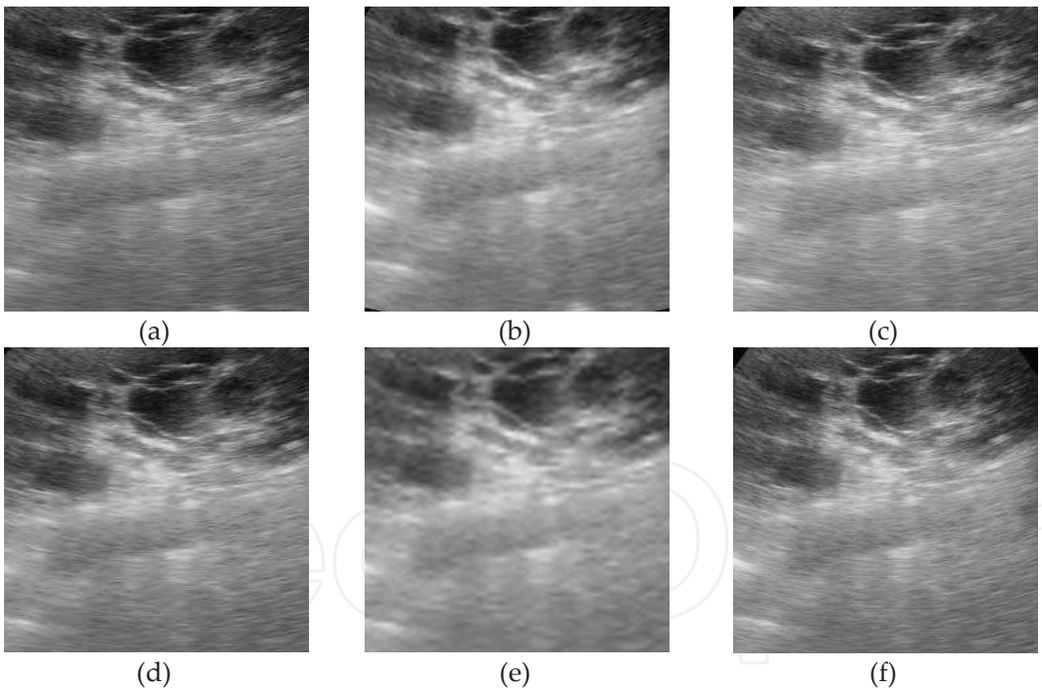

Figure 23. a) A sub image of original ultrasound image (b) sub image of despeckling using Wiener filter (c) sub image of despeckling using WT method (d) sub image of despeckling using CT method (e) sub image of despeckling using cycle spinning based CT method (f) sub image of despeckling using proposed linear regression model.

let transform method and proposed linear regression model. The prominent visual enhancement is observed using the proposed linear regression model.

The proposed method estimates the Gaussian noise content in the input medical ultrasound image for denoising the image efficiently. Hence, it is easily amenable for building embedded system software for ultrasound imaging equipments in order to display the high quality images, which helps the medical expert in the diagnosis with greater accuracy.

6. Conclusion

In this chapter, a despeckling method, based on a 2D directional non separable transform known as contourlet transform is presented. Conventional 2D wavelet transform is separable and thus cannot sparsely represent non separable structures of the image, such as directional curves. It is found that pyramidal directional filter bank feature of contourlet transform makes it a good choice for representation of curves and edges in the image. But, the contourlet transform, one of the recent geometrical image transforms, lacks the feature of translation invariance due to sub sampling in its filter bank structure. In cycle spinning, CT is improved by averaging the estimation of all translations of the degraded image. The Gibbs effect is considerably reduced by the contourlet transform with cycle spinning, because the average of different estimations of the image reduces the oscillations. In the literature, the authors [33,41,45,54,55,61] have considered ultrasound images (natural/synthetic) with artificially added speckle noise content and have proposed methods for despeckling such images. However, in the present study, we considered ultrasound images captured by the ultrasound equipment which contain inherent speckle noise and have proposed methods for removing the speckle noise more effectively.

When the noise characteristics of the images are unknown, it is proposed to denoise by a linear regression model, which is cost effective compared to the other methods. We have proposed a novel linear regression model for Gaussian noise estimation and removal in despeckling medical ultrasound images. The experimental results demonstrate its efficacy both in terms of speckle reduction and computational time required for denoising. Further, the proposed regression model is simple, generic and computationally inexpensive. Hence, it is easily amenable for building embedded system software for ultrasound imaging equipments in order to display the high quality images, which help the medical experts for speedy accurate image analysis and diagnosis. Further, the proposed regression model is simple, generic and computationally inexpensive.

Acknowledgements

Authors are grateful to the reviewers for their helpful comments which improved the quality of the paper. Further, authors are thankful to Dr. Ramesh Mankare, Radiologist, Sangamesh-

war Scanning Centre, Bijapur, Karnataka, India, for providing the ultrasound images of kidney, liver and also for helpful discussions.

Author details

1 Dept. of P.G. Studies and Research in Computer Science, Gulbarga University, Gulbarga, Karnataka, India

2 Dept. of Computer Science and Engineering, B.L.D.E.A's Dr. P.G.H. College of Engineering, Bijapur, Karnataka, India

3 Dept. of Medicine, Sri.B.M.Patil Medical College, BLDE University, Bijapur, Karnataka, India

References

[1] Suetens Paul, Fundamentals of Medical Imaging, (1st Edition), Cambridge university, U.K.; 2002.p145-182.

[2] Hedrick W.R. and Hykes D.L., Image and signal processing in diagnostic ultrasound imaging, Journal of Diagnostic Medical Sonography 1989; 5(5): 231–239.

[3] Godman J.W., Some Fundamental Properties of Speckle, Jl. Opt. Soc. Am. 1976; 66 (11):1145-1149.

[4] Burckhardt C.B., Speckle in Ultrasound B Mode Scans, IEEE Trans. Sonics Ultrasonics 1978;25:1-6.

[5] Yongjian Y. and Acton S.T. Speckle reducing anisotropic diffusion, IEEE Trans. Image Processing. Nov. 2002; 11(11):1260–1270.

[6] Prager R.W., Gee A.H., Treece G.M., and Berman L., Speckle detection in ultrasound images using first order statistics, GUED/ F-INFENG/TR 415, University of Cambridge, Dept. of Engineering, July, 2002: 1–17.

[7] Zong X., Laine A. F., and Geiser E. A. Speckle reduction and contrast enhancement of echocardiograms via multiscale nonlinear processing, IEEE Trans.on Medical. Imaging., 1998;17:532-540.

[8] Netravati A.N. and Haskell B.G., Digital Pictures: Representation, Compression and standards, (2nd ed.) 2000, New York Plenum.

[9] Loizou C.P., Pattichis,Pantziaris M.,Tyllis T.,and Nicolaides A. Quality evaluation of Ultasound Imaging in the carotid Artery Based on Normalization and Speckle Reduction Filtering, International Federation for Medical and Biological Engineering, 2006; 414-426.

[10] Lee J.S. Speckle Analysis and Smoothing of Synthetic Aperture Radar Images, Comp. Graphics Image Processing 1981; 17: 24-32.

[11] Insana M., Hall T.J,Glendon., G.C., and Posental S.J., Progress in quantitative ultrasonic imaging, SPIE Vol. 1090 Medical Imaging III, Image Formation,1989; 2-9.

[12] Lee J.S. Refined filtering of image noise using local statistics Computer Graphic and Image Processing,1981;15: 380-389.

[13] Kuan D.T. Sawchuk A. A., Strand T. C., and Chavel P., Adaptive restoration of images with speckle IEEE Trans. ASSP, 1987; 35(3): 373-383.

[14] Wiener Norbert Extrapolation, Interpolation and Smoothing of Stationary Time Series, New York: Wiely, 1949.

[15] Jain A. K. 1989, Fundamental of Digital Image Processing. NJ: Prentice-Hall,

[16] Singh Y.K., Parui S.K., ISITRA: A generalized way of signal decomposition and reconstruction Digital Signal Processing, Elsevier, 2006, 16(1):3-23.

[17] Kalaivani Narayanan S. and Wahidabanu R.S.D., A View of Despeckling in Ultrasound Imaging., Int'l. Jl. of Signal Processing, Image processing and Pattern Recognition, 2009; 2(3): 85-98.

[18] Kaur Jappreet, Kaur Jasdeep, Kaur Manpreet, Survey of Despeckling Techniques for Medical Ultrasound Images, Int'l. Jl. Comp.Tech. Appl. 2011 July-august ;2(4): 1003-1007.

[19] Achim A., and Bezerianos A, Novel Bayesian Multiscale Method for Speckle Removal in Medical Ultrasound Images, IEEE Trans. on Medical Imaging, 2001; 20(8): 772-783.

[20] Nikhil gupta and Swamy M.N., Despeckling of Medical Ultrasound Images Using Data and Rate Adaptive Lossy Compression. IEEE Trans. Medical Imaging, 2005;24(6):682-695.

[21] Ruikar S.D. and Doye D.D., Wavelet Based Image Denoising Technique. Int'l. Jl. of Advanced Computer Science and Applications, March 2011; 2(3):49-53.

[22] Mallat S., A theory of multiresolution signal decomposition: The wavelet representation IEEE Trans. Pattern Anal. Machine Intell., July 1989; 11: 674-693.

[23] Gonzalez Rafael C., Woods Richard E., Digital Image Processing, 2nd Edition, Prentice Hall, Upper Saddle River, NJ, 2002; 350-402

[24] Cohen A., Daubechies I., and Feauveau J. C. Biorthogonal bases of compactly supported wavelets. Comm. Pure Appl. Math., 1992; 45:485-500.

[25] Mallat S. Wavelet tour of signal processing 3rd Edition, Academic press, 2009; 535-606.

[26] Donoho D.L., Johnstone I.M. De-noising by soft-thresholding. IEEE Trans. on Information Theory, 1995; 41(3):613-27.

[27] Hiremath P.S. Akkasaligar Prema T. and Badiger Sharan, Performance Evaluation of Wavelet Based Thresholding for Despeckling Medical Ultrasound Images,Proceedings of the Int'l Conf. on Cognition and Recognition(ICCR-08), 10th-12th April 2008, Mysore, Karnataka, India:574-579.

[28] Donoho, D.L., Johnstone I.M. Ideal Spatial Adaptation By Wavelet Shrinkage, Biometrika, 1994, 81:425-455.

[29] Chang S. G. Bin Yu and Martin Vetterli, Adaptive Wavelet Thresholding for Image Denoising and Compression, IEEE Trans. Image Processing, 2000, 9 (9): 1532-1546.

[30] Minh N. Do, Framing Pyramids, IEEE Trans. on Signal Processing, 2003 Sept, 51(9): 2329-2342.

[31] Vladimir P.M. Ilya Shmulevich, Karen Egiazarian, Jaakko Astola, Block Median Pyramidal Transform:Analysis and Denoising Applications IEEE Trans.on Signal Processing, 2001 Feb.; 49(2):364-372.

[32] Bruno Aiazzi, Luciano alparone and Stefano Baronti, Multiresolution Local - Statistics speckle filtering based on a ratio Laplacian pyramid, IEEE Trans. on Geosciences and Remote Sensing, 1998 Sept.; 36(5):1466-1476.

[33] Saad Ali, Visual enhancement of digital ultrasound images: Wavelet Versus Gauss-Laplace contrast Pyramid, Int'l. Jl. of Computer Assisted radiology and Surgery, 2007 Aug. ; 2(2),63-70:117-125.

[34] Zhang F.,Koh L.M., Yoo Y.M. and Kim Y.,2007, Nonlinear diffusion in Laplacian pyramid domain for ultrasonic speckle reduction, IEEE Trans. on Medical Imaging,26(2): 200-211.

[35] Burt P. J. and Adelson E. H., The Laplacian pyramid as a compact image code, IEEE Trans. on Commun,1983; 31(4):532-540.

[36] Hiremath P.S., Akkasaligar Prema T., Badiger Sharan, Visual Enhancement of Digital Ultrasound Images using Multiscale Wavelet Domain, Int'l. Jl. of Pattern Recognition and Image Analysis, 2010; 20(3): 303-315

[37] Do Minh N., Vetterli Martin, Framming pyramids, IEEE Trans. on Signal Processing,: 2003; 2329-2342

[38] Huang Mao yu, Huang yueh Min and Wang Ming-Shi, Dec. 15-17, 2004, Taipei, Taiwan. Speckle reduction of ultrasound image based on contourlet transform, Int'l. Computer Symposium :178-182.

[39] Hiremath P.S., Akkasaligar Prema T., Badiger Sharan, Despeckling Medical Ultrasound Images Using the Contourlet Transform,In: Proceedings of the 4th AMS Indian Int'l Conf. on Artificial Intelligence(IICAI-09),16-18 Dec. 2009,Tumkur, Karnataka,India,:1814-27.

[40] Hiremath P.S., Tegnoor Jyothi R., Automatic Detection of Follicles in Ultrasound Images of ovaries using Edge Based Method, IJCA Special Issue on Recent Trends in Image Processing and Pattern Recognition, 2010; 120-125.

[41] Song Xiao-yang, Chen Ya-zhu, Zhang Su, and Yang Wei, Speckle Reduction Based on Contourlet Transform Using Scale Adaptive Threshold for Medical Ultrasound Image, Jl. Shanghai Jiaotong Univ. (Sci), 2008; 13(5):553-558.

[42] Phoong S. M., Kim C. W., Vaidyanathan P. P., and Ansari R., A new class of two-channel biorthogonal filter banks and wavelet bases, IEEE trans. Signal Processing, 1995 Mar.; 43(3):649-665.

[43] Coifman R.R. and Donoho D.L., Translation invariant denoising, in Wavelets and statistics, Springer Lecture notes in Statistics, 103, Newyork, springer-Verlang,1994; 125-150.

[44] Eslami Ramin and Radha Hayder, The contourlet transform for image denoising using cycle spinning, Proceedings of Asilomar Conference on Signals, Systems and Computers, 2003;p1982-1986.

[45] Xiaobo Qu, Jingwen Yan, The cycle spinning based sharp frequency localized contourlet transform for image denoising, Proceedings of 2008 3rd Int'l. Conference on Intelligent System and Knowledge Engineering. 2008;p1247-1251.

[46] Hiremath P.S.,Akkasaligar Prema T.and Badiger Sharan, The Cycle Spinning Based Contourlet Transform for Despeckling Medical Ultrasound Image, Proc. Int,l Conf. on Trends in Information Technology and Applications, U.A.E., 11th-13th Dec. 2010, 72-76.

[47] Hiremath P.S., Akkasaligar Prema T. and Badiger Sharan, Speckle Reducing Contourlet Transform for Medical Ultrasound Images World Academy of Science, Engineering and Technology-Special Journal Issue, 2011; 80:1217 - 1224.

[48] Goshtasby Ardershir, On edge focusing Int'l. Jl. of Image and Vision Computing, 1994; 12(4):247-256.

[49] Fisher R., Perkins S., Walker A., Wolfart E.,2003, Gaussian Smoothing, Hypermedia image Processing Reference (HIPR2), Available from: URL: http:/ homepages. inf. ed.ac.uk / rbf/ HIPR2/gsmooth.html.

[50] Bracewell R., The Fourier transform and its applications, McGraw Hill: 1965; 160-163.

[51] Badulescu P. and Zaciu R. Removal of mixed-noise using order statistic filter and wavelet domain wiener filter. Semiconductor conference,Circuits And Systems'99 procedings, 1999;1:301-304.

[52] Saraswati J. S. and Mary brinda, Denoising of mixed noise in ultrasound images Int'l. Jl. of Computer Science Issues, July 2011; 8(4):517-523.

[53] Hiremath P.S., Akkasaligar Prema T. and Badiger Sharan, Removal of Gaussian Noise in Despeckling Ultrasound Images, The Int'l. Jl. of Computer Science and Applications (2278-1080), July 2012; 1(5): 25-35.

[54] Hiremath P.S., Akkasaligar Prema T. and Badiger Sharan, Performance Comparison of Wavelet Transform and Contourlet Transform based methods for Despeckling Medical Ultrasound Images Int'l. Jl. of Computer Applications (0975 - 8887), 2011; 26(9):34-41.

[55] Bamber J.C. and Daft C. Adaptive Filtering for Reduction of Speckle in Ultrasound Pulse Echoim ages. Ultrasonics, 1986: 41-44.

[56] Polzehl J. and Spokoiny V.G., Adaptative weights smoothing with applications to image restoration Journal of the Royal Statistical Society B-62: 2000; 335-354.

[57] Qiu P., The local piecewisely linear kernel smoothing procedure for fitting jump regression surfaces Technometrics 2004; 46:87-98.

[58] Perona P. and Malik J., Scale -space and edge detection using anisotropic diffusion, IEEE Trans. Pattern Anal. Machine Intell., 1990; 12:629-639.

[59] Black M.J., Sapiro Guillermo, Marimont David,and Heeger David, Robust Anisotropic Diffusion, IEEE Trans. on Image Processing, 1998; 7(3):421- 432.

[60] Black M.J., Fleet D., and Yacoob Y., Robustly Estimating changes in Image Appearance, Computer Vision and Image Understand, 2000; 78:8-31.

[61] Rajalaxmi S., Arun Kumar V., and Baskar P., Window Based Linear Regression Filter for Echocardiographic Image Denoising, Int'.l Jl. of Systems algorithms and Applications, May 2(ICRAET12), 2012, 180-183.

[62] Hiremath P.S., Akkasaligar Prema T., Badiger Sharan, Linear Regression Model for Gaussian Noise Estimation and Removal for Medical Ultrasound Images, Int'l. Jl. of Computer Applications (0975 - 8887), July 2012, 50(3),11-15.

Chapter 1

3D Ultrasound Imaging in Image-Guided Intervention

Aaron Fenster, Jeff Bax, Hamid Neshat,
Nirmal Kakani and Cesare Romagnoli

Additional information is available at the end of the chapter

http://dx.doi.org/10.5772/55230

1. Introduction

Soon after the discovery of x-rays, physicians recognized the importance of using imaging to guide interventional procedures. As imaging technology became more advanced with the development of fluoroscopic, CT, MR and ultrasound systems, image-guided interventions have become a critical tool for physicians in dealing with complex interventional and surgical procedures. Today, image-guided procedures make use of computer-based systems to provide real-time three-dimensional (3D) information of the anatomy of the patient being treated. The information is presented in various ways, such as virtual graphical image overlays, or multi-screen approaches to help the physician precisely visualize and target the anatomical site.

Since the development of Computed Tomography (CT) in the early 1970s, the availability of 3D anatomical information has revolutionized diagnostic radiology by providing physicians with 3D images of anatomical structures. The pace of development has continued with the development of 3D magnetic resonance imaging (MRI), positron Emission Tomography (PET), and multi-slice and cone beam CT imaging. These imaging modalities have stimulated the development of a wide variety of image-guided interventional procedures.

Although 2D ultrasound (2D US) imaging has been used extensively for interventional procedures, such as biopsy and guidance of ablation procedures, 3D ultrasound is slowly growing in clinical applications [1]. Today, the majority of US-based diagnostic and interventional procedures are still performed using conventional 2D imaging. Over the past two decades, university-based investigators and commercial companies have utilized both 1D and 2D arrays while developing 3D ultrasound (3D US) imaging techniques. 3D US techniques have been increasingly used in diagnosis, minimally invasive image-guided interventions and intra-operative use of imaging [2-4]. Today, most US system manufacturers provide 3D US imaging capability as part of the systems. Advances in 3D US imaging technology have resulted in high quality 3D images of complex anatomical structures and pathology, which are used in diagnosis of disease and to guide interventional and surgical procedures [5-9].

In this chapter we focus on the recent development of 3D US imaging as it applies to image-guided interventions. The chapter will briefly review how 3D US images are obtained and then will provide two examples of recent development of 3D US- guided interventional procedures.

2. 3D ultrasound imaging systems

2.1. Benefits of 3D ultrasound imaging

Conventional 2D US imaging systems making use of 1D transducer arrays allow users to manipulate the hand-held US transducer freely over the body in order to generate images of organs and pathology. While this capability is sufficient for many interventional procedures such as breast biopsy, some interventional procedures require 3D image visualization, which 3D US imaging attempts to provide. More specifically:

- Freely manipulating the conventional US transducer during the interventional procedure over the anatomy to generate 2D US images requires that users mentally integrate many 2D images to form an impression of the anatomy and pathology in 3D. In cases of interventions of complex anatomy or pathology, this approach leads to longer procedures and may result in variability in guidance of the interventional procedures.
- Since the conventional 2D US imaging transducer is held and manipulated manually, it is difficult to relocate the 2D US image at the exact location and orientation in the body at a later time. Since monitoring the progression of the interventional procedure often requires imaging of the same location (plane) of the anatomy, manual manipulation of a 2D US image is suboptimal.
- Conventional 2D US imaging does not permit viewing of planes parallel to the skin – often called C-mode. This approach is, at times, suboptimal since interventional procedures sometimes require an arbitrary selection of the image plane for optimal viewing of the pathology and guiding the interventional procedure.
- Planning the interventional procedure and therapy monitoring often require accurate lesion volume measurements. Since conventional 2D US imaging only provides a cross-section of the lesion, measurements of organ or lesion volume is variable and at times inaccurate.

The following sections review approaches used in generation of 3D US images based on 1D. An emphasis is placed on the geometric accuracy of the generated 3D images as well as the use of this technology in interventional and quantitative monitoring applications.

2.2. Mechanical 3D US scanning systems

Mechanical 3D US systems make use of mechanisms using motors to translate, tilt, or rotate a conventional 2D US transducer. A sequential digitized series of 2D US images and their relative positions and orientation are acquired rapidly by a computer as the 2D US transducer is moved, while the 3D US image is reconstructed. Since the scanning geometry in mechanical 3D US systems is predefined and precisely controlled by a mechanical motorized system, the relative position and orientation of the acquired 2D US images are known accurately and precisely.

These mechanical 3D scanning systems allow the user to optimize the image resolution by adjusting the angular or spatial interval between the acquired 2D image [10].

Two approaches have been used in the development of mechanical 3D US scanning systems: integrated 3D US transducers with the scanning mechanism within the transducer housing; and external mechanical fixtures that hold the housing of a conventional 2D US transducers. Both approaches have been successfully used for a variety of clinical applications including interventional applications.

2.2.1. Wobbling or tilting mechanical 3D US scanners

Most US system manufacturers offer integrated 3D US transducers that are based on a mechanically-swept transducer or "wobbler". In these systems a 1D US array is wobbled or swept back and forth inside the 3D transducer housing. Digital 2D US images that are generated while the 1D US array is wobbled, which are used in the 3D US image reconstruction. These 3D transducers are larger than conventional 2D US transducers. These types of 3D US transducers are convenient to use but require a special US machine that can control the 3D scanning and reconstruct the acquired 2D images into a 3D image.

Many interventional 3D US-guided interventional systems are currently using external fixtures for mechanical 3D scanning since researchers typically do not get access to the control of the US system for development of novel interventional systems. In this approach, a motorized custom made fixture is used to house the conventional 2D US transducer. A computer is used to control the motor to cause the US transducer to tilt or "wobble". The video stream from the US machine is digitized using an analogue or digital frame grabber. Since the relative angle between the acquired 2D images is known, a 3D image can be reconstructed as the 2D images are acquired.

Although the external mechanical 3D scanning fixtures are bulkier than integrated 3D transducers, they can be used with any US manufacturer's transducer, obviating the need to purchase a special 3D US machine. In addition, the external fixture approach can take advantage of improvements in the US machine (e.g., image compounding, contrast agent imaging) and flow information (e.g., Doppler imaging) without any changes in the scanning mechanism.

Both approaches used in mechanical 3D US scanning allow short imaging times, ranging from about 3 to 0.2 3D images/s. The 3D images are of high quality and also include B-mode and Doppler information.

Figure 1a is a diagram of the mechanical tilt approach of a conventional 1D array US transducer about an axis parallel to the face of the transducer, and 1b shows the tilting axis away from the face of the transducer. The latter approach is typically used in integrated 3D scanning mechanisms. In both approaches, the acquired 2D US images are arranged as a fan with an adjustable angular spacing, e.g., 1.0°. To generate a 3D image, the housing of the 3D probe or external fixture remains fixed on the skin of the patient while the US transducer is wobbled. The time required to generate a 3D US image depends on the 2D US image update rate and the number of 2D images needed to generate the 3D image. The 2D US image update rate depends on the US machine settings (i.e., depth setting and number of focal zones) and number of acquired 2D US images is determined by the chosen angular separation between the acquired 2D images,

and the total scan angle needed to cover the desired anatomy. Typically, these parameters can be adjusted to optimize scanning time, image quality and the size of the volume imaged [11-16]. The most common integrated 3D transducers using the wobbling technique are used for abdominal and obstetrical imaging [17-19].

The 3D image resolution will not be isotropic. The resolution in the 3D US image will degrade in the axial direction away from the transducer due to the increasing US beam spread in the lateral and elevational directions of the acquired 2D US images. Since the acquired 2D images used to generate a 3D image are arranged as a fan, the distance between the acquired US images increases with increasing axial distance. Increasing axial distances result in decreasing spatial sampling resulting in further loss of spatial resolution in the elevational direction of the acquired 2D US images of the reconstructed 3D image [20].

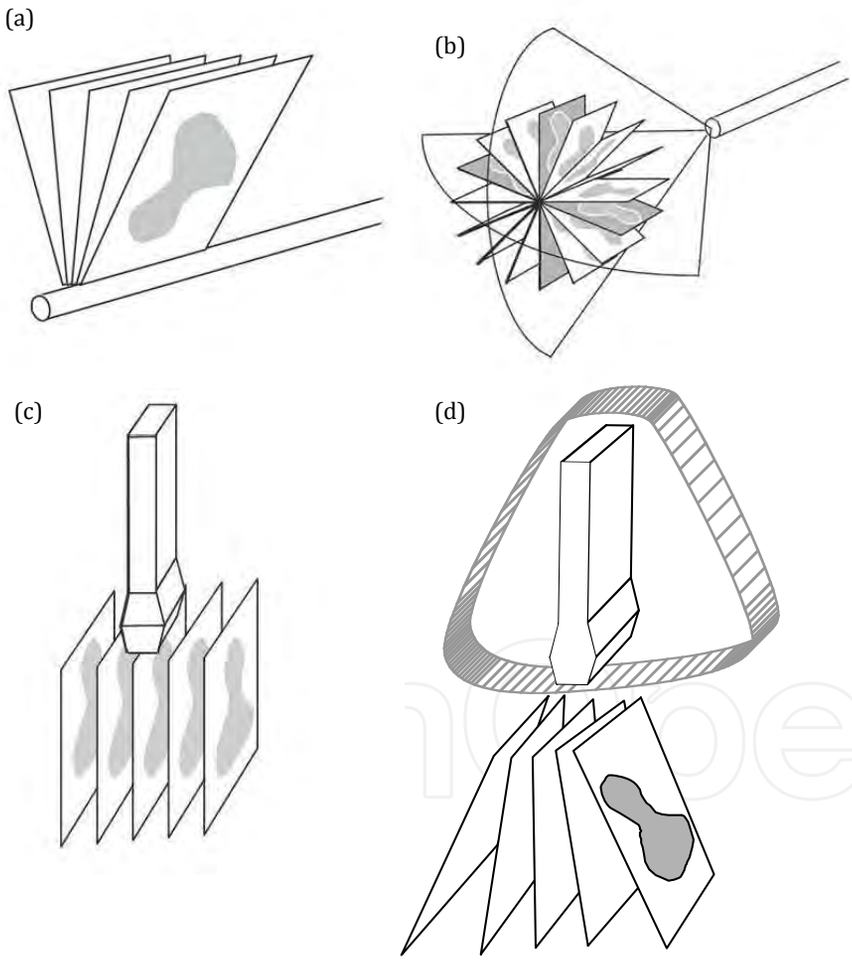

Figure 1. Schematic diagrams of 3D US mechanical scanning methods. (a) A side-firing TRUS transducer is mechanically rotated and the acquired images have equal angular spacing. The same approach is used in a mechanically-wobbled transducer. (b) A rotational scanning mechanism using an end-firing transducer, typically used in 3D TRUS guided prostate biopsy. The acquired images have equal angular spacing. (c) A linear mechanical scanning mechanism, in which the acquired images have equal spacing. (d) The mechanically tilting mechanism, but integrated into a 3D US transducer. The US transducer is "wobbled" inside the housing of the transducer.

http://dx.doi.org/10.5772/55230

2.2.2. Linear mechanical 3D scanners

Linear scanners mechanisms use an external motorized fixture to move the conventional 2D transducer across the skin of the patient. The 2D transducer can be fixed to be perpendicular to the surface of the skin or at an angle for acquiring Doppler images. The spacing between the acquired 2D images is adjustable but constant during the scan so that the acquired 2D images are parallel and uniformly spaced (see Fig. 1c). The velocity of the transducer as it is being scanned is adjusted to obtain 2D images with an appropriate spatial interval for generating high quality 3D images [10].

The predefined spacing between the acquired 2D US images allows 3D images to be reconstructed while the 2D US images are being acquired. In the direction parallel to the acquired 2D US images the resolution of the reconstructed 3D US image will be the same as the original 2D US images. However, in the direction of the 3D scanning, the resolution of the reconstructed 3D image will be equal (if spatial sampling is appropriate) to the elevational resolution of the acquired 2D US images. Thus, the resolution of the 3D US image will be poorest in the 3D scanning direction due to greater spread of the US beam in the elevational direction [21].

This scanning approach is not typically used in interventional applications; however, it has been successfully implemented in many vascular B-mode and Doppler imaging applications, particularly of for carotid arteries [11, 22-30] and tumor vascularization [25, 31-33].

2.2.3. Endo-cavity rotational 3D scanners

The endo-cavity rotational 3D scanning approach has been used extensively in 3D US-guided prostate interventional procedures. In this approach an external fixture or internal mechanism is used to rotate an endo-cavity transducer (*e.g.*, a transrectal ultrasound (TRUS) probe, see Fig. 1b) about its long axis. Endo-cavity transducers using an end-firing approach are typically used for prostate biopsy. When these types of conventional transducers are rotated by the motorized fixture, the set of acquired 2D images will be arranged as a fan (Fig. 1b), intersecting in the center of the 3D US image, resulting in an image as shown in Fig. 2. To obtain a 3D image of the prostate as in Fig. 2, an end-firing transducer is typically rotated by 180° [16].

Endo-cavity transducers using a side-firing 1D array are typically used in prostate brachytherapy, cryotherapy and focal therapy. When using these types of conventional transducers, the acquired images will also be arranged as a fan, but intersect at the axis of rotation of the transducer (see Fig. 1a). The side-firing transducer is typically rotated from 80° to 110° to obtain a 3D TRUS image of the prostate [16, 34, 35]. Figure 2 shows that endo-cavity scanning transducer used to image the prostate for 3D US-guided therapy [6, 9, 11, 25, 34, 36-39]

For scanning systems used for 3D US-guided prostate biopsy, the end-firing transducer is rotated by at least 180° about a fixed axis that perpendicularly bisects the transducer array. In this approach, the resolution of the 3D image will not be isotropic. Since the spatial sampling is highest near the rotation axis of the transducer and the poorest away from the axis of rotation of the transducer, thus the resolution of the 3D US image will degrade as the distance from the rotational axis of the transducer is increased. In addition, the axial and elevational resolution will decrease as the distance from the transducer is increased, as discussed above. The

combination of these effects will result in a 3D US image resolution that is best near the transducer and the rotational axis, while being poorest away from the transducer and rotational axis.

3D rotational scanning with an end-firing transducer is most sensitive to the motion of the transducer and patient since the axis of rotation is in the center of the 3D US image. Any motion during the 3D scan will cause a mismatch in the acquired 2D US images, resulting in artifacts in the center of the 3D US image. Artifacts in the center of the 3D US image will also occur if the axis of rotation is not accurately known; however, proper calibrations can remove this source of potential error. Thus, for interventional applications such as 3D US-guided prostate biopsy or brachytherapy, the rotational scanning mechanism is typically supported by a stabilization apparatus [16, 34, 40].

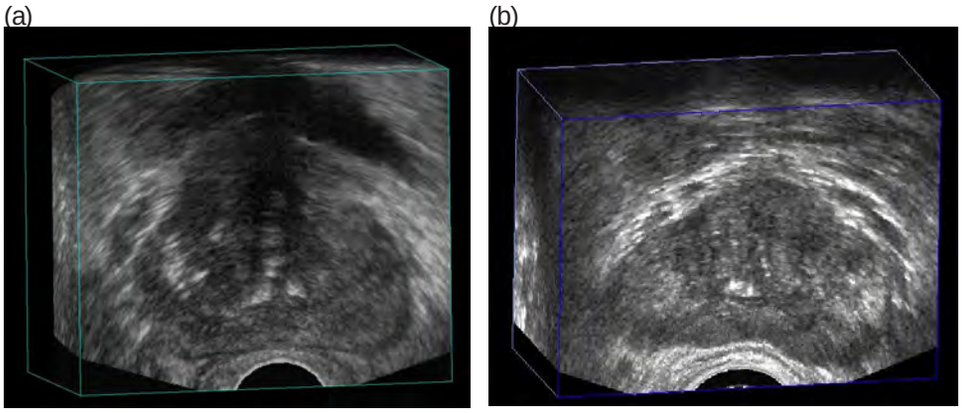

Figure 2. The 3D US of the prostate displayed using the multi-planar reformatting approach: (a) An end-firing TRUS prostate cube-view 3D image, allowing the sides to be translated and angles to reveal the desired anatomy. (b) A 3D TRUS image acquired using a side-firing transducer using the mechanical rotation approach.

2.2.4. Free-hand scanning with position sensing

Some 3D US-guided interventional procedures are making use of 3D scanning techniques that do not require a mechanical scanning device. In this approach, the user holds and manipulates a conventional US transducer to cover the patient's anatomy being investigated. Since construction of a 3D US image requires that the position and orientation of the conventional transducer be known, free-hand scanning requires a method to track the positions and orientations of the transducer as it is being moved. All methods to accomplish this task require a sensor to be mounted on the transducer to allow measurement of the conventional 2D transducer's position and orientation as it is moved over the body.

Over the past 2 decades, several approaches for free-hand scanning have been developed: tracked 3D US with articulated arms, free-hand 3D US with acoustic sensing, free-hand 3D US with magnetic field sensing, and image-based sensing (speckle decorrelation). The method used most commonly is the magnetic field sensing approach with several companies providing

the sensing technology: Ascension – Bird sensor [3] Polhemus – Fastrack sensor [41] and Northern Digital – Aurora sensor [4].

The most successful free-hand 3D US scanning approach used in interventional procedures makes use of magnetic field sensors, as well as applications such as echocardiography, obstetrics, and vascular imaging [3, 4, 41-51]. To track the transducer during generation of a 3D US image, a small receiver is mounted on the transducer containing three orthogonal coils allowing six-degrees-of-freedom sensing. The small receiver mounted on the transducer measures the strength of the magnetic field in three orthogonal directions, which is generated by a time-varying 3D magnetic field transmitter placed near the patient. The position and orientation of the transducer is calculated by continuously measuring the strength of the three components of the local magnetic field.

Since magnetic field sensors are small and unobtrusive devices, they allow the transducer to be tracked without the need for bulky mechanical devices, and without the need to keep a clear line of sight as required by optical tracking methods. Since magnetic field sensors are sensitive to electromagnetic interference or ferrous (or highly conductive) metals located nearby, geometric tracking errors can occur leading to distortions in the 3D US image. Thus, metal beds used in procedures, or surgical rooms can cause significant distortions. However, modern magnetic field sensors have been produced to be less susceptible to these sources of error, particularly ones that use a magnetic transmitter placed between the bed and the patient.

3. 3D Ultrasound-guided focal liver ablation

3.1. Clinical problem

Hepatocellular carcinoma (HCC) is the fifth most common diagnosed malignancy and the third most frequent cause of cancer related deaths worldwide [52]. Incidence is particularly high in Asia and sub-Saharan Africa due to the large incidence of hepatitis B and C, both of which are complicated by hepatic cirrhosis, which is the greatest risk factor for HCC. Recently, increasing trends in HCC have been reported from several Western countries [53]. Furthermore, the liver is the second most common site of metastatic cancer arising in other organs.

When feasible, surgical resection or liver transplant is the accepted standard therapeutic approach, and currently has the highest success rate of all treatment methods for primary and metastatic liver cancer. Unfortunately, only 15% of patients are candidates for surgery [54, 55]. Patients who do not qualify for surgery usually are offered other therapeutic solutions such as chemotherapy and radiotherapy, but unfortunately have variable limited success rates.

Minimally invasive percutaneous techniques, such as radio-frequency (RF) and microwave (MW) ablation of malignant tissue in the liver is a rapidly expanding research field and treatment tool for those patients who are not candidates for surgical resection or transplant. In some cases this acts as a bridge to liver transplantation [54, 56]. Due to low complications rates and shorter recovery times, the indications for these minimally invasive procedures are constantly increasing. However, these methods have a higher local recurrence rate than surgical resection, mostly due to insufficient or inaccurate local ablation of cancerous cells [56, 57].

Microwave energy-induced tissue heating by near-field probes is emerging as a common thermal treatment of liver tumors [58]. Application of MW for tumor ablation has multiple advantages over other techniques, including higher treatment temperatures and the ability to create larger uniformly shaped ablation zones in shorter time periods. However, the accurate placement of the probe is critical in achieving the predicted treatment goal [59]. The current standard of care uses CT images for planning and 2D US image guidance for intra-operative guidance of the ablation probe(s) into the target lesion. However, this approach suffers from several disadvantages, such as: (1) 2D US imaging requires physicians to mentally integrate many 2D images to form an impression of the anatomy and pathology, leading to more variability in guidance during interventional procedures; (2) 2D US does not permit the viewing of planes parallel to the skin, (3) liver deformation and motion artifact due to breathing reduces targeting accuracy, (4) 2D US-based for measurement of tumor volume needed for the treatment plan is variable and at times inaccurate, and (5) the detection and tracking of the needle delivering the thermal energy in the liver is crucial for accurate placement of the needle relative to the tumor, but can be difficult using 2D US. 3D US imaging of the liver and target may help to overcome these disadvantages resulting in improved accuracy of probe placement and improved ablation of the lesion.

The use of 3D US-guidance for focal liver tumor ablation is based on the fact that the use of 3D US will show the features of liver masses and the hepatic vasculature more clearly, allow guidance of the ablation probes to the target more accurately, and allow more accurate monitoring of the ablation zone during the procedure and at follow up.

3.2. 3D US Scanner for focal liver tumor ablation

We have developed 3D US guidance systems for improving cancer diagnosis and treatment by introducing hardware and software innovations [21, 60-64]. Our previous efforts have been extended to the development of a 3D US-guidance system for treating HCC. Specialized hardware and software tools are used that allow 3D acquisition of 3D US images, real-time registration of the pre-operative CT to intra-operative 3D US images, and tracking of the ablation probes during insertion into the target. This is accomplished by registering previously acquired contrast CT images that show the location of the target lesion to near real-time 3D US images, plus providing visualization and guidance tools to guide the procedure.

The 3D US scanning system consists of: a hand-held electro-mechanical motor/encoder assembly to move a conventional 2D US imaging transducer in a fan shaped, linear or hybrid motion to a maximum angular limit of 60 degrees and/or 30 mm linear extent to acquire a series of 2D US images; and, a PC equipped with a digital frame grabber and software components to control the motor assembly, acquire 2D images, reconstruct them in 3D, and visualize them in 3D.

3.2.1. Mechanical design

The handheld 3D scanning device is motorized and constructed with two mechanical systems for generating a linear and tilt scanning motions of the transducer is shown schematically and photographically in Figs. 3 and 4. The linear scanning system is operated with a geared DC motor and lead screw providing linear translation. The tilt motion is generated via a paralle-

http://dx.doi.org/10.5772/55230

logram linkage, which is mounted on the carriage of the linear slide. A second geared DC motor is used to generate the tilt motion, allowing for independent control of the two systems.

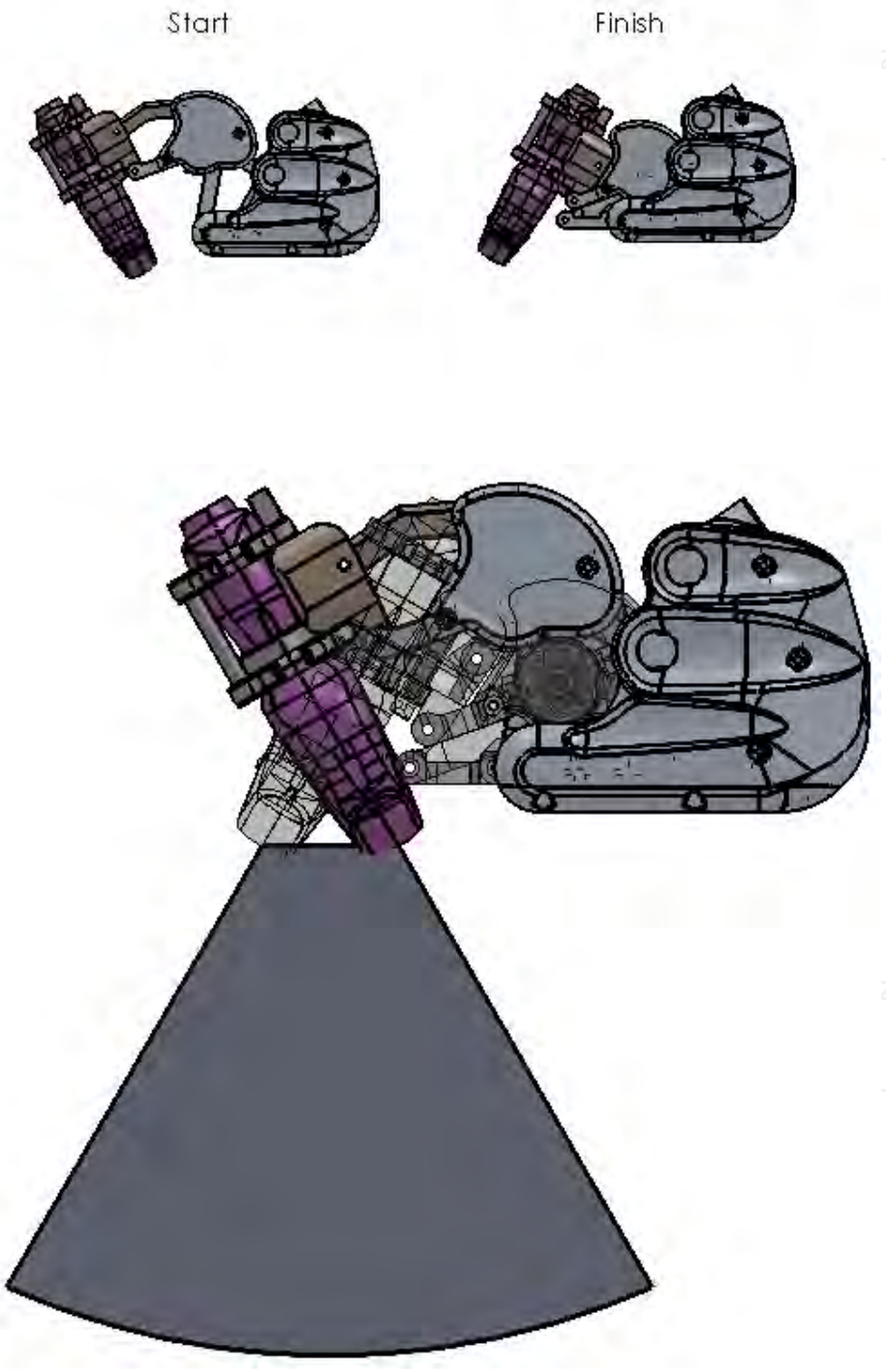

Figure 3. Schematic diagram of the hybrid 3D US scanner for used in the focal liver ablation procedure. The diagram shows the start and end positions of the hybrid (linear and tilt) scan.

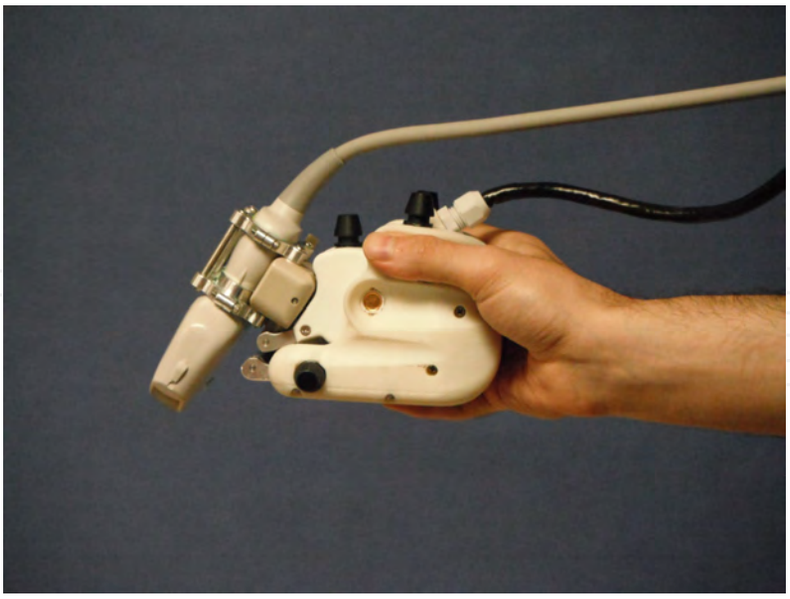

Figure 4. Photograph of hybrid scanner with abdominal ultrasound transducer mounted and ready for scanning.

The 3D scanning device has three modes of operation: a linear translation, in which the transducer (oriented perpendicular to the surface or at an angle for Doppler imaging) is translated along a straight line parallel to the patient's surface. This motion generates a rectangular volume shown in Fig. 5a. The second mode generates a tilt motion (or wobbling), in which the transducer is rotated about its face resting on the patient's skin surface (Fig. 5b). The third mode is a combination of the first two modes that creates a combined (or hybrid) motion. The transducer is rotated as it is moved along a surface covering a larger volume than either of the first two modes (Fig. 5c). For example, if transducer with linear array is used at 15cm depth setting on the ultrasound machine (typical depth for abdominal imaging), hybrid scanning gives a volume that is three times larger than the linear mode and 47% larger than the tilt mode only.

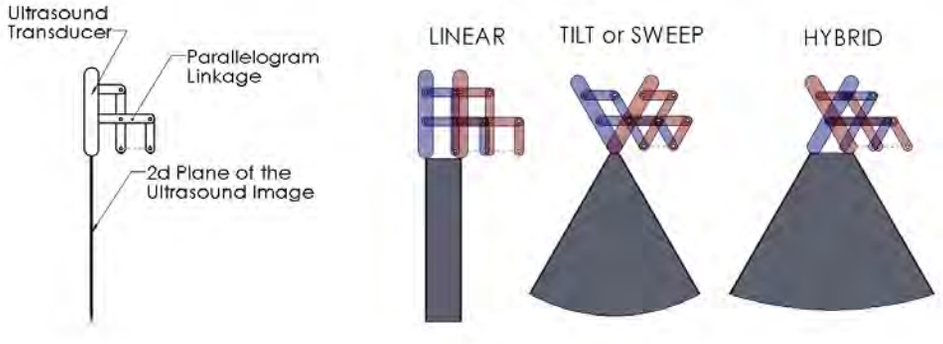

Figure 5. Schematic diagrams showing the three modes of operation of the mechanical compound 3D US scanning device. On the left is the schematic of the linkage and the right are the linear, tilt and hybrid motions.

The 3D scanning system parameters can be set by the user: *Scanning mode:* Three different modes of linear, tilt and combined (or hybrid, a combination of both linear and tilt imaging modes to maximize the field-of-view) are available depending on the anatomy of body parts being scanned and the image requirements. *Scan Extent:* Maximum extent of linear translation (typically 2.5 cm) or tilt angle (typically 60 deg) can be set individually to the extremes values. *Scan Spacing:* Elevational linear and angular spacing can be set to optimize the trade-off between the scanning time and the scan spacing. *Frame-Rate:* The rate at which images are digitized by the frame grabber is set (typically 15 frames/s). *Scanning Depth:* Maximum scanning depth can be set prior to each scan for accurate reconstruction of the volumes.

3.2.2. Validation methods

Since the hybrid scanning mode involves coordination between two acquisition methods, it was tested in terms of accuracy of 3D image generation. We used two custom made phantoms with known geometry. The validation experiments where performed using the handheld 3D US scanning device in hybrid scanning mode using a two-dimensional conventional curved array ultrasound transducer used for abdominal applications (Toshiba, PVT-375BT).

Geometrical Error in 3D reconstruction: This test was designed to measure the accuracy of the 3D reconstruction of the 3D hybrid scanner in three directions. The test phantom was made of a grid of known dimensions made with 0.1 mm thick nylon monofilament threads wrapped around an accurately machined frame to form a 4-layer grid. Each layer was slightly shifted from the layer above to avoid acoustic shadowing. The distance between any two layers was 1cm. The phantom was submerged in a 15% glycerol solution [61] and imaged at different depth settings. The acquired 3D US images were then viewed and analyzed by measuring the distances between the images of the monofilaments and comparing them to the expected values.

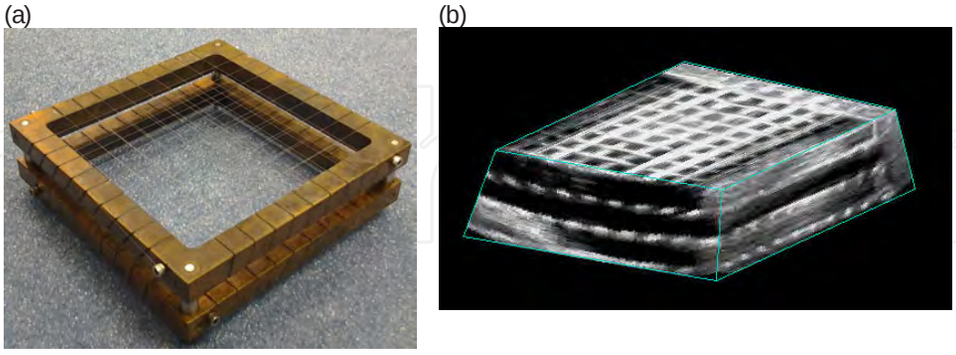

Figure 6. (a) Photograph of the 3D monofilament thread grid, which was used to validate the 3D reconstruction of the ultrasound image. (b) The 3D ultrasound image of the phantom, showing the grid of threads.

Error in 3D volume measurements: In the second test, we assessed the accuracy in measuring volumes using our system. For this experiment, several spherical phantoms with different sizes were made of tissue mimicking agar [65]. The volume of each of these spherical phantoms was measured prior to embedding them in a cube of tissue mimicking agar phantom. The spherical

phantoms were then imaged with our hybrid scanner, viewed in the 3D visualization software, and manually segmented. The volume of spherical structures were calculated and compared with the expected values.

3.2.3. Validation results

Testing the 3D hybrid scanner with the 3D thread phantom showed that mean error in the measured values of the distances in the X, Y and Z directions were 3.6%, 2.5% and 5.7% respectively. A one-sample t-test was performed to compare the measured distance values with the known distance value of 1cm, showed there was no statistical significant difference between the measured values and expected values between the threads.

Validation of volume measurements using the hybrid scanner were carried out by imaging a tissue mimicking agar sphere with a volume of 10 cm^3 embedded in a block of tissue mimicking agar phantom. The measurements were performed at two different depth settings on the ultrasound machine (10 and 15 cm). The mean errors of the volume measurement were 5.7% and 4.4% for the 10cm and 15cm depth settings respectively, demonstrating that the hybrid scanner can be used to make sufficiently accurate volumetric measurements.

In-vivo experiments: After obtaining institutional research board (IRB) approvals, we investigated the use of the scanner in thermal ablation treatment of primary hepatic tumors. Figure 7 shows a 3D US image acquired during the microwave ablation procedure of a primary (hepatocellular) tumor. It shows application of the hybrid mode in acquiring volumes large enough to include both the ablated tumor region as well as all ablation needles in two different views.

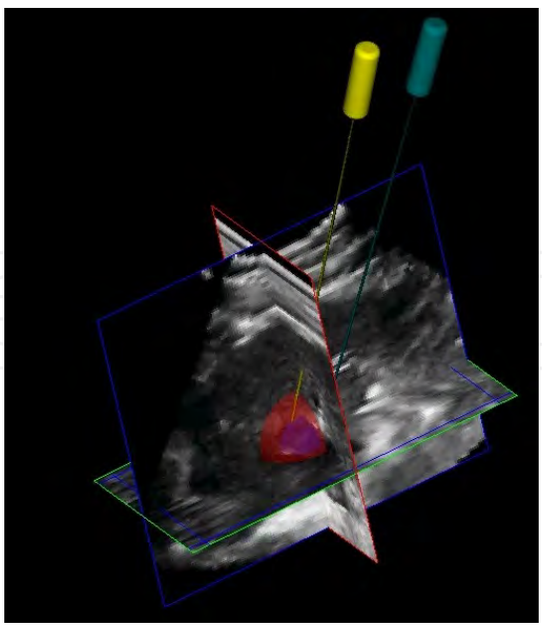

Figure 7. 3D ultrasound image of a primary (hepatocellular) tumor with two microwave applicators in place. The applicators and tumor have been segmented and displayed in 3D allowing the interventional radiologist to examine the placement accuracy of the applicators in the tumor. In addition, the ablation zone has also been superimposed.

4. 3D ultrasound guided prostate biopsy

4.1. The clinical problem

Prostate Cancer (PCa) is the most commonly diagnosed malignancy in men, and is found at autopsy in 30% of men at age 50, 40% at age 60, and almost 90% at age 90 [66, 67]. Worldwide, it is the second leading cause of death due to cancer in men, accounting for between 2.1% and 15.2% of all cancer deaths [68, 69]. Symptoms PCa are generally absent until extensive local growth or metastases develop. When diagnosed at an early stage, the disease is curable [70, 71], and even at later stages treatment can be effective [72]; however, once the tumor has extended beyond the prostate, the risk of metastases and locally aggressive cancer increases. Clearly, early diagnosis, accurate staging of prostate cancer, and appropriate therapies are critical to the patient's well-being.

In managing patients with possible PCa, the challenges facing physicians are to: (a) diagnose clinically relevant cancers at a curable stage; (b) stage the disease accurately; (c) apply appropriate therapy accurately to optimize destruction of cancer cells while preserving normal tissues and function; and (d) follow patients to assess side effects and therapy effectiveness. This section focuses on improving early PCa diagnosis and staging with the use of 3D ultrasound-guided prostate biopsy.

Since not all cancers are palpable by digital rectal exam (DRE), PCa diagnosis is established by histological examination of prostate tissue obtained most commonly by trans-rectal ultrasound (TRUS)-guided biopsy. Prostate needle biopsy is the only definitive diagnostic modality capable of confirming malignancy, and is now always performed with TRUS guidance.

Since many small tumors are not detected by TRUS or DRE, biopsy samples are obtained from predetermined regions of the prostate known to have a high probability of harboring cancer. These are typically in the peripheral zone (PZ), which harbors 80% of all PCs and a higher proportion of clinically significant ones, and close to the capsule, as most cancers are thought to start within 5*mm* of the prostate capsule. Most centers are now taking 8-12 cores or more as part of their routine assessment [73-76].

TRUS biopsies are now performed with a thin, 18-gauge needle mounted on a spring-loaded gun connected to the TRUS probe, forcing the needle to stay in the imaging plane. Each core is separately identified as to the prostate region from which it was drawn, so that the pathologist can report the extent and grade of the cancer within each region.

Since prostate volume sampled by the biopsy is small, and PCa is often multi-focal, involving only a small volume of the prostate in the early stages of the disease [77, 78], the probability for obtaining a sample of the tumour on biopsy is small. Thus, a negative biopsy may be, in fact, false, and the patient may be harbouring cancer at an early and curable stage. Various reports have shown that the false negative rate ranges from 10% to 25% [73, 74]. Since cancer is still present in 1/10 to 1/4 of patients with a negative first biopsy, the current biopsy procedure is still suboptimal [74, 79]. Clearly, an improved procedure with improved planning and recording of biopsy locations is necessary to resolve these issues.

Due to the increasing number of younger men with early and potentially curable PCa undergoing repeated prostate biopsy, it is therefore vital not to re-biopsy the same area if the original biopsy was negative, and it is particularly vital to re-biopsy the same area if a possible abnormal area was detected on first biopsy as ASAP [80]. Thus, the locations of the cores obtained from the prostate must be known accurately to help guide the physician during the repeat biopsy [81, 82], to help in correlating any imaging evidence of the disease, and to provide improved planning for subsequent therapy.

4.2. Multi-modality directed prostate biopsy

A variety of imaging techniques and molecular imaging probes are being investigated to improve early detection of PCa. Different magnetic resonance imaging (MRI) techniques have been evaluated using body and endo-rectal coils, contrast enhancement, and different pulse sequences [83-85] resulting in disease detection sensitivity and specificity of 80-88% and 75-95%, respectively [84, 86, 87]. Positron emission tomography (PET) (combined with CT or MRI) is used to detect early disease, with the newer PET imaging probes proving to be the more promising [88-90]. Although progress has been made with improved PET and MRI techniques, they do not yet have ideal specificity or sufficient accuracy to assess the grade of the cancer; thus a biopsy of suspicious lesions on MRI or PET is required to provide a definitive diagnosis and grade of the disease. Systems have been developed to perform biopsies in the MRI suite; however, the cost of the equipment and prolonged use of the MRI is extremely expensive and likely prohibitive given the large number of patients requiring biopsy. Unfortunately, conventional 2D TRUS guidance of the biopsy procedure limits the physician's ability to target locations identified as suspicious on other modalities.

As we currently do not have a highly sensitive and specific imaging test for local staging of PCa, there is a growing belief that the optimal method to guide prostate biopsy will involve not just one, but a combination of imaging modalities. 3D TRUS imaging combined with functional or molecular imaging from another imaging modality such as radiopharmaceutical imaging (PET, SPECT), or magnetic resonance imaging (MRS, MRI) may provide the best approach for guiding prostate biopsy.

4.3. 3D TRUS-guided prostate biopsy system

Since ultrasound imaging is the clinical standard for image-guided biopsy of the prostate, we have developed a 3D TRUS-based navigation system that provides a reproducible record of the 3D locations of the biopsy targets throughout the procedure and allows fusion with MR images with identified lesions for targeting.

The system we have developed is a mechanical 3D biopsy system that maintains the procedural workflow, minimizing costs and physician retraining. This mechanical system has 4 degrees-of-freedom (DOF) and has an adaptable cradle that supports commercially available end-firing TRUS transducers used for prostate biopsy [16]. It also allows real time tracking and recording of the 3D position and orientation of the biopsy needle as the physician manipulates the TRUS transducer. The following describes the components of the system, including hardware,

http://dx.doi.org/10.5772/55230

modeling and segmentation algorithms, and system validation using a multi-modal US/CT prostate phantom.

Our approach involves the use of a device composed of two mechanisms shown as a schematic in Figure 8. The system is composed of an articulated multi-jointed stabilizer and a transducer tracking mechanism.

Figure 8. A schematic diagram of the mechanical tracker, which supports the TRUS transducer and attached cradle. This configuration constrains the TRUS probe motion to three degrees-of-freedom and one degree of translation along the axis of the probe. The system is mounted at the base of a stabilizer while the linkage allows the TRUS transducer to be manually manipulated about a remote center of motion (RCM), which is at the center of the ultrasound transducer tip.

The end-firing TRUS transducer with the biopsy needle guide in place is mounted to the mechanical tracking mechanism in a manner where the US probe is free to rotate around its longitudinal axis (Fig. 8). The tracking assembly is attached to a stabilizer, which is mounted on a free-standing cart. Thus, the physician can manipulate the tracking mechanism freely, insert the transducer through the anus, and rotate the transducer in order to acquire a 3D image of the prostate. The tracking linkage contains angle-sensing encoders mounted to each joint in order to transmit to the computer the angles between the arms. This arrangement allows the computer to determine the relative position of the transducer as it is being manipulated. Since the biopsy gun is mounted onto the transducer and its position relative to the transducer is calibrated, the needle location can be calculated.

The mechanical tracking device is a spherical linkage assembly, in which the axis of the joints converge to a common point on the remote center of motion (RCM). The RCM design minimizes targeting errors within the prostate. As the TRUS transducer is constrained through a stationary point, the physician's movements are replicated at a scaled down rate (minified through the RCM), minimizing changes in morphology and dislocation of the prostate. In addition, the RCM enables a precision equivalent to that of robotic assisted machines. Thus,

the system improves the physician's ability to accurately biopsy a point of interest within the patient's prostate.

4.4. Prostate biopsy procedure

To perform a 3D US-guided prostate biopsy, the end-firing US transducer is mounted onto the tracking assembly such that the tip of the probe is initially set to the RCM point of the tracker linkage. The physician inserts the TRUS transducer into the patient's rectum and aligns the prostate to the center of the 2D TRUS image. A 3D image of the prostate is then acquired by rotating the transducer 180 degrees about its longitudinal axis (Fig. 1b) [91]. A graphical model of the prostate is then generated by a semi-automatic 3D segmentation algorithm [61, 92-94]. After the prostate model has been constructed, the physician can then manipulate the 3D image on the computer screen and select locations to biopsy. After all of the biopsy targets have been selected, the system then displays the 3D needle guidance interface (Fig. 9), which facilitates the systematic targeting of each biopsy location previously selected. Other images or information (*e.g.*, MRI or PET/CT images), if available, are registered to the 3D TRUS image and displayed as an overlay on the computer screen (Fig. 10).

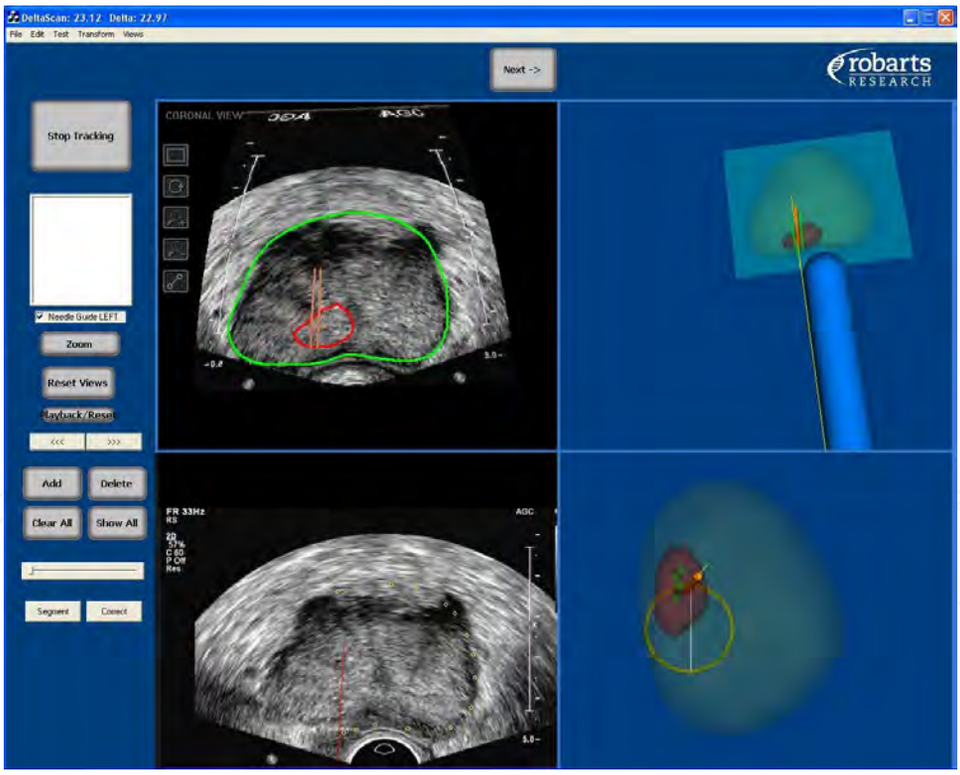

Figure 9. The 3D US-guided prostate biopsy system interface is composed of 4 windows: (top left) the 3D TRUS image dynamically sliced to match the real-time TRUS probe 3D orientation, (bottom left) the live 2D TRUS video stream, (right side) and the 3D location of the biopsy core is displayed within the 3D prostate models. The targeting ring in the bottom right window shows all the possible needle paths that intersect the preplanned target by rotating the TRUS about its long axis. This allows the physician to move the TRUS probe to the target (highlighted by the red dot) in the shortest possible distance. The segmented tumor to be targeted is outlined and rendered in red.

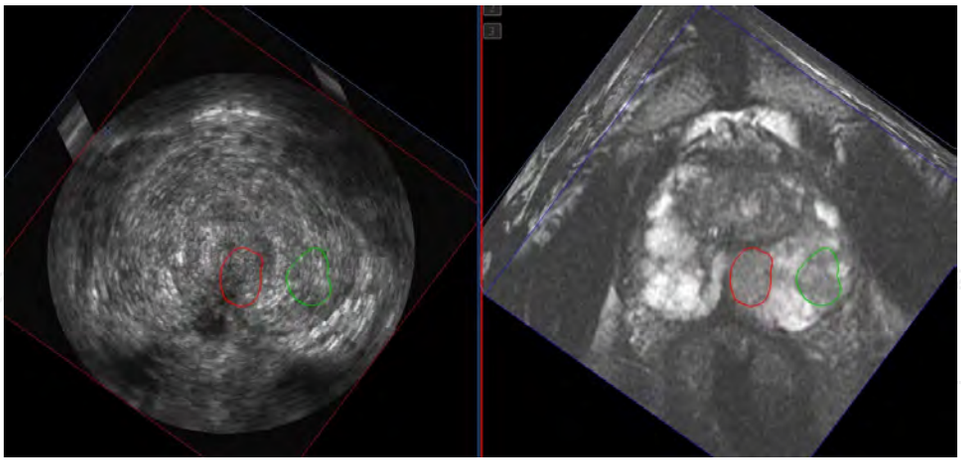

Figure 10. Registered 3D TRUS and MRI images of the same patient showing delineated suspicious lesions identified in the MR images (right panel). The MR images were then registered with the 3D TRUS images (left panel) and the delineated two regions (red and green) superimposed on the 3D TRUS images. These regions were then targeted with the 3D TRUS-guided biopsy system shown in Figs. 8 and 9.

As the physician manually manipulates the TRUS transducer, the 3D location and orientation of the transducer and needle trajectory are tracked in real-time throughout the procedure on the computer screen. Figure 9 illustrates the biopsy interface, which is composed of 4 windows: the live 2D TRUS video stream, the 3D TRUS image, and two 3D model views. The 2D TRUS window displays the real-time 2D TRUS image from the US machine. The 3D TRUS window contains a 2D slice of the 3D static model in real-time to reflect the expected orientation and position of the TRUS probe. This correspondence allows the physician to compare the 3D image with the real-time 2D image to determine if the prostate has moved or deformed to a prohibitive extent. After each biopsy, the biopsy location is recorded in 3D from the tracker orientation, and the system is ready for the next biopsy. After the needle is withdrawn, a 3D image may be obtained to determine if there is any movement or swelling of the prostate.

4.5. Clinical evaluation of 3D TRUS/MRI-guided biopsy

Clinical studies are being performed at a number of centers to evaluate the clinical impact of fusion of MRI to intra-biopsy 3D TRUS for 3D US-guided targeted biopsy of suspicious MRI lesions on prostate cancer detection and grading. At the London Health Sciences Centre in London, Canada, prostate MR imaging was performed on 31 patients with clinical suspicion for prostate cancer in advance of their 3D TRUS-guided biopsy. T2, diffusion-weighted and dynamic-contrast enhanced MR sequences were collected in a 3T MRI system with an endo-rectal RF coil. All suspicious lesions in the MR images were then identified and delineated on the images, which were then registered to the 3D TRUS image obtained during the biopsy procedure (see Figure 10). Using the 3D TRUS-guided biopsy system, prostate biopsy cores were targeted toward each suspicious delineated MRI lesion, which were displayed on the 3D TRUS image. A standard 12-core set of random biopsies was also performed on each patient and used as an internal control.

The results of this study showed that MRI-3D TRUS fusion was successfully performed and the targeted biopsy needle cores had a significantly higher rates of prostate malignancy (30.0%) compared to random, sextant cores (10.0%). In total, prostate cancer was biopsy confirmed in 11 patients; however, only 7 of these patients had abnormal MRI findings (even in retrospective analysis) and were sampled with targeted MRI-3D TRUS fusion. Random sampling detected the remaining four patients. A significantly higher percentage of the targeted biopsy cores (47+/-26%) contained cancer compared to the randomly sampled cores (28+/-26%), and for 3 patients, the MRI-targeted cores detected a higher Gleason cancer grade than the random cores, modifying potential treatment modalities. This study showed that MRI-3D TRUS fusion allows for superior sampling of prostate cancer visible on MRI. This technology may benefit both cancer detection and accurate malignancy grading for appropriate therapeutic management; however, further testing is needed to establish the full utility of this technology.

5. Conclusions

Clinical evaluation of the mechanical tracking systems for use in 3D ultrasound guidance for focal liver ablation and prostate biopsy have been found to be easy to use. The tracker permits manual motions identical to the current conventional procedure, where restricted movements are produced by the US probe in the patient's rectum.

Reconstruction of 3D TRUS images using the hybrid approach for focal liver ablation, and rotational approach for prostate biopsy can produce accurate 3D images without significant visible discontinuity or artefacts. Volume calculations from the 3D TRUS image have shown that the 3D US systems can generate accurate volume measurements.

The patient studies have demonstrated that it is possible to minimize the effects of liver and prostate motion through a variety of mechanical and software mechanisms. However, improved solutions, which correct any patient motion automatically are still needed. It is not possible to control all patient/organ motion during the procedures, particularly if the patient moves during the prostate biopsy procedure after the firing of the prostate biopsy needle. To overcome this problem, a software module would have to be developed to inform the physician that the prostate has moved and then correct for the motion and deformation. This task must be done quickly, possibly in real-time, using an implementation of the software in a graphical processing unit (GPU).

Acknowledgements

The authors gratefully acknowledge the financial support of the Canadian Institutes of Health Research, the Ontario Institute for Cancer Research, the Ontario Research Fund, the National Science and Engineering Research Council, and the Canada Research Chair program.

Author details

© 2013 Aaron Fenster[1,2,3], Jeff Bax[1,2,] Hamid Neshat[1,2], Nirmal Kakani[3] and Cesare Romagnoli[3.]

1 Robarts Research Institute, University of Western Ontario, London, Canada
2 Biomedical Engineering Department, University of Western Ontario, London, Canada
3 Department of Medical Imaging, University of Western Ontario, London, Canada

References

[1] Elliott ST. Volume ultrasound: the next big thing? Br J Radiol. 2008;81(961):8-9.

[2] Downey DB, Fenster A, Williams JC. Clinical utility of three-dimensional US. Radiographics. 2000;20(2):559-71.

[3] Boctor EM, Choti MA, Burdette EC, Webster Iii RJ. Three-dimensional ultrasound-guided robotic needle placement: an experimental evaluation. Int J Med Robot. 2008;4(2):180-91.

[4] Hummel J, Figl M, Bax M, Bergmann H, Birkfellner W. 2D/3D registration of endoscopic ultrasound to CT volume data. Phys Med Biol. 2008;53(16):4303-16.

[5] Carson PL, Fenster A. Anniversary paper: evolution of ultrasound physics and the role of medical physicists and the AAPM and its journal in that evolution. Med Phys. 2009;36(2):411-28.

[6] Wei Z, Wan G, Gardi L, Mills G, Downey D, Fenster A. Robot-assisted 3D-TRUS guided prostate brachytherapy: system integration and validation. Med Phys. 2004;31(3):539-48.

[7] Smith WL, Surry K, Mills G, Downey D, Fenster A. Three-dimensional ultrasound-guided core needle breast biopsy. Ultrasound in Med and Bio. 2001;27(8):1025-34.

[8] Chin JL, Downey DB, Onik G, Fenster A. Three-dimensional prostate ultrasound and its application to cryosurgery. Tech Urol. 1996;2(4):187-93.

[9] Chin JL, Downey DB, Mulligan M, Fenster A. Three-dimensional transrectal ultrasound guided cryoablation for localized prostate cancer in nonsurgical candidates: a feasibility study and report of early results. J Urol. 1998;159(3):910-4.

[10] Smith WL, Fenster A. Optimum Scan Spacing for Three-Dimensional Ultrasound by Speckle Statistics. Ultrasound in Medicine and Biology. 2000;26(4):551-62.

[11] Fenster A, Tong S, Sherebrin S, Downey DB, Rankin RN. Three-dimensional ultrasound imaging. SPIE Physics of Medical Imaging. 1995;2432:176-84.

[12] Delabays A, Pandian NG, Cao QL, Sugeng L, Marx G, Ludomirski A, et al. Transthoracic real-time three-dimensional echocardiography using a fan-like scanning approach for data acquisition: methods, strengths, problems, and initial clinical experience. Echocardiography. 1995;12(1):49-59.

[13] Downey DB, Nicolle DA, Fenster A. Three-dimensional orbital ultrasonography. Can J Ophthalmol. 1995;30(7):395-8.

[14] Downey DB, Nicolle DA, Fenster A. Three-dimensional ultrasound of the eye. Administrative Radiology Journal. 1995;14:46-50.

[15] Gilja OH, Thune N, Matre K, Hausken T, Odegaard S, Berstad A. In vitro evaluation of three-dimensional ultrasonography in volume estimation of abdominal organs. Ultrasound Med Biol. 1994;20(2):157-65.

[16] Bax J, Cool D, Gardi L, Knight K, Smith D, Montreuil J, et al. Mechanically assisted 3D ultrasound guided prostate biopsy system. Med Phys. 2008;35(12):5397-410.

[17] Goncalves L, Nien J, Espinoza J, Kusanovic J, Lee W, Swope B, et al. Two-Dimensional (2D) versus three- and four-dimensional (3D/4D) us in obstetrical practice: Does the new technology add anything? American Journal of Obstetrics and Gynecology. 2005;193(6):S150-S.

[18] Peralta CF, Cavoretto P, Csapo B, Falcon O, Nicolaides KH. Lung and heart volumes by three-dimensional ultrasound in normal fetuses at 12-32 weeks' gestation. Ultrasound Obstet Gynecol. 2006;27(2):128-33.

[19] Kurjak A, Miskovic B, Andonotopo W, Stanojevic M, Azumendi G, Vrcic H. How useful is 3D and 4D ultrasound in perinatal medicine? J Perinat Med. 2007;35(1): 10-27.

[20] Blake CC, Elliot TL, Slomka PJ, Downey DB, Fenster A. Variability and accuracy of measurements of prostate brachytherapy seed position in vitro using three-dimensional ultrasound: an intra- and inter-observer study. Med Phys. 2000;27(12):2788-95.

[21] Fenster A, Downey DB, Cardinal HN. Three-dimensional ultrasound imaging. Phys Med Biol. 2001;46(5):R67-99.

[22] Downey DB, Fenster A. Vascular imaging with a three-dimensional power Doppler system. AJR Am J Roentgenol. 1995;165(3):665-8.

[23] Picot PA, Rickey DW, Mitchell R, Rankin RN, Fenster A. Three-dimensional colour Doppler imaging. Ultrasound Med Biol. 1993;19(2):95-104.

[24] Pretorius DH, Nelson TR, Jaffe JS. 3-dimensional sonographic analysis based on color flow Doppler and gray scale image data: a preliminary report. J Ultrasound Med. 1992;11(5):225-32.

[25] Downey DB, Fenster A. Three-dimensional power Doppler detection of prostate cancer [letter]. 1995;165(3):741.

[26] Landry A, Fenster A. Theoretical and experimental quantification of carotid plaque volume measurements made by 3D ultrasound using test phantoms. Medical Physics. 2002.

[27] Landry A, Ainsworth C, Blake C, Spence JD, Fenster A. Manual planimetric measurement of carotid plaque volume using three-dimensional ultrasound imaging. Medical Physics. 2007;34(4):1496-505.

[28] Landry A, Spence JD, Fenster A. Quantification of carotid plaque volume measurements using 3D ultrasound imaging. Ultrasound Med Biol. 2005;31(6):751-62.

[29] Ainsworth CD, Blake CC, Tamayo A, Beletsky V, Fenster A, Spence JD. 3D Ultrasound Measurement of Change in Carotid Plaque Volume; A Tool for Rapid Evaluation of New Therapies. Stroke. 2005;35:1904-9.

[30] Krasinski A, Chiu B, Spence JD, Fenster A, Parraga G. Three-dimensional Ultrasound Quantification of Intensive Statin Treatment of Carotid Atherosclerosis. Ultrasound in Medicine & Biology. 2009;35(11):1763-72.

[31] Bamber JC, Eckersley RJ, Hubregtse P, Bush NL, Bell DS, Crawford DC. Data processing for 3-D ultrasound visualization of tumour anatomy and blood flow. SPIE. 1992;1808:651-63.

[32] Carson PL, Li X, Pallister J, Moskalik A, Rubin JM, Fowlkes JB. Approximate quantification of detected fractional blood volume and perfusion from 3-D color flow and Doppler power signal imaging. 1993 ultrasonics symposium proceedings. Piscataway, NJ: IEEE; 1993. p. 1023-6.

[33] King DL, King DLJ, Shao MY. Evaluation of in vitro measurement accuracy of a three-dimensional ultrasound scanner. J Ultrasound Med. 1991;10(2):77-82.

[34] Tong S, Downey DB, Cardinal HN, Fenster A. A three-dimensional ultrasound prostate imaging system. Ultrasound Med Biol. 1996;22(6):735-46.

[35] Tong S, Cardinal HN, McLoughlin RF, Downey DB, Fenster A. Intra- and inter-observer variability and reliability of prostate volume measurement via two-dimensional and three-dimensional ultrasound imaging. Ultrasound Med Biol. 1998;24(5): 673-81.

[36] Downey DB, Chin JL, Fenster A. Three-dimensional US-guided cryosurgery. Radiology. 1995;197(P):539.

[37] Chin JL, Downey DB, Elliot TL, Tong S, McLean CA, Fortier M, et al. Three dimensional transrectal ultrasound imaging of the prostate: clinical validation. Can J Urol. 1999;6(2):720-6.

[38] Onik GM, Downey DB, Fenster A. Three-dimensional sonographically monitored cryosurgery in a prostate phantom. J Ultrasound Med. 1996;15(3):267-70.

[39] Wei Z, Gardi L, Downey DB, Fenster A. Oblique needle segmentation and tracking for 3D TRUS guided prostate brachytherapy. Med Phys. 2005;32(9):2928-41.

[40] Cool D, Sherebrin S, Izawa J, Chin J, Fenster A. Design and evaluation of a 3D transrectal ultrasound prostate biopsy system. Med Phys. 2008;35(10):4695-707.

[41] Treece G, Prager R, Gee A, Berman L. 3D ultrasound measurement of large organ volume. Med Image Anal. 2001;5(1):41-54.

[42] Detmer PR, Bashein G, Hodges T, Beach KW, Filer EP, Burns DH, et al. 3D ultrasonic image feature localization based on magnetic scanhead tracking: in vitro calibration and validation. Ultrasound Med Biol. 1994;20(9):923-36.

[43] Hodges TC, Detmer PR, Burns DH, Beach KW, Strandness DEJ. Ultrasonic three-dimensional reconstruction: in vitro and in vivo volume and area measurement. Ultrasound Med Biol. 1994;20(8):719-29.

[44] Hughes SW, D'Arcy TJ, Maxwell DJ, Chiu W, Milner A, Saunders JE, et al. Volume estimation from multiplanar 2D ultrasound images using a remote electromagnetic position and orientation sensor. Ultrasound Med Biol. 1996;22(5):561-72.

[45] Leotta DF, Detmer PR, Martin RW. Performance of a miniature magnetic position sensor for three-dimensional ultrasound imaging. Ultrasound Med Biol. 1997;23(4): 597-609.

[46] Gilja OH, Detmer PR, Jong JM, Leotta DF, Li XN, Beach KW, et al. Intragastric distribution and gastric emptying assessed by three-dimensional ultrasonography. Gastroenterology. 1997;113(1):38-49.

[47] Nelson TR, Pretorius DH. Visualization of the fetal thoracic skeleton with three-dimensional sonography: a preliminary report. AJR Am J Roentgenol. 1995;164(6): 1485-8.

[48] Pretorius DH, Nelson TR. Prenatal visualization of cranial sutures and fontanelles with three-dimensional ultrasonography. J Ultrasound Med. 1994;13(11):871-6.

[49] Raab FH, Blood EB, Steiner TO, Jones HR. Magnetic position and orientation tracking system. IEEE Transactions on Aerospace and Electronic systems. 1979;AES-15:709-17.

[50] Riccabona M, Nelson TR, Pretorius DH, Davidson TE. Distance and volume measurement using three-dimensional ultrasonography. J Ultrasound Med. 1995;14(12): 881-6.

[51] Hsu PW, Prager RW, Gee AH, Treece GM. Real-time freehand 3D ultrasound calibration. Ultrasound Med Biol. 2008;34(2):239-51.

[52] Jemal A, Bray F, Center MM, Ferlay J, Ward E, Forman D. Global cancer statistics. CA Cancer J Clin. 2011;61(2):69-90.

[53] Jemal A, Siegel R, Xu J, Ward E. Cancer statistics, 2010. CA Cancer J Clin. 2010;60(5): 277-300.

[54] Solbiati L, Ierace T, Tonolini M, Cova L. Ablation of Liver Metastases: Springer, Berlin; 2004. 311 - 21 p.

[55] El-Serag HB, Marrero JA, Rudolph L, Reddy KR. Diagnosis and treatment of hepatocellular carcinoma. Gastroenterology. 2008;134(6):1752-63.

[56] Adam A, Mueller P. Interventional Radiological Treatment of Liver Tumors. Cambridge, UK: Cambridge University Press; 2009.

[57] McKay A, Fradette K, Lipschitz J. Long-term outcomes following hepatic resection and radiofrequency ablation of colorectal liver metastases. HPB Surg. 2009;2009:346863.

[58] Seki T. "Microwave Coagulation Therapy for Liver Tumors", Tumour Ablation, Principle and Practice: Springer; 2004. 218 - 27 p.

[59] Haemmerich D, Laeseke PF. Thermal tumour ablation: devices, clinical applications and future directions. Int J Hyperthermia. 2005;21(8):755-60.

[60] Cool DW, Gardi L, Romagnoli C, Saikaly M, Izawa JI, Fenster A. Temporal-based needle segmentation algorithm for transrectal ultrasound prostate biopsy procedures. Med Phys. 2010;37(4):1660-73.

[61] Wang Y, Cardinal HN, Downey DB, Fenster A. Semiautomatic three-dimensional segmentation of the prostate using two-dimensional ultrasound images. Med Phys. 2003;30(5):887-97.

[62] Ding M, Cardinal HN, Fenster A. Automatic needle segmentation in three-dimensional ultrasound images using two orthogonal two-dimensional image projections. Med Phys. 2003;30(2):222-34.

[63] Ding M, Fenster A. A real-time biopsy needle segmentation technique using Hough transform. Med Phys. 2003;30(8):2222-33.

[64] Karnik VV, Fenster A, Bax J, Gardi L, Gyacskov I, Montreuil J, et al. Evaluation of inter-session 3D-TRUS to 3D-TRUS image registration for repeat prostate biopsies. Med Image Comput Comput Assist Interv. 2010;13(Pt 2):17-25.

[65] Rickey DW, Picot PA, Christopher DA, Fenster A. A wall-less vessel phantom for Doppler ultrasound studies. Ultrasound Med Biol. 1995;21(9):1163-76.

[66] McNeal JE, Bostwick DG, Kindrachuk RA, Redwine EA, Freiha FS, Stamey TA. Patterns of progression in prostate cancer. Lancet. 1986;1(8472):60-3.

[67] Garfinkel L, Mushinski M. Cancer incidence, mortality and survival: trends in four leading sites. Stat Bull Metrop Insur Co. 1994;75(3):19-27.

[68] Silverberg E, Boring CC, Squires TS. Cancer statistics, 1990 [see comments]. CACancer J Clin. 1990;40:9-26.

[69] Abbas F, Scardino PT. The natural history of clinical prostate carcinoma [editorial; comment]. Cancer. 1997;80(5):827-33.

[70] Shinohara K, Scardino PT, Carter SS, Wheeler TM. Pathologic basis of the sonographic appearance of the normal and malignant prostate. Urol Clin North Am. 1989;16(4): 675-91.

[71] Terris MK, McNeal JE, Stamey TA. Estimation of prostate cancer volume by transrectal ultrasound imaging. J Urol. 1992;147(3 Pt 2):855-7.

[72] Rifkin MD. Ultrasound of the prostate-Imaging in the diagnosis and therapy of prostatic disease. 2 ed. Ryan JD, Patterson D, DiFrancesco R, editors. Philadelphia, New York: Lippincott-Raven Publishers; 1997.

[73] Djavan B, Zlotta AR, Ekane S, Remzi M, Kramer G, Roumeguere T, et al. Is one set of sextant biopsies enough to rule out prostate Cancer? Influence of transition and total prostate volumes on prostate cancer yield. Eur Urol. 2000;38(2):218-24.

[74] Djavan B, Remzi M, Schulman CC, Marberger M, Zlotta AR. Repeat prostate biopsy: who, how and when?. a review. Eur Urol. 2002;42(2):93-103.

[75] Matlaga BR, Eskew LA, McCullough DL. Prostate biopsy: indications and technique. J Urol. 2003;169(1):12-9.

[76] Presti JC, Jr., O'Dowd GJ, Miller MC, Mattu R, Veltri RW. Extended peripheral zone biopsy schemes increase cancer detection rates and minimize variance in prostate specific antigen and age related cancer rates: results of a community multi-practice study. J Urol. 2003;169(1):125-9.

[77] Jemal A, Thomas A, Murray T, Thun M. Cancer statistics, 2002. CA Cancer J Clin. 2002;52(1):23-47.

[78] Nelson WG, De Marzo AM, Isaacs WB. Prostate cancer. N Engl J Med. 2003;349(4): 366-81.

[79] Park SJ, Miyake H, Hara I, Eto H. Predictors of prostate cancer on repeat transrectal ultrasound-guided systematic prostate biopsy. Int J Urol. 2003;10(2):68-71.

[80] Iczkowski KA, Chen HM, Yang XJ, Beach RA. Prostate cancer diagnosed after initial biopsy with atypical small acinar proliferation suspicious for malignancy is similar to cancer found on initial biopsy. Urology. 2002;60(5):851-4.

[81] Thorson P, Humphrey PA. Minimal adenocarcinoma in prostate needle biopsy tissue. Am J Clin Pathol. 2000;114(6):896-909.

[82] San Francisco I, DeWolf W, Rosen S, Upton M, Olumi A. Extended prostate needle biopsy improves concordance of Gleason grading between prostate needle biopsy and radical prostatectomy. Urology. 2003;169:136-40.

[83] Futterer JJ, Heijmink SW, Scheenen TW, Veltman J, Huisman HJ, Vos P, et al. Prostate cancer localization with dynamic contrast-enhanced MR imaging and proton MR spectroscopic imaging. Radiology. 2006;241(2):449-58.

[84] Hricak H, Choyke PL, Eberhardt SC, Leibel SA, Scardino PT. Imaging prostate cancer: a multidisciplinary perspective. Radiology. 2007;243(1):28-53.

[85] Manenti G, Carlani M, Mancino S, Colangelo V, Di Roma M, Squillaci E, et al. Diffusion tensor magnetic resonance imaging of prostate cancer. Invest Radiol. 2007;42(6): 412-9.

[86] Heijmink SW, Futterer JJ, Hambrock T, Takahashi S, Scheenen TW, Huisman HJ, et al. Prostate cancer: body-array versus endorectal coil MR imaging at 3 T--comparison of image quality, localization, and staging performance. Radiology. 2007;244(1): 184-95.

[87] Morgan VA, Kyriazi S, Ashley SE, DeSouza NM. Evaluation of the potential of diffusion-weighted imaging in prostate cancer detection. Acta Radiol. 2007;48(6):695-703.

[88] Farsad M, Schiavina R, Castellucci P, Nanni C, Corti B, Martorana G, et al. Detection and localization of prostate cancer: correlation of (11)C-choline PET/CT with histopathologic step-section analysis. J Nucl Med. 2005;46(10):1642-9.

[89] Martorana G, Schiavina R, Corti B, Farsad M, Salizzoni E, Brunocilla E, et al. 11C-choline positron emission tomography/computerized tomography for tumor localization of primary prostate cancer in comparison with 12-core biopsy. J Urol. 2006;176(3):954-60; discussion 60.

[90] Schoder H, Gonen M. Screening for cancer with PET and PET/CT: potential and limitations. J Nucl Med. 2007;48 Suppl 1:4S-18S.

[91] Fenster A, Downey DB, Cardinal HN. Topical Review: Three-dimensional ultrasound imaging. Phys Med Biol. 2001;46(5):R67-99.

[92] Ladak HM, Mao F, Wang Y, Downey DB, Steinman DA, Fenster A. Prostate boundary segmentation from 2D ultrasound images. Med Phys. 2000;27(8):1777-88.

[93] Hu N, Downey DB, Fenster A, Ladak HM. Prostate boundary segmentation from 3D ultrasound images. Med Phys. 2003;30(7):1648-59.

[94] Cool D, Downey D, Izawa J, Chin J, Fenster A. 3D prostate model formation from non-parallel 2D ultrasound biopsy images. Med Image Anal. 2006;10(6):875-87.

Chapter 2

Ultrasound-Based Guidance and Therapy

Frank Lindseth, Thomas Langø, Tormod Selbekk,
Rune Hansen, Ingerid Reinertsen,
Christian Askeland, Ole Solheim,
Geirmund Unsgård, Ronald Mårvik and
Toril A. Nagelhus Hernes

Additional information is available at the end of the chapter

http://dx.doi.org/10.5772/55884

1. Introduction

Minimally invasive and non-invasive image guided therapy can reduce surgical traumas and improve outcome for patients suffering from a wide variety of diseases. It may also reduce hospital stays and costs. Ultrasound is an important intraoperative imaging modality for guidance and monitoring of these therapeutic methods. Ultrasound has emerged as one of the main modalities for medical imaging in healthcare, the main reason being its ability to image soft tissue, blood flow, organ function and physiology with considerably improved image quality. Furthermore, ultrasound has the unique advantages of real time imaging, equipment portability, safety, and low costs. Ultrasound is now facing a paradigm shift in technology and clinical usability over the coming 10 years. The future potential will be released through exploration in knowledge and innovation deliveries in transducer arrays, ultrasound electronics, software beam forming, parallel imaging and compressed sensing, minimum diffractive wave imaging, model powered acquisition and new technology for a wide range of methods related to physiology, tissue properties and organ function in real time and on site. High-frequency ultrasound imaging makes it possible to obtain significantly improved spatial resolution, however, with limitations related to how deep into the tissue the imaging can be performed. In many image-guided surgery and therapy applications, ultrasound is performed with probes placed directly on the tissue and organ of interest (e.g. intravascular ultrasound, open chest cardiac surgery, esophagus probes for cardiac imaging, probes dedicated to surgery of pituitary gland). These applications limit the size of the ultrasound probe head and thus also the quality of the images. However, with miniaturization based on nanomaterials and

nanoelectronics technology, significant improvements in image quality may be obtained. Furthermore, new ultrasound technology can greatly enhance the detection of contrast agents and drug carriers in the tissue. Integration of imaging with navigation technologies will ease image interpretation and further improve precision and accuracy of the therapeutic procedure. Ultrasound technology may also be used for therapeutic purposes. High intensity focused ultrasound (HIFU) for ablation of tumor tissue is already a commercial product. It has also been shown that ultrasound may improve the delivery and distribution of nanoparticles and local drug delivery by enhancing the local release, improving the penetration across the capillary wall and through the extracellular matrix as well as enhance the cellular uptake. The underlying mechanisms are cavitation, radiation force and heating. The ultrasound induced transient increase in porosity and permeability of cell membranes can potentially enhance drug uptake through tissue barriers (also the blood-brain barrier) and improve local drug delivery.

Therapeutic use of ultrasound will be addressed at the end of this chapter, which is mainly about guiding instruments into the body in a safe way using ultrasound, as well as the technological solutions involved to augment ultrasound in combination with other modalities and techniques. Ultrasound has been used to guide interventional instruments into the body for a long time. Different approaches have been used. From freehand 2D guidance, via "needle" guides mounted on conventional ultrasound probes to ultrasound-based navigation using tracking technology and 3D ultrasound (see figure 1). Surgical navigation will be the focus of this chapter and the analogy to GPS-navigation in a car is clear; instead of plotting the position of the car onto electronic maps of the terrain using satellites and GPS-receivers the position of important surgical instruments are shown on medical images of the patient using highly accurate tracking systems. Systems for image-guided surgery are now well established within many clinical disciplines. Surgical tools may be tracked by positioning systems and the surgeon may accurately navigate the tools into the patient with high precision based on image information only. Intraoperative imaging has shown to be important for obtaining improved tumor resection and increased survival for cancer patients undergoing surgery. Integration of intraoperative imaging with navigation technology, providing the surgeon with *updated* image information, is important to deal with tissue shifts and deformations that occur during surgery. MR, CT and ultrasound have been presented as alternative intraoperative imaging modalities showing complementary information and having different benefits and drawbacks. These intraoperative imaging modalities are reported to be useful for accurate navigation of surgical instruments, monitoring the progression of surgery and solving the shift problem. Intraoperative imaging has been used for updating preoperative images, which may be important for accurate guidance. In recent years ultrasound has gained increased attention as a useful intraoperative imaging modality (see figure 2), due to improved image quality and relatively low price. In addition, more integrated solutions, that makes the technology user friendly and flexible has been presented. In the evolution of the next generation of ultrasound-based multimodal navigation systems, advances in ultrasound imaging, registration algorithms, visualization and display techniques and navigation accuracy are important ingredients. We will therefore start by looking into the technology that is needed in order to make ultrasound-based navigation a reality and then show key applications of the navigation technology. Recent advances in ultrasound imaging will be useful also for intraoperative imaging. Furthermore,

http://dx.doi.org/10.5772/55884

ultrasound needs to be integrated with tracking technology in order to make a navigation system with intraoperative imaging capabilities. In addition, such a system might be able to use preoperative CT/MR data, update these data to match the current patient anatomy using intraoperative ultrasound, extract important structures from the different datasets, present the available multimodal information to the surgeon in an optimal way and be able to track all the surgical tools. Last but not least we need to make sure that the navigation system is highly accurate so that we know that the navigation scene presented to the surgeon on the computer screen is a realistic representation of what's really going on inside the patient.

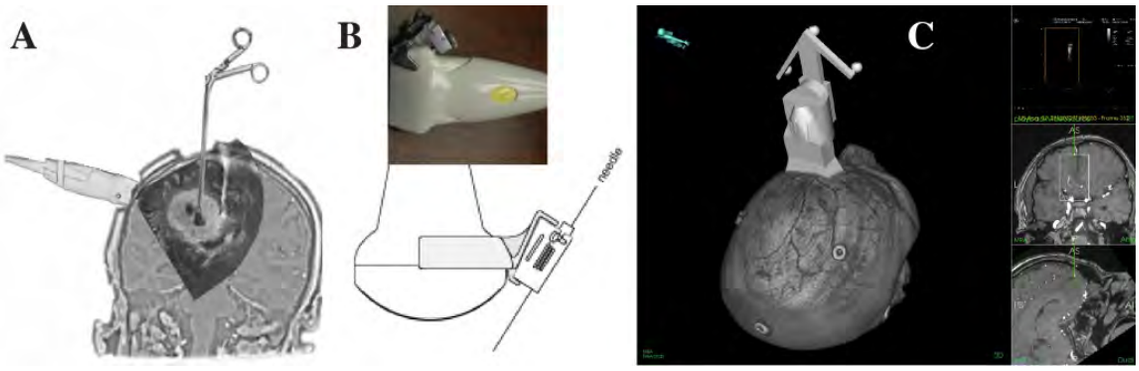

Figure 1. Ultrasound-based guidance: A) Freehand guidance: challenge to have the long axis of the instrument in the 2D ultrasound plane. B) Needle guides: an adapter mounted on the probe makes sure that the instrument is within the 2D ultrasound plane. C) Navigation: tracking technology and 3D data from modalities like CT, MR and ultrasound is used to guide relevant surgical instruments in place. Here an ultrasound probe is guided by MR during a freehand 3D ultrasound aquistion

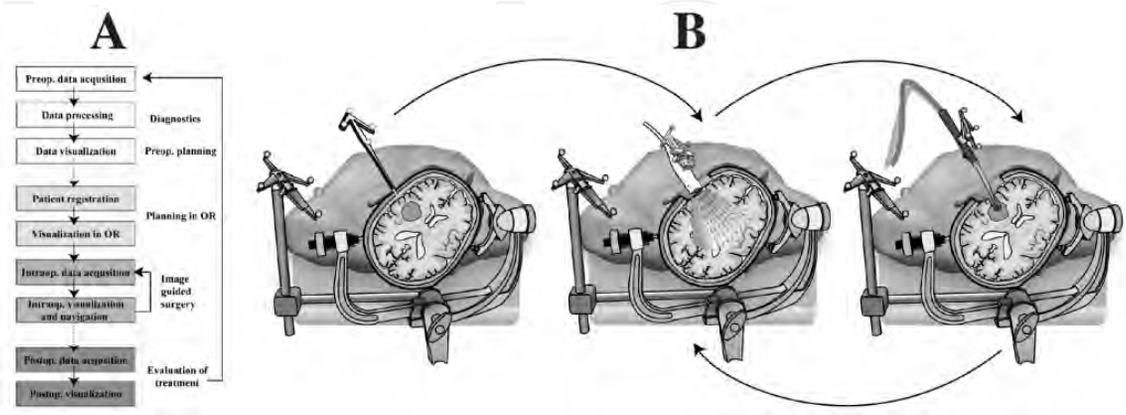

Figure 2. A) Workflow: Important steps in image-guided surgery. B) Ultrasound-based navigation example from neurosurgery: Plan using preoperative MR. Acquire intraoperative 3D ultrasound. Navigation and resection control based on updated ultrasound images. Acquire additional ultrasound data when needed.

2. Recent advances in ultrasound imaging

Sound in the human audible range have frequencies between 20 and 20 000 Hz. Ultrasound is defined as sound with frequencies above 20 kHz. In medical imaging, the ultrasound frequencies are usually between 2 and 40 MHz, with the highest frequencies currently used in intravascular ultrasound (IVUS).

The generation of an ultrasound image is based on transmission of sound pulses and receiving the echoes that have been reflected from tissue boundaries or scattered from smaller objects. In most conventional scanners today, a narrow ultrasound beam is transmitted from the ultrasound transducer. When the transmitted pressure pulse meets a hinder in form of a boundary between different soft tissues, or scatter points within the tissue with different acoustic properties, some of the energy of the transmitted sound pulse is echoed back to the transducer. This pulse-echo principle forms the basis of all ultrasound-imaging techniques, such as conventional brightness mode (B-mode) imaging of organs, imaging of blood flow using Doppler techniques and exploration of mechanical tissue properties using ultrasound elastography techniques.

2.1. Advances in ultrasound hardware and transducer technology

The ultrasound machines and ultrasound probes have gone through massive improvements in the last decade. The general increase in computer power is opening new possibilities for implementing sophisticated methods for beam forming. This may lead to higher resolution and better image quality than for existing solutions [1]. The general trend with miniaturization of components has also strongly influenced the size of the ultrasound imaging systems. Small handheld ultrasound devices have been developed, which makes ultrasound an extremely portable imaging technology. One example of such a pocket sized ultrasound device is the Vscan from GE Healthcare (figure 3), which has been explored for use in echocardiography [2]. The ultrasound transducer technology has made tremendous progress the last decade. The number of elements used by a transducer is increasing and the trend is to go from a single row of elements (1D) to multi-row arrays (1.25D / 1.5D) and 2D matrix arrays. The latter provides the possibility to perform 4D ultrasound imaging, in which a 3D ultrasound volume is acquired and displayed in real time. 4D ultrasound imaging may also be used for monitoring of treatment, e.g. radiofrequency ablation [3].

Ultrasound arrays today are mostly based on piezoelectric materials. The research activities in MUT (Micromachined Ultrasound Transducer) technology, and perhaps especially CMUT (capacitive MUT) transducers, pave the way for silicon-based arrays [4]. This may introduce probes that are cheaper, more customizable and have higher frequencies and bandwidth compared to piezoelectric transducers. In combination with the everlasting trend of miniaturization, the CMUTs may in a long-term perspective allow complete ultrasound systems to be seamlessly integrated with surgical tools. It may very well be that the future surgical instrument has an ultrasound transducer integrated on the tip, and a display unit integrated in the handle.

http://dx.doi.org/10.5772/55884

Figure 3. Pocket-sized ultrasound (Vscan from GE Healthcare)

2.2. Ultrasound elastography

The concept of ultrasound imaging of tissue strain or elasticity is often referred to as ultrasound elastography and the corresponding 2D images are frequently called elastograms. The imaging technique is often explained to be analogue to palpation, where the physician uses the fingers to apply a slight pressure in order to examine the stiffness of the tissue. If a organ is vibrating or excited, ultrasound elastography methods can in a similar fashion be used to map areas with differences in strain (figure 4).

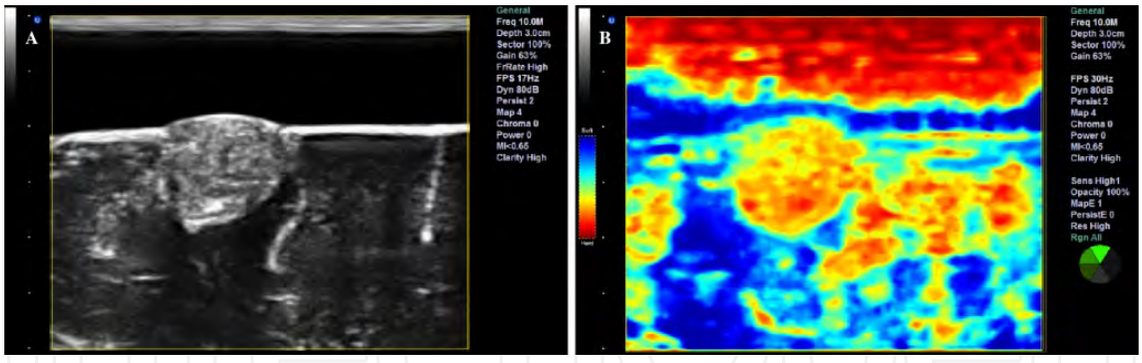

Figure 4. Elastography. A) Ultrasound B-mode image of a small meningioma, and B) the ultrasound elastogram of the tumour as displayed on an Ultrasonix MDP scanner.

The theoretical framework for the study of behavior of vibrating soft tissue was established in the early 1950ies. Von Gierke et al. published *"Physics of vibrations in living tissues"* in 1952 [5], for example. However, it was not until 30 years later that tissue movement was first measured for clinical purposes by using ultrasound in a study of tissue motion in the liver caused by vascular pulsation [6, 7]. In the late 1980ies, techniques for vibration elastography imaging, also known as vibration amplitude sonoelastography or simply sonoelasticity imaging was developed [8]. In this technique a low frequency vibration (20-1000 Hz) is applied externally to the skin surface to investigate the subcutaneous structures. The internal

motion of the tissue is investigated with a pulsed Doppler technique. Stiff tissue responds differently to the vibrations than softer tissue, and can therefore be distinguished in the real-time images.

In the early 1990ies, the development of compression elastography, also referred to as quasi-static elasticity imaging, begun. Ophir published a paper in 1991 where ultrasound radio frequency (RF) data before and after applying compression were compared and processed using cross-correlation to obtain the time-shifts of the echoes. This allowed the subsequent calculation of elastograms [9]. The quasi-static elasticity imply that the force is applied for a sufficiently long time for the tissue strain to stabilize, and the resulting difference in echo travel time between ultrasound data acquired before and after compression can be calculated. The tissue may also be excited by applying forces at the surface (manually or by electromechanical devices) or by physiological processes within the organ, as for example the pulsation of the arteries. The generated elastograms are usually displayed as a color-coded overlay on the conventional ultrasound brightness mode image. The color mapping may cover a range of unit-less strain values as percentages from minimum (negative) strain to maximum (positive) strain. Alternatively, it may also be mapped from "soft" to "hard" tissue, thereby not quantifying the strain range displayed. Quasi-static elasticity imaging has been evaluated in a broad range of clinical applications. It has been reported used in diagnostics of tumors in for example breast, prostate, liver, the thyroid gland and in the brain (figure 4) [10-15]. Quasi-static elasticity imaging is an emerging ultrasound imaging modality, now becoming more and more available as an option on commercial ultrasound systems.

As previously explained, the elastography methods require that the tissue is excited. The tissue movement can be caused by physiological processes internally in the organ such as the pulsation of the arteries. The tissue can also be externally excited by manually pushing the tissue or by using an electromechanical vibrating device. An alternative approach is to use the acoustic radiation force of an ultrasonic focused beam to generate displacements in the tissue with subsequent detection of the mechanical properties. One example of such an approach is the Acoustic Radiation Force Impulse (ARFI) method developed at Duke University [16]. In this technique, short duration acoustic pulses (push pulses) are used to generate small localized displacements deep in the tissue. These displacements are tracked by ultrasonic cross correlation, in a similar fashion as for the quasi-static elasticity imaging. The method has been investigated for imaging of focal liver lesions, prostate and breast [17-19].

Another example is the innovative Supersonic Shear Imaging (SSI) method developed by the research group at the Laboratoire Ondes et Acoustique [20]. In SSI the acoustic radiation force is used to generate low-frequency shear waves (50-500 Hz) remotely in the tissue. The shear modulus of the tissue can be quantified by imaging the share wave propagation in the tissue by using ultrasound frame rates of several kHz. The method has been explored for diagnosis of liver fibrosis, breast lesions and cornea [21-23].

For a more detailed overview about methods for ultrasound elasticity imaging and its clinical use we recommend to read the review papers by Wells and Liang [24] and Parker, Doyley and Rubens [25].

2.3. Nonlinear acoustics and contrast agents

In 1980, Carstensen and Muir published two papers describing the importance of nonlinear acoustics within the field of medical ultrasound imaging [26, 27]. These papers predicted and demonstrated nonlinear acoustical effects relevant for intensities and frequencies common in biomedical imaging. There has been an increasing interest with respect to nonlinear biomedical acoustics during the last 30 years. This interest was further escalated by the introduction of ultrasound contrast agents in the form of microbubbles and the study of these microbubbles was the main impetus for the introduction of the tissue harmonic imaging technique.

Nonlinear effects can be important in the forward wave propagation. The back-scattered pressure levels of the echoes are typically too low to induce any significant nonlinear effects. One source of nonlinear terms is produced by the deformation of tissue volume elements during compression and expansion with strongly curved phase fronts. It is, however, common to use transmit beams with relatively smooth phase fronts. Consequently, this nonlinear source is usually not the most dominant. The other important nonlinear source is nonlinear terms in the tissue elasticity and hence in the relation between acoustic pressure and tissue compression/expansion. Nonlinear terms in the tissue elasticity are responsible for the fact that the tissue becomes stiffer during compression and softer during expansion. The compression also increases the mass density of the tissue, but this effect is inferior to the increased stiffness and the propagation velocity and will therefore be pressure dependent and will increase with increasing compressions and thus with increasing pressure. The resulting distortion of the transmit pressure field produces harmonic components which today are utilized in tissue harmonic imaging, especially in transcutaneous cardiac and abdominal imaging to suppress multiple scattering [28-31].

Ultrasound imaging is based on several assumptions, and one important assumption is that multiple scattering is neglected. For many organs, this approximation is valid. However, for the body wall, where larger variations in material parameters often are found, this assumption can be inadequate. Interfaces between soft tissue components with significant differences in material parameters give so strong echoes from the transmitted acoustic pulses that multiple scattering can get significant amplitudes. Such multiple scatterings are usually termed pulse reverberations [32, 33]. These reverberations reduce the ratio of the strongest to the weakest scatterer that can be detected in the neighborhood of each other, defined as the contrast resolution in the image. Reduced contrast resolution is in particular a problem when imaging hypo-echoic structures such as the heart chambers, the lumen of large blood vessels, some atherosclerotic lesions, cysts, some tumors, the gallbladder as well as in fetal imaging. The contact interface between the ultrasound transducer itself and the soft tissue is also a strong reflector enhancing the problem with multiple scattering.

Ultrasound contrast agents are made as a suspension of gas microbubbles encapsulated in thin stabilizing shells made from lipid or albumin. Typical bubble size is in the 1-5 μm range and the contrast bubbles are intravenously injected to increase the scattering from blood, which is weak compared to the scattering from soft tissues. Commercially available contrast bubbles are stable and small enough to enable transpulmonary passage and the blood half-life is typically in the range of 1-10 minutes. Scattering from microbubbles occurring within a liquid

is resonant through an interaction between a co-oscillating liquid mass around the bubble and the bubble compression elasticity [34] with typical resonance frequencies of 1-7 MHz. With adequately flexible shells, the gas bubble has a very high compliance relative to the surrounding blood and when driven by ultrasound pulses at frequencies below or around the bubble resonance frequency, large bubble radius excursions on the order of one micrometer is achieved due to mainly shear deformation and limited volume compression of the blood surrounding the bubble. This bubble radius displacement is then between one and two orders of magnitude larger than typical particle displacements obtained within soft tissues. The radius oscillation of a bubble may be obtained from the Rayleigh-Plesset equation [35, 36]:

$$\rho\left(a\ddot{a} + \frac{3}{2}\dot{a}^2\right) = -B(a, \dot{a}) - p_i(t) \tag{1}$$

where ρ is the mass density of the surrounding liquid, a is the bubble radius (where the time dependence has been omitted for convenience), B is the pressure produced by the gas and the encapsulating shell, p_i is the incident drive pressure and the dots represent differentiation with respect to time so that $\dot{a}$ and $\ddot{a}$ represent the velocity and acceleration of the bubble wall, respectively. The terms on the left-hand side represent acceleration forces of the co-oscillation liquid mass whereas the terms on the right-hand side represent pressure terms due to gas and shell elasticity in addition to the drive pressure. The bubble pressure B can be written

$$B(a, \dot{a}) = -\left(p_0 + \frac{2\sigma}{a_0}\right)\left(\frac{a_0}{a}\right)^{3\kappa} - S(a_0, a) + p_0 + \frac{2\sigma}{a} + \mu\frac{\dot{a}}{a} \tag{2}$$

where the first term is the gas pressure and where κ is the polytropic exponent of the gas and a_0 is the equilibrium bubble radius. The second term S is the pressure contribution from the encapsulating shell and p_0 is the ambient hydrostatic pressure. The fourth term accounts for surface tension due to the gas-liquid interface and the last term accounts for damping effects. When a contrast bubble is insonified by frequencies below or around its resonance frequency, the local nonlinear scattering from the contrast bubble is usually much larger than from soft tissues [37, 38]. This has resulted in several nonlinear ultrasound contrast agent detection techniques with the purpose to suppress the linear part of a received signal while maintaining as much as possible of the nonlinear part of a received signal. This is then used for low transmit pressure levels. The forward wave propagation is close to linear whereas the scattering from microbubbles can be highly nonlinear. Common techniques in use today are Pulse Inversion methods that detect even harmonic components [39, 40]. Amplitude Modulation methods are also in use [41], often in combination with Pulse Inversion methods [42-44].

The equations describing the bubble oscillations can be solved numerically. An example of a bubble with equilibrium radius of 2 μm is shown in figure 5. An incident drive pulse with center frequency around 2 MHz is displayed in the time and frequency domain in the upper panel. In the middle panel, the resulting bubble radius oscillation is depicted and in the lower panel, the resulting normalized far-field component of the scattered pressure from the bubble is displayed. It can bee seen that the response is highly nonlinear and several harmonic

http://dx.doi.org/10.5772/55884

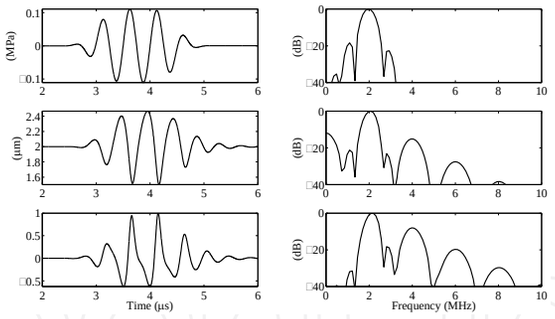

Figure 5. Numerical simulation of oscillation for a bubble with equilibrium radius of 2 μm and resonance frequency of 2.5 MHz. The upper panels show the drive pulse, the middle panels show the resulting bubble radius oscillation and the lower panels show the far-field component of the scattered pressure from the bubble. The left panels display the pulses in the time domain whereas the modulus of the Fourier Transform is displayed in the right panels.

components are present in the scattered pressure from the bubble. This response is obtained with an incident drive pulse having a mechanical index equal to 0.07, which is very low compared to what is used for regular tissue imaging. At such low transmit pressure levels, the forward wave propagation will be close to linear and distortion of the transmit field due to nonlinear tissue elasticity will thus be very low. The harmonic components can then be used to differentiate bubble echoes from tissue echoes through Pulse Inversion and Amplitude Modulation pulsing schemes. In most clinical applications of ultrasound contrast agents, it is desirable to assess the micro-circulation or the tissue perfusion which cannot be done without the use of contrast agents and which often is related to various diseases. It is then necessary to obtain a strong suppression of the tissue signal for detection of the contrast bubble signal.

An example of the use of ultrasound contrast agents in relation to minimally invasive interventions is radiofrequency ablation of liver tumors where contrast-enhanced ultrasound is used for improved detection and imaging of the lesions, for planning and guidance of multiple needle electrodes and finally for immediate evaluation of the treatment [45].

SURF (Second order UltRasound Field) imaging is a nonlinear ultrasound imaging technique being developed in Trondheim [46-50]. It is based on transmission of dual frequency band pulse complexes consisting of a low frequency manipulation pulse and a high frequency imaging pulse that are co-propagating. Two transmit pulse complexes that may be used with the SURF technique are displayed in figure 6. With the use of conventional single frequency band transmit pulses, nonlinear effects are mainly restricted to the generation of harmonic components of the imaging pulse. With dual frequency band transmit pulses, other nonlinear effects also come into play. SURF imaging aims at further utilizing nonlinear acoustics for improved imaging of various tissues and ultrasound contrast agents.

For imaging of ultrasound microbubbles, conventional techniques relies on driving the bubble into strong nonlinear oscillations with the imaging pulse at relatively low mechanical indexes. This is typically feasible when the imaging frequency is below or around the bubble resonance frequency (as in the example of figure 5) and conventional contrast agents typically have resonance frequencies below 7 MHz. However, when the imaging frequency is above the bubble resonance frequency a much higher mechanical index is required to obtain significant

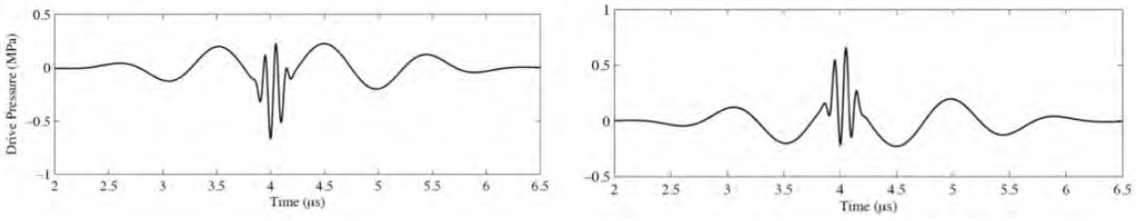

Figure 6. Example of SURF transmit pulse complexes where a low frequency manipulation pulse at 1 MHz is co-propagating with a high frequency imaging pulse at 10 MHz. The high frequency imaging pulse is in the left and right panel placed at low and high manipulation pressure, respectively.

nonlinear back-scattering from the bubble. At higher mechanical indexes the tissue will also respond nonlinearly and it then becomes difficult to differentiate the tissue signal from the bubble signal. For contrast imaging at high frequencies, such as 10 – 30 MHz, that can be used in minimal invasive interventions where the probe can be close to the object being imaged, conventional contrast imaging techniques often have limitations. The dual band SURF technique then has some advantages where the low frequency manipulation pulse can be tuned to match the bubble resonance frequency (typically around 2-3 MHz) whereas the high frequency imaging pulse can be optimized for the object being imaged and can for example be 20 MHz. The low frequency then manipulates the bubble oscillation and back-scattering which is interrogated by the high frequency pulse. The high frequency imaging pulse is hence decoupled from the resonance properties of the contrast bubbles.

3. Ultrasound-based navigation — Enabling technologies

State of the art ultrasound imaging is crucial for guiding interventions. But unlike freehand guidance and guidance based on ultrasound guides (figure 1) having optimal images on the ultrasound scanner is not enough to enable surgical navigation. In order to use ultrasound-based navigation to guide such procedures we usually have to:

- Get the images out of the ultrasound scanner and into the navigation software in real-time.
- Track the position and orientation of the ultrasound probe at all times.
- Synchronize the image and tracking streams (temporal calibration) and find the transformation between the tracking sensor mounted on the ultrasound probe and the ultrasound scan plane (spatial calibration), which is the interesting part to track.
- Reconstruct all the position tagged ultrasound frames from a conventional 2D ultrasound probe into a regular 3D volume that can be used in the same way as preoperative MR or CT is.

3.1. Streaming of ultrasound data

Convenient ultrasound-based navigation of surgical instruments requires real-time access to the ultrasound data in the navigation software (figure 7). This is required in order to tag the ultrasound frames with position and orientation data from the tracking system (alternatively

http://dx.doi.org/10.5772/55884

the tracking data could be directed directly into the scanner and the ultrasound frames could be used off-line, e.g. to generate a 3D volume from the tagged 2D frames). The traditional way of getting real-time access to ultrasound frames is to connect the analog output (e.g., composite video, S-video) of the ultrasound scanner to a frame-grabbing card on the navigation computer. Using the analog output might affect the image quality due to the double digital-to-analog-to-digital conversion and no metadata (e.g. depth) follow the ultrasound images. Alternatively digital data can be streamed directly from the ultrasound scanner and into the navigation computer. Traditionally this has required some kind of research collaboration between the ultrasound manufacturer and the user but open ultrasound scanners are becoming available (e.g. the Ultrasonix scanner). These systems usually provide just a one-way streaming interface but two-way communication protocols where the scanner can be controlled (e.g. depth) by the navigation system exists making more integrated solutions possible (figure 7). Either way, the protocol (or interface / API) used is typically proprietary, although proposals for real-time standards are starting to emerge (e.g. OpenIGTLink, DICOM in surgery (WG24)). When the link between the ultrasound scanner and navigation system is digital, ultrasound data at different stages in the processing chain on the scanner can be transferred (e.g. scan-converted, scan-line and RF-data). Furthermore, a digital streaming interface will be required in order to use the real-time 3D scanners that are now becoming available also for navigation. It's difficult to capture the 3D content in the scanner display using a frame grabber so the data needs to be transferred in real-time or tagged with a tracking reference on the ultrasound scanner.

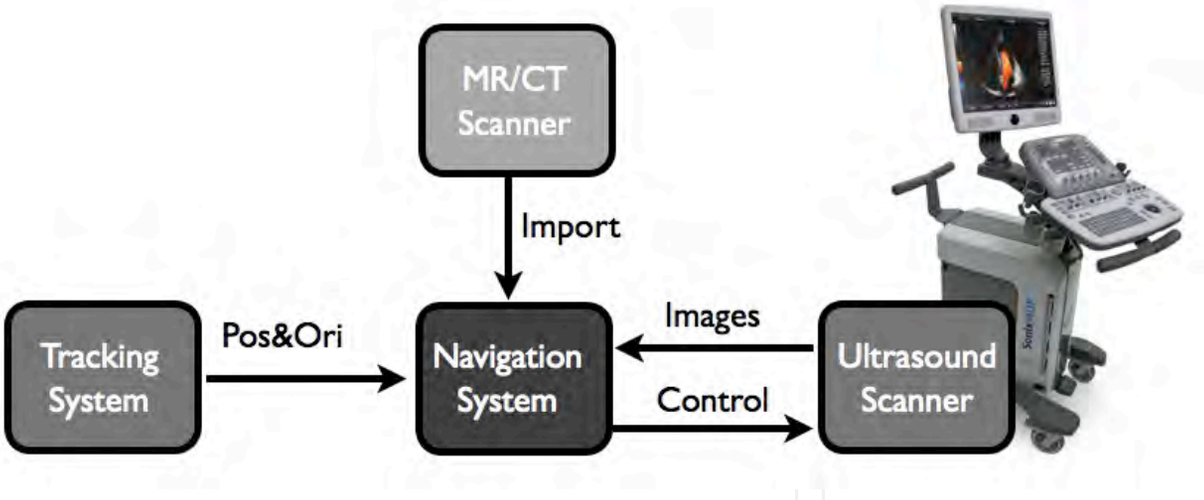

Figure 7. Streaming ultrasound data into the navigation system. The interface can either be analog using a frame grabber or digital using a direct link and a proprietary protocol. A digital interface can either be one-way (i.e. streaming) or two-way (i.e. optionally control the scanner from the navigation system as well). In any case the image stream must be tagged with tracking data and in order to do that the two streams need to be synchronized.

3.2. Tracking of ultrasound probes

In order to use ultrasound to guide surgical procedures the ultrasound probe must be tracked. Several tracking technologies have been proposed over the years (mechanical, acoustical,

optical and electromagnetic), but currently the most widely used solutions are optical or electromagnetic systems (see figure 8). Choosing the best tracking technology depends on the application at hand and the ultrasound probes used. If possible optical tracking systems should be preferred as magnetic tracking in the operating room can be challenging due to disturbances from metallic objects and the accuracy is close but not as good as optical systems under favorable conditions. For flexible us-probes or probes that are inserted into the body magnetic tracking is required as the transformation between the sensor and the scan plane must be rigid and optical tracking demands clear line of sight to the cameras. In addition the magnetic sensors are very small, crucial in order to be embedded in instruments and put into the body. When the ultrasound probe is tracked it becomes one of several tools and the streamed ultrasound data can either be shown in real time at the right spot in the patient or made into a 3D volume and shown together with other images to the surgeon. A brief description of the two main tracking technologies can be found below [51, 52]:

- *Optical tracking systems*: The basic idea is to use one or more cameras with markers distributed on a rigid structure where the geometry is specified beforehand (figure 8A). At least three markers are necessary to determine the position and orientation of the rigid body in space. Additional markers allow a better camera visibility of the tracked object and improve the measurement accuracy. The markers can be infrared light-emitting diodes (active markers), infrared light reflectors (passive markers) or some kind of pattern (usually a checker board) that can be identified using visual light and image analysis.

- *Electromagnetic tracking systems*: A receiver (sensor) is placed on the ultrasound probe and the system measures the induced electrical currents when the sensor is moved within a magnetic field generated by either an alternating current (AC) or direct current (DC) transmitter / generator (figure 8B). The AC and DC devices are both sensitive to some types of metallic objects placed too close to the transmitter or receiver, and to magnetic fields generated by power sources and devices such as cathode-ray tube monitors. Therefore, both types of electromagnetic systems are challenging to use in an environment such as an operating room, where various metallic objects are moved around in the field [53]. The two metal related phenomena that influence the performance of electromagnetic tracking systems are ferromagnetism and eddy currents [54]. Ferromagnetic materials (e.g., iron, steel) affect both AC and DC systems, because they change the homogeneity of the tracker-generated magnetic field, although the DC systems may be more sensitive to these effects. In contrast, the AC technology is more affected by the presence of conductors such as copper and aluminum because of distortions caused by eddy currents [53, 55]. DC systems minimize the eddy-current related distortions by sampling the field after eddy currents have decayed.

- *Comparisons between optical and magnetic tracking systems - pros and cons:* The main advantages with optical tracking systems are their robustness and high accuracy and the challenges are line of sight problems and the relatively big sensor frames. For electromagnetic tracking system it's basically the other way around.

http://dx.doi.org/10.5772/55884

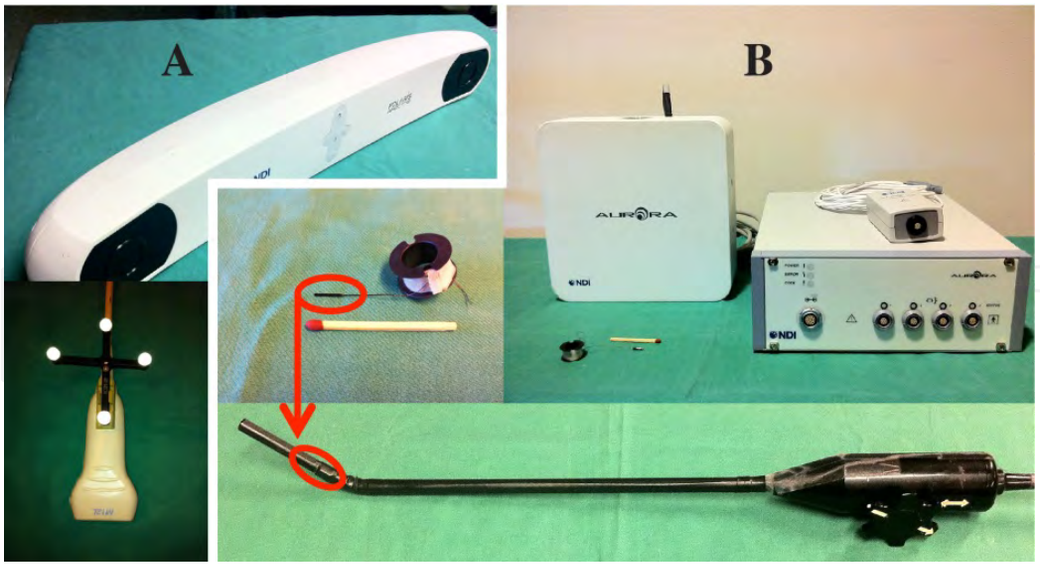

Figure 8. Optical (A) and electromagnetic (B) tracking of ultrasound probes.

3.3. Ultrasound probe calibration

After streaming ultrasound data into the navigation software and tracking the ultrasound probe, calibration is needed in order to integrate the image stream with the tracking stream. Ultrasound probe calibration is an important topic as this is the main error source for ultrasound-based navigation (see section on accuracy). Two types of calibration are necessary; temporal calibration to find the lag between the image and tracking streams and spatial calibration [56, 57] to find the transformation between the ultrasound scan plane and the tracking sensor mounted on the ultrasound-probe (see figure 9):

- *Temporal calibration (find the time lag between the image stream and the tracking stream, see figure 9A)*: The most common way to do this is to move the ultrasound probe up and down in a water bath and extract some feature in the generated us-images (or correlate the images and measure the displacement). This gives us two sinus-like curves, one for the vertical position of the extracted feature in the images and one for the vertical component in the tracking data. The two curves are compared and one of them is fitted to the other to find the time lag between the two streams.

- *Spatial calibration (find the transformation between the image and the sensor, see figure 9B)*: Considerable effort has been spent on probe calibration over the last decade, and it still seems to be a hot research topic. Maybe because it is a challenging task to make it accurate, especially if the same method / phantom is to be used for substantially different probes. It is not possible to measure this transform with a ruler because the orientation of the scan plane relative to the sensor frame is unknown, we do not know the origin of the us-plane inside the probe housing and magnetic sensors do not have a known origin. A commonly used approach for probe calibration is to acquire 2-D images of a phantom with known geometry and to identify distinct features in the images. Because the location of the same

features are known in the global coordinate system, the probe calibration matrix can be found from a relatively simple matrix equation. The probe calibration methods reported in the literature mainly differ with respect to the phantom geometry, whereas the processing of the acquired data is more or less common for all methods. The majority of probe calibration methods can be categorized into one of three different classes: single- point or line; 2-D alignment; and freehand methods. The calibration matrix can be calculated as follows. Acquire the necessary amount of calibration images and find the coordinates of all the calibration points in each image. Next, we transform the corresponding physical points from global reference coordinates into sensor frame coordinates by using the inverse of the tracking matrix. The rigid body transformation that minimizes the mean Euclidian distance between the two homologous point sets will be the probe calibration matrix. The matrix can be calculated using a direct least squares error minimization technique [58].

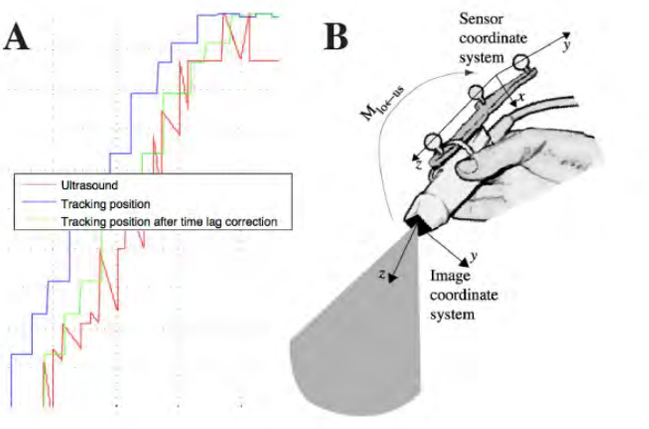

Figure 9. Temporal (A) and spatial (B) calibration of the ultrasound probe.

3.4. 3D Ultrasound

It is difficult to guide an instrument into place using conventional 2D ultrasound only (freehand guidance): in order to know where the instrument is we need to see it in the ultrasound image and to reach the target we have to know where to go from there, a challenging hand-eye coordination task. It's much more convenient to acquire a 3D ultrasound volume first and let the tracked instrument extract slices from the volume that can be annotated with the position and / or orientation of the instrument (see section on visualization).

3D ultrasound data can be acquired in different ways [59]. A conventional 1D array probe (2D +t) can be moved over the area of interest, either by freehand motion or by a motor. If freehand movement is used all the ultrasound frames can be put together into a volume using tracking data (figure 10) or correlation. A motor inside the probe hosing or external to it can also be used to cover the ROI by tilt, translation or rotation of the 1D array (figure 11). Furthermore, with a 2D matrix probe the ultrasound beam can be steered in the elevation direction in

http://dx.doi.org/10.5772/55884

addition to the lateral (azimuth) direction so that the ROI can be covered while the probe is standing still making real-time 3D ultrasound imaging possible (figure 12).

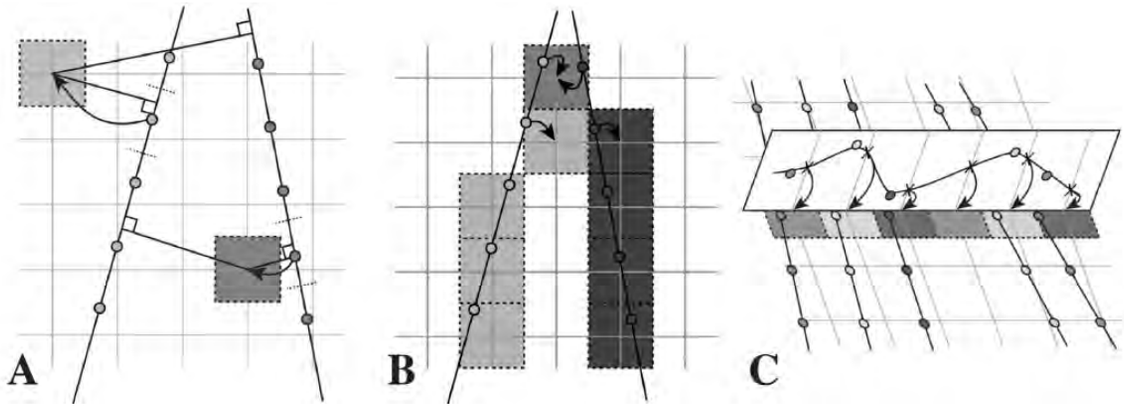

Figure 10. Reconstruction methods: A) Voxel Nearest Neighbor (VNN), B) Pixel Nearest Neighbor (PNN), Distribution Step (DS) and C) Functional Based Methods (FBM).

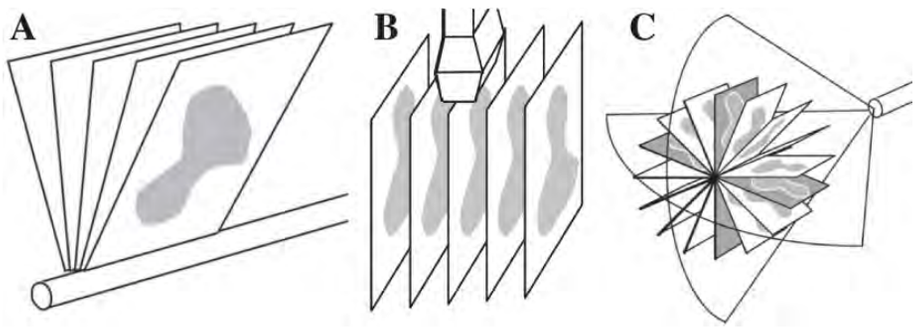

Figure 11. Motorized / mechanical tilting (A), translation (B) and rotation (C). Source: Fenster [59]

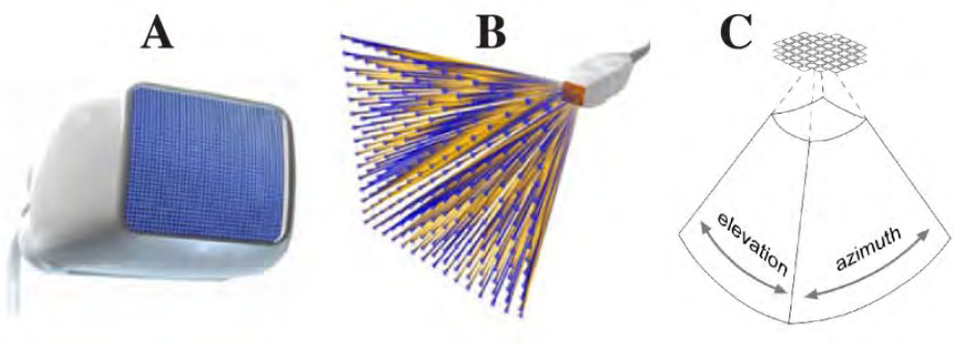

Figure 12. Matrix probes. Using a 2D array of elements (A) the beam can be steered in two directions (B) and a truncated pyramid of data is acquired (C).

In practice the following methods are in use:

- *Freehand 3D ultrasound:* This is still the most wildly used method (mainly because of its flexibility) and usually the method works in the following manner: *Scan* the area of interest using a conventional 2D probe that is tracked and *reconstruct* the position tagged ultrasound frames into a regular 3D volume that can be used in the same way as preoperative MR or CT. The ultrasound probe is usually tracked by optical or electromagnetic sensors, but other methods have been proposed. Furthermore, different methods exist to reconstruct all the 2D frames into a regular 3D volume. The methods can be categorized into tree main groups [60]:
  - *Voxel-based methods (VBM)*: VBM traverse each voxel in the target voxel grid and gather information from the input 2D images to be placed in the voxel. One or several pixels may contribute to the value of each voxel. The simplest method in this category is Voxel Nearest Neighbor (VNN), which traverses each voxel in the target volume and assigns the value of the nearest image pixel (see figure 10A).
  - *Pixel-based methods (PBM)*: PBM usually consists of two steps: a Distribution Step (DS) where the input pixels are traversed and applied to one or several voxels and a Hole-Filling Step (HFS) where the voxels are traversed and empty voxels are being filled. The simplest method in this category is Pixel Nearest Neighbor (PNN) that runs through each pixel in all the 2D input images and assigns the pixel value to the nearest voxel in the target volume (see figure 10B).
  - *Function based methods (FBM)*: FBM choose a particular function (like a polynomial) and determine the coefficients to make the functions pass through the input pixels. Afterwards, the function can be used to create a regular voxel array by evaluating the function at regular intervals (see figure 10C). These methods produce reconstructed volumes with the highest quality but are very computational intensive and are in limited use today.
- *Motorized (or mechanical) 3D ultrasound*: Instead of using freehand movement of the ultrasound probe over the area of interest a motor can cover the same region by tilting (figure 11A), translating (figure 11B) or rotating (figure 11C) a conventional 1D ultrasound array. Motorized probes have existed for a long time and the motor can either be mounted inside the probe housing (easy to use but requires a specially build ultrasound probe) or be applied externally (more flexible as conventional probes can be used). Many of the benefits with freehand scanning also apply to motorized scanning, e.g. the possibility to use high frequency probes with higher spatial resolution, also in the elevation direction (1.25D/1.5D probes). Motorized scanning can use the same kind of reconstruction methods as freehand scanning but usually more optimized methods are used as the movement is known and the probe do not need to be tracked during the acquisition. Compared to freehand ultrasound the motorized probes are easier to use in an intraoperative setting, but on the other hand, they are not as flexible in general.
- *Real-time 3D ultrasound using 2D matrix probes* [61-65]: Instead of using a conventional 1D array transducer that is moved by freehand or by a motor to sweep out the anatomy of interest, transducers with 2D phased arrays (figure 12A) that can generate 3D images in real time have been developed. Electronics is used to control and steer the ultrasound beam

http://dx.doi.org/10.5772/55884

(figure 12B) and sweep out a volume shaped like a truncated pyramid (figure 12C). The main challenge with this technology is the large and heavy cable that would be required to connect all the elements in the array to a wire. Fortunately technological achievements in terms of multiplexing, sparse arrays and parallel processing over the last decade have made these systems commercially available. They are used extensively in echocardiology, which requires dynamic three-dimensional imaging of the heart and its valves.

3.5. Integrated ultrasound-based navigation solutions

Ultrasound and navigation can be integrated in different ways as we have seen. Complete systems can usually be categorized as follows:

- *Two-rack systems:* Where the navigation computer with tracking system etc. and the ultrasound scanner are two separate systems. This is most common, especially in a research environment. The main reason for this is flexibility, in principle any ultrasound scanner with an analog output can be used together with a navigation system that is equipped with ultrasound-based navigation software. An example of such a configuration is our in house research system for us-based navigation called CustusX (figure 13A). The system is used for different clinical applications (e.g. neurosurgery and laparoscopy), each navigation rack is equipped with both optical and magnetic tracking and can be connected to a variety of ultrasound scannersusing analog and digital interfaces.
- *One-rack systems:* Here the ultrasound scanner and the navigation computer have been integrated in the same system. These systems are more convenient to use in the operating room but are less flexible. Most commercial solutions belong to this category. Two variations exists:
  - *An ultrasound scanner with navigation software integrated*. The PercuNav system from Philips, an integrated solution for navigation and intraoperative imaging, is an example of this (figure 13B).
  - *A navigation system with an ultrasound scanner integrated*: The SonoWand system (Trondheim, Norway), where an ultrasound scanner has been embedded in the navigation rack, is an example of this (figure 13C). The system can be used in three distinct ways: 1) as a navigation system based on preoperative MR/CT data, 2) as a standalone ultrasound scanner and 3) as an ultrasound-based navigation system with intraoperative imaging capabilities, its main use.

4. Registration and segmentation in ultrasound-based navigation

Registration is the process of transforming an image into the coordinate system of a patient, or another image. After registration, the same anatomical features have the same coordinates in both the image and the patient, or in both images. Image-to-patient registration is one of the cornerstones of any navigation system, and is necessary for navigation using pre-operative

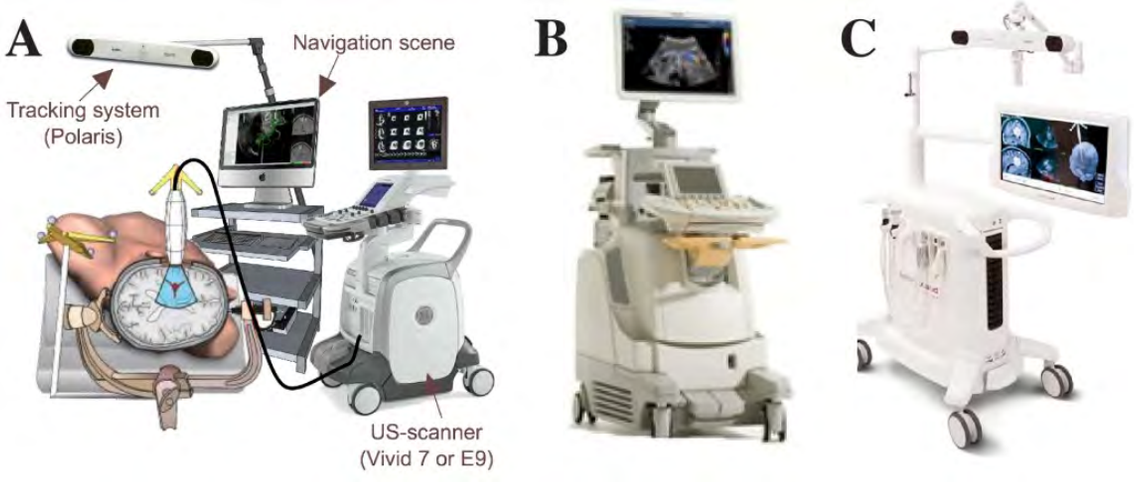

Figure 13. Different approaches to integrating (3D) ultrasound and navigation. A) A two-rack solution and examples of one-rack solutions (B and C).

images such as MR and/or CT. Image-to-image registration is useful to align pre-operative images before registration to the patient, and also to update the pre-operative images during surgery using for example intra-operative US. Only the latter involves US and will be the focus in this section, but image-to-patient registration is important for proper initialization of the MR/CT-to-US registration. The main motivation behind image-to-image registration is that different images contain different and complimentary information about the patient at a given point in time. When we bring the images into the same coordinate system and into the coordinate system of the patient, we can take advantage of more of the useful information in the different images. Such information can be the size and location of the surgical target, important blood vessels, critical structures that should be avoided etc. The registration method used in each case depends heavily on the type of images we want to register. The type of spatial transformation, how we measure the similarity between the images and how this measure is optimized are key components of any registration procedure.

4.1. Registration of preoperative images to the patient

Image-to-patient registration is a necessary and crucial step in order to use pre-operative images for guidance. Intraoperative ultrasound only shows a limited portion of the surgical field and might require some experience to appreciate. Preoperative data can therefore be used for overview and interpretation. In neurosurgery, for example, it is not possible to acquire ultrasound images before opening of the dura. Pre-operative images are therefore necessary for planning the craniotomy.

One of the most frequently used registration methods consists in using self-adhesive markers, also called fiducials. The fiducials are glued to the patient's skin before MR or CT imaging. The markers can be identified in the images and the corresponding markers can be identified on the patient using a tracked pointer once the patient is immobilized on the operating table (figure 14). A spatial transformation can then be computed transforming the image into the coordinate system of the patient. The surgeon can then point on the patient using a tracked

pointer and see the corresponding location in the images on the computer screen. The use of markers for image-to-patient registration presents some limitations both for the patient and the hospital staff. First, fiducial based registration requires an imaging session shortly before surgery to minimize the risk for markers to fall off or be displaced. In many cases this imaging session comes in addition to an initial session needed for diagnosis. Any displacement of the fiducial markers between the imaging session and surgery will compromise the image-to-patient registration accuracy. The placement of fiducials also represents an inconvenience for patients and hospital staff in the preparations for the procedure.

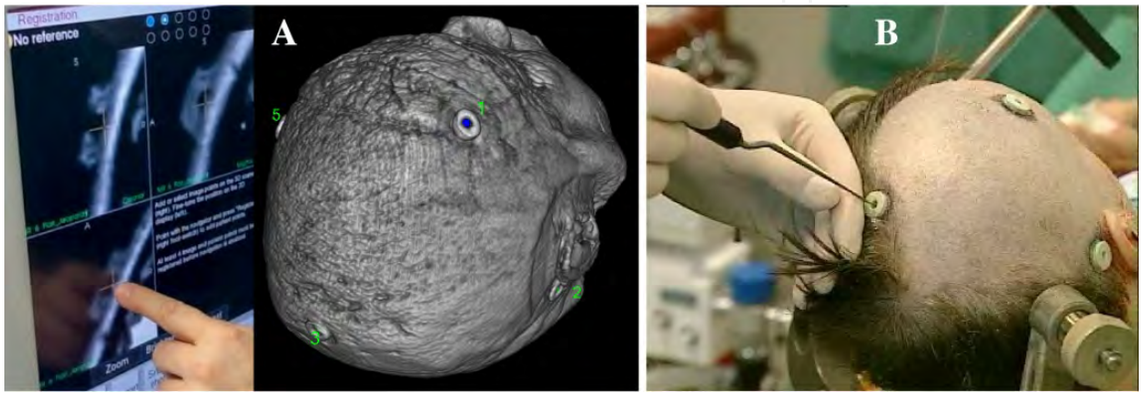

Figure 14. Image-to-Patient registration using corresponding points between image space (A) and physical space (B).

In order to avoid the use of fiducial markers, natural anatomical landmarks can be used for patient registration. Typical features in the context of neurosurgery are the medial and lateral corners of the eyes, the nose and ears. Like fiducial based registration, an image-to-patient registration framework using natural anatomical landmarks requires identification of points in the pre-operative images. The typically used landmarks are almost coplanar, and they are all located in a relatively small area around the face and ears. This might compromise the registration accuracy in other parts of the head, and possibly close to the surgical target [66]. A number of groups have presented surface matching techniques to address this issue. The skin surface of the patient is segmented from pre-operative data and registered to a set of surface points acquired in the operating room. Techniques to acquire surface points in the operating room include cameras [67, 68], laser surface scanners [69-71] and tracked pointers [72]. The accuracy of the different methods has been evaluated and compared [71, 73-75]. Both landmarks and surface based registration alone are less accurate than fiducial based registration. Different approaches combining registration based on anatomical landmarks and alignment of surfaces have therefore been developed.

As surgery proceeds, tissue will shift and deform due to gravity, retraction, resection and administration of drugs. Consequently, the pre-operative images do not correspond to the patient anymore. In this case, intraoperative ultrasound can be used for direct guidance and to update the location of the pre-operative data according to the surgical reality at a given point in time.

4.2. Ultrasound-based update of preoperative data

As surgery proceeds the pre-operative images no longer reflect the reality and updated information is necessary for accurate navigation. Intra-operative ultrasound can be acquired when needed during the procedure and be used for direct guidance and resection control, but also as a registration target for pre-operative images in order to update their position. This is particularly important for images such as functional MRI (fMRI) and diffusion tensor imaging (DTI) in neurosurgery because the information contained in these images cannot be easy re-acquired during the procedure. By performing MR/CT-to-US registration, the information contained in the pre-operative images can be shifted to the correct position at any given point in time (figure 15). Registration of MR/CT to US is a challenging task due to differences in image appearance and noise characteristics. The existing methods can be divided into two main categories:

- *Intensity-based methods*: These methods take the original images (MR/CT and B-mode US) as input, and the optimization of the registration parameters is computed from the image intensities, either directly or indirectly (blurring, gradients etc.). Some of the existing methods use well-known similarity measures such as mutual information and cross-correlation, while others have developed similarity measures particularly adapted to the registration of MR/CT and ultrasound [76-82].
- *Feature-based methods*: These methods require segmentation or "enhancement" of particular features in the images to be registered. The registration algorithm will then align the corresponding features in each image. In MR/CT-to-US registration such feature might be the vascular tree [83-85]. Blood vessels are relatively easy to identify and segment in both MR angiography and Doppler ultrasound images, and are present in nearly any region of interest. A centerline or skeleton can be computed from the segmented vessels and be used for registration. The most commonly used method for feature-based registration is the iterative closest point algorithm (ICP) [86]. In the case of vessel registration, all the points in the moving dataset are paired with the closest point in the fixed dataset. Based on these point correspondences, the registration parameters can be computed using the least squares method. The resulting transformation is then applied to the moving dataset and new point correspondences can be computed. The process is then iterated until convergence.

Several methods within the two main categories have been validated using retrospective clinical data [12, 14, 15]. So far no automatic method has been thoroughly validated intraoperatively (figure 15). The use of automatic registration methods in the operating room requires high quality data and straightforward, accurate, robust and fast image processing. With all this in place, image registration using intraoperative ultrasound will be able to correct the position of pre-operative data and thereby provide updated and reliable information about anatomy, pathology and function during surgery.

4.3. Motion correction using 4D ultrasound

Intensity based registration of ultrasound images can also be used to track the motion of an organ of interest. In the case of high-intensity focused ultrasound (HIFU or FUS) or radiotherapy, the

http://dx.doi.org/10.5772/55884

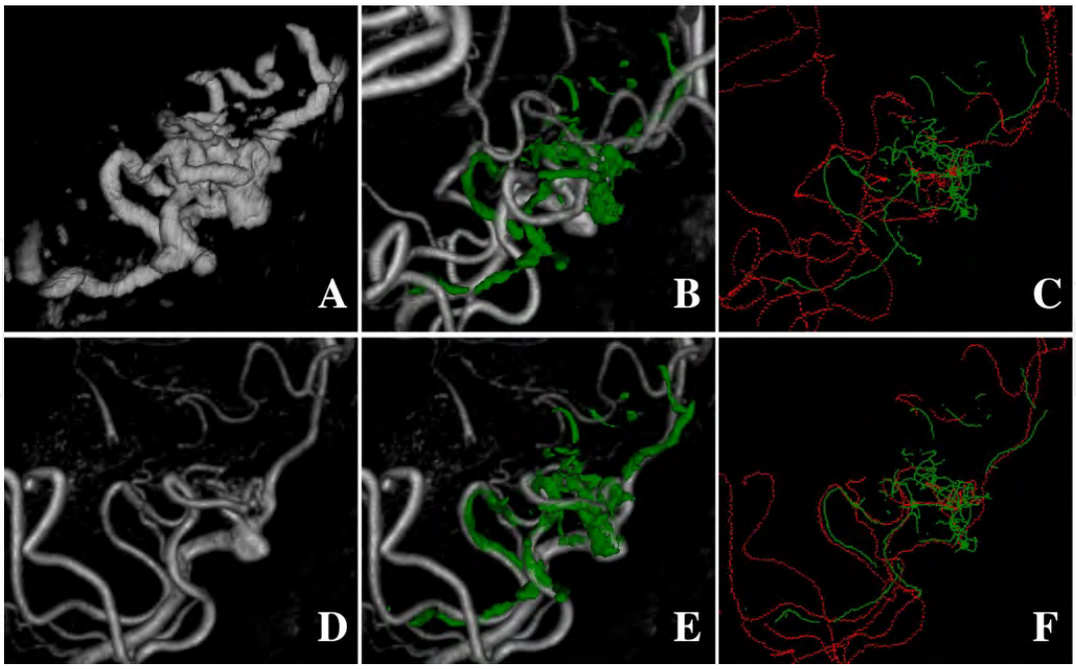

Figure 15. Ultrasound-based shift correction of preoperative MR data during an AVM operation. Top and bottom row shows the situation before and after the MR-to-US registration respectively. A) Ultrasound. D) MR. MR (gray) and US (green) before (B) and after (E) registration. Centerlines from US (green) and MR (red) before (C) and after (F) registration.

organ can be imaged using 4D ultrasound (3D + time or real-time 3D) in order to monitor the temporal changes in anatomy during the imaging, planning and delivery of treatment. The consecutive 3D images can then be registered in order to estimate the organ motion (figure 16). The positioning of the HIFU or radiation beam can then be modified accordingly in order to hit the target at any point in time. We have validated automatic motion estimation from 4D ultrasound in the liver using a non-rigid registration algorithm and a group-wise optimization approach as part of an ongoing study to be published in the near future. The offline analysis was performed using a recently published non-rigid registration algorithm that was specifically designed for motion estimation from dynamic imaging data [87]. The method registers the entire 4D sequence in a group-wise optimization fashion, thus avoiding a bias towards a specifically chosen reference time point. Both spatial and temporal smoothness of the transformations are enforced by using a 4D free-form B-spline deformation model. For the evaluation, three healthy volunteers were scanned over several breath cycles from three different positions and angles on the abdomen (nine 4D scans in total). A skilled physician performed the scanning and manually annotated well-defined anatomic landmarks for assessment of the automatic algorithm. Four engineers each annotated these points in all time frames, the mean of which was taken as a gold standard. The error of the automatic motion estimation method was compared with inter-observer variability. The registration method estimated liver motion better than the individual observers and had an error (75% percentile over all datasets) of 1 mm. We conclude that the methodology was able to accurately track the motion of the liver in the 4D ultrasound data. This methodology may be used intraoperatively to guide ablation of moving targets in the abdomen if the registration method can be run in real-time and the ultrasound probe can be made MR compatible (required for MR-guided HIFU).

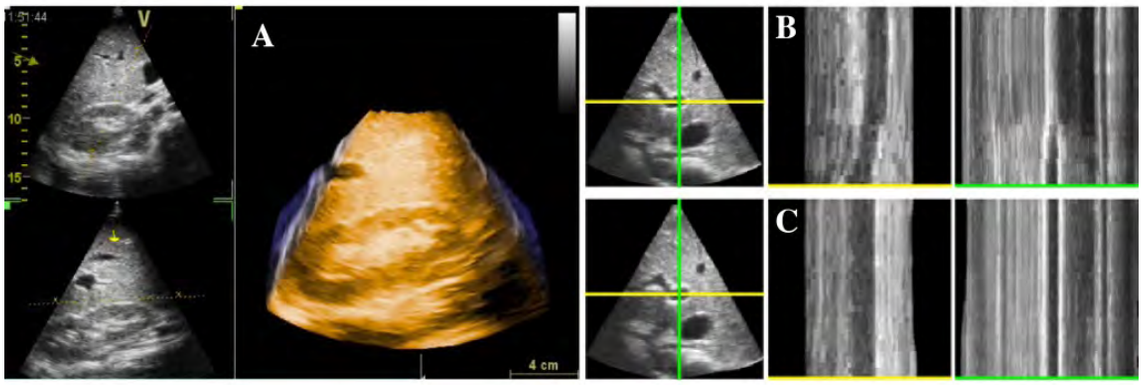

Figure 16. A) 4D (3D+t) Ultrasound of the liver. Example image before (top row B) and after (bottom row C) registration. The middle (B-C) and right panel, respectively, show the evolution over time (vertical axis) of the horizontal and vertical profile indicated by the cross in the left panel. After registration, the motion has been successfully removed from the image (streight vertical lines).

4.4. Segmentation of ultrasound data

Fully automatic segmentation of structures from B-mode ultrasound images is a challenging task. The clarity and contrast of structure boundaries depend heavily on their orientation relative to the sound wave and the acoustic properties of the surrounding tissues. Consequently, the boundaries of interest are often broken or at least unclear in parts of the image volume. It is therefore necessary to use *a priori* knowledge about the shape and appearance of the structure of interest in order to obtain reliable segmentation results. This *a priori* knowledge can be obtained by manually segmenting the structure of interest in a set of training data. Then, shape and appearance statistics can be used to segment the structure in new datasets. Akbari et al. [88] and Zhan et al. [89] used this approach for segmentation of the prostate in 3D ultrasound images of the prostate, and Xie et al. [90] used a similar approach for segmentation of the kidneys from 2D ultrasound images. The disadvantage of this method is the requirement for a database of training data with manual segmentations. This method can also be difficult to employ if the shape and appearance of the structure is unknown or presents large variations such as tumors and other pathologies. Several groups have also presented segmentation algorithms for ultrasound images of bone surfaces, and particularly the spine [91-94]. In these cases, the purpose of the segmentation process is to extract the bone surface from intra-operative ultrasound images for registration to pre-operative CT images. The ultrasound images are filtered in order to highlight the bone surface and in some cases the characteristic shadow behind the bone surface can be used for segmentation purposes as shown by Yan et al. [94]. They used backwards scan-line tracing to extract the bone surface from ultrasound images of the spine.

One of the great advantages of ultrasound is real time dynamic imaging. Methods based on shape and appearance statistics are in general not able to run fast enough to capture the dynamics of a moving organ such as the heart. Orderud et al. [95] proposed a method for real time segmentation of the beating heart. They fitted a set of control points of a model of the left ventricle to 4D ultrasound data (figure 17). The fitting process was run in real time

using a state estimation approach and a Kalman filter. When the shape, appearance and localization of the structure are unknown semi-automatic or manual segmentation by an expert might be the only solution to obtain satisfactory results. Segmentation of Doppler ultrasound images, on the other hand is usually straightforward using simple thresholding methods. Vascular structures, however, often appear with a diameter that is to large in the Doppler ultrasound images causing neighboring vessels to be smeared together. Reliable segmentation of the vascular tree can therefore be challenging due to the spatial resolution of the images.

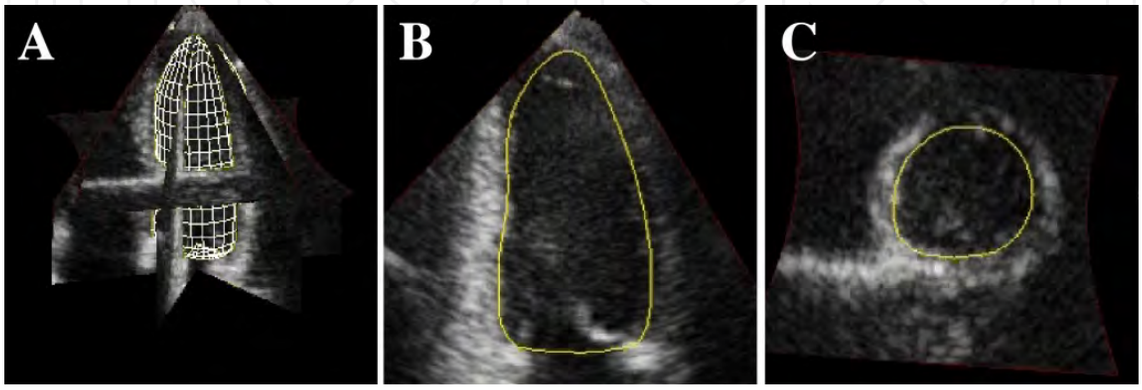

Figure 17. A 3D model of the left ventricle (A) matched in real-time to 4D Ultrasound shown here as slices in 3D (A) and 2D (B and C). Source: Orderud [95].

5. Ultrasound-based visualization and navigation

The amount of image data available for any given patient is increasing and may include pre-operative structural data such as CT and MRI (T1, T2, FLAIR, MR angiography etc.), pre-operative mapping of important gray (fMRI) and white matter (DTI), functional data from PET, intra-operative 3D ultrasound (B-mode and Doppler) in addition to images from microscopes, endoscopes and laparoscopes. All these sources of information are not equally important at all times during the procedure, and a selection of data has to be made in order to present only those images that are relevant for the surgeon at that particular point in time.

There are various ways to classify the different visualization techniques that exist. For medical visualization of 3D data from modalities like CT, MRI and US, it is common to refer to three approaches:

- *Slicing*: Slicing means extracting a 2D plane from the 3D data and can further be classified according to how the 2D slice data are generated and how this information is displayed. The sequence of slices acquired by the modality and used to generate a regular image volume is often referred to as the raw or natural slices. From the reconstructed volume we can extract both orthogonal (figure 18A) and oblique (figure 18B) slices. Orthogonal slicing is often used in systems for pre- and postoperative visualization, as well as in intraoperative

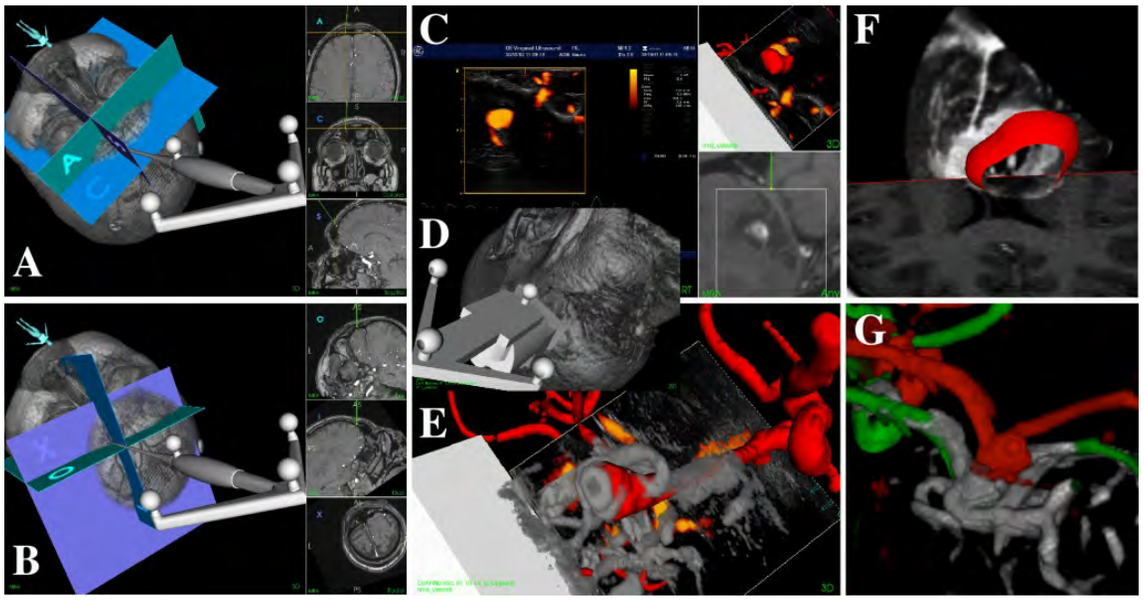

Figure 18. Multimodal visualization. Orthogonal (A) and oblique (B) slicing, the position as well as the position and the orientation of the tool are used to extract the slices respectively. The three basic visualization types are shown in each image. The head is volume rendered in a 3D view that also shows geometric representations of both the tool and slice indicators. Corresponding slices are shown in a 2D view at the right. C) Display during freehand 3D ultrasound acquisition: Real-time 2D ultrasound to the left and an indication of the us-scanplane relative to MR data in a 3D and 2D view to the top and bottom right respectively. D) Overview of probe relative to head. E) Detailed view of real-time 2D ultrasound relative to MRA (read) and 3D power Doppler data (gray). F) Slice from ultrasound (top part) and MR (bottom part), surface model in red from MR (middle part). Mismatch between US (slice) and MR (tumor model) is clearly visible. G) 3D ultrasound (gray) is used to correct MRA (moved from red to green position) during an aneurysm operation.

navigation systems, where the tip of the tracked instrument determines the three extracted slices. The slices can also be orthogonal relative to the tracked instrument or the surgeon's view (i.e., oblique slicing relative to the volume axis or patient), and this is becoming an increasingly popular option in navigation systems. When a surgical tool cuts through multiple volumes several slices are generated. These slices can then be combined in different ways using various overlay and fusion techniques.

- *Direct volume rendering*: Volume- and geometric rendering techniques are not easily distinguished. Often the two approaches can produce similar results, and in some cases one approach may be considered both a volume rendering and a geometric rendering technique. Still, the term volume rendering is used to describe a direct rendering process applied to 3D data where information exists throughout a 3D space instead of simply on 2D surfaces defined in (and often extracted from) such a 3D space. The two most common approaches to volume rendering are volumetric ray casting and 2D/3D texture mapping (figure 17 A, B, D, E, G). In ray casting, each pixel in the image is determined by sending a ray into the volume and evaluating the voxel data encountered along the ray using a specified ray function (maximum, isovalue, compositing). Using 2D texture mapping, polygons are generated along the axis of the volume that is most closely aligned with the viewing direction. The data is then mapped onto these quads and projected into a picture using standard graphics hardware.

- *Geometric surface rendering*: The technique used to render the texture-mapped quads is essentially the same technique that is used to render geometric surface representations of relevant structures (figure 17 A-F). However, the geometric representations must first be extracted from the image information. While it is possible in some cases to extract a structure and generate a 3D model of it by directly using an isosurface extraction algorithm [96], the generation of an accurate geometric model from medical data often requires a segmentation step first. The most common surface representation is to use a lot of simple geometric primitives (e.g., triangles), though other possibilities exist. Furthermore, the surfaces can be made transparent so that it's possible to see what's beneath the structure.

The challenge is to combine the available data and visualization methods to present an optimal integrated multimodal scene that shows only the relevant information at any given time to the surgeon. Multimodal visualization and various image fusion techniques can be very beneficial when trying to take advantage of the best features in each modality. It is easier to perceive an integration of two or more volumes in the same scene than to mentally fuse the same volumes when presented in separate display windows. This also offers an opportunity to pick relevant and necessary information from the most appropriate of the available datasets. Ideally, relevant information should include not only anatomical structures for reference and pathological structures to be targeted, but also important structures to be avoided. Finally, augmented reality techniques can be used to mix the virtual representation of the patient provided by 3D medical data and models extracted from these and the real representation provided by a microscope or a laparoscope for example, giving an even more realistic picture of the treatment delivered through small incisions in minimally invasive procedures.

6. Ultrasound-based navigation accuracy

The delicacy, precision and extent of the work the surgeon can perform based on image information rely on his/her confidence in the overall clinical accuracy and the anatomical or pathological representation. The overall clinical accuracy in image-guided surgery is the difference between the location of a surgical tool relative to some structure as indicated in the image information, and the location relative to the same structure in the patient. This accuracy is difficult to assess in a clinical setting due to the lack of fixed and well-defined landmarks inside the patient that can be accurately reached with a pointer. Common practice is therefore to estimate the system's overall accuracy in a controlled laboratory setting using precisely built phantoms. In order to conclude on the potential clinical accuracy, the differences between the clinical and the laboratory settings must be carefully examined.

6.1. Error sources and key points

A comprehensive analysis of the error sources involved in neuronavigation based on intraoperative ultrasound as well as preoperative MRI can be found in Lindseth et al. [97]. The overall accuracy is often referred to as the Navigation System Accuracy (NSA) and the essential points to remember can be summarized like this:

- The accuracy associated with navigation based on pre.op. MR/CT is independent of the accuracy associated with navigation based on intraoperative ultrasound, and vice versa.
- The main error sources associated with preoperative MR/CT-based navigation are related to the patient registration process in a clinical setting, and the fact that the image maps are not updated to reflect the changing patient terrain as surgery proceeds.
- In contrast, intraoperative ultrasound volumes are acquired in the same coordinate system as navigation is performed. Patient registration is therefore not necessary, and a new ultrasound volume can be acquired to reflect the current patient anatomy whenever needed. However, navigation based on ultrasound is associated with its own error chain. The main error source in this chain is the ultrasound probe calibration process. In addition, small variations in the speed of sound in different tissue types are a potential problem [97].

These points have major implications for the rational behind testing a navigation system in the lab using a phantom, and make a statement about the interesting parameter to the surgeon: the overall clinical navigation system accuracy. A lab test of a system based on preoperative MR/CT using a rigid phantom will give a very good navigation system accuracy (NSA<0.5mm, se figure 19, red line). Such a test will have limited validity in the general clinical situation, but is important to make sure that the system works as expected. The next phase in the evaluation of such a system would be to conduct a clinical study to investigate the system's ability to deal with a variety of different patient registration problems. Documenting that the system performs well in the rigid case and can deal in a satisfactory way with difficult patient registration cases is the best a system vendor can do. This does not give any information about the NSA experienced during a clinical case though. The surgeon must verify that the accuracy is acceptable after he has performed the patient registration procedure and anatomical landmarks inside the patient must be used to gain an impression about the amount of tissue shift and deformation. This shift and deformation makes systems based on preoperative MR/CT of limited use during the procedure.

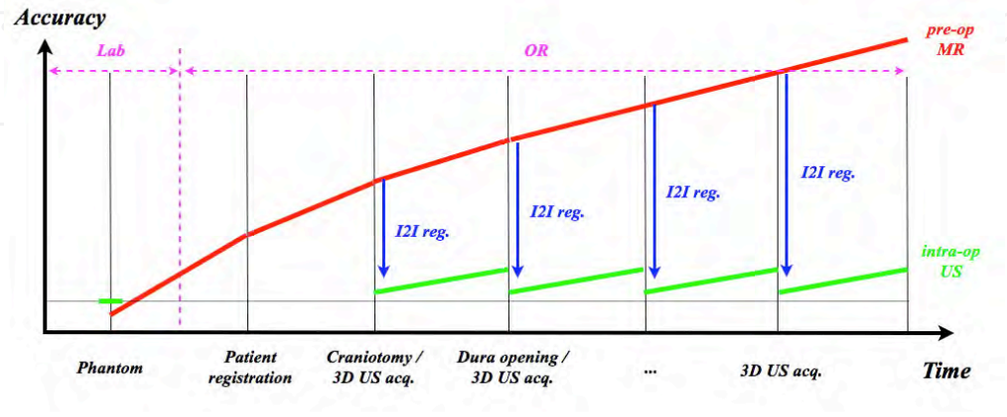

Figure 19. Navigation System Accuracy (NSA) based on preoperative (p) MR (red line) and intraoperative (i) US (green line). iUS can be used to correct pMR using various image-to-image registration techniques (blue line).

In contrast, probe calibration, the major error source associated with ultrasound-based navigation, is included in the NSA resulting from accuracy evaluations using a rigid phantom in a laboratory setting. Furthermore, the surgeon is in control of the amount of tissue shift and deformation that is acceptable in a particular clinical case. A new scan can be acquired whenever needed in order to navigate using an updated image map (se figure 19, green line). As a consequence, the NSA found in a controlled laboratory setting will also be valid in the clinical case given that navigation is based on a recently acquired ultrasound scan (real-time 3D ultrasound being the extreme case) and that the speed of sound used in the ultrasound scanner corresponds to the average speed of sound in the tissue.

A common mistake is to interpret a mismatch between MR/CT and Ultrasound in corresponding or fused displays as tissue shift. An observed mismatch between MR/CT and Ultrasound can only be interpreted as brain shift if 1a) navigation based on pre.op. data is accurate in the rigid case, 1b) the NSA, after the patient registration process, has been verified to be low, 2a) the NSA of ultrasound-based navigation in a controlled setting is low and 2b) the ultrasound data shown originate from an ultrasound volume that has recently been acquired.

Preoperative MR/CT data can be "corrected" for brain shift using intraoperative ultrasound and advanced image-to-image registration techniques [85] as can be seen in figure 19. However this is a challenging task introducing additional error sources. Therefore the NSA associated with corrected preoperative MR/CT will not be as good as the NSA for ultrasound (see figure 19, blue lines). In addition, the independence between the NSA based on MR/CT and Ultrasound will be broken (NSA for MR/CT will be dependent on NSA for Ultrasound).

The overall clinical accuracy of a navigation system will be determined by the contribution from all the individual error sources involved [97]. The net effect will not be the sum of all the error sources, but rather a stochastic contribution from all the terms. Stochastically independent contributions are summed using the following equation: $\sqrt{\sum (...)^2}$

6.2. Clinical navigation system accuracy

As stated previously, the most important parameter for the surgeon is the overall clinical Navigation System Accuracy (NSA). Although this parameter is difficult to assess, we believe that for ultrasound-based navigation an estimate can be made, based on a comprehensive laboratory evaluation and a thorough understanding of the significant additional error sources that occur in the clinical setting. Table 1 summarizes how such a calculation can be carried out assuming that a comprehensive evaluation of the system gives a NSA below 1.4 mm in a controlled laboratory setting. The error sources are assumed to be stochastically independent so that their contributions can be added on a sum-of-squares basis.

NSA using a phantom in the lab	< 1.4 mm
+ Calibration and position tracking of rigid surgical tool	< 0.5 mm
+ Interpolation of a 2D slice from a 3D volume / tool cross indication	< 0.1 mm

= Overall NSA	< 1.5 mm
+ Sound speed uncertainty	0 – 2.0 mm
+ Brain shift	0 – 10.0 mm
= Overall clinical NSA	1.5 – 10.5 mm

Table 1. Overall clinical NSA estimates

As can be seen from table 1 it is possible to achieve an overall clinical NSA close to the NSA found in the laboratory under favorable conditions, i.e., when the speed of sound used in the scanner is close to the average speed of sound in the tissue imaged, and the ultrasound volumes are frequently updated. The need for updates can be determined by real-time 2D imaging. If these conditions are not met, the accuracy becomes poorer.

6.3. Method for assessing ultrasound-based navigation accuracy

As we have seen the ultrasound-based NSA found in the lab using a phantom is valid in the OR (Operating Room) as well, under normal conditions. This makes it very interesting to develop a method that can measure the NSA automatically. We have previously suggested a method based on a phantom with 27 wire crosses and correlating an ultrasound sub-image of each cross to a synthetic template of the cross [98], and the method has been used in a thorough accuracy evaluation of a commercial navigation system [97]. We have since that developed a method that seems to be even more robust, in addition to being more flexible and more convenient to integrate in a navigation system (see figure 20). The method can be used for substantially different ultrasound probes and the phantom is easier to build and to measure accurately. The technique is based on sweeping over the single wire cross with the ultrasound probe, reconstruct all the frames into a volume containing the cross, segment and extract the centerline of the cross and register it to a centerline representation of the accurately measured physical cross, acting as a gold standard, using a modified version of the ICP algorithm [86].

7. Ultrasound-based guidance of minimally invasive procedures

While the main focus of this chapter will be navigation and image guidance using 3D ultrasound images, conventional 2D ultrasound is used for guidance in a variety of clinical applications. The simplest form of ultrasound guidance is placement of a needle inside a target using freehand 2D ultrasound imaging. First, the operator has to localize the target using ultrasound imaging, and second place the needle inside the target while keeping the needle tip in the image plane in order to verify its position. This technique requires a skilled and experienced operator due to the difficulty in keeping the needle in the image plane and the fact that the ultrasound image is not oriented relative to the patient. Despite the difficulties, this technique has been used for biopsies of the liver [99-101], lung [102] and prostate [103], placement of central vein catheters [104, 105] and for brain operations [106].

http://dx.doi.org/10.5772/55884

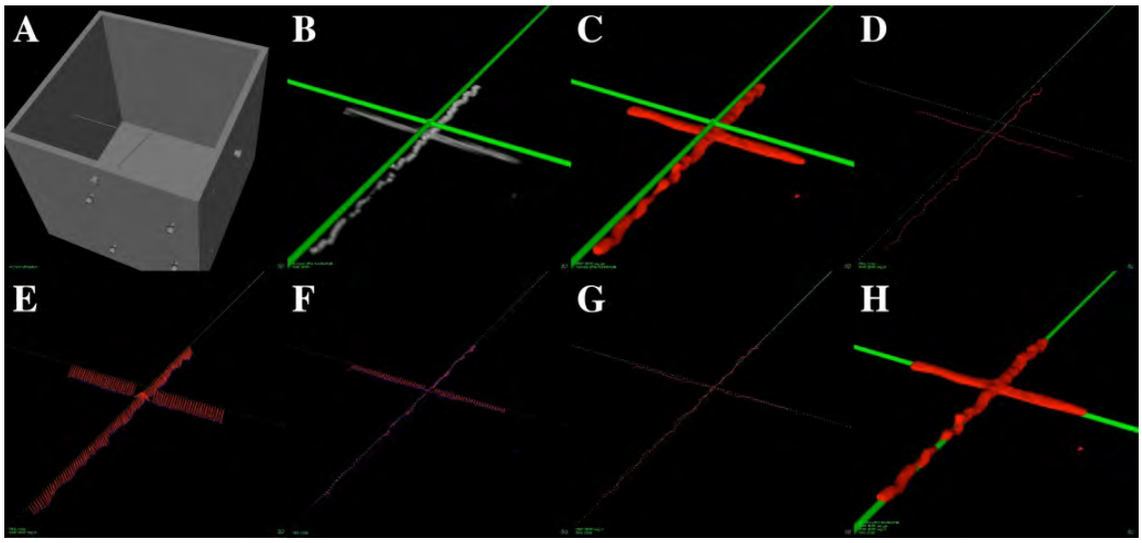

Figure 20. Automatic method for evaluating the accuracy in ultrasound-based navigation. A) The phantom with a single wire cross in the middle of the water tank and a reference frame in the front. B) Physical wire cross in green and an ultrasound volume of the wire cross in gray. C) The ultrasound data is segmented (red) and a small mismatch to the gold standard in green can be observed, i.e. small inaccuracies exist. D) Centerlines of the green and red wire crosses. E) Iterative closest point (ICP) registration between the two centerlines, initial correspondence shown. F) After some iterations. Final results showing the centerlines (G) and the wire crosses (H). The displacement is equal to the NSA.

A slightly more advanced technique for 2D ultrasound guidance includes a needle guide mounted on the ultrasound probe. The guide will ensure that the needle tip is in the image plane at a given depth depending of the ultrasound image sector and the angle of the needle guide. The angle of the needle guide has to be adapted to the depth of the target. Even though this system provides assistance in keeping the needle in the image plane, the operator has to do imaging and puncturing at the same time. In addition, the orientation issues concerning the ultrasound image relative to the patient is not solved and the anatomical overview is restricted to the current real time 2D image. However, the method is fast, does not require specialized equipment or complicated logistics, and provides sufficient guidance for a number of applications such as biopsy of thyroid nodules [107], placement of ventricular catheters in the brain [108, 109] and amniocentesis [110].

7.1. Ultrasound-based navigation in neurosurgery

Neuronavigation is the term used to describe the use of computer-assisted methods to guide or navigate instruments within the confinements of the scull (or spinal column) during surgery. A neuronavigation system should ideally provide high navigation accuracy throughout the surgical procedure. However, the anatomy of the brain is known to shift position after opening of the skull and dura due to drainage of cerebrospinal fluid (CSF), gravity effects and/or removal of tumor masses or hematomas. This shift in the position of the anatomy is often referred to as *brain shift* and has been shown to occur in the early stage of the surgery with displacement values ranging up to several centimeters [111-113]. The brain shift may therefore significantly impair the accuracy of navigation based on preoperative images as the surgery proceeds. Intraoperative ultrasound imaging provides a solution to the brain shift problem.

Compared to using only preoperative images for guidance, the navigation of instruments based on recently acquired intraoperative images can be performed with higher accuracy and precision [97].

The combined use of ultrasound imaging and navigation technology has been explored since the early 1990ies. The University of Oulu was one of the pioneers and demonstrated the clinical use of a passive mechanical arm-based navigation system, which could display reconstructions of preoperative images (CT/MR) and corresponding real-time intraoperative ultrasound images [114].

By attaching position sensors (also referred to as 3D localizers) on the ultrasound probe it is possible to establish the relative spatial position of the image pixels, and it is possible to reconstruct 2D images into an image volume, hence the term 3D ultrasound. The localizer attached to the probe is usually ultrasonic, electromagnetic or optic, and the two latter options (optic, electromagnetic) are currently the most established in commercial systems. Hata *et al* described in a paper from 1997 the initial clinical experience with a frame- and armless navigation system incorporating an ultrasound scanner and an ultrasound probe equipped with an ultrasonic positioning sensor [115]. In 1998 Jödicke *et al* presented a system for detection of brain shift, by comparing preoperative MR images and intraoperative 3D ultrasound [116]. The integration of ultrasound and navigation technology was also explored in Trondheim, Norway, and a system with the feasibility of 3D ultrasound and navigation guidance was developed. Using this system Unsgaard et al. performed the first brain tumour operation with 3D ultrasound guidance in 1996, and the system development and clinical experience was described in several papers [117-119]. The technology was further developed and commercialized by the company Sonowand AS (Trondheim, Norway), which is a spin-off company from the research activities of the National Centre for 3D Ultrasound in Neurosurgery (1995-present (2013)) at St. Olavs University Hospital. The technology has been explored for use in several neurosurgical procedures, but its predominant use is within resection of brain tumours [120]. The Sonowand system allows navigation of pre-calibrated tools equipped with an optic localizer, and it allows tools like biopsy forceps to be calibrated to the navigation system *in situ* in the operating room (figure 21) and used for image guided biopsies. The system facilitates simultaneous displays of reformatted image slices of intraoperative ultrasound and any preoperative MR series like T1, T2, FLAIR, etc. that has been registered to the patient. The position of navigated instruments is indicated in the displayed image slices.

7.1.1. 3D Ultrasound in intracranial tumour surgery

Intracranial tumours include primary and secondary tumours in the brain, pituitary gland, and meninges. Primary tumours are neoplasms originating from supportive tissue in the brain, from meninges, or from pituitary tissue. Secondary brain tumours are metastases of malignant cells that originate from a primary tumour situated in another organ of the body that spreads with the blood flow to the brain. Surgery is the primary treatment for most intracranial tumours. The patient's prognosis is in most cases related to the degree of resection of tumour. The surgical goal is usually to perform a total extirpation of the tumour, but without damaging

http://dx.doi.org/10.5772/55884

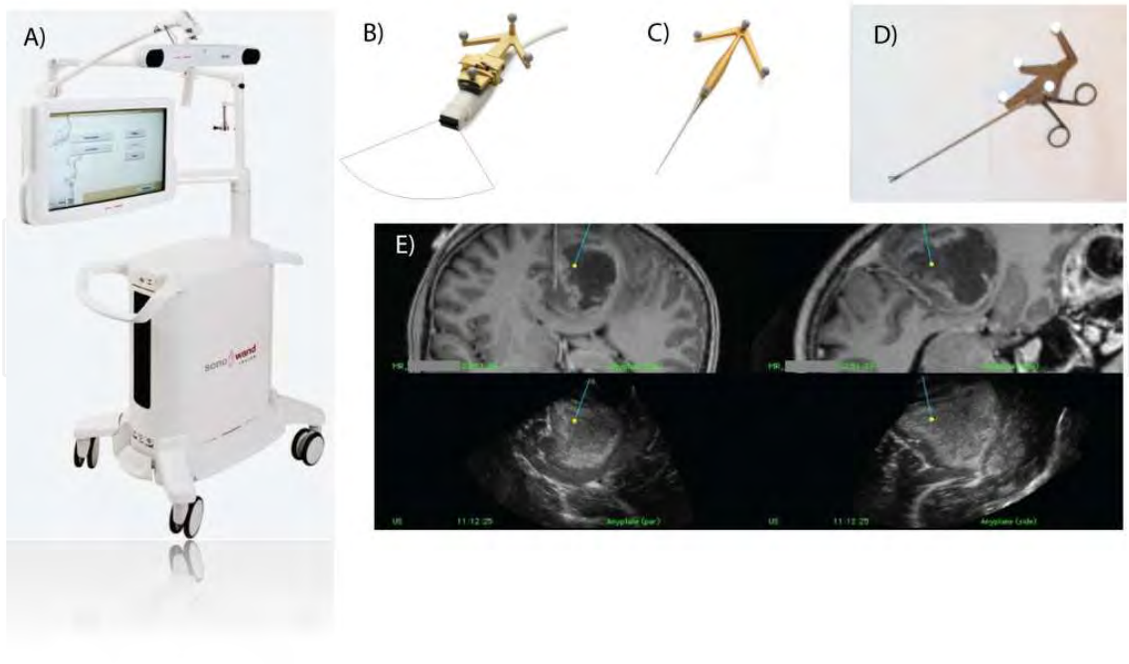

Figure 21. The Sonowand Invite® system for intraoperative ultrasound imaging and navigation (A), various tools of the navigation system equipped with optical localizer units showing one phased array ultrasound probe (B), a navigation pointer (C), a biopsy forceps (D), and a screen dump of the navigation display showing reformatted MR images in top row, and corresponding reformatted ultrasound images in bottom row (E). The tip of the navigated instrument is indicated with a bright spot in the reformatted image slices

adjacent normal brain tissue. If the tumour is located in so-called eloquent regions, harboring important functional tissue for movement, speech or vision, less extensive resections is often the result. Brain tumour surgery can therefore be a delicate balance between obtaining extensive resections and avoiding functional deficits and loss of quality of life due to the surgical trauma.

3D ultrasound is an established technique for intraoperative imaging in surgery of brain tumours, and is used for localization of the tumour and for resection control. The first acquisition of 3D ultrasound images is usually performed after opening the bone (craniotomy), but before opening the dura. Several ultrasound volumes (typically 3 to 6) are acquired during the operation to compensate for brain shift and to monitor the progress of tumour removal (figure 22).

Preoperative MR data can be displayed along with one or several ultrasound image volumes acquired at different stages of surgery. It may also be possible to import functional MR images to the navigation system. One way of doing this is to import anatomical MR images (e.g. T1/T2/FLAIR) with bold fMRI enhancements and DTI tractography overlaid as contours on the anatomical images [121-123], as shown in figure 23. The navigation system may therefore provide multimodal visualization of medical images, incorporating functional and anatomical information.

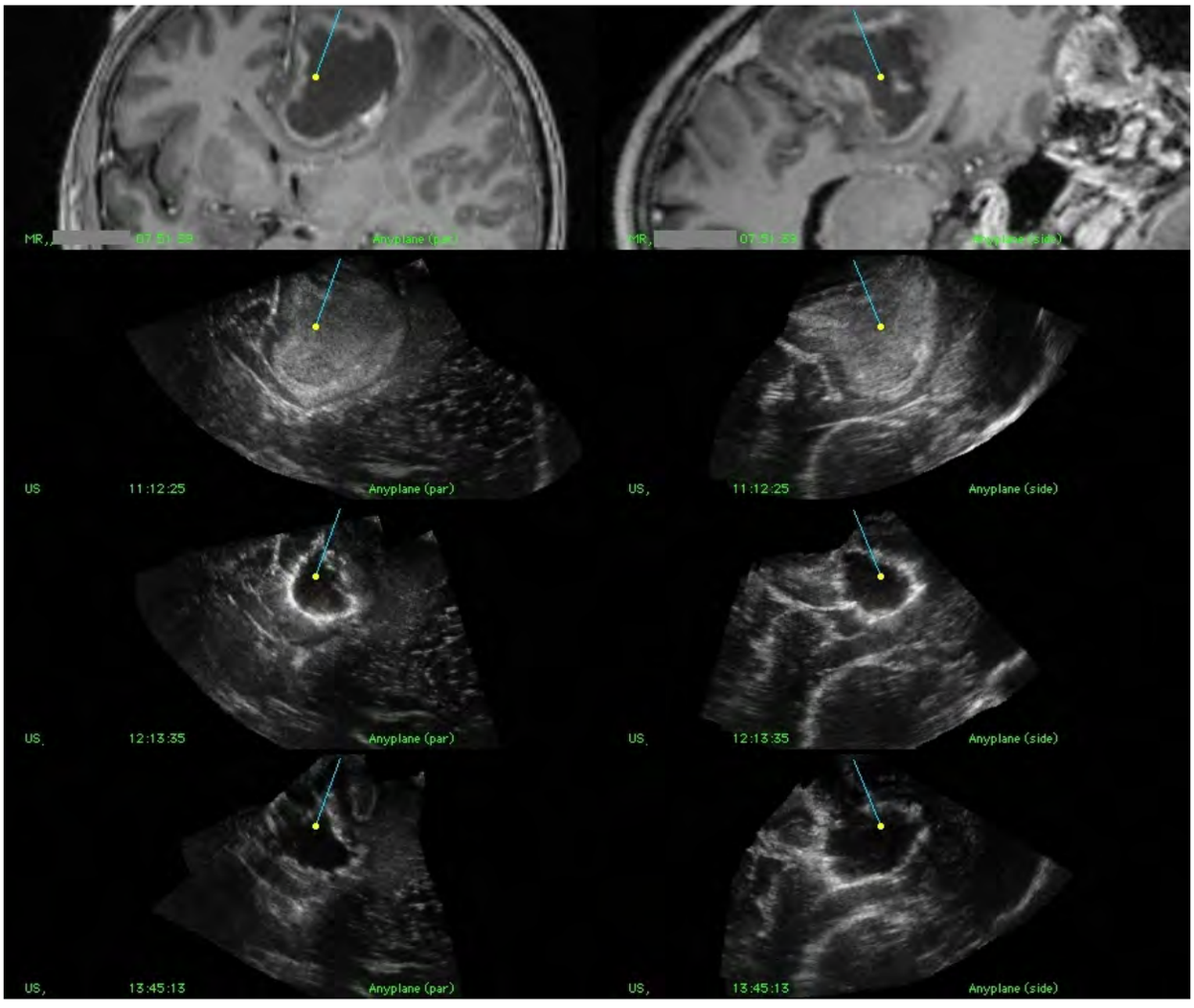

Figure 22. Navigation display showing two perpendicular reformatted image slices from each image volume. Preoperative MR slices in top row followed by slices from 3 different ultrasound volumes acquired at different stages in the operation. The ultrasound volumes in row 2, 3, and 4 were acquired prior to the resection, during the resection with some tumor tissue remaining, and after the end of the resection, respectively

Clinically, modern image technology has enabled more targeted surgical approaches, as compared to standardized explorative brain dissections that were more common two decades ago. This reduces the surgical trauma, eases anatomical orientation within the surgical field, and makes it possible for less experienced surgeons to obtain the same results as their more experienced peers. Today, even in eloquent regions where surgery is associated with increased risk, good clinical results can be obtained [121]. We have also observed that survival increased after the introduction of 3D ultrasound imaging in malignant primary brain tumour surgery [124]. Intraoperative imaging with ultrasound has also enabled more aggressive treatment strategies in tumours that microscopically resemble the brain tissue and therefore are difficult to remove with sufficient accuracy. This has improved survival without compromising risks [125]. Tailored probes designed for special surgical procedures such as the transphenoidal approach [126] through the nose can guide operations in narrow approaches with limited abilities for direct visualization. With further developments in ultrasound technology, clinical results can continue

http://dx.doi.org/10.5772/55884

to improve since good ultrasound image quality has direct consequences for the obtained clinical results, both in terms of resection grades [127] and for patient's quality of life [128].

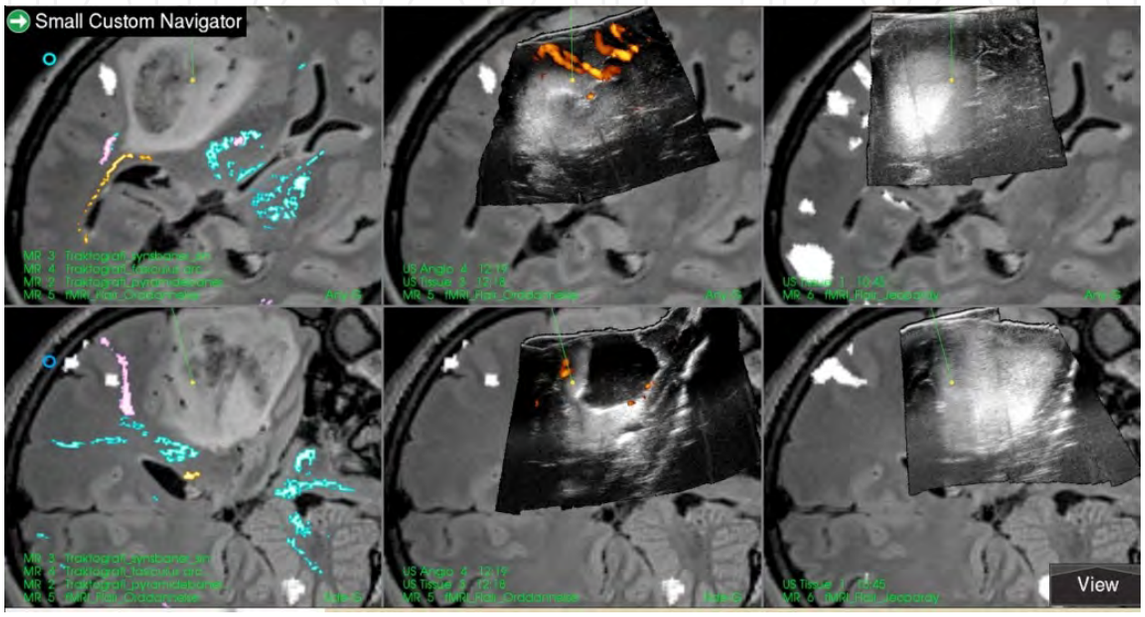

Figure 23. Example of multimodal visualization in navigation display. Left column shows anatomical MR image slices (FLAIR) with functional data shown as color overlay. The white spots indicate language area, the turquoise contours represent the pyramidal tract, the pink represent fasiculus arcuate (tract between language areas), the yellow represents the optic tract. Middle column shows preoperative MR image slices with intraoperative ultrasound acquired after some resection as overlay. Right column is identical as the middle, but with ultrasound data acquired prior to the start of the resection.

7.1.2. 3D Ultrasound in intracranial vascular surgery

It's also possible to acquire power Doppler based 3D ultrasound data of the vascular tree in the target area. This can be useful in both tumor and vascular surgery. In tumor operations the objective is to avoid injury to the vessels caused by the surgical instruments. In vascular surgery power Doppler can be useful in surgical treatment of both aneurysms (figure 18G) and arteriovenous malformations (AVMs, figure 15). For surgical treatment of aneurysms this mode is most useful for evaluating the flow in distal vessels after clipping of the aneurysm. In addition, 3D power Doppler can be used to localize peripheral aneurysms and guide direct surgical approaches. For AVM surgery intra-operative 3D power Doppler has been found to be useful in localizing deep-seated AVMs, identifying feeders and draining veins and for resection control [129]. Navigated display of 3D power Doppler based data can be used to identify and clip the larger feeders of AVMs in the initial phase of the operation, thus making it easier to perform the extirpation of the AVM.

Power Doppler based 3D ultrasound data are usually displayed in reddish color superimposed on the B-mode ultrasound slices, but the vessels are usually shown in a more optimal way using 3D rendering techniques. The power Doppler signal is often too intense and smeared out to give a sharp delineation of the small vessels. Robust acquisition of power Doppler based 3D ultrasound data of sufficient quality is essential for vessel-based shift correction and it's important to increase the spatial resolution of such data in the coming years.

7.2. Ultrasound-based navigation in laparoscopic surgery

Open surgery is the gold standard for abdominal surgeries. But over the last few decades, there has been an increasing demand to shift from open surgery to a minimally invasive approach to make the intervention and the post-operative phase less traumatizing for the patient. Advantages of laparoscopic surgery include decreased morbidity, reduced costs for society (less hospital time and quicker recovery), and also improved long-term outcomes when compared to open surgery. During laparoscopy, the surgeons make use of a video camera for instrument guidance. However, the video laparoscope can only provide two-dimensional (2D) surface visualization of the abdominal cavity. Laparoscopic ultrasound (LUS) provides information beyond the surface of the organs, and was therefore introduced by Yamakawa and coworkers in 1958 [130]. In 1991, Jakimowicz and Reuers introduced LUS scanning for examination of the biliary tree during laparoscopic cholecystectomy [131]. It seemed that LUS gave valuable information and has since expanded in use with the increase in laparoscopic procedures. LUS is today applied in laparoscopy in numerous ways for screening, diagnostics and therapeutic purposes [132, 133]. Some examples of use are screening, like stone detection or identification of lymph nodes, diagnostics, like staging of disease or assessment of operability and resection range, and therapeutic, like resection guidance or guidance of radio frequency and cryoablation. Harms and coworkers were the first to integrate an electromagnetic (EM) tracking sensor into the tip of a conventional laparoscopic ultrasound probe [134] and this made it possible to combine LUS with navigation technology, solving some of the orientation problems experienced when using laparoscopic ultrasound. The combination of navigation technology and LUS is becoming an active field of research to further improve the safety, accuracy, and outcome of laparoscopic surgery.

Navigation, as explained earlier, is the combined use of tracking and imaging technology to provide a visualization of the position of the tip of a surgical instrument relative to a target and surrounding anatomy. Various display and visualizations methods of both instruments and the medical images can be used in laparoscopic surgery. Preoperative images are useful for planning as well as for guidance during the initial phase of the procedure as long as the target area is in the retroperitoneum [135]. When preoperative images are registered to the patient, the surgeon is able to use navigation to plan the surgical pathway from the tip of the instrument to the target site inside the patient. Thus, navigation provides the intuitive correspondence between the patient (physical space), the images (image space that represent the patient) and the tracked surgical instruments. However, when the surgical procedure starts, tissue will shift and deform and preoperative data will no longer represent the true patient anatomy. LUS then makes it possible to update the map for guidance and acquire image

http://dx.doi.org/10.5772/55884

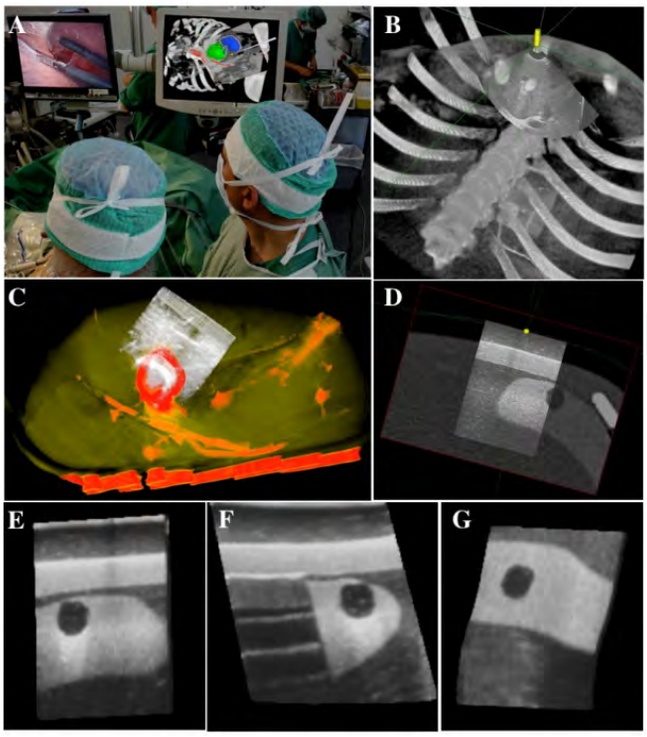

Figure 24. Illustration of visualization methods for navigation in laparoscopy. A) Navigation during adrenalectomy using preoperative CT (3D and 2D). B) Live animal model (pig) experiment showing navigated LUS combined with preoperative images (CT volume rendering). This solves the orientation problems and improves overview. C) Multimodal display of 3D LUS (volume rendering) and 3D CT from an ex vivo experiment showing that the tumor position has changed. D) Anyplane slicing from CT controlled by the LUS probe and overlaying the LUS onto the corresponding CT slice (phantom). E-G) Orthogonal slices from a 3D LUS scan (phantom).

data that display the true patient anatomy during surgery. Preoperative CT images will, however, still be useful for reference and overview as illustrated in figure 24, showing various display possibilities using LUS and navigation in laparoscopy. An example of simple overlay of tracked surgical tools onto a 3D volume rendering of computerized tomography (CT) images is shown in figure 24A. In this figure, we used the preoperative 3D CT images for initial in-the-OR planning of the procedure. The view direction of the volume was set by the view direction of the laparoscope. The LUS image could be displayed in the same scene, with an indication of the probe position in yellow. Furthermore, when 3D preoperative images are displayed together with 3D LUS, anatomic shifts can easily be visualized and measured, thereby providing updated information of the true patient anatomy to the surgical team as illustrated in figure 24C. This may improve the accuracy and precision of the procedure. Additionally, the tracked position of the LUS probe can be used to display the corresponding slice from a preoperative CT volume, providing improved overview of the position of the LUS image as shown in figure 24D. Having 3D LUS available, it is possible to display these data the same way as traditional orthogonal display of MR and CT volumes, as shown in figure 24E-G. Intraoperative augmented reality visualizations in combination with navigation technology could be valuable for the surgeons [136]. A possible future development, useful

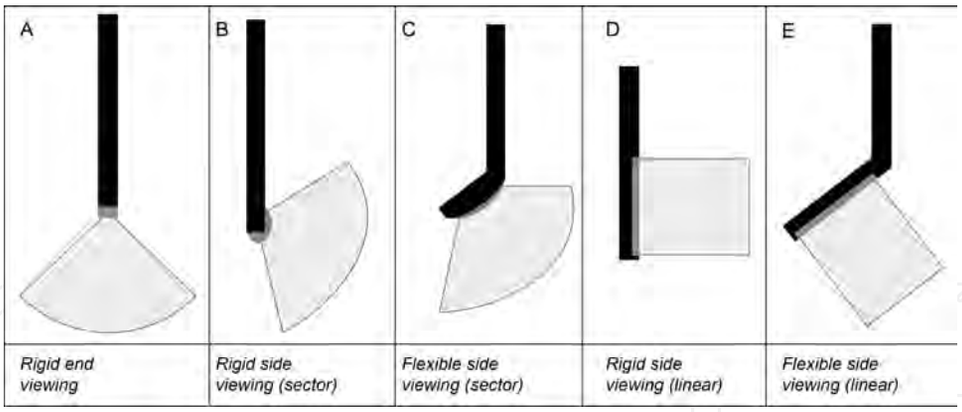

Figure 25. Different LUS probes.

for spotting the true position of lesions and vessels and hence detect anatomic shifts quickly, would be to introduce LUS data into such a multimodal display.

Intraoperative ultrasound systems are inexpensive, compact, mobile, and have no requirements for special facilities in the operating room (OR) compared to MRI or CT. Ultrasound image quality is continuously improving and for certain cases (e.g. liver) LUS could obtain image quality comparable to what is achieved in neurosurgery, as the probe is placed directly on the surface of the organ. In neurosurgery, the image quality of ultrasound has been demonstrated above. The most common LUS probe is a flexible 2- or 4-way array, linear or curved, with a frequency range of 5-10 MHz. Typical imaging depths are in the range 0-10 cm, but with 5MHz deeper imaging can be performed. The LUS transducers usually have a footprint of less than 10 mm wide to fit through trocars and 20-50 mm long. They can be manipulated at the shaft allowing real time images at user-controlled orientations and positions, depending only on the specific probe configuration. Figure 25 shows various configurations of LUS probes, while Table 2 provides an overview of currently available probes. Most LUS probes [137] can be sterilized [138].

Vendor	Probe	Frequency	Type of probe (see Fig. 2)	Transducer length, scan angle, other
Aloka	UST-52109	3-7.5 MHz	A	10 mm, 90°
	UST-5524-LAP	4-10 MHz	E	38 mm
	UST-5526L-7.5	5-10 MHz	D	33 mm
	UST-5536-7.5	5-10 MHz	E	38 mm
BK Medical	8666-RF	5-10 MHz	E	30 mm, Puncture and biopsy guide
Hitachi	EUP OL531	5-10 MHz	C	120°, Biopsy and therapy
Toshiba	PEF 704LA	5, 7.5, 10 MHz	E	34 mm
	PVM 787LA	5, 7.5, 10 MHz	B	85°

http://dx.doi.org/10.5772/55884

Vendor	Probe	Frequency	Type of probe (see Fig. 2)	Transducer length, scan angle, other
Gore	Tetrad VersaPlane	7.5 MHz (center frequency)	E	56 mm
Philips / ATL	LAP L9-5	5-9 MHz	E	NA
Esaote	LP323	4-13 MHz	E	NA

Table 2. LUS probe from various manufacturers. Relevant specifications are also given.

Being a relatively new area of research, it is interesting to note that the number of active research groups in the field of navigated laparoscopic ultrasound is approximately ten. Based on literature and almost two decades working with surgeons on developments for advanced laparoscopic surgery, a complete system designed for navigated LUS could be used according to the following clinical scenario:

- The preoperative data are imported and reconstructed into 3D volumes; several structures and organs are segmented automatically (e.g. vessels from contrast CT scan) or semi-automatically (e.g. seed point set inside the tumor).
- A quick plan is made from the visualization in the navigation system just prior to surgery, perhaps in the OR during other preparations.
- Registration is performed without fiducials using a pointer (orientation of patient) and two landmarks for a rough first approximation.
- Before mobilizing the target organ (e.g. the liver) a 3D LUS scan of major vessels near or around the tumor is performed.
- The LUS images are reconstructed in 3D and an automatic vessel based registration (CT-to-ultrasound) is performed to fine tune the patient registration.
- Augmented reality visualization, e.g. on/off overlay of preoperative data and LUS on the video laparoscope view is preformed as needed by the surgeons during the procedure
- 3D LUS scans are updated a few times during the procedure, while the real time 2D LUS image is available as either:
  - A full size image with a corresponding indication in a 3D CT rendering of its orientation and position, or
  - An overlay on the video laparoscope view with or without elements from the CT data (segmented structures for instance).

For rigid organ navigation, a single preoperative scan, highly accurate tracking (optical), and rigid surgical tools are sufficient to guide the procedure. However, for soft tissue navigation, additional tools are needed due to deformation and mobile organs in the abdominal cavity, resulting in more complex systems and additional devices in the OR. LUS can provide real time behind-the-surface information (tissue, blood flow, elasticity). When combined with

advanced visualization techniques and preoperative images, LUS can enhance an augmented reality scene to include updated images of details, important for high precision surgery thus enhancing the perception for surgeons during minimal access therapy. LUS integrated with miniaturized tracking technology is likely to play an important role in guiding future laparoscopic surgery.

7.3. Other applications

One of the first, and still one of the most important applications of ultrasound imaging is in diagnostics of various heart conditions. The dynamic real-time imaging makes ultrasound the modality of choice for characterization of a moving organ such as the heart. Some examples of the use of echocardiography are evaluation of cardiovascular anomalies in fetuses and newborns [139], assessment of aortic stenosis [140], evaluation of the function of the valves and examination of the flow and function after heart attacks. These examples are purely diagnostic applications without any kind of intervention associated, but ultrasound has also been used for guidance in cardiac surgery. One example was presented by Wang et al. [141]. They evaluated 129 patients who underwent robotic cardiac surgery. Transesophageal echocardiography was used for guidance of the cannula for peripheral cardiopulmonary bypass. Ultrasound imaging can potentially also be used for guidance in minimally invasive mitral valve repair on the beating heart [123].

Intra-operative guidance during endovascular procedures is usually performed with x-ray fluoroscopy. However, some investigators have reported the use of transabdominal ultrasound for guidance. Lie et al. [142] studied the use of 2D transabdominal ultrasound during endovascular procedures. They found that ultrasound could be useful for guiding the insertion of guidewires, and control the wire position before connecting the second graft limb to the main limb of bifurcated grafts. Kaspersen et al. [143] reported a feasibility study registering ultrasound to pre-operatve CT data. This may be useful for updating the CT data used for navigation and correct for breathing motion and deformation of the blood vessels during the procedure. With recent advances in ultrasound technology, we believe that real-time 3D ultrasound have potential for further advancing the accuracy in the insertion of stentgrafts, and in particular the placement of fenestrated stentgrafts. Specifically, it is easier to track the tip of guidewires in three dimensions, while simultaneously visualizing a focused area of the 3D anatomy in real-time. A systematic review by Malkawi et al [144] concluded that percutaneous endovascular repair was associated with fewer access related complications and reduced operative time. In a study by Arthurs et al [145], it was shown that use of ultrasound guided access significantly reduced access-related complications compared to percutanous access without ultrasound guidance. Successful ultrasound guidance in secondary interventions, for sealing endoleak after endovascular repair, has also been reported. Boks et al. [146] described transabdominal embolization using duplex ultrasound guidance, and Kasthuri et al. [147] used ultrasound for guiding percutaneous thrombin injection. Navigation of stentgrafts during endovascular procedures has also been demonstrated in patients using CT imaging [148]. However, 3D or 4D ultrasound integrated with navigation technology for guidance of endovascular procedures has not yet been demonstrated in patients.

http://dx.doi.org/10.5772/55884

3D ultrasound has also been used to guide surgery of the spine. Kolstad et al [149] reported in 2006 a study, where spinal cord tumors were visualized using ultrasound imaging, and 3D ultrasound-guided tumor resection were performed using navigation technology. The technical application of integrating ultrasound and navigation seems feasible since it solves the orientation problem with conventional 2D ultrasound and may have the potential of improving functional outcome of spinal cord tumor surgery.

8. Ultrasound and non-invasive therapy

8.1. High Intensity Focused Ultrasound (HIFU)

High-intensity focused ultrasound (HIFU or FUS) has been known and developed for decades and can be applied to produce sharply delineated lesions in biological tissue (figure 26) [150-153]. The development of magnetic resonance (MR) thermometry enabled the thermal ablation progress to be monitored during sonication [154]. MR-guided HIFU (MRgFUS) has been approved by the FDA for the symptomatic treatment of uterine fibroids since 2004 [155]; clinical trials have been reported for breast [156, 157] and brain [158, 159] therapy, as well as pain palliation in bone [160, 161]. The MRgFUS treatment of abdominal organs, such as the kidney, pancreas or liver, poses additional technological and clinical challenges. First, for most therapeutic applications within the human body, tissue displacement caused by respiration and/or the cardiac cycle must be considered, and can be assumed to be periodic in anaesthetized patients. However, this may not be the case for free-breathing patients. This movement in addition to drift due to gravity and the intestine and bowel movement is important to account for during sonication in order to achieve accurately located FUS with respect to the target (e.g. tumour in the liver). Secondly, the presence of the rib cage affects the HIFU treatment planning and set-up. The rib cage acts as an aberrator that might affect the focusing [162, 163] and on the other hand, due to the high value of the absorption coefficient of the bone [164], the overheating on the ribs can be quite significant. These two aspects are currently the main challenges in order to achieve MRgFUS in moving abdominal organs.

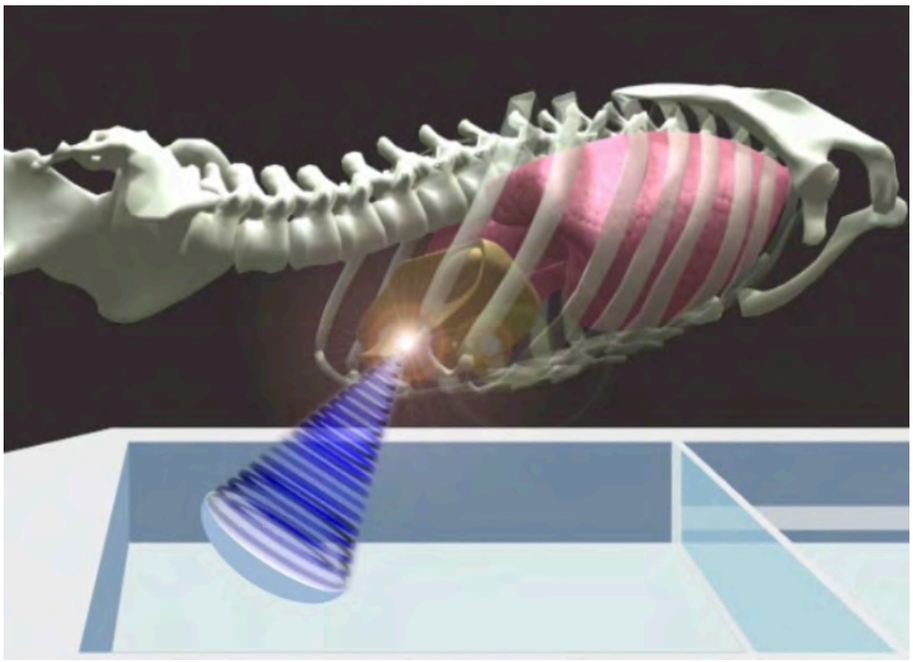

Figure 26. Illustration shows the targeting of a tumor in the liver using high intensity focused ultrasound. Currently, to perform this, the patient has to be anesthetized and breathing must be stopped during sonications. This results in long treatment times. In order to overcome this, emerging technologies in motion tracking (e.g. 4D ultrasound) can be used to track the target over time and at the same time simulate and predict the motion in order to target tumors moving due to free breathing patients.

Ultrasound is an inexpensive, flexible, real-time imaging modality, with high temporal and spatial resolution, i.e. sub-millimeter spatial resolution inplane along the beam direction. However, it provides little contrast between normal tissue and FUS-treated tissue and so far ultrasound-based temperature monitoring has not been validated under a clinical scenario.

Motion of the abdominal organs is an important issue to be accounted for during FUS treatment, but also in other therapies like radiotherapy [165, 166]. The motion estimation is useful in delineating the target and organs at risk and also determining the dosage of treatment during therapeutic irradiation. Several techniques exist and are in development to handle abdominal organ motion during FUS. A straightforward approach is to use respiratory gating. However, respiratory gating generally increases treatment time, which has been demonstrated in controlled apnea on anesthetized pigs [167, 168]. Another approach is to employ repeated breath-holds and breathing feedback to ensure a reproducible liver position [169]. De Senneville and coworkers [170] proposed a system that generates an atlas of motion fields during an initial learning phase based on magnitude data of temperature-sensitive gradient-recalled sequence acquisition. The motion field of the most similar image in the atlas is then used to correct the target position. Under the hypothesis of periodic motion, the focal point position for the next cycle is estimated. The method can only manage liver deformations caused by the periodic breathing cycle and is not capable of handling the non-rigid liver deformations, i.e. drift, caused by intestinal activity (peristalsis) or muscle relaxation [171]. Although it is established that MR imaging can provide motion estimates with a high spatial resolution, it is difficult in practice to acquire online three-dimensional (3D) isotropic images because of

technical limitations, spatial and temporal resolution trade-offs, and low signal-to-noise ratio associated with fast 3D acquisition sequences [172]. In addition, the time duration between the actual target displacement and the availability of the motion information from MR data is not negligible [173]. Hence, MR information-based real-time motion compensation generally compromises spatial resolution, geometric distortion and the precision of the MR thermometry [174], of which the latter is of crucial importance during MRgFUS.

A first attempt at ultrasound-based motion tracking during MRgFUS was reported in phantoms undergoing periodic and rigid motion of small amplitude [173]. Continuous 1D ultrasound echo detection, along a direction parallel to the main axis of motion was used. This setup is not suitable for clinical applications as the external ultrasound imaging probe cannot send beams parallel to the axis of respiratory motion. Moreover, the local motion in the liver is spatially dependent and a 1D projection would not be sufficient. Truly simultaneous ultrasound and MR imaging has only been reported in literature recently [175-178]. Only one of these studies was targeted towards MRgFUS and moving abdominal organs sonication [175]. They demonstrated in moving phantoms the feasibility of ultrasound-based 2D motion-compensated sonications integrated with reference free MR temperature monitoring, using a clinical ultrasound probe and a phased-array HIFU transducer [175]. An overview of our own efforts for motion correction using 4D ultrasound can be found in section 4.3.

8.2. Ultrasound-induced drug delivery

Although diagnostic ultrasound is considered safe with no adverse effects, ultrasound can with high acoustic outputs induce significant bioeffects (e.g. HIFU) and these bioeffects are divided into thermal and mechanical effects. The thermal effect is related to energy absorption in the tissue where part of the mechanical wave energy is converted to thermal energy and hence results in an increase in tissue temperature. The mechanical effects are related to cavitation and to radiation forces. Radiation forces arise when part of the forward propagating wave is back-scattered or absorbed and result in a pushing force on the tissue along the direction of the forward propagating wave. Within fluids, such radiation forces can give rise to acoustic streaming. Cavitation is related to the oscillation and possible collapse of gas nuclei occurring naturally within the body or artificially introduced as contrast agent in the form of microbubbles. Oscillating gas bubbles will generate streaming currents in surrounding liquids and hence shear forces on nearby cells that potentially result in bioeffects. Collapsing gas bubbles can result in high local temperatures, release of free radicals, emitted shock waves and high velocity micro jets piercing into nearby cell membranes.

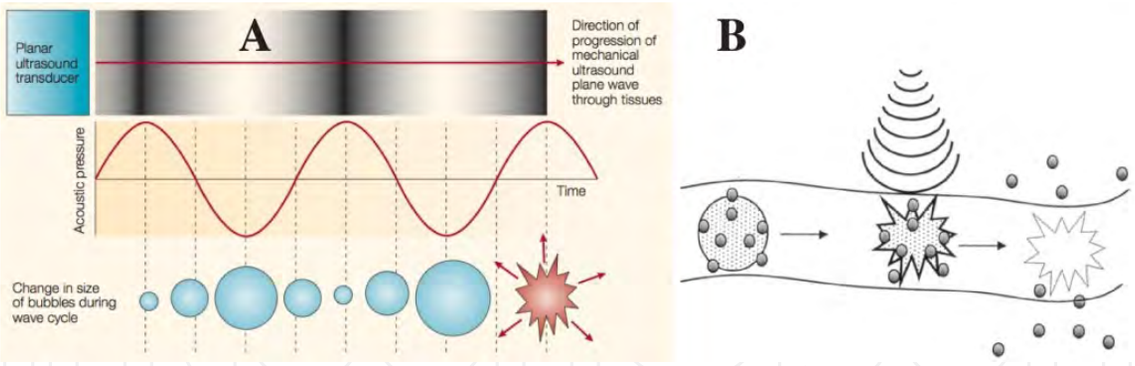

Figure 27. Ultrasound-induced drug delivery. Microbubbles carrying drugs are destructed by ultrasound (A) and the transported substances are released into the surrounding tissue (B).

The indicated bioeffects can be utilized in ultrasound induced drug delivery. The general goal of encapsulated drug delivery and targeting is to improve the efficacy of drugs within the region of diseased tissue while reducing undesired side effects in the healthy tissues. As an example, with non-encapsulated conventional chemotherapy systemic toxicity limits the drug concentration that can be obtained within the tumor and hence the efficacy of the therapy. With focused ultrasound, it is possible to obtain release of encapsulated drugs and this release can be controlled both temporally and spatially.

Ultrasound energy deposition within a localized tissue region provides a potentially efficient way of releasing drugs encapsulated in thermally sensitive carriers [179-181] by inducing a temperature increase and in sonosensitive carriers [182-184] by inducing cavitation (figure 27). The thermal and especially the mechanical cavitation effects of ultrasound also provide ways of perturbing cell membranes and thus increasing their permeability for improved drug delivery. With the introduction of microbubbles administered intraveneously that will serve as cavitation nuclei, the threshold for cavitation is significantly reduced hence facilitating this effect for endothelial cells that are close to the administered microbubbles. This effect of increased cell membrane permeability has been investigated extensively in the brain where the blood-brain barrier acts as an effective barrier for delivery of more than 95% of the drugs that potentially could be interesting for treatment of diseases in the central nervous system [185, 186]. For blood clot dissolution the combined use of ultrasound, microbubbles and thrombolytic agents have been demonstrated in several clinical trials to result in faster clot dissolution without release of large amounts of potentially hazardous clot fragments [187, 188].

9. Conclusions

Ultrasound has been used for many years as a diagnostic and interventional imaging modality, and the use is increasing in a number of different clinical areas. It is often conceded that the image quality of ultrasound is inferior to that attainable with MR or CT, but the rapid development of new ultrasound technology (scanners, transducers, specialized probes, etc.) has

resulted in significantly improved image quality and make ultrasound the modality of choice for several applications. Some of the obvious advantages being real-time imaging even for blood flow, portability, flexibility, safety and low cost. In addition, ultrasound images can be acquired in the coordinate system of a patient when combined with a tracking system without any need for registration. This makes surgical guidance based on intra-operative ultrasound highly accurate. The combination of several image modalities such as MR, CT and ultrasound registered to each other and to the patient make the interpretation of the individual images easier and enables the surgeon to take advantage of the complimentary information contained in each image. In this context, the ultrasound images provide real-time information in the region of interest, while MR and CT provide anatomical overview facilitating the interpretation of the ultrasound data. The use of contrast agents enhance the visualization of vessels and increase the number and types of lesions that can be detected using ultrasound. New technol-ogies such as high-intensity focused ultrasound and the use of microbubbles for targeted drug delivery are examples of non-invasive therapeutic applications where ultrasound will play an increasingly important role in the future.

Author details

1 SINTEF Medical Technology, Norway

2 The Norwegian University of Science and Technology (NTNU), Norway

3 St. Olavs University Hospital, Norway

4 National Centre for Ultrasound and Image Guided Therapy, Norway

References

[1] Mehdizadeh, S., et al., Eigenspace based minimum variance beamforming applied to ultrasound imaging of acoustically hard tissues. IEEE Trans Med Imaging, 2012. 31(10): p. 1912-21.

[2] Mjolstad, O.C., et al., Assessment of left ventricular function by GPs using pocket-sized ultrasound. Fam Pract, 2012. 29(5): p. 534-40.

[3] Hotta, N., et al., Usefulness of Real-Time 4D Ultrasonography during Radiofrequency Ablation in a Case of Hepatocellular Carcinoma. Case Rep Gastroenterol, 2011. 5(1): p. 82-7.

[4] Rønnekleiv, A. Design Modeling of CMUT's for Medical Imaging. in IEEE International Ultrasonics Symposium (IUS). 2009, p. 442-450.

[5] Gierke, H.E., et al., Physics of vibrations in living tissues. J Appl Physiol, 1952. 4(12): p. 886-900.

[6] Dickinson, R.J. and C.R. Hill, Measurement of soft tissue motion using correlation between A-scans. Ultrasound in Medicine and Biology, 1982. 8(3): p. 263-71.

[7] Wilson, L.S. and D.E. Robinson, Ultrasonic measurement of small displacements and deformations of tissue. Ultrason Imaging, 1982. 4(1): p. 71-82.

[8] Lerner, R.M., S.R. Huang, and K.J. Parker, "Sonoelasticity" images derived from ultrasound signals in mechanically vibrated tissues. Ultrasound in Medicine and Biology, 1990. 16(3): p. 231-9.

[9] Ophir, J., et al., Elastography: a quantitative method for imaging the elasticity of biological tissues. Ultrason Imaging, 1991. 13(2): p. 111-34.

[10] Bae, U., et al., Ultrasound thyroid elastography using carotid artery pulsation: preliminary study. J Ultrasound Med, 2007. 26(6): p. 797-805.

[11] Emelianov, S.Y., et al., Elasticity Imaging of the Liver: Is a Hemangioma Hard or Soft? Proceedings of the 1998 IEEE Ultrasonics Symposium, 1998. 7: p. 1749-1752.

[12] Hiltawsky, K.M., et al., Freehand ultrasound elastography of breast lesions: clinical results. Ultrasound in Medicine and Biology, 2001. 27(11): p. 1461-9.

[13] Salomon, G., et al., Evaluation of prostate cancer detection with ultrasound real-time elastography: a comparison with step section pathological analysis after radical prostatectomy. Eur Urol, 2008. 54(6): p. 1354-62.

[14] Selbekk, T., J. Bang, and G. Unsgaard, Strain processing of intraoperative ultrasound images of brain tumours: initial results. Ultrasound in Medicine and Biology, 2005. 31(1): p. 45-51.

[15] Souchon, R., et al., Visualisation of HIFU lesions using elastography of the human prostate in vivo: preliminary results. Ultrasound in Medicine and Biology, 2003. 29(7): p. 1007-15.

[16] Nightingale, K., et al., Acoustic radiation force impulse imaging: in vivo demonstration of clinical feasibility. Ultrasound in Medicine and Biology, 2002. 28(2): p. 227-35.

[17] Gallotti, A., et al., Acoustic Radiation Force Impulse (ARFI) ultrasound imaging of solid focal liver lesions. Eur J Radiol, 2012. 81(3): p. 451-5.

[18] Tozaki, M., S. Isobe, and E. Fukuma, Preliminary study of ultrasonographic tissue quantification of the breast using the acoustic radiation force impulse (ARFI) technology. Eur J Radiol, 2011. 80(2): p. e182-7.

[19] Zhai, L., et al., Acoustic radiation force impulse imaging of human prostates: initial in vivo demonstration. Ultrasound in Medicine and Biology, 2012. 38(1): p. 50-61.

[20] Bercoff, J., M. Tanter, and M. Fink, Supersonic shear imaging: a new technique for soft tissue elasticity mapping. IEEE Trans Ultrason Ferroelectr Freq Control, 2004. 51(4): p. 396-409.

[21] Athanasiou, A., et al., Breast lesions: quantitative elastography with supersonic shear imaging--preliminary results. Radiology, 2010. 256(1): p. 297-303.

[22] Bavu, E., et al., Noninvasive in vivo liver fibrosis evaluation using supersonic shear imaging: a clinical study on 113 hepatitis C virus patients. Ultrasound in Medicine and Biology, 2011. 37(9): p. 1361-73.

[23] Tanter, M., et al., High-resolution quantitative imaging of cornea elasticity using supersonic shear imaging. IEEE Trans Med Imaging, 2009. 28(12): p. 1881-93.

[24] Wells, P.N. and H.D. Liang, Medical ultrasound: imaging of soft tissue strain and elasticity. J R Soc Interface, 2011. 8(64): p. 1521-49.

[25] Parker, K.J., M.M. Doyley, and D.J. Rubens, Imaging the elastic properties of tissue: the 20 year perspective. Phys Med Biol, 2011. 56(1): p. R1-R29.

[26] Carstensen, E.L., et al., Demonstration of nonlinear acoustical effects at biomedical frequencies and intensities. Ultrasound in Medicine and Biology, 1980. 6(4): p. 359-68.

[27] Muir, T.G. and E.L. Carstensen, Prediction of nonlinear acoustic effects at biomedical frequencies and intensities. Ultrasound in Medicine and Biology, 1980. 6(4): p. 345-57.

[28] Caidahl, K., et al., New concept in echocardiography: harmonic imaging of tissue without use of contrast agent. Lancet, 1998. 352(9136): p. 1264-70.

[29] Choudhry, S., et al., Comparison of tissue harmonic imaging with conventional US in abdominal disease. Radiographics, 2000. 20(4): p. 1127-35.

[30] Duck, F.A., Nonlinear acoustics in diagnostic ultrasound. Ultrasound in Medicine and Biology, 2002. 28(1): p. 1-18.

[31] Spencer, K.T., et al., Use of harmonic imaging without echocardiographic contrast to improve two-dimensional image quality. American Journal of Cardiology, 1998. 82(6): p. 794-799.

[32] Feldman, M.K., S. Katyal, and M.S. Blackwood, US artifacts. Radiographics, 2009. 29(4): p. 1179-89.

[33] Kossoff, G., Basic physics and imaging characteristics of ultrasound. World J Surg, 2000. 24(2): p. 134-42.

[34] Leighton, T.G., The Acoustic Bubble 1994, San Diego: Book from Academic Press.

[35] Plesset, M., The dynamics of cavitation bubbles. J Appl Mech, 1949. 16: p. 277–282.

[36] Rayleigh, L., On the pressure developed in a liquid during collapse of a spherical cavity. Phil Mag, 1917. 34: p. 94–98.

[37] de Jong, N. and R. Cornet, Higher harmonics of vibrating gas-filled microspheres. Part one: Simulations. Ultrasonics, 1994. 32: p. 447–453.

[38] de Jong, N. and R. Cornet, Higher harmonics of vibrating gas-filled microspheres. Part two: Measurements. Ultrasonics, 1994. 32: p. 455–459.

[39] Burns, P.N., S.R. Wilson, and D.H. Simpson, Pulse inversion imaging of liver blood flow: improved method for characterizing focal masses with microbubble contrast. Invest Radiol, 2000. 35(1): p. 58-71.

[40] Simpson, D.H., C.T. Chin, and P.N. Burns, Pulse inversion Doppler: a new method for detecting nonlinear echoes from microbubble contrast agents. IEEE Trans Ultrason Ferroelectr Freq Control, 1999. 46(2): p. 372-82.

[41] Mor-Avi, V., et al., Combined assessment of myocardial perfusion and regional left ventricular function by analysis of contrast-enhanced power modulation images. Circulation, 2001. 104(3): p. 352-7.

[42] Eckersley, R.J., C.T. Chin, and P.N. Burns, Optimising phase and amplitude modulation schemes for imaging microbubble contrast agents at low acoustic power. Ultrasound in Medicine and Biology, 2005. 31(2): p. 213-9.

[43] Haider, B. and R.Y. Chiao, Higher order nonlinear ultrasonic imaging. 1999 IEEE Ultrasonics Symposium Proceedings, Vols 1 and 2, 1999: p. 1527-1531.

[44] Phillips, P.J., Contrast Pulse Sequences (CPS): Imaging nonlinear microbubbles. 2001 IEEE Ultrasonics Symposium Proceedings, Vols 1 and 2, 2001: p. 1739-1745.

[45] Leen, E., et al., Contrast-enhanced 3D ultrasound in the radiofrequency ablation of liver tumors. World J Gastroenterol, 2009. 15(3): p. 289-99.

[46] Hansen, R. and B.A. Angelsen, SURF imaging for contrast agent detection. IEEE Trans Ultrason Ferroelectr Freq Control, 2009. 56(2): p. 280-90.

[47] Hansen, R. and B.A. Angelsen, Contrast imaging by non-overlapping dual frequency band transmit pulse complexes. IEEE Trans Ultrason Ferroelectr Freq Control, 2011. 58(2): p. 290-7.

[48] Hansen, R., et al., Utilizing dual frequency band transmit pulse complexes in medical ultrasound imaging. J Acoust Soc Am, 2010. 127(1): p. 579-87.

[49] Hansen, R., et al., Nonlinear propagation delay and pulse distortion resulting from dual frequency band transmit pulse complexes. J Acoust Soc Am, 2011. 129(2): p. 1117-27.

[50] Masoy, S.E., et al., SURF imaging: in vivo demonstration of an ultrasound contrast agent detection technique. IEEE Trans Ultrason Ferroelectr Freq Control, 2008. 55(5): p. 1112-21.

[51] Cinquin, P., et al., Computer assisted Medical Interventions. IEEE Engineering in medicine and biology, 1995. May/June: p. 254-263.

[52] Meyer, K., H.L. Applewhite, and F.A. Biocca, A survey of position trackers. Presence: Teleoperators and Virtual Environments, 1992. 1(2): p. 173-200.

[53] Birkfellner, W., et al., Systematic distortions in magnetic position digitizers. Med Phys, 1998. 25(11): p. 2242-8.

[54] Kindratenko, V., A survey of electromagnetic position tracker calibration techniques. Virtual Reality, 2000(5): p. 169-182.

[55] Birkfellner, W., et al., Calibration of tracking systems in a surgical environment. IEEE Trans Med Imaging, 1998. 17(5): p. 737-42.

[56] Lindseth, F., et al., Probe calibration for freehand 3-D ultrasound. Ultrasound Med Biol, 2003. 29(11): p. 1607-23.

[57] Mercier, L., et al., A review of calibration techniques for freehand 3-D ultrasound systems. Ultrasound Med Biol, 2005. 31(4): p. 449-71.

[58] Arun, K.S., T.S. Huang, and S.D. Blostein, Least-Squares Fitting of Two 3-D Point Sets.

[59] Fenster, A., G. Parraga, and J. Bax, Three-dimensional ultrasound scanning. Interface Focus, 2011. 1(4): p. 503-19.

[60] Solberg, O.V., et al., Freehand 3D ultrasound reconstruction algorithms--a review. Ultrasound Med Biol, 2007. 33(7): p. 991-1009.

[61] Smith, S.W., G.E. Trahey, and O.T. von Ramm, Two-dimensional arrays for medical ultrasound. Ultrason Imaging, 1992. 14(3): p. 213-33.

[62] Turnbull, D.H. and F.S. Foster, Beam steering with pulsed two-dimensional transducer arrays. IEEE Trans Ultrason Ferroelectr Freq Control, 1991. 38(4): p. 320-33.

[63] Choe, J.W., et al., Volumetric real-time imaging using a CMUT ring array. IEEE Trans Ultrason Ferroelectr Freq Control, 2012. 59(6): p. 1201-11.

[64] Wygant, I.O., et al., Integration of 2D CMUT arrays with front-end electronics for volumetric ultrasound imaging. IEEE Trans Ultrason Ferroelectr Freq Control, 2008. 55(2): p. 327-42.

[65] Oralkan, O., et al., Volumetric ultrasound imaging using 2-D CMUT arrays. IEEE Trans Ultrason Ferroelectr Freq Control, 2003. 50(11): p. 1581-94.

[66] West, J.B., et al., Fiducial point placement and the accuracy of point-based, rigid body registration. Neurosurgery, 2001. 48(4): p. 810-6; discussion 816-7.

[67] Marmulla, R., et al., New Augmented Reality Concepts for Craniofacial Surgical Procedures. Plastic and Reconstructive Surgery, 2005. 115(3): p. 1124-1128.

[68] Shamir, R.R., et al., Surface-based facial scan registration in neuronavigation procedures: a clinical study. J Neurosurg, 2009.

[69] Marmulla, R., G. Eggers, and J. Muhling, Laser surface registration for lateral skull base surgery. Minim Invasive Neurosurg, 2005. 48(3): p. 181-5.

[70] Raabe, A., et al., Laser surface scanning for patient registration in intracranial image-guided surgery. Neurosurgery, 2002. 50(4): p. 797-801; discussion 802-3.

[71] Schlaier, J., J. Warnat, and A. Brawanski, Registration accuracy and practicability of laser-directed surface matching. Comput Aided Surg, 2002. 7(5): p. 284-90.

[72] Maurer, C.R., Jr., R.J. Maciunas, and J.M. Fitzpatrick, Registration of head CT images to physical space using a weighted combination of points and surfaces. IEEE Trans Med Imaging, 1998. 17(5): p. 753-61.

[73] Hoffmann, J., et al., Validation of 3D-laser surface registration for image-guided cranio-maxillofacial surgery. J Craniomaxillofac Surg, 2005. 33(1): p. 13-8.

[74] Knott, P.D., et al., Contour and Paired-Point Registration in a Model for Image-Guided Surgery. The Laryngoscope, 2006. 116: p. 1877-1881.

[75] Schicho, K., et al., Comparison of laser surface scanning and fiducial marker-based registration in frameless stereotaxy. Journal of Neurosurgery, 2007. 106: p. 704-709.

[76] Arbel, T., et al., Automatic Non-linear MRI-Ultrasound Registration for the Correction of Intra-operative Brain deformations, in In Proc. MICCAI 20012001. p. 913-922.

[77] Arbel, T., et al., Automatic non-linear MRI-ultrasound registration for the correction of intra-operative brain deformations. Comput Aided Surg, 2004. 9(4): p. 123-36.

[78] Coupe, P., et al., 3D Rigid Registration of Intraoperative Ultrasound and Preoperative MR Brain Images Based on Hyperechogenic Structures. Int J Biomed Imaging, 2012. 2012: p. 531319.

[79] De Nigris, D., D. Collins, and T. Arbel, Multi-Modal Image Registration based on Gradient Orientations of Minimal Uncertainty. IEEE Trans Med Imaging, 2012.

[80] Ji, S., et al., Mutual-information-based image to patient re-registration using intraoperative ultrasound in image-guided neurosurgery. Med Phys, 2008. 35(10): p. 4612-24.

[81] Penney, G.P., et al., Deforming a Preoperative Volume to Represent the Intraoperative Scene, in Computer Aided Surgery2002. p. 63-73.

[82] Roche, A., et al., Rigid Registration of 3D Ultrasound with MR Images: A New Approach Combining intensity and Gradient Information, in IEEE Transactions on Medical Imaging2001. p. 1038-1049.

[83] Reinertsen, I., et al., Vessel Driven Correction of Brain Shift, in In Proc. MICCAI 20042004. p. 208-216.

[84] Reinertsen, I., et al., Validation of Vessel-based Registration for Correction of Brain-shift. Medical Image Analysis, 2007. 11(4): p. 374-88.

[85] Reinertsen, I., et al., Clinical validation of vessel-based registration for correction of brain-shift. Med Image Anal, 2007. 11(6): p. 673-84.

[86] Besl, P.J. and N.D. McKay, A Method for Registration of 3D Shapes. IEEE Transactions on Pattern Analysis and Machine Intelligence, 1992. 14(2): p. 239-256.

[87] Metz, C.T., et al., Nonrigid registration of dynamic medical imaging data using nD + t B-splines and a groupwise optimization approach. Medical image analysis, 2011. 15(2): p. 238-49.

[88] Akbari, H. and B. Fei, 3D ultrasound image segmentation using wavelet support vector machines. Med Phys, 2012. 39(6): p. 2972-84.

[89] Zhan, Y. and D. Shen, Deformable segmentation of 3-D ultrasound prostate images using statistical texture matching method. IEEE Trans Med Imaging, 2006. 25(3): p. 256-72.

[90] Xie, J., Y. Jiang, and H.T. Tsui, Segmentation of kidney from ultrasound images based on texture and shape priors. IEEE Trans Med Imaging, 2005. 24(1): p. 45-57.

[91] Foroughi, P., et al., Ultrasound Bone Segmentation Using Dynamic Programming, in IEEE Ultrasonics Symposium2007. p. 2523-2526.

[92] Hacihaliloglu, I., et al., Non-iterative partial view 3D ultrasound to CT registration in ultrasound-guided computer-assisted orthopedic surgery. Int J Comput Assist Radiol Surg, 2012.

[93] Rasoulian, A., P. Abolmaesumi, and P. Mousavi, Feature-based multibody rigid registration of CT and ultrasound images of lumbar spine. Med Phys, 2012. 39(6): p. 3154-66.

[94] Yan, C.X., et al., Validation of automated ultrasound-CT registration of vertebrae. Int J Comput Assist Radiol Surg, 2012. 7(4): p. 601-10.

[95] Orderud, F., J. Hansgard, and S.I. Rabben, Real-time tracking of the left ventricle in 3D echocardiography using a state estimation approach. Med Image Comput Comput Assist Interv, 2007. 10(Pt 1): p. 858-65.

[96] Lorensen, W.E. and H.E. Cline, Marching Cubes: A high resolution 3D surface construction algorithm. Computer Graphics, 1987. 21(4): p. 163-169.

[97] Lindseth, F., et al., Accuracy evaluation of a 3D ultrasound-based neuronavigation system. Comput Aided Surg, 2002. 7(4): p. 197-222.

[98] Lindseth, F., J. Bang, and T. Lango, A robust and automatic method for evaluating accuracy in 3-D ultrasound-based navigation. Ultrasound Med Biol, 2003. 29(10): p. 1439-52.

[99] Matos, H., et al., Effectiveness and safety of ultrasound-guided percutaneous liver biopsy in children. Pediatr Radiol, 2012. 42(11): p. 1322-5.

[100] Copel, L., et al., Ultrasound-guided percutaneous liver biopsy: indications, risks, and technique. Surg Technol Int, 2003. 11: p. 154-60.

[101] Tzortzis, D., et al., Percutaneous US-guided liver biopsy in focal lesions using a semi-automatic device allowing to perform multiple biopsies in a single-pass. Minerva Gastroenterol Dietol, 2012. 58(1): p. 1-8.

[102] Fontalvo, L.F., et al., Percutaneous US-guided biopsies of peripheral pulmonary lesions in children. Pediatr Radiol, 2006. 36(6): p. 491-7.

[103] Pinto, F., et al., Imaging in prostate cancer diagnosis: present role and future perspectives. Urol Int, 2011. 86(4): p. 373-82.

[104] Froehlich, C.D., et al., Ultrasound-guided central venous catheter placement decreases complications and decreases placement attempts compared with the landmark technique in patients in a pediatric intensive care unit. Crit Care Med, 2009. 37(3): p. 1090-6.

[105] Palepu, G.B., et al., Impact of ultrasonography on central venous catheter insertion in intensive care. Indian J Radiol Imaging, 2009. 19(3): p. 191-8.

[106] Unsgaard, G., et al., Brain operations guided by real-time two-dimensional ultrasound: new possibilities as a result of improved image quality. Neurosurgery, 2002. 51(2): p. 402-11; discussion 411-2.

[107] Tublin, M.E., et al., Ultrasound-guided fine-needle aspiration versus fine-needle capillary sampling biopsy of thyroid nodules: does technique matter? J Ultrasound Med, 2007. 26(12): p. 1697-701.

[108] Strowitzki, M., et al., Accuracy of ultrasound-guided puncture of the ventricular system. Childs Nerv Syst, 2008. 24(1): p. 65-9.

[109] Whitehead, W.E., et al., Accurate placement of cerebrospinal fluid shunt ventricular catheters with real-time ultrasound guidance in older children without patent fontanelles. J Neurosurg, 2007. 107(5 Suppl): p. 406-10.

[110] Tonni, G., et al., 4D vs 2D ultrasound-guided amniocentesis. J Clin Ultrasound, 2009. 37(8): p. 431-5.

[111] Letteboer, M.M.J., et al., Brain shift estimation in image-guided neurosurgery using 3-D ultrasound. Ieee Transactions on Biomedical Engineering, 2005. 52(2): p. 268-276.

[112] Reinges, M.H.T., et al., Course of brain shift during microsurgical resection of supratentorial cerebral lesions: limits of conventional neuronavigation. Acta Neurochirurgica, 2004. 146(4): p. 369-377.

[113] Roberts, D.W., et al., Intraoperative brain shift and deformation: A quantitative analysis of cortical displacement in 28 cases. Neurosurgery, 1998. 43(4): p. 749-758.

[114] Koivukangas, J., et al., Ultrasound-controlled neuronavigator-guided brain surgery. J Neurosurg, 1993. 79(1): p. 36-42.

[115] Hata, N., et al., Development of a frameless and armless stereotactic neuronavigation system with ultrasonographic registration. Neurosurgery, 1997. 41(3): p. 608-613.

[116] Jodicke, A., et al., Intraoperative three-dimensional ultrasonography: An approach to register brain shift using multidimensional image processing. Minimally Invasive Neurosurgery, 1998. 41(1): p. 13-19.

[117] Grønningsæter, Å., et al., SonoWand, an Ultrasound-based Neuronavigation System. Neurosurgery, 2000. 47(6): p. 1373-1380.

[118] Hirschberg, H. and G. Unsgaard, Incorporation of ultrasonic imaging in an optically coupled frameless stereotactic system. Acta Neurochir Suppl. (Wien), 1997. 68: p. 75-80.

[119] Unsgaard, G., et al., Neuronavigation by intraoperative three-dimensional ultrasound: initial experience during brain tumor resection. Neurosurgery, 2002. 50(4): p. 804-12; discussion 812.

[120] Unsgaard, G., et al., Intra-operative 3D ultrasound in neurosurgery. Acta Neurochir (Wien), 2006. 148(3): p. 235-53; discussion 253.

[121] Berntsen, E.M., et al., Functional magnetic resonance imaging and diffusion tensor tractography incorporated into an intraoperative 3-dimensional ultrasound-based neuronavigation system: impact on therapeutic strategies, extent of resection, and clinical outcome. Neurosurgery, 2010. 67(2): p. 251-64.

[122] Gulati, S., et al., Surgical resection of high-grade gliomas in eloquent regions guided by blood oxygenation level dependent functional magnetic resonance imaging, diffusion tensor tractography, and intraoperative navigated 3D ultrasound. Minim Invasive Neurosurg, 2009. 52(1): p. 17-24.

[123] Rasmussen, I.A., Jr., et al., Functional neuronavigation combined with intra-operative 3D ultrasound: initial experiences during surgical resections close to eloquent

brain areas and future directions in automatic brain shift compensation of preoperative data. Acta Neurochir (Wien), 2007. 149(4): p. 365-78.

[124] Saether, C.A., et al., Did survival improve after the implementation of intraoperative neuronavigation and 3D ultrasound in glioblastoma surgery? A retrospective analysis of 192 primary operations. J Neurol Surg A Cent Eur Neurosurg, 2012. 73(2): p. 73-8.

[125] Jakola, A.S., et al., Comparison of a strategy favoring early surgical resection vs a strategy favoring watchful waiting in low-grade gliomas. JAMA, 2012. 308(18): p. 1881-8.

[126] Solheim, O., et al., Intrasellar ultrasound in transsphenoidal surgery: a novel technique. Neurosurgery, 2010. 66(1): p. 173-85; discussion 185-6.

[127] Solheim, O., et al., Ultrasound-guided operations in unselected high-grade gliomas--overall results, impact of image quality and patient selection. Acta Neurochir (Wien), 2010. 152(11): p. 1873-86.

[128] Jakola, A.S., G. Unsgard, and O. Solheim, Quality of life in patients with intracranial gliomas: the impact of modern image-guided surgery. J Neurosurg, 2011. 114(6): p. 1622-30.

[129] Unsgaard, G., et al., Operation of arteriovenous malformations assisted by stereoscopic navigation-controlled display of preoperative magnetic resonance angiography and intraoperative ultrasound angiography. Neurosurgery, 2005. 56(2 Suppl): p. 281-90; discussion 281-90.

[130] Yamakawa, K., S. Naito, and K. Azuma, Laparoscopic diagnosis of the intraabdominal organs. Jpn J Gastroenterol, 1958. 55: p. 741–7.

[131] Jakimowicz, J.J. and T.J.M. Ruers, Ultrasound-Assisted Laparoscopic Cholecystectomy: Preliminary Experience. Dig Surg, 1991. 8: p. 114-117.

[132] Jakimowicz, J.J., Intraoperative ultrasonography in open and laparoscopic abdominal surgery: an overview. Surg Endosc, 2006. 20 Suppl 2: p. S425-35.

[133] Richardson, W., et al., SAGES guidelines for the use of laparoscopic ultrasound. Surg Endosc, 2010. 24: p. 745–756.

[134] Harms, J., et al., Three-dimensional navigated laparoscopic ultrasonography. Surg Endosc, 2001. 15(12): p. 1459–62.

[135] Mårvik, R., et al., Laparoscopic navigation pointer for 3-D image guided surgery. Surg Endosc, 2004. 18(8): p. 1242-8.

[136] Langø, T., et al., Navigation in laparoscopy – prototype research platform for improved image-guided surgery. Minimally Invasive Therapy and Allied Technologies, 2008. 17(1): p. 17-33.

[137] Solberg, O.V., et al., Navigated ultrasound in laparoscopic surgery. Minim Invasive Ther Allied Technol (MITAT), 2009. 18(1): p. 36-53.

[138] Rutala, W.A., APIC guideline for selection and use of disinfectants. 1994, 1995, and 1996 APIC Guidelines Committee. Am J Infect Control, 1996. 24(4): p. 313-42.

[139] El Guindi, W., et al., 3D ultrasound and Doppler angiography for evaluation of fetal cardiovascular anomalies. Int J Gynaecol Obstet, 2012, http://dx.doi.org/10.1016/j.ijgo.2012.08.015

[140] Rajani, R., J. Hancock, and J.B. Chambers, The art of assessing aortic stenosis. Heart, 2012. 98 Suppl 4: p. iv14-iv22.

[141] Wang, Y., et al., Transesophageal echocardiography guided cannulation for peripheral cardiopulmonary bypass during robotic cardiac surgery. Chin Med J (Engl), 2012. 125(18): p. 3236-9.

[142] Lie, T., et al., Ultrasound imaging during endovascular abdominal aortic aneurysm repair using the Stentor bifurcated endograft. J Endovasc Surg, 1997. 4(3): p. 272-8.

[143] Kaspersen, J.H., et al., Three-dimensional ultrasound-based navigation combined with preoperative CT during abdominal interventions: a feasibility study. Cardiovasc Intervent Radiol, 2003. 26(4): p. 347-56.

[144] Malkawi, A.H., et al., Percutaneous access for endovascular aneurysm repair: a systematic review. Eur J Vasc Endovasc Surg, 2010. 39(6): p. 676-82.

[145] Arthurs, Z.M., et al., Ultrasound-guided access improves rate of access-related complications for totally percutaneous aortic aneurysm repair. Ann Vasc Surg, 2008. 22(6): p. 736-41.

[146] Boks, S.S., et al., Ultrasound-guided percutaneous transabdominal treatment of a type 2 endoleak. Cardiovasc Intervent Radiol, 2005. 28(4): p. 526-9.

[147] Kasthuri, R.S., S.M. Stivaros, and D. Gavan, Percutaneous ultrasound-guided thrombin injection for endoleaks: an alternative. Cardiovasc Intervent Radiol, 2005. 28(1): p. 110-2.

[148] Manstad-Hulaas, F., et al., Three-dimensional electromagnetic navigation vs. fluoroscopy for endovascular aneurysm repair: a prospective feasibility study in patients. J Endovasc Ther, 2012. 19(1): p. 70-8.

[149] Kolstad, F., et al., Three-dimensional ultrasonography navigation in spinal cord tumor surgery. Technical note. J Neurosurg Spine, 2006. 5(3): p. 264-70.

[150] Fry, W.J., Intense ultrasound; a new tool for neurological research. The Journal of mental science, 1954. 100(418): p. 85-96.

[151] Fry, W.J., et al., Production of focal destructive lesions in the central nervous system with ultrasound. Journal of neurosurgery, 1954. 11(5): p. 471-8.

[152] Lele, P.P., A simple method for production of trackless focal lesions with focused ultrasound: physical factors. The Journal of physiology, 1962. 160: p. 494-512.

[153] Lynn, J.G., et al., A New Method for the Generation and Use of Focused Ultrasound in Experimental Biology. The Journal of general physiology, 1942. 26(2): p. 179-93.

[154] Cline, H.E., et al., MR-guided focused ultrasound surgery. Journal of computer assisted tomography, 1992. 16(6): p. 956-65.

[155] Chapman, A. and G. ter Haar, Thermal ablation of uterine fibroids using MR-guided focused ultrasound-a truly non-invasive treatment modality. European radiology, 2007. 17(10): p. 2505-11.

[156] Furusawa, H., et al., The evolving non-surgical ablation of breast cancer: MR guided focused ultrasound (MRgFUS). Breast cancer, 2007. 14(1): p. 55-8.

[157] Huber, P.E., et al., A new noninvasive approach in breast cancer therapy using magnetic resonance imaging-guided focused ultrasound surgery. Cancer research, 2001. 61(23): p. 8441-7.

[158] Martin, E., et al., High-intensity focused ultrasound for noninvasive functional neurosurgery. Annals of neurology, 2009. 66(6): p. 858-61.

[159] McDannold, N., et al., Transcranial magnetic resonance imaging- guided focused ultrasound surgery of brain tumors: initial findings in 3 patients. Neurosurgery, 2010. 66(2): p. 323-32; discussion 332.

[160] Catane, R., et al., MR-guided focused ultrasound surgery (MRgFUS) for the palliation of pain in patients with bone metastases--preliminary clinical experience. Annals of oncology : official journal of the European Society for Medical Oncology / ESMO, 2007. 18(1): p. 163-7.

[161] Liberman, B., et al., Pain palliation in patients with bone metastases using MR-guided focused ultrasound surgery: a multicenter study. Annals of surgical oncology, 2009. 16(1): p. 140-6.

[162] Aubry, A. and A. Derode, Multiple scattering of ultrasound in weakly inhomogeneous media: application to human soft tissues. The Journal of the Acoustical Society of America, 2011. 129(1): p. 225-33.

[163] Kennedy, J.E., R.L. Clarke, and G.R. ter Haar. The effects of absorbers such as ribs in the HIFU Beam-path on the focal profile. in 2nd Intl. Symp. on Therapeutic Ultrasound. 2002.

[164] Goss, S.A., L.A. Frizzell, and F. Dunn, Ultrasonic absorption and attenuation in mammalian tissues. Ultrasound in medicine & biology, 1979. 5(2): p. 181-6.

[165] Al-Bataineh, O., J. Jenne, and P. Huber, Clinical and future applications of high intensity focused ultrasound in cancer. Cancer treatment reviews, 2012. 38(5): p. 346-53.

[166] Jenne, J.W., T. Preusser, and M. Gunther, High-Intensity Focused Ultrasound: Principles, Therapy Guidance, Simulations and Applications. Zeitschrift fur medizinische Physik, 2012. Online 9 August 2012.

[167] Kopelman, D., et al., Magnetic resonance-guided focused ultrasound surgery (MRgFUS). Four ablation treatments of a single canine hepatocellular adenoma. HPB : the official journal of the International Hepato Pancreato Biliary Association, 2006. 8(4): p. 292-8.

[168] Kopelman, D., et al., Magnetic resonance-guided focused ultrasound surgery (MRgFUS): ablation of liver tissue in a porcine model. European journal of radiology, 2006. 59(2): p. 157-62.

[169] Okada, A., et al., A case of hepatocellular carcinoma treated by MR-guided focused ultrasound ablation with respiratory gating. Magnetic resonance in medical sciences : MRMS : an official journal of Japan Society of Magnetic Resonance in Medicine, 2006. 5(3): p. 167-71.

[170] de Senneville, B.D., C. Mougenot, and C.T. Moonen, Real-time adaptive methods for treatment of mobile organs by MRI-controlled high-intensity focused ultrasound. Magnetic resonance in medicine : official journal of the Society of Magnetic Resonance in Medicine / Society of Magnetic Resonance in Medicine, 2007. 57(2): p. 319-30.

[171] von Siebenthal, M., et al., 4D MR imaging of respiratory organ motion and its variability. Physics in medicine and biology, 2007. 52(6): p. 1547-64.

[172] Ries, M., et al., Real-time 3D target tracking in MRI guided focused ultrasound ablations in moving tissues. Magnetic resonance in medicine : official journal of the Society of Magnetic Resonance in Medicine / Society of Magnetic Resonance in Medicine, 2010. 64(6): p. 1704-12.

[173] de Oliveira, P.L., et al., Rapid motion correction in MR-guided high-intensity focused ultrasound heating using real-time ultrasound echo information. NMR in biomedicine, 2010. 23(9): p. 1103-8.

[174] de Senneville, B.D., et al., Motion correction in MR thermometry of abdominal organs: a comparison of the referenceless vs. the multibaseline approach. Magnetic resonance in medicine : official journal of the Society of Magnetic Resonance in Medicine / Society of Magnetic Resonance in Medicine, 2010. 64(5): p. 1373-81.

[175] Auboiroux, V., et al., Ultrasonography-based 2D motion-compensated HIFU sonication integrated with reference-free MR temperature monitoring: a feasibility study ex vivo. Physics in medicine and biology, 2012. 57(10): p. N159-71.

[176] Feinberg, D.A., et al., Hybrid ultrasound MRI for improved cardiac imaging and real-time respiration control. Magnetic resonance in medicine : official journal of the

Society of Magnetic Resonance in Medicine / Society of Magnetic Resonance in Medicine, 2010. 63(2): p. 290-6.

[177] Tang, A.M., et al., Simultaneous ultrasound and MRI system for breast biopsy: compatibility assessment and demonstration in a dual modality phantom. IEEE transactions on medical imaging, 2008. 27(2): p. 247-54.

[178] Viallon, M., et al., Observation and correction of transient cavitation-induced PRFS thermometry artifacts during radiofrequency ablation, using simultaneous ultrasound/MR imaging. Medical physics, 2010. 37(4): p. 1491-506.

[179] Yatvin, M.B., et al., Design of liposomes for enhanced local release of drugs by hyperthermia. Science, 1978. 202(4374): p. 1290-3.

[180] Lindner, L.H., et al., Novel temperature-sensitive liposomes with prolonged circulation time. Clin Cancer Res, 2004. 10(6): p. 2168-78.

[181] de Smet, M., et al., Magnetic resonance imaging of high intensity focused ultrasound mediated drug delivery from temperature-sensitive liposomes: an in vivo proof-of-concept study. J Control Release, 2011. 150(1): p. 102-10.

[182] Evjen, T.J., et al., Sonosensitive dioleoylphosphatidylethanolamine-containing liposomes with prolonged blood circulation time of doxorubicin. Eur J Pharm Sci, 2011. 43(4): p. 318-24.

[183] Hernot, S. and A.L. Klibanov, Microbubbles in ultrasound-triggered drug and gene delivery. Adv Drug Deliv Rev, 2008. 60(10): p. 1153-66.

[184] Tinkov, S., et al., Microbubbles as ultrasound triggered drug carriers. J Pharm Sci, 2009. 98(6): p. 1935-61.

[185] Ting, C.Y., et al., Concurrent blood-brain barrier opening and local drug delivery using drug-carrying microbubbles and focused ultrasound for brain glioma treatment. Biomaterials, 2012. 33(2): p. 704-12.

[186] Hynynen, K., Ultrasound for drug and gene delivery to the brain. Adv Drug Deliv Rev, 2008. 60(10): p. 1209-17.

[187] Porter, T.R., et al., Thrombolytic enhancement with perfluorocarbon-exposed sonicated dextrose albumin microbubbles. Am Heart J, 1996. 132(5): p. 964-8.

[188] Molina, C.A., et al., Microbubble administration accelerates clot lysis during continuous 2-MHz ultrasound monitoring in stroke patients treated with intravenous tissue plasminogen activator. Stroke, 2006. 37(2): p. 425-9.

Chapter

Ultrasound Empowered Trauma Management

Mohammad Meshkini

Abstract

Using ultrasound to empower the way of traumatic patient early and by-side management as its ability to discover what bare eyes and hands could not find out solely. The most known EFAST protocol for traumatic patients management may be extended more wisely by introducing the ultrasound probe(s) through a head-to-toe secondary survey and giving a better idea of what is going on with the patient before transferring him/her out of the emergency department and could save the time and the patient's condition. This chapter would summarize what we know about ultrasound application on a traumatic patient by his/her side before sending him/her out for any further investigation, a new point of care for the standard of patient management by ultrasound.

Keywords: ultrasound, sonography, RUSH, POCUS, EFAST

1. Introduction

Observation has been one of the essentials of the clinical examination that can be found in almost every medical textbook. The use of various examination equipment due to the development of technology has improved clinical examinations and patient care. For example, we can mention the history of the invention of the stethoscope. Before the stethoscope was produced, physicians used to place their ears directly on the patient's body for auditory examinations, which was sometimes beyond the considerations of society; for this purpose, the first tool was made of a piece of paper, and later, better and advanced types were prepared, produced, and distributed.

It was mentioned the necessity of observation as one of the first steps of examining people; the possibility of using ultrasound to examine the internal organs of the body makes this purpose possible for a physician to observe and examine the inside of the patient's body by using an ultrasound probe even before auscultation, palpation, and percussion. By using ultrasound, the examiner can make a better clinical diagnosis of the patient. Also, due to the low invasiveness of this technology, it is possible to use it near the patient and reduce the complications caused by the clinical procedures, e.g., the success of the venipuncture with the use of ultrasound is more than the usual IV cannulation [1–4].

In this chapter, we will refer to the various applications of ultrasound from the perspective of its use in the management and treatment of trauma patients. And for detailed consideration, the tutorial videos are referenced from Youtube and Aparat streaming channels.

2. Orientation to the machine and probes

Proper recognition of a tool will make its use much more effective and efficient. For a more detailed understanding of the possible software and hardware features of the device, one should get familiar with the machine's instruction manual. However, in this chapter, we will discuss how to properly place the probes on the patient's body and the general tips for using medical ultrasound machines.

The ultrasound device's probes with an indicator will determine whether we should approach the patient. The placement of the piezoelectric crystals on the probe is in the same direction, and this will create only one row of sound that is interpreted by the operator in the plane of axial, coronal, or sagittal images (**Figures 1** and **2**).

At the beginning and for a general purpose, like other standard radiological images, the right side of the patient must be on the right side of the screen. For this purpose, the indicator is placed on the patient's right side and the resulting image is interpreted. On the other hand, if a coronal or sagittal view is needed, the indicator is placed toward the patient's head, which makes the image from the head toward the patient's feet.

Three common probes are:

- High-frequency Linear
- Low-frequency Convex
- Phased-Array (Echo), which is also a low-frequency probe

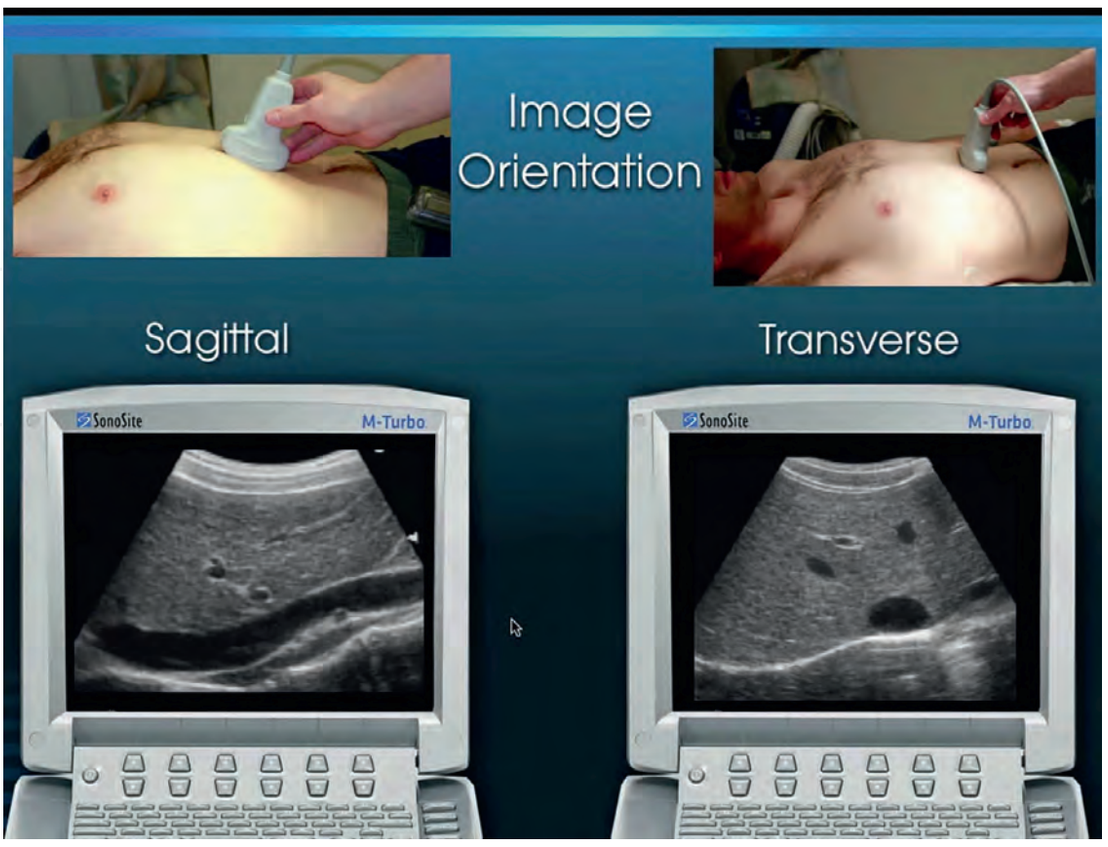

Figure 1.
How the image changes with different positioning of the probe (Courtesy of Dr. John Christian Fox).

DOI: http://dx.doi.org/10.5772/intechopen.108506

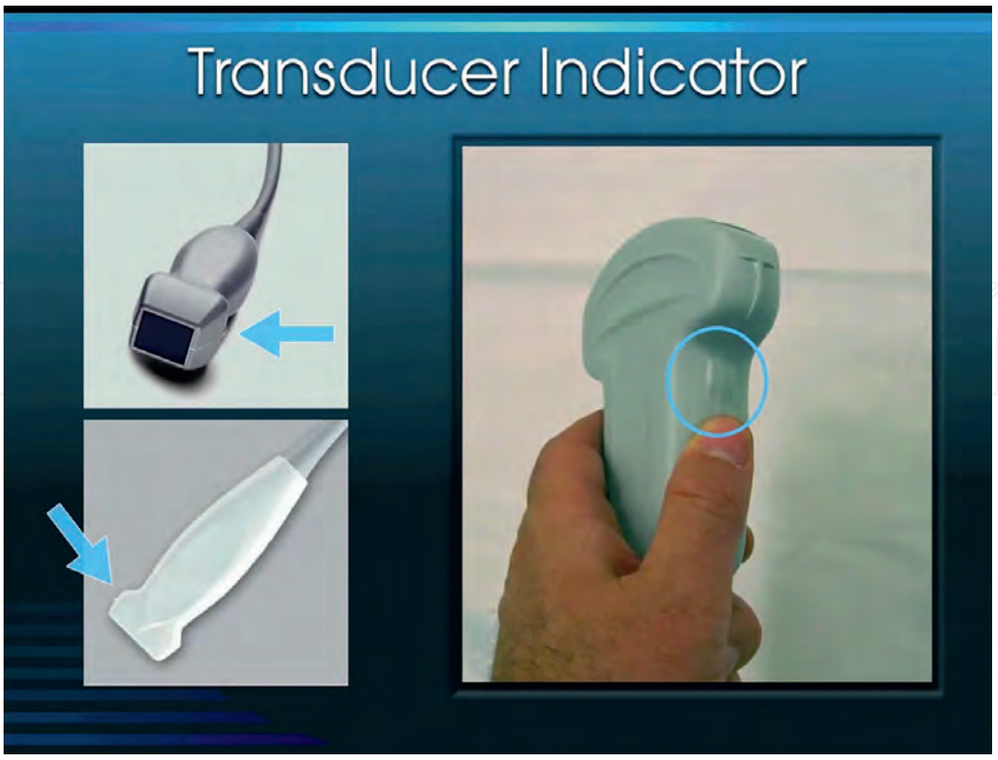

Figure 2.
Probes' indicators (Courtesy of Dr. John Christian Fox).

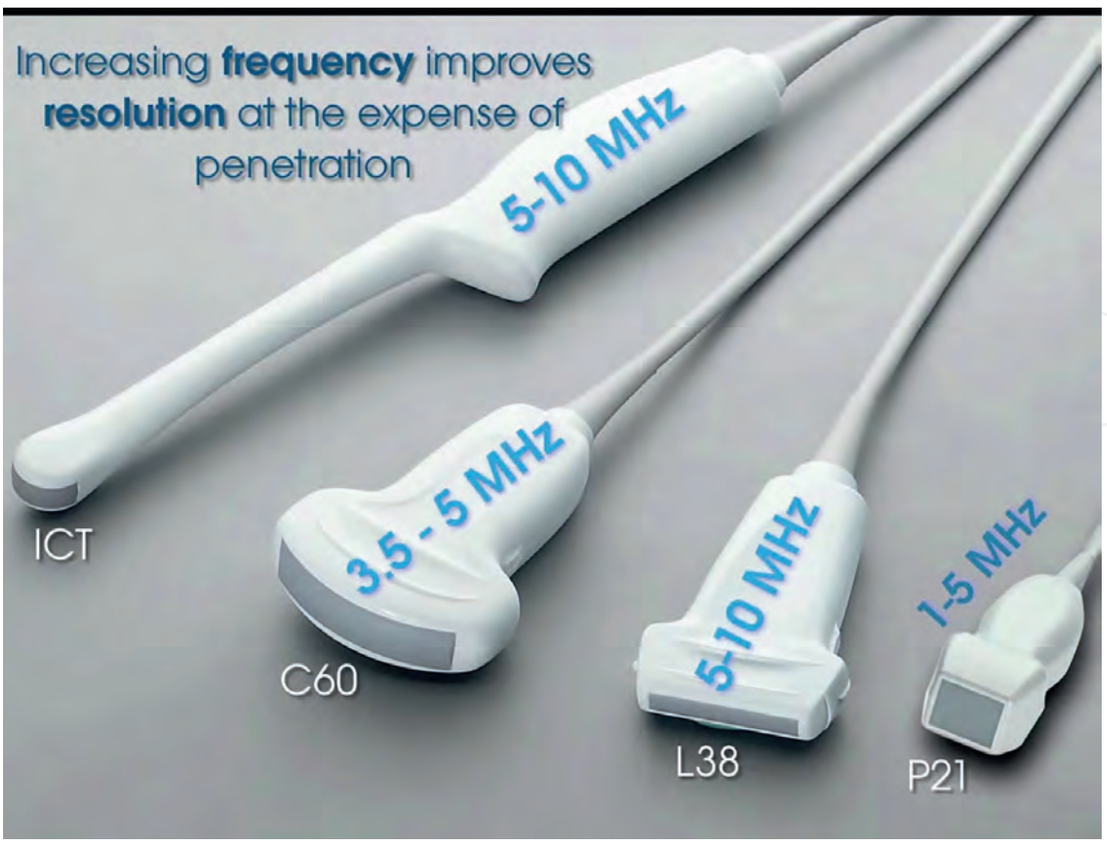

Figure 3.
Diverse types of probes (Courtesy of Dr. John Christian Fox).

A little physics of wave may be useful here; as the wave moves in the surrounding medium (environment), they have interactions with each other; the medium may reflect, absorb, or pass (with some changes) the wave, and what we see on the ultrasound machine's screen are those reflected from the medium. The body as a medium may absorb most of the high-frequency waves; however, the low-frequency waves may travel through the body more easily (**Figure 3**).

The air and bone are the two most reflective media (sound waves cannot penetrate them and may reflect through making an acoustic shadow phenomenon); however, other media (such as musculature, fat, fibro-skeletal, and internal solid organs) may pass the wave with some interactions on its amplitude (power) or velocity (speed); however, water and liquid may pass almost every part of the wave but when the wave reaches to the other medium due to media difference, it may get reflected and make acoustic echo phenomenon (**Figures 4–6**).

Though the high-frequency probes are used for surface study, their wave cannot penetrate deep into the body. But low-frequency probes are used for deeper studies. However, some use low-frequency convex probes for surface studies by reducing their penetrating depth, it may speed up their examination of the patient but could not display the detailed view like a high-frequency probe can.

By the way, the higher frequency of a wave makes it for better images, (e.g., 60 Hz vs. 90 Hz vs. 120 Hz commercial displays may be a good example of image sharpness and brings this topic to mind) (Video 1, https://www.youtube.com/watch?v=VBHCmw8iHCc&list=PL539B142177BA83F7, https://www.aparat.com/v/9ifZw).

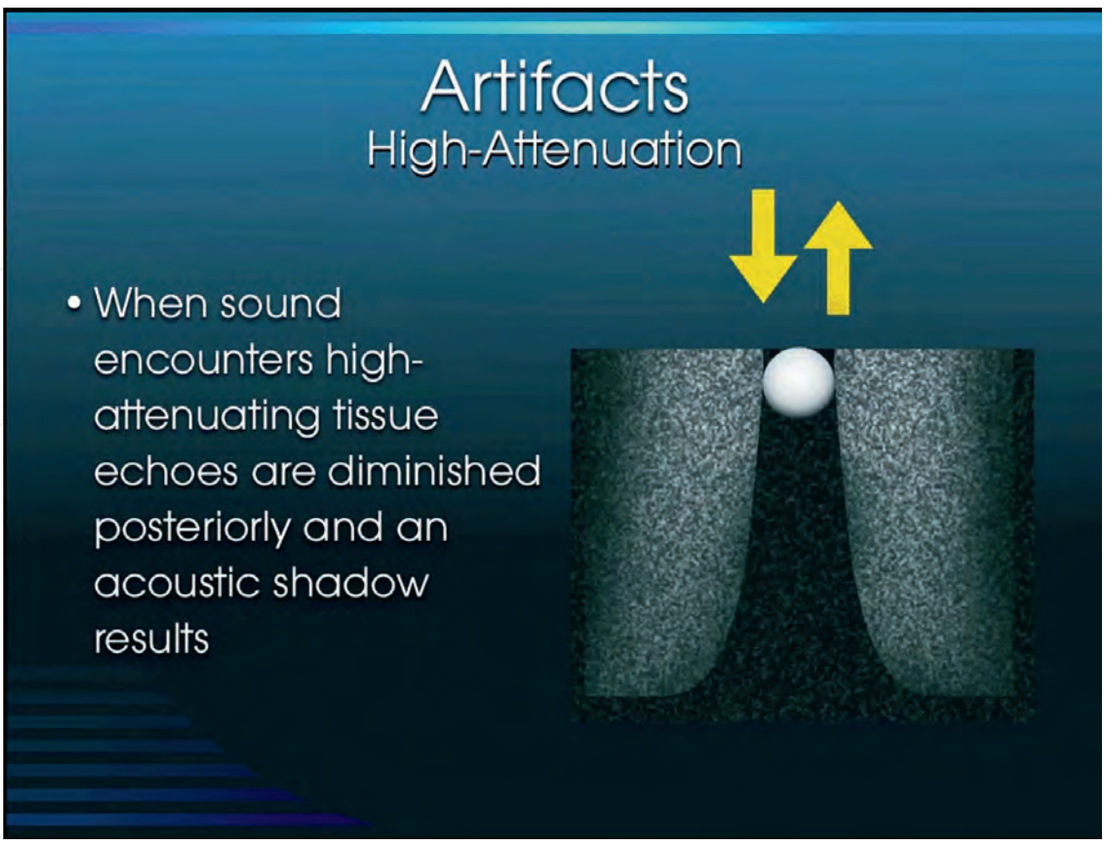

Figure 4.
Posterior shadow (Courtesy of Dr. John Christian Fox).

DOI: http://dx.doi.org/10.5772/intechopen.108506

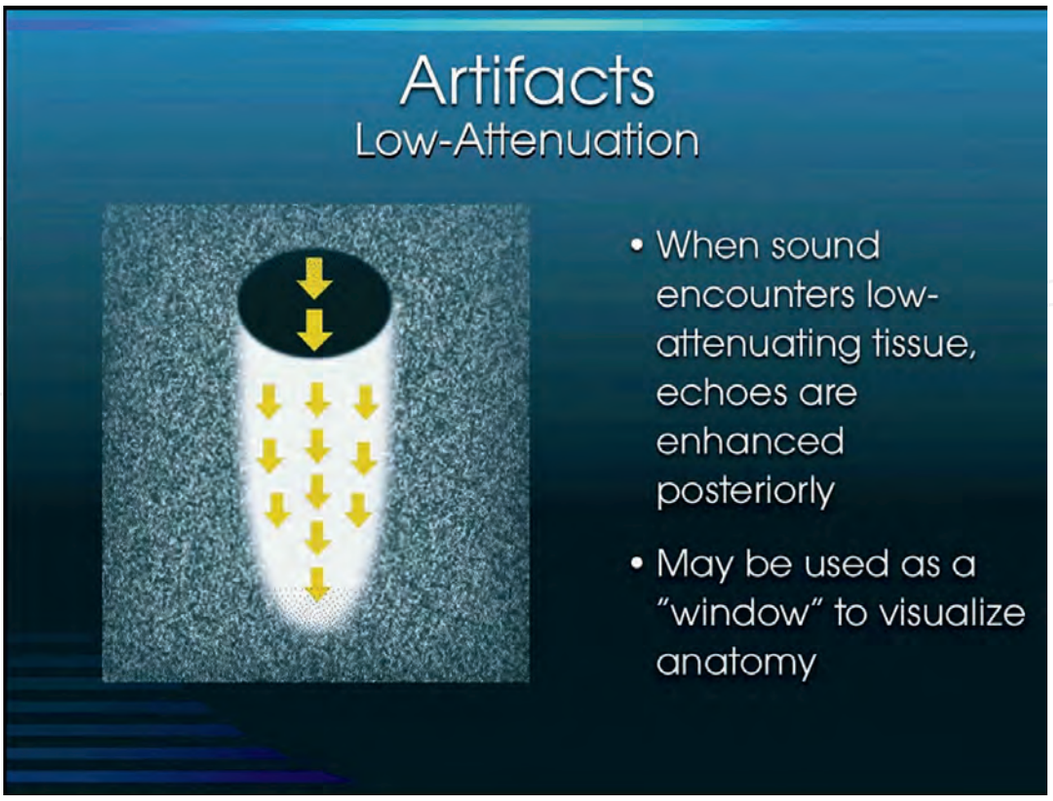

Figure 5.
Posterior echo (Courtesy of Dr. John Christian Fox).

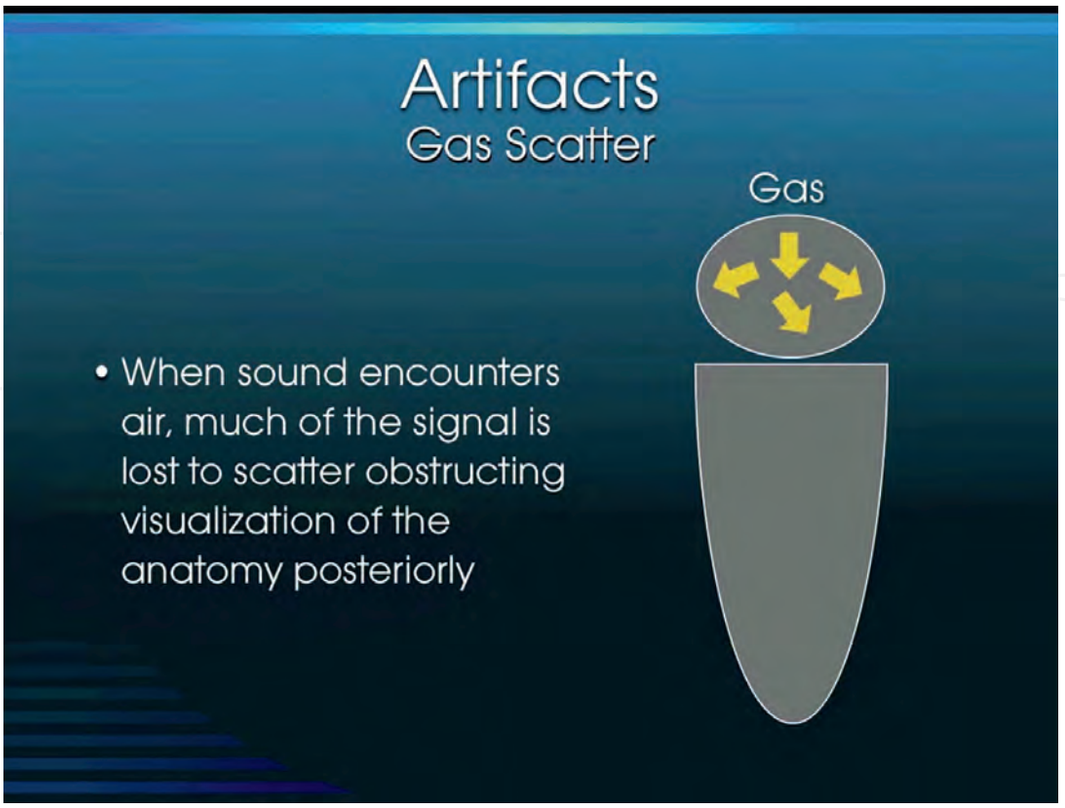

Figure 6.
Gas scattering (Courtesy of Dr. John Christian Fox).

3. Empowering airway assessment

Guidelines of the ATLS emphasize on airway as a priority in the ABCDE approach; for airway assessment other than using LEMON criteria, the ultrasound could be used for further evaluation and even intubation confirmation; however, as ultrasound is non-penetrating through the air, it may be out of mind. Here's how we could use ultrasound for assessing airway:

For assessing the larynx and its cartilages, put the linear probe with the indicator pointing to the patient's head on the anterior cervical mid-line. A white line should be observed, which may show the triangular shape on the beginning and right side of the screen, it is the thyroid cartilage, above this structure (right side of the screen), the hyoid bone (and vocal cords) could be studied, and beneath the thyroid cartilage is the place for cricoid and three or four tracheal rings (above manubrium), the thyroid gland, which is a normo-echoic structure, is placed superficial to these beneath structures.

By turning the probe's indicator to the right side, it provides axial plane images from the body, the vocal cords may be seen in this way more accurately; however, for evaluating and confirmation of the endo-tracheal tube (ETT) with ultrasound, the most specific approach is to not find it through the esophagus, which mostly lay right-posterior to the trachea. Also, the ETT has air inside the tube and reflects the ultrasound wave in a scattering pattern (Video 2, https://www.aparat.com/v/0cZr5?t=638).

This method may also be useful in forecasting the size of the trachea, ETT, and LMA size(s) too [5].

4. Empowering breathing assessment

As lung ultrasound was introduced with BLUE protocol about 10–15 years ago, it could even change the FAST exam into E-FAST [6]. However, searching for

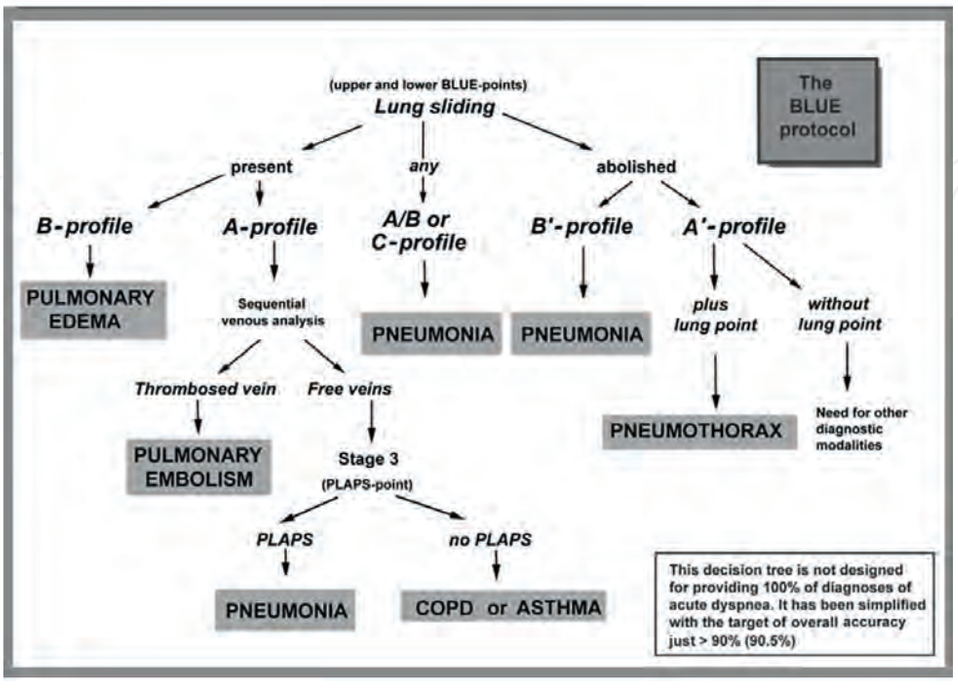

Figure 7.
BLUE-protocol algorithm.

pneumothoraces or hemothoraces is not the only application of the lung ultrasound, searching for rocket b-lines (b-lines that extend more deep in the field), vascular profile, etc., may help the physician for diagnosing the probable reasons for the acute respiratory failure (**Figure 7** and Video 3, https://www.youtube.com/watch?v=RFrPO-8jQP4&list=PL2AGl6-lzXJQt3LGH0Fqc5rjIn_hwmfhZ, https://www.aparat.com/v/aqSYt?t=664). Because it's out of consideration for trauma management, we leave it for your own for further investigation. The latest chest journal paper in 2015 is highly recommended [7]. Also the E-FAST and RUSH protocols are covered in the circulation section.

5. Empowering circulation assessment

The Focused Abdominal Sonography for Trauma (FAST) was first introduced to get a surrogate for Deep Peritoneal Lavage (DPL), it covered only three windows: right-side hepato-renal (Morrison Punch), left-side splenorenal, and supra-pubic peri-vesical views. Then it has been changed into Focused Assessment Sonography for Trauma (FAST) due to the advancement of the 4th window, Sub-Xiphoid pericardial assessment, and nowadays the Extended-Focused Assessment Sonography for Trauma(E-FAST) protocol took place for this purpose by assessing for the pneumothorax and hemothorax [6, 8].

To cover this examination by patient side, mostly we start with a low-frequency probe (To reduce the effects of ribs concealing shadows, most experts use a phased-array probe rather than a convex probe.) from the right hepatorenal side putting the probe in the

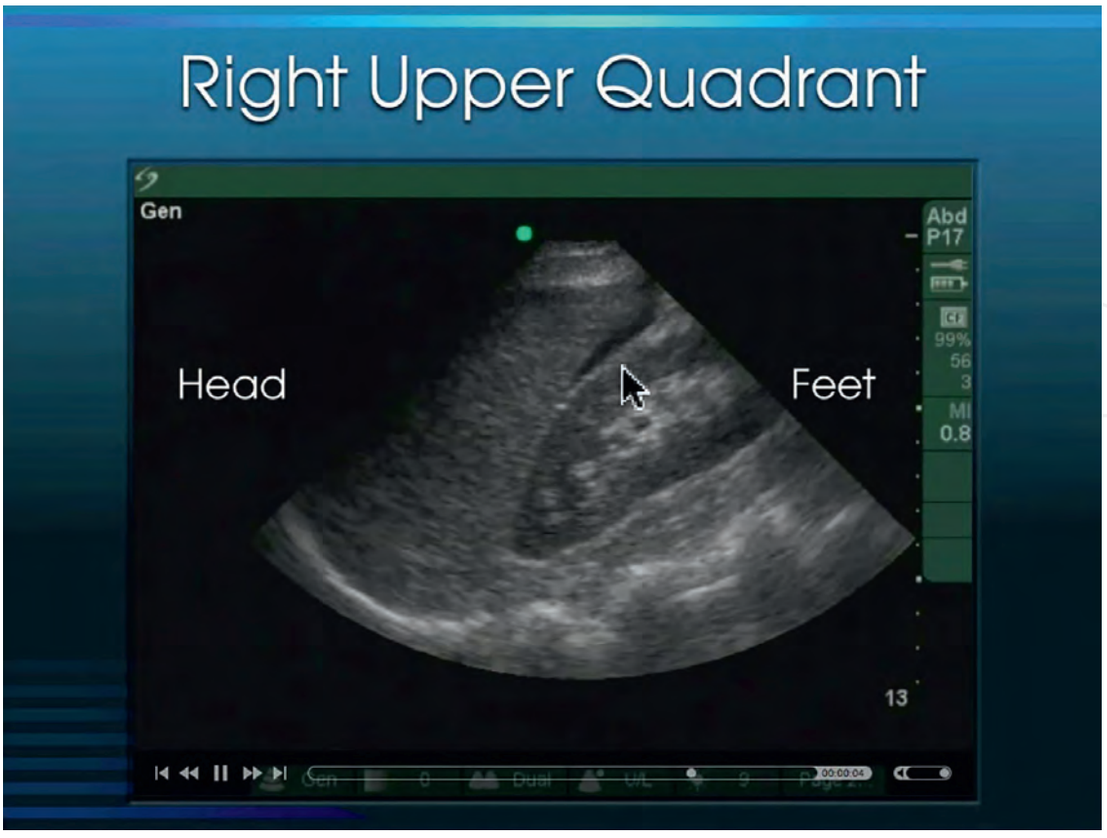

Figure 8.
A positive FAST exam on right hepatorenal (Courtesy of Dr. John Christian Fox).

sagittal plane of the right mid-axillary and beneath 7-8th inter-costal space, indicator of which lays toward the head of the patient; some fanning also could be helpful to find out the right kidney, and the Morrison punch is the potential space between right kidney and the liver, if any kind of fluid (a dark hypoechoic media with bright posterior acoustic echo) may be observed in this place, it would be positive FAST and needs surgical considerations. It's recommended to not lose as much information as needed and to set the depth of examination up to the posterior spinal column (**Figure 8**).

Like the right side, the examination of the splenorenal in the left needs the same approach; however, the left spleen mostly is posterior and superior, which needs probe positioning in the left mid to posterior axillary line and sometimes full inspiration of the patient to the full view of the space (**Figure 9**).

For studying the suprapubic perivesical site, put the probe with the indicator toward the right side of the body just above the pubic symphysis and slightly tilt and fan the probe toward the pelvic, the bladder will come out as a pouch full of fluid, for determining whether there is any free fluid around the bladder, the most specific site is its posterior (Douglas pouch in female, and also posterior to the womb is potential to get fluid in there); for this goal, just tilt the probe somehow to see the posterior part of the bladder better and then change it into coronal position as the indicator toward the head, this maneuver will change the operator's point of view from axial into coronal and the posterior side of the bladder may come into the field better, i.e., what is shown on the right side of the screen (probe is indicating toward the head) is lay on the posterior side of the bladder (**Figure 10**).

Meanwhile, the sub-xiphoid pericardial view is the 4th side of the classic FAST, in case it could not achievable, some recommend for left sternal border window for

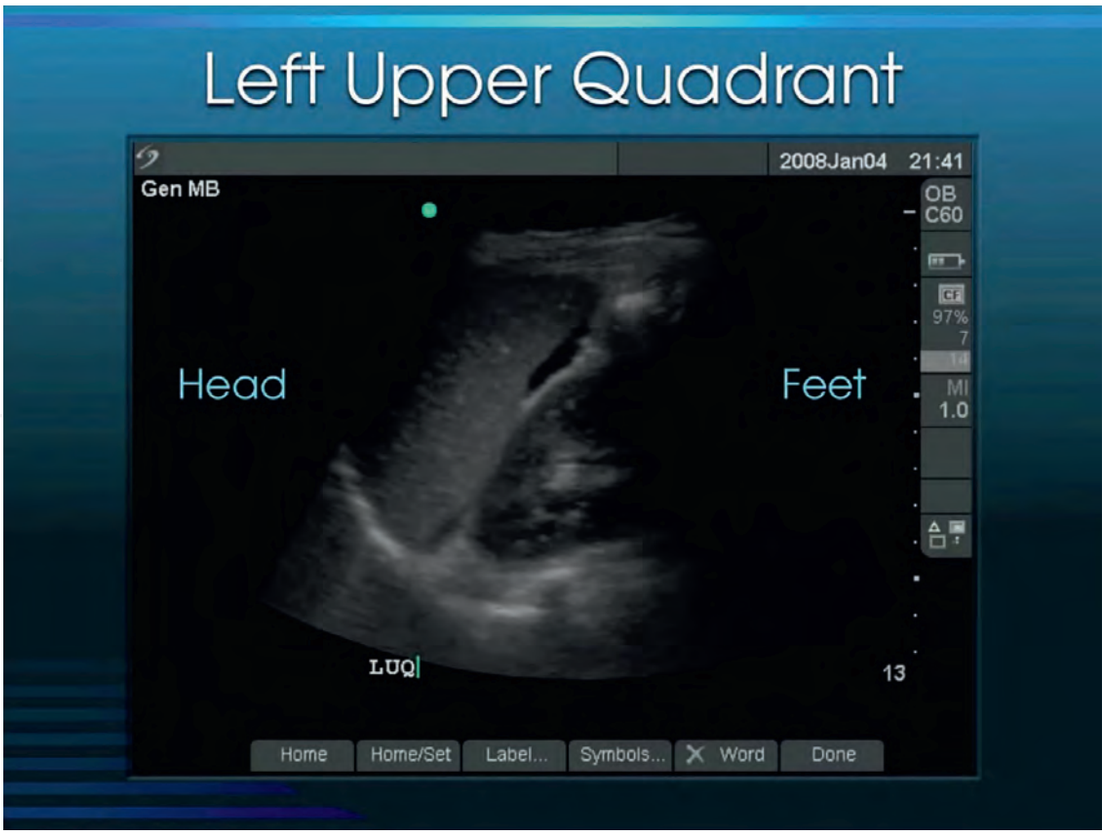

Figure 9.
A positive FAST exam on left splenorenal (Courtesy of Dr. John Christian Fox).

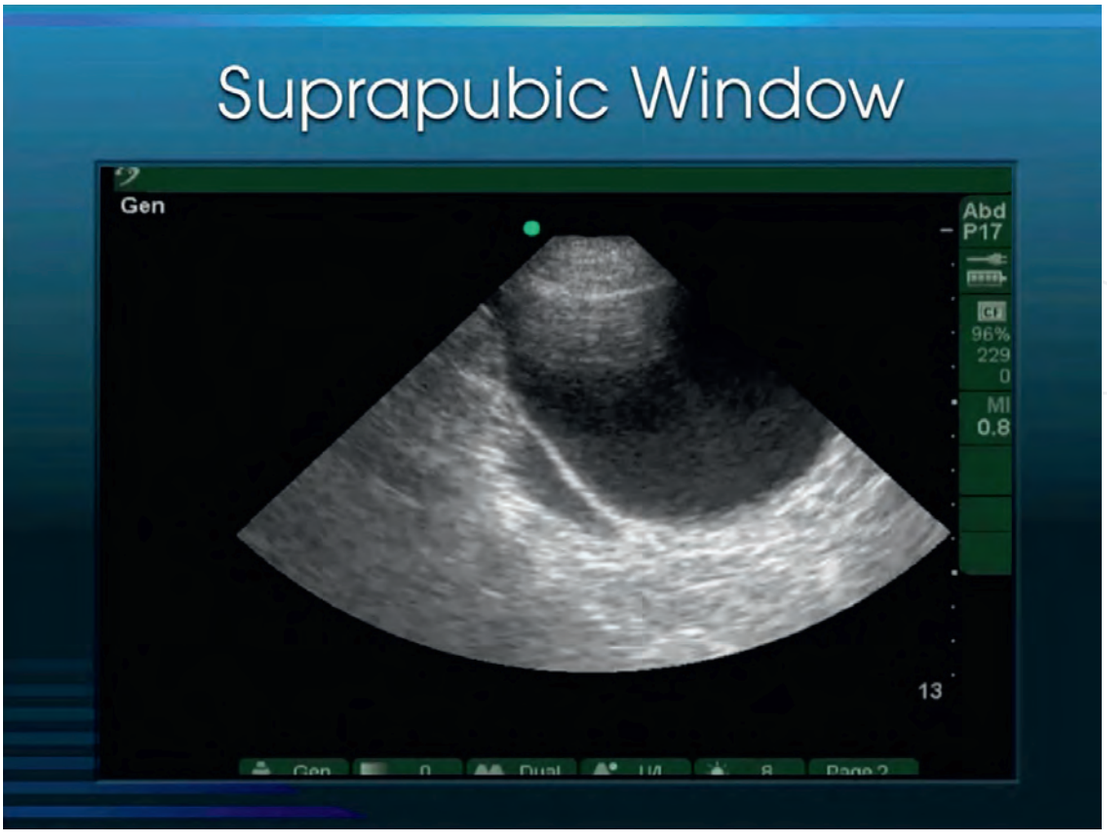

Figure 10.
A positive FAST exam on suprapubic perivesial (Courtesy of Dr. John Christian Fox).

this goal. However, before starting from the sub-xiphoid, increase the depth of the machine for more than 20 cm in an adult patient, put the probe with the indicator toward the right side, and try to open this window using the liver medium on the right side, because of the scattering phenomenon of the gastric gas that may obscure the field, if the image came out to study the heart as a four-chamber view with right ventricle, which lays on top of the liver (the chamber is near to the probe), the left ventricle is behind it on the screen, the right atrium is the chamber lays on the right side of the screen, and the left atrium is what leftover far from the probe (**Figure 11**). However, in case this image was not available, more pressure may be needed to better visualize the field, but some references prohibit it in children due to the probability of sudden cardiac arrest, at this time the parasternal view may be much more helpful.

After completing this four-site ultrasound examination, for extending the assessment for the trauma, it's time for assessing chest fields for possible pneumothorax or hemothorax. We would expect the gas to be higher and the liquid to be lower, so if pneumothorax is made, it could be on the anterior part of the chest. Using motion mode (M-Mode) should determine the pleural motion better than a normal lung sliding (or sea-shore sign) (**Figure 12**); however, in pneumothorax, this sliding is not shown because all of the points from the skin to the pleura are standstill (they do not move like normal lung movement), they demonstrate a stratosphere (or barcode) sign, by the way sometimes in pneumothoraces that does not fulfill the field, a lung point be may observed (**Figure 13**). For this purpose, use a high-frequency linear probe or decrease the depth of the curve probe, which was used during other parts of the FAST exam to 3–4 cm. Put the probe with the indicator toward the patient's head and start studying the lung for possible pneumothoraces on the anterior part of each

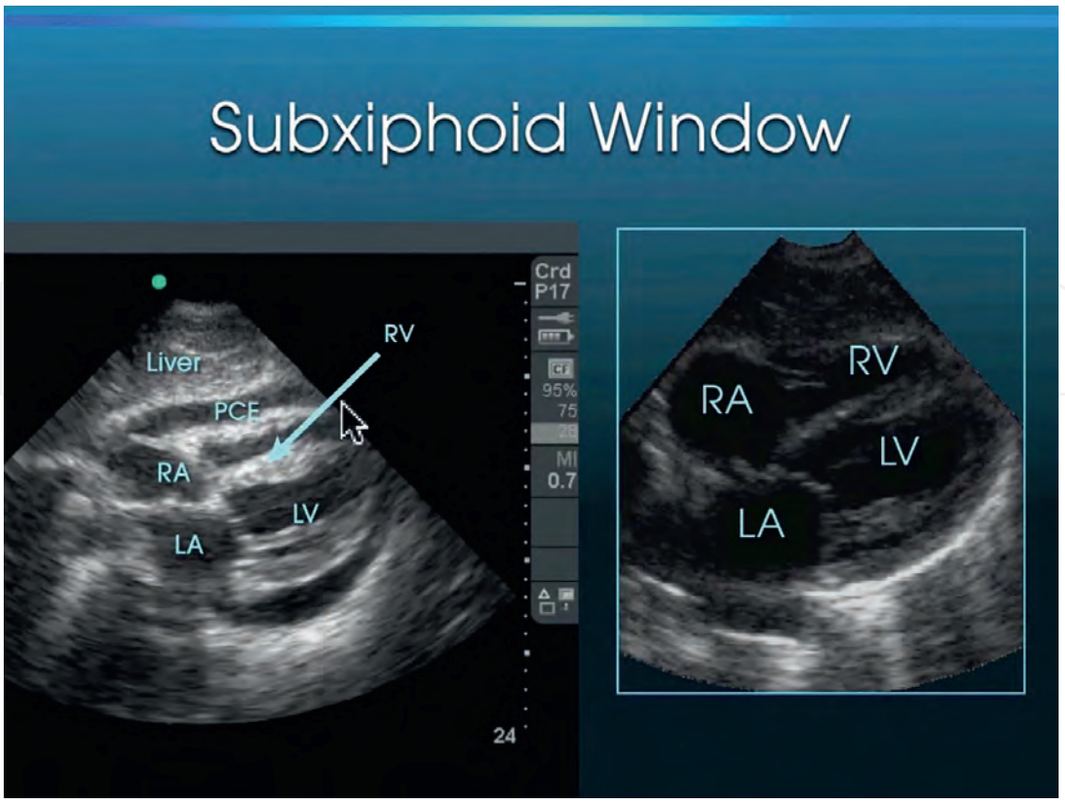

Figure 11.
A positive FAST exam as pericardial effusion (Courtesy of Dr. John Christian Fox).

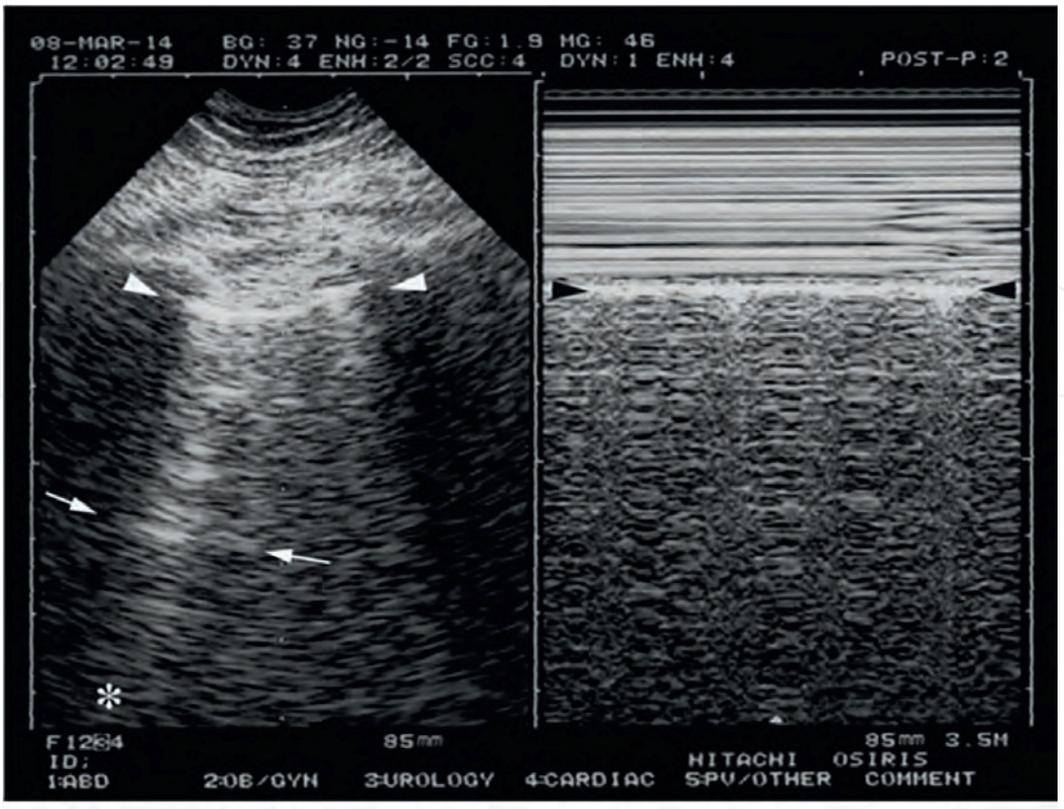

Figure 12.
Normal Lung-Sliding (Sea-Shore sign) (Courtesy of Daniel A. Lichtenstein).

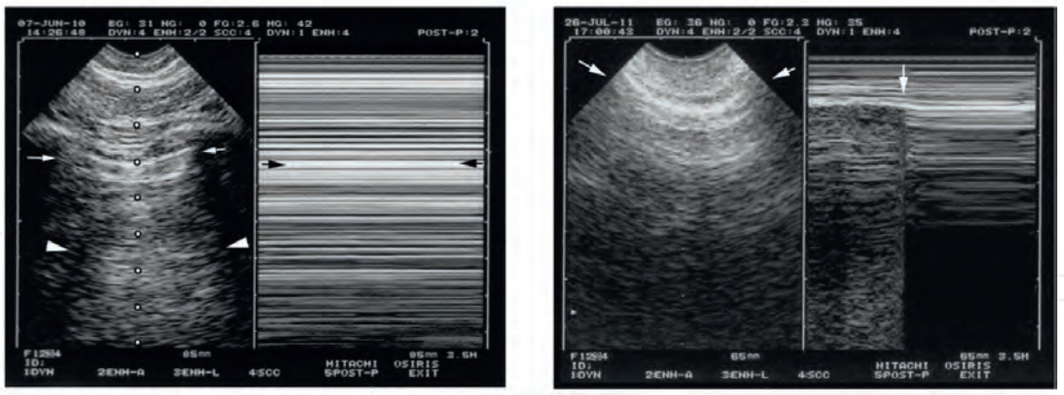

Figure 13.
Stratosphere & lung-point signs of pneumothorax (Courtesy of Daniel A. Lichtenstein).

side from the upper clavicular region up to down rib cages. For assessing the fluid (e.g., hemothorax or pleural effusion), the best place is superior to the diaphragm, where it's expected that the chest fluid may be stuck, it could also be examined while hepatorenal and splenorenal examination and considering diminished mirror effect of the diaphragm toward the head site. Video 4 (https://www.youtube.com/watch?v=klqeADRgvkM&list=PL2AGl6-lzXJTRn113DAv1Iybh_AFHBwFX, https://www.aparat.com/v/RBo4v) has a full list play of the E-FAST exam.

Even IV cannulation is much safer and easier with the power of ultrasound; however, in almost every procedure using ultrasound, two operators are recommended, the sono-expert to hold the probe and bring the good field of action, and the other operator to do the procedure. For this goal, first the vein should find in the axial plane and place the target in mid-line with the probe; measure the depth of the target from the skin (that probe lies on it), with the law of trigonometry in mind, presume an isosceles right triangle by manipulating the needle in the equal length of the target depth in a 45-degree angle. Change the probe position from axial, parallel to the needle that indicates toward needle (this maneuver shows all of the vein in a longitudinal view) and advance the needle then, popping into the vessel could also be seen on the screen, and cannulation is achieved [2]. This technique is the principal for almost every vascular cannulation or regional nerve block, Videos 5 (https://www.youtube.com/watch?v=uHfeyAYiWOc&list=PL9883F0497505F4B1, https://www.aparat.com/v/U1TA0?t=199), 6 (https://www.youtube.com/watch?v=EUMqxKJ2mPA&list=PL2AGl6-lzXJRBLHhfE-VsywsfUxqnHBHXG, https://www.aparat.com/v/0cZr5?t=807) and 14 (https://www.youtube.com/watch?v=ndnZxAcNjdg&list=PL09BFE9E4CB8A7050, https://www.youtube.com/watch?v=xvAY_bu_S7A&list=PL2AGl6-lzXJSYEVni4b7V8yAC8pmtccaX) are playlists of these procedures [3, 4, 9].

There's another ultrasound protocol for critical-care and hypotensive patients that is known as the RUSH exam, the Rapid Ultrasound for Shock and Hemorrhage [1, 10, 11]. It was first described in 2006 and got into medical literature 3–4 years by. Also, trauma patients may be in shock, and other than "Blood on the floor, and four/five more (Chest, Abdomen, Pelvic, Femur(long bones) and SCALP are potential sites for life-threatening bleeding)," a RUSH exam may empower the physicians' consideration on the possible reason of the shock (other than blood loss). The RUSH protocol divides the homeostatic system into "Pump," "Tank," and "Pipes." Which is an example of "Heart," "Potential spaces," and "Vessels," respectively.

Focused primary echocardiography could study the heart for its musculature and valve movements, their insufficiency could be obtained, and more results

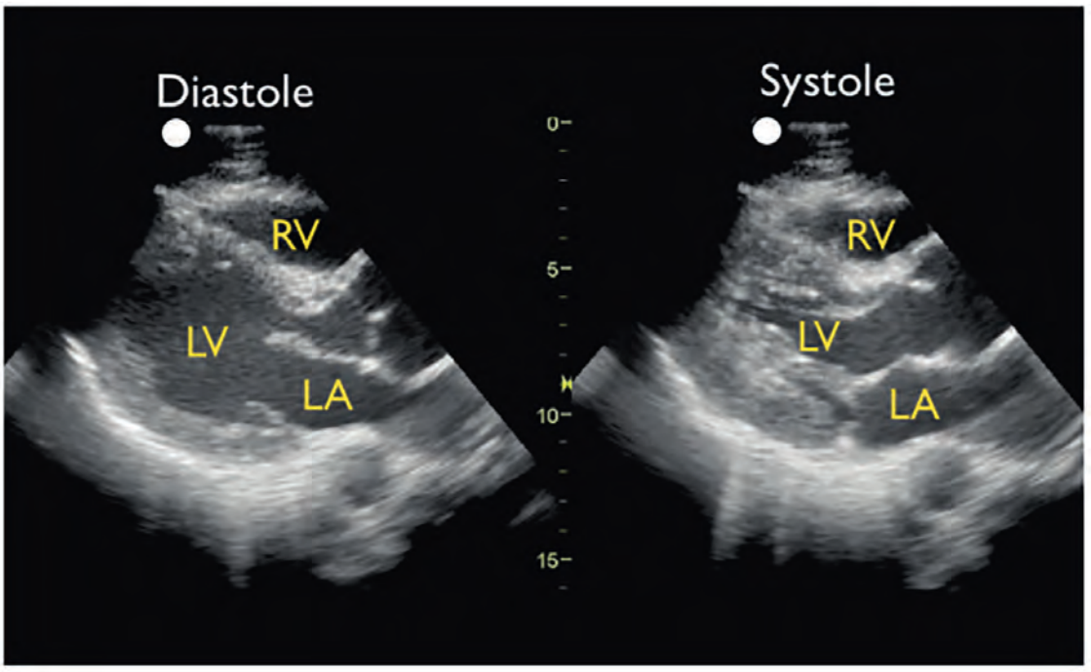

Figure 14.
Long-axis parasternal view.

could be achieved than just pericardial effusion purpose of the E-FAST exam. For this goal, start with the parasternal, then apical four-chamber, and finally the sub-xiphoid windows. On the long-axis parasternal the indicator of the probe toward the right shoulder, while on the short-axis parasternal, it aims at the left shoulder. The long-axis and short-axis views are demonstrated in **Figures 14** and **15** in systole and diastole, also ventricular contractility and LVEF could be obtained through this window using M-Mode, which is demonstrated in **Figure 16**. for achieving the apical view, put the probe on the Point of Maximum Impulse (PMI) on the left 5–6th mid-clavicular inter-costal space, both the probe and screen indicator should be in the same position (if it wasn't changed after the short-axis view, it's expected to be on the left side), what appear in the four-chamber view are two ventricles adjacent to the probe and two atria far from the probe, the right heart is on the right side and the left is on the left-side (pay attention to the probe and screen indicators' sameness), using Color-Doppler mode could bring the valves functionality and chambers' flow very well. And finally, the sub-xiphoid view, which is the standard recommended view in the FAST exam and was discussed there (Video 7, https://www.youtube.com/watch?v=1UJ6RodOSTw&list=PL2AGl6-lzXJRp3Dh0t1YZ2qsyic0msYDd, https://www.aparat.com/v/bmzqQ).

The "tank" or potential spaces are mostly covered by E-FAST examinations, the potential spaces for free fluid and great vessels like the Aorta and the IVC. The aorta and IVC both could be part of a cardiac exam too, thus they are great vessels of the body, in a shock patient, the aorta could be torn or aneurysmal, where both could be evaluated in descending abdominal aorta by using low-frequency convex or phased-array probe, both in axial and sagittal planes. Just it should be kept in mind that it may need extra force to pull over intestinal and gastric gas to find out vascular structures, also IVC lay just on the right side of the aorta and could be examined with the aorta or from the right hepatic window in sagittal plain (**Figure 17** and Video 8, https://www.youtube.com/

DOI: http://dx.doi.org/10.5772/intechopen.108506

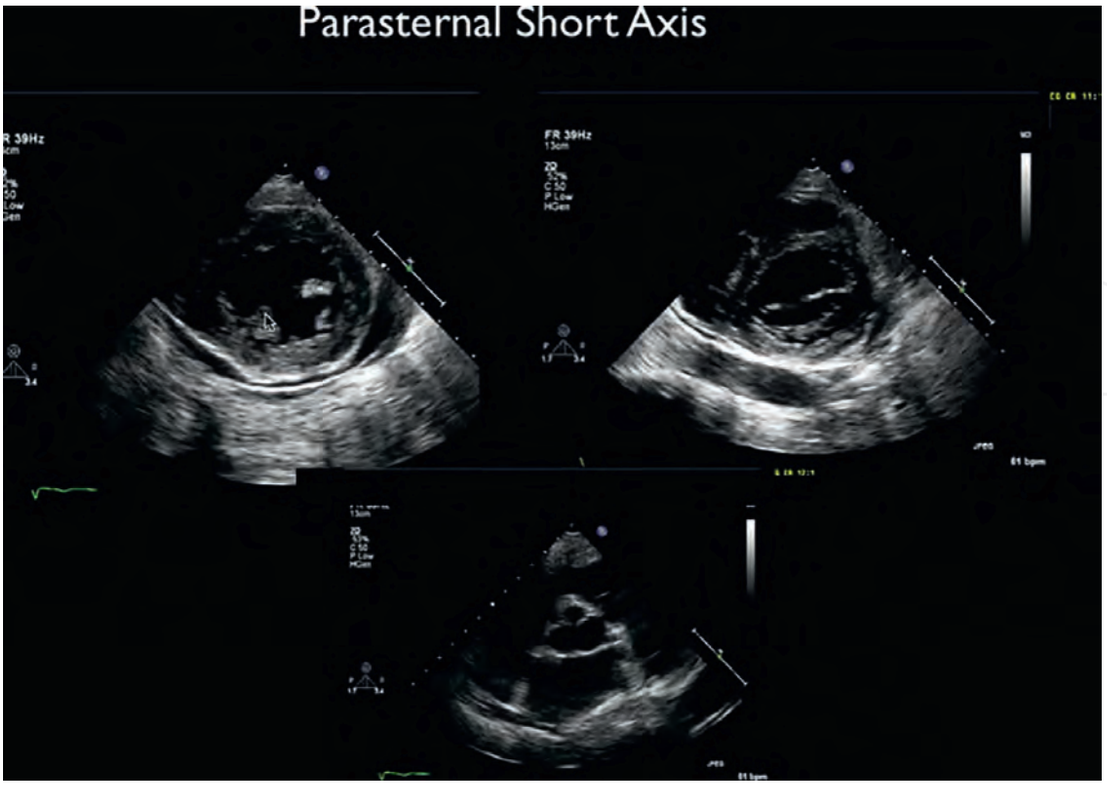

Figure 15.
Short-axis parasternal view for mitral valve (Courtesy of Dr. John Christian Fox).

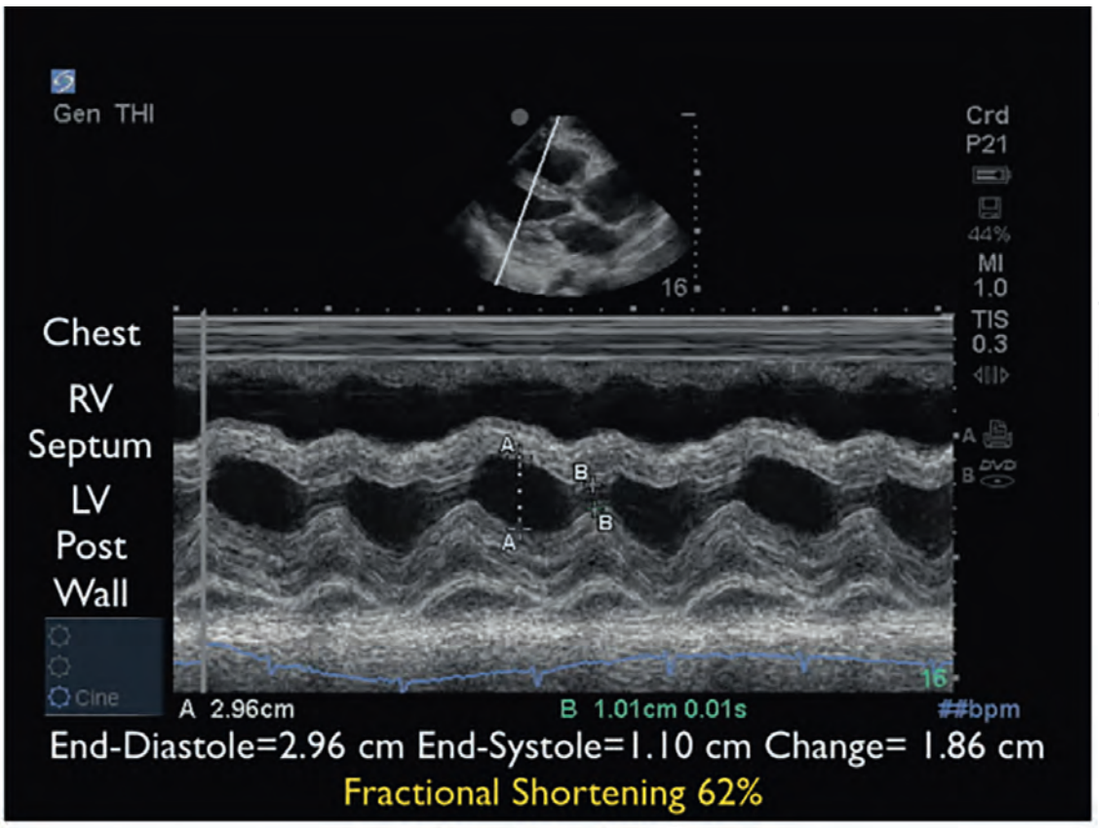

Figure 16.
Using M-mode for assessing contractility.

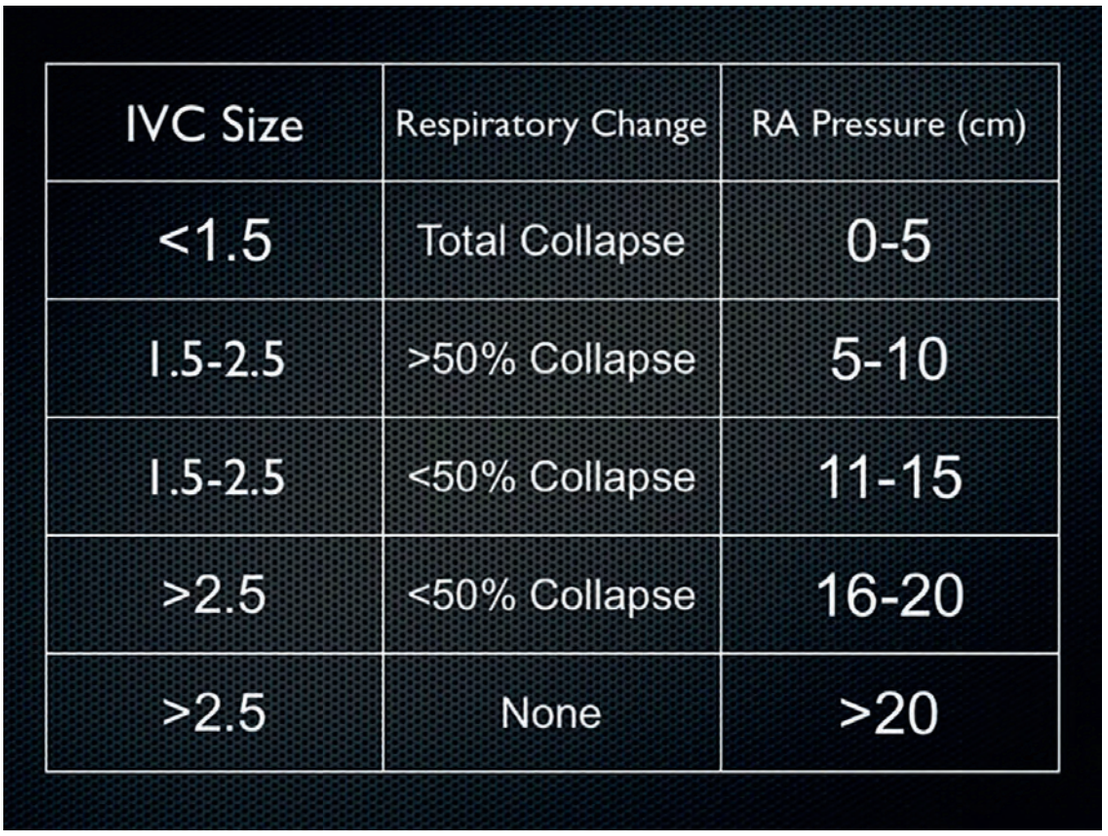

IVC Size	Respiratory Change	RA Pressure (cm)
<1.5	Total Collapse	0-5
1.5-2.5	>50% Collapse	5-10
1.5-2.5	<50% Collapse	11-15
>2.5	<50% Collapse	16-20
>2.5	None	>20

Figure 17.
IVC size and changes correlation with CVP.

watch?v=khD3dnxEt2o&list=PL2AGl6-lzXJRtdqShRXDozbmtx6Pw4fZC, https://www.aparat.com/v/bmzqQ?t=1247).

And finally, the "pipes" are mostly referred to deep veins for DVTs. The three-point access that consists of femoral, popliteal, and greater saphenous veins on each side is the acceptable examination for Deep Vein studies (Video 8, https://www.youtube.com/watch?v=khD3dnxEt2o&list=PL2AGl6-lzXJRtdqShRXDozbmtx6Pw4fZC, https://www.aparat.com/v/bmzqQ?t=1247).

All of these exams could be summarized as "HI MAP ED" mnemonic [11]:

	Step no. 1	Step no. 2	Step no. 3
Pump	Pericardial effusion: (a) Effusion present? (b) Signs of tamponade? Diastolic collapse of R Vent +/− R Atrium?	Left ventricular contractility: (a) Hyperdynamic? (b) Normal? (c) Decreased?	Right ventricular strain: (a) Increased size of RV? (b) Septal displacement from right to left?
Tank	Tank volume: (1) Inferior vena cava: (a) Large size/small Insp collapse? —CVP high— (b) Small size/large Insp collapse? —CVP Low— (2) Internal jugular veins: (a) Small or large?	Tank leakiness: (1) E-FAST exam: (a) Free fluid Abd/Pelvis? (b) Free fluid thoracic cavity? (2) Pulm edema: Lung rockets?	Tank compromise: Tension pneumothorax? (a) Absent lung sliding? (b) Absent comet tails?
Pipes	Abdominal aorta aneurysm: Abd aorta > 3 cm?	Thoracic aorta aneurysm/dissection: (a) Aortic root > 3.8 cm? (b) Intimal flap? (c) Thor aorta > 5 cm?	(1) Femoral vein DVT? Noncompressible vessel? (2) Popliteal vein DVT? Noncompressible vessel?

Figure 18.
Using the RUSH protocol to diagnose the type of shock.

RUSH exam	Hypovolemic shock	Cardiogenic shock	Obstructive shock	Distributive shock
Pump	Hypercontractile heart Small heart size	Hypocontractile heart Dilated heart size	Pericardial effusion, RV strain Hypercontractile heart	Hypercontractile heart (early sepsis) Hypocontractile heart (late sepsis)
Tank	Flat IVC Flat IJV Peritoneal fluid Pleural fluid	Distended IVC Distended IJV Lung rockets Pleural effusions, ascites	Distended IVC Distended IJV Absent lung sliding (PTX)	Normal/small IVC Normal/small IJV Pleural fluid (empyema) Peritoneal fluid (peritonitis)
Pipes	AAA Aortic dissection	Normal	DVT	Normal

Figure 19.
RUSH protocol summary.

- Heart
- IVC
- Morrison pouch and complete FAST exam
- Aorta
- Pleural space and pneumothorax
- Ectopic pregnancy (Video 13, https://www.youtube.com/watch?v=GBpiF7ML1CA&list=PL2AGl6-lzXJT4sk_DMVQtBNapC36AgTZp, https://www.aparat.com/v/ukBwf)
- DVTand the final diagnosis of shock reason could get whether the "pump," "tank," or "pipes" are responsible; **Figures 18** and **19** summarize the RUSH protocol (Video 9, https://www.youtube.com/watch?v=9UyVHqvGgHE&list=PL2AGl6-lzXJS9fkywFRsQIwzp31-Lc1nX, https://www.aparat.com/v/zEvcw).

6. Empowering diagnosis and neurological assessment

The high-frequency linear probe could be used for skin and soft tissue examination, e.g., cellulitis and soft tissue infection's cobblestone pattern (Video 12, https://www.aparat.com/v/U1TA0?t=71). Using this probe also could be the on-site tool for assessing tendons and muscles movements, bone fractures (also to assess whether fracture bone has been reduced after manipulation), and other orthopedic examinations (Video 11, https://www.youtube.com/watch?v=7G56DN38mz8&list=PLEF41F6DAEE3FD1A8, https://www.aparat.com/v/0cZr5?t=5). As described in IV canulation, the regional nerve block could be done using ultrasound power though with fewer complications (Video 14, https://www.youtube.com/watch?v=ndnZxAcNjdg&list=PL09BFE9E4CB8A7050, https://www.youtube.com/watch?v=xvAY_bu_S7A&list=PL2AGl6-lzXJSYEVni4b7V8yAC8pmtccaX).

However, ocular ultrasound may be the indescribable use of the linear probe in the emergency department, other than studying the orbit structure for lens and retinal placement or detachments, Iris muscles movement and pupil reflex, and anterior and posterior chambers of the eyeball, the rise of Intra Cranial Pressure (ICP) could affect optic nerve (Cranial Nerve II) and widen its diameter, this could be assessed after freezing the image on the screen and measuring the optic nerve's external diameter in 3 mm length to the orbit entrance, whether this sheath is more than 5 mm

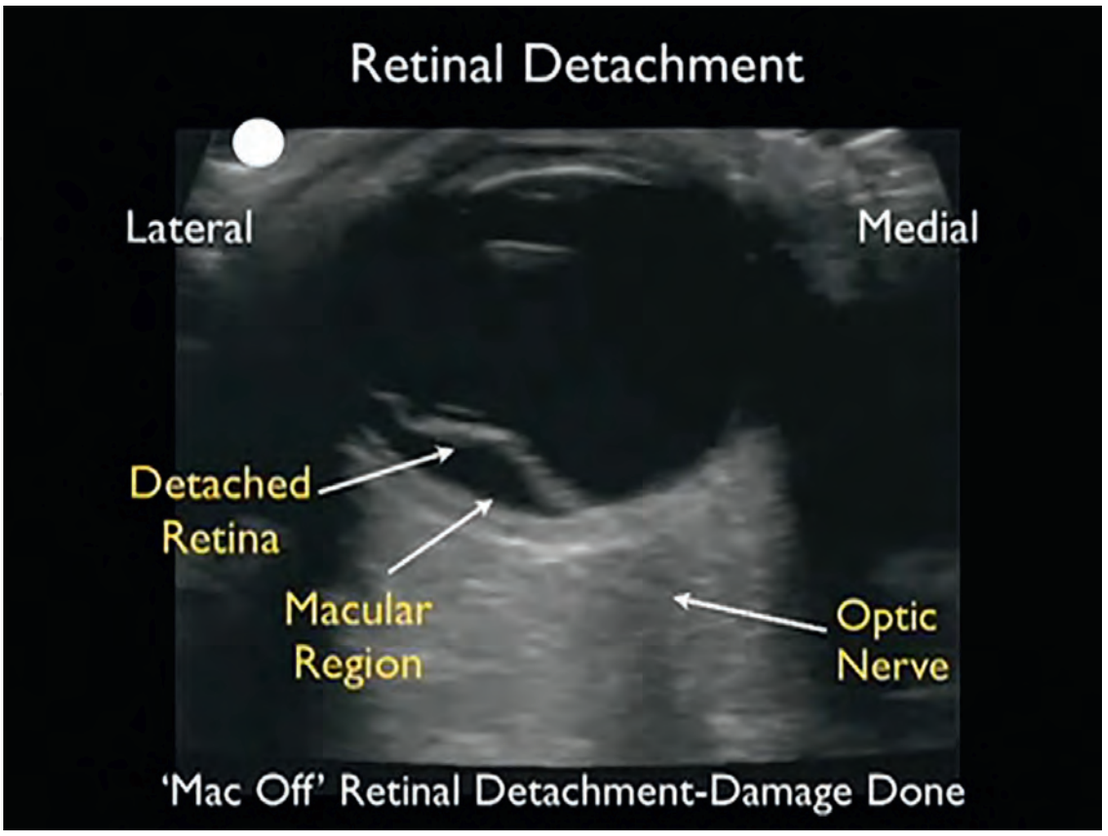

Figure 20.
Retinal detachment in occular B-mode ultrasound.

in diameter length it shows a rise in ICP, **Figure 20** shows retinal detachment, while other ocular ultrasound anatomical structures (Video 10, https://www.youtube.com/watch?v=uPqTz4OuNd0&list=PL2AGl6-lzXJTPj1GxVxCVyeg_srRs7oVg, https://www.aparat.com/v/0cZr5?t=235).

7. Conclusions

Using ultrasound alongside clinical examinations or during critical-care procedures empowers the ability of healthcare providers and physicians for better clinical decision makings and less invasive procedures. Like other clinical procedures, those who try and study more on the ultrasound could achieve better results, we recommend the use of ultrasound in any possible clinical situation for all providers, and the links that are mentioned in the appendices are highly recommended for reference.

Acknowledgements

I would like to mention the support and consideration of my kind family, especially my lovely wife who has always been there; besides, I need to acknowledge all my colleagues in the emergency department of Imam Khomeini hospital, Sarab, Iran; specifically the ward supervisor Mr. Masoud Abeshzadeh, ward-nurses Mrs. Feyzi, Mr. Reza Sayyareh, Mr. Mohammad Shokri, and my supportive alumni Dr. Roghayyeh Yaghoubi and Dr. Saba Nemati, for all of their kind and support during working shifts

and recording tutorial videos. Also, I have to greet whoever tries to make the knowledge and experience sharing free and achievable for all around the world, especially "InTech Open" and "Free Software Foundation."

Conflict of interest

There is no conflict of interest to report.

Acronyms and abbreviations

ACS	American College of Surgeons
ACLS	Advanced Cardiac Life Support
AHA	American Heart Association
ATLS	Advanced Trauma Life Support
BLUE	Bedside Lung Ultrasound in Emergency department
COT	Committee On Trauma
DVT	Deep Vein Thrombosis
EFAST	Extended Focused Assessment Sonography for Trauma
ETT	Endo Tracheal Tube
ICP	Intra Cranial Pressure
IVC	Inferior Vena Cava
LEMON	Look externally, Evaluate 3-3-2, Mallampati score, Obstruction, Neck mobility
LMA	Laryngeal Mask Airway
PMI	Point of Maximum Impluse
POCUS	Point Of Care UltraSound
RUSH	Rapid Ultrasound in Shock and Hemorrhage

Appendices and nomenclature

1. https://www.aparat.com/v/9ifZw?playlist=1629800 (My Aparat.com channel's playlist for Ultrasound Tutor—In Persian Language).

2. https://www.youtube.com/c/sonosite (Fujifilm—Sonosite Youtube! Channel).

3. https://www.youtube.com/user/jfoxmd (Dr. John Christian Fox's Youtube! Channel).

Author details

© 2022 Mohammad Meshkini[1,2]*. Originally published in "Ultrasound Empowered Trauma Management." IntechOpen under the terms of the Creative Commons Attribution License (http://creativecommons.org/licenses/by/3.0). Available from http://dx.doi.org/10.5772/intechopen.108506

1 Road Traffic Injury Research Center (Tabriz International Safe Community Support Center), Tabriz University of Medical Sciences, Tabriz, Iran

2 Emergency Medicine Department, Sarab Faculty of Medical Sciences, Sarab, Iran

References

[1] Díaz-Gómez JL, Mayo PH, Koenig SJ. Point-of-care ultrasonography The New England Journal of Medicine 2021;**385**(17):1593-1602.

[2] Joing S, Strote S, Caroon L, Wall C, Hess J, Roline C, et al. Ultrasound-guided peripheral IV placement. The New England Journal of Medicine. 2012;**366**(25):e38

[3] Schulman PM, Gerstein NS, Merkel MJ, Braner DA, Tegtmeyer K. Ultrasound-guided cannulation of the subclavian vein. The New England Journal of Medicine. 2018;**379**(1):e1

[4] Ortega R, Song M, Hansen CJ, Barash P. Ultrasound-guided internal jugular vein cannulation. The New England Journal of Medicine. 2010;**362**(16):e57

[5] Adi O, Kok MS, Abdull Wahab SF. Focused airway ultrasound: An armamentarium in future airway management. Journal of Emergency and Critical Care Medicine. 2019;**3**:31-31

[6] Canelli R, Leo M, Mizelle J, Shrestha GS, Patel N, Ortega R. Use of eFAST in patients with injury to the thorax or abdomen. The New England Journal of Medicine. 2022;**386**(10):e23

[7] Lichtenstein DA. BLUE-protocol and FALLS-protocol. Chest. 2015;**147**(6):1659-1670

[8] Chardouli M, Yasinzadeh M, Meshkini M, Jalilvand H, Basir Ghafouri H, Sadeghi-Bazargani H, et al. A review on using ultrasound for evaluation of pediatric blunt abdominal trauma. Frontiers in Emergency Medicine. 2021. Available from: https://publish.kne-publishing.com/index.php/FEM/article/view/7680

[9] Peris A, Tutino L, Cianchi G, Gensini G. Ultrasound guidance for pleural-catheter placement. The New England Journal of Medicine. 2018;**378**(14):e19

[10] Seif D, Perera P, Mailhot T, Riley D, Mandavia D. Bedside ultrasound in resuscitation and the rapid ultrasound in shock protocol. Critical Care Research and Practice. 2012;**2012**:1-14

[11] EmCrit Project. Rapid ultrasound for shock and hypotension. Available from: https://emcrit.org/rush-exam/original-rush-article/

Chapter 10

Breaking Through the Speed Barrier — Advancements in High-Speed Imaging

G. P. P. Gunarathne

Additional information is available at the end of the chapter

http://dx.doi.org/10.5772/56378

1. Introduction

1.1. Origin, expansion and applications of ultrasonic imaging

History and the discoveries of the use of ultrasound can be traced back to late 18th century, but one of the major steps toward the practical use of ultrasound may be attributed to Lewis Nixon who invented the very first sonar type listening device in 1906 as a way of detecting icebergs [1]. Rapid developments of the use of ultrasound occurred since then, particularly after world war II; initially for underwater (sonar) and industrial uses, followed by developments for medical applications [2, 3]. Today, the technology is widespread in Medicine, Non Destructive Testing (NDT) and Sonar in many specialised areas such as: industrial and medical imaging, study and classification of the properties of material and biological tissues, seismic explorations high-intensity applications etc. and the applications are growing. These rapid advances are directly related to the parallel advancements in electronics, computing, and transducer technology together with sophisticated signal processing techniques.

Irrespective of the field of applications, arguably one of the most important applications of ultrasound is "Imaging", which is the chosen subject of this chapter. However, it is important to note that imaging as applied to the three main application areas mentioned above; namely, NDT, Sonar and Medicine have fundamental similarities and also differences. For example, the speed of sound in water in the case of sonar and biological tissues are comparable (~1450m/s) but sonar is extremely long range.

In the case of NDT, the speeds of sound in industrial materials are generally very much higher, although the penetration distances are comparable to that for medical imaging. On the other hand, sonar and medical imaging primarily relies on one form of ultrasound propagation, namely, compressional waves while in solid material, there are multiple propagational modes,

such as compressional, shear, surface, creep, lamb and torsional waves etc. These different modalities have widely different characteristics and they can coexist with possible mode conversions depending on the particular geometry and test scenario. In NDT, the co-existence or co-generation of this multimode propagation can be both advantages in some situations, and equally become a nuisance in other cases.

In processing and assessing an ultrasound image, one of the most striking differences between industrial NDT and medical imaging is that in the case of the latter, there is good pre-anatomical knowledge of the part of the anatomy being examined; often with the possibility of supplementary data obtained from other forms of imaging such as MRI, CT scans etc. However, for NDT inspection, the target features (shapes, sizes and orientation etc.) are almost always largely unknown, thus the interpretation is largely based on the reliability of the images being produced. This is a major challenge in industrial imaging applications. On the positive side, the targets being imaged in NDT applications e.g. a crack in a structure generally tends to appear as a good acoustic discontinuity yielding good Signal-to-noise ratio (SNR) compared to that from a tissue boundary, since the latter is dependent on small impedance contrast.

1.1.1. Dynamic range considerations

For all imaging applications, the signal dynamic range is an extremely important consideration. Usually this could be very high; far above that may be accommodated by display equipment. For medical Imaging, the dynamic range of signals could be of the order of order of 100dB covering both backscattered signals from tissues and specular reflections. (However, the range of interest is of the order of 40 to 50 dB, which is the range covered by backscattered signals). Although impedance contrast is generally high in NDT and sonar, dynamic range of signals can still be very large depending on the application, not necessarily because of high attenuation as in the case of biological tissues but because of the size of the targets such as micro-defects in NDT or beam divergence in the case of sonar. In the case of sonar, the range is extreme and the signals of interest could be of the order of several hundred millivolts to sub-micro volts. The dynamic range can be evaluated for homogeneous media, such as water, by considering signal loss between targets of same strength placed at different axial distances (R_1 & R_2) form equation 1 below, which helps formulating compensating strategies.

$$Loss(dB) = 20\log \frac{R_2}{R_1} + 2 \propto (R_2 - R_1) \tag{1}$$

Where $\propto$ is the attenuation coefficient of the medium at the frequency of interest. Accommodating large dynamic range and depth gain compensation are therefore features common to all imaging systems; albeit for different reasons. Once the ranges and the loss characteristics are known, accommodation can be handled electronically, e.g. by using logarithmic compression and Time-varying-gain (TVG) functions to accommodate the signals within the much limited display dynamic range.

In order to understand the potential of imaging and areas of improvement, it is necessary to examine the fundamental characteristics of common imaging modalities, which is the subject

http://dx.doi.org/10.5772/56378

of the following section. The discussion does not include a comprehensive treatment of imaging techniques in use, but the ones that represent properties central to the understanding of primary limitations.

1.2. General principles

The simplest form of ultrasonic visualisation is what is known as the A-scan. Here an ultrasonic transducer generates a short pulse of high frequency sound which is coupled to the test medium. Echoes generated from any acoustic discontinuities within the path of the ultrasound beam are received, usually by the same transducer, and are displayed on a screen or a monitor as intensity modulated signals. The technique essentially provides (a) Target-depth information (b) An indication of the extent of the discontinuity and to a much lesser extent information on its orientation or shape. Since the time required for displaying the echoes is virtually equal to the time of flight of the acoustic pulse within the object medium, it gives the maximum temporal resolution for moving targets. However, the interpretation and information obtained from an A-scan (1- spatial dimension) or that derived from it is very limited, highly operator-dependent and therefore of limited use in diagnostic applications.

However, a collection of A-scans in a given plane in the test object could provide a two-dimensional map (or an image) of the acoustic discontinuities. This requires acquisition, storage and display of successive A-scan lines requiring digital data storage and processing. These line-serial scans may be generated in a number of ways: mechanically moving the transducer along a given direction; using an array of transducers which are switched on in succession to mimic a mechanical movement (linear or curvilinear array scanning). Images thus generated represent a two-dimensional (2-D) view of the target medium and are commonly known as B-scans.

Alternatively, the ultrasound beam may be electronically steered using a transducer array (phased array scanning) or by a mechanically rotating transducer. The 2-D images thus obtained are normally referred to as sector B-scans.

1.2.1. Real-time versus determinism

One of the confusing terminologies in imaging (or any other form of data presentation) is *"Real-time"*. The naturally implied meaning of the term real-time is: *"as it happens"*. This meaning is incompatible with laws of Physics since nothing can be observed at the same instant as something happens. So, image presentation can only approach this ideal of real-time, provided that what an observer sees in an image is close enough to what was happening to the object as a whole, both in time and spatial resemblance. Then the expression "real-time" can be considered appropriate. For example, an observer seeing a trajectory of a meteoroid views this in real-time because the velocity of light is at least 6 to7 orders of magnitude higher than the moving object. But this is not the case, for example, seeing a moving heart valve in an ultrasound image taking a few milliseconds to form just one frame. Obviously, the image is temporally and spatially distorted. Therefore a target that appears to be moving in a succession of image frames is not seen "as it happens" and therefore not true real-time. The term *"Pseudo*

Real-time" is a more meaningful definition in such cases where the image is seen to be live, while the velocity ratio (i.e. the speed of the target to that of sound) is significant, or forming an image frame takes significant time.

On the other hand, *"Determinism"* can be an important concept in defining a key aspect of image integrity. This can be a predominant requirement – for example in quantitative image analysis where accurate spatial information is important. The use of the term "determinism" in this context does not really mean "as it happens" (although the time interval between a moving target and its presentation as an image is usually small). Determinism essentially means that the spatial integrity of a moving target is persevered in the image to a high degree. In the case of ultrasound the theoretical limit of spatial determinism can only be reached if a single ultrasound pulse emitted by an imaging device produces a complete image field of the object within its time of flight. This is clearly not achievable with the existing line-serial imaging technology, but it is one of the main features of the new hybrid imaging system described later in this chapter.

1.3. State-of-the-art techniques

In late 1980's, the techniques for generating 3-D images from a collection of 2-D images have been demonstrated [4]. Producing a single frame of such an image may have taken about 20 minutes then, but with the advancement of computing power and processing techniques, live 3-D and 4-D volume imaging reaching pseudo-real time volumes of surface features have now come into existence [4, 5].

One of the fairly recent additions to B-mode imaging is the so called Zone-sonography [6]. A main feature in this system is the acquisition of data from a relatively low number of zone sectors, as opposed to line-by-line acquisition, thereby significantly improving the temporal artefacts inherent with the conventional methods. It has been claimed that in some cases, this approach could produce speed improvements of up to 10 times compared to conventional line-serial imaging systems [6], although the zones in themselves are produced using serial scanning.

In addition, in the case of medical imaging, various echo enhancement techniques such as Coded Excitation (CE) and Digitally Encoded Ultrasound (DEU) which improve sensitivity, penetration and contrast are now been widely used [7, 8]. CE is a pulse compression technique which is designed to differentiate and boost weak return signals from deep within the body. This is done by transmitting an encoded pulse sequence, isolating the coded return signal and amplifying only this signal, while regaining longitudinal resolution which is distributed within the insonifying pulse train [7]. Some systems using CE can also show blood flow together with the body tissue as a B-mode image, without the need for overlay as would be the case with Doppler imaging. Tissue Harmonic Imaging (THI) is another widely used technique which reduces haze, clutter and image artefacts. In this approach, higher harmonic components of the echoes generated by the tissues due to non-linear propagation are used instead of the fundamental [9].

http://dx.doi.org/10.5772/56378

It is also important to note that there has been renewed interest in some of the early developments that uses direct imaging technology such as ultrasonic cameras and other imaging modalities [10, 11].

2. Limitations of the conventional technology

2.1. Basic limitations

A fundamental limitation with all of the above existing technology, which arises from the need for line-serial scanning, is the loss of temporal resolution. Attempts to improve this aspect by increasing computing power alone cannot give the full-potential of real-time imaging and may only give improvements with largely diminishing returns.

The second limitation, for example when using linear-array technology, is the use of smaller effective aperture compared to the size of the total array aperture, hence affecting the lateral resolution achievable. These two limitations are analysed below in order to reveal the extent to which they affect potential performance in ultrasonic imaging. Although the discussion is based on using linear arrays for clarity, the same considerations are valid for other configurations.

Figure 1 below shows a linear array transducer coupled to a test medium. The test object is assumed to be homogeneous and have a depth (d). The array consists of (N) elements with a total aperture size (A). The elements are usually switched on as a group (as shown) rather than single elements to improve lateral resolution, since this depends on the effective aperture, as depicted in equation 3. The next group in the firing sequence advance by only one element thus keeping the line resolution equal to the spacing of the array elements.

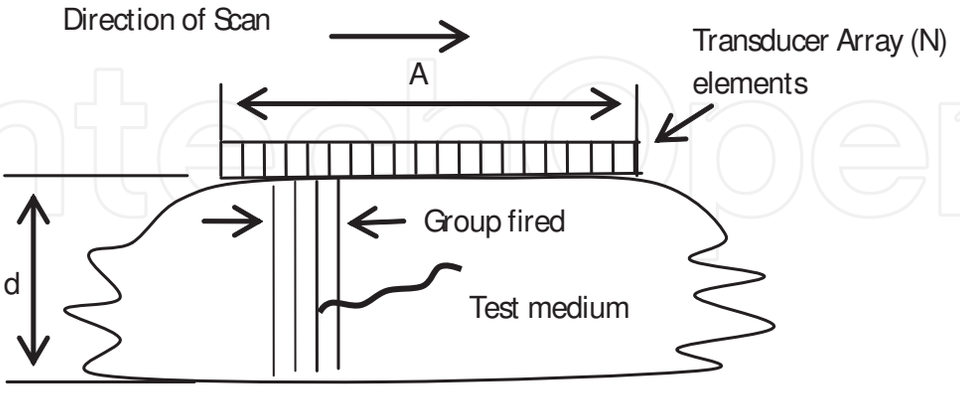

Figure 1. Line-serial scanning

Between individual scanning lines, a rest period (t_{rest}) is applied before firing the second consecutive group of elements as a practical requirement to allow multiple echoes to die down and time for acquisition, storage and display of data.

$$t_f = (N - N_G)\left[\left(\frac{2d}{c}\right) + t_{rest}\right]$$
$$\therefore \text{ Frame rate } \approx \frac{1}{t_f} \quad (2)$$

With reference to Figure 1, time (t_f) taken to produce one frame is:

where, N_G is the number of elements in the group firing at any one time and c is the speed of sound. Hence, as an example, when using an array with 150 elements, coupled to a medium in which the velocity of sound is 1.54 mm/μs, thickness 20 cm, $N_G = 50$, and neglecting t_{rest}, it can be seen that the maximum frame-rate achievable is about 75. This will be even less when t_{rest} is applied.

However, the above frame rate may sound adequate, and indeed so for many cases, but the line-serial scanning introduces a basic limitation in the case of fast moving targets such as heart valves or machinery. During the scanning time within a frame, one part of the target may have displaced significantly relative to another, causing spatial distortion, thus a frozen image of the target at any time may differ significantly from its actual position or shape. This is illustrated in Figure 2.

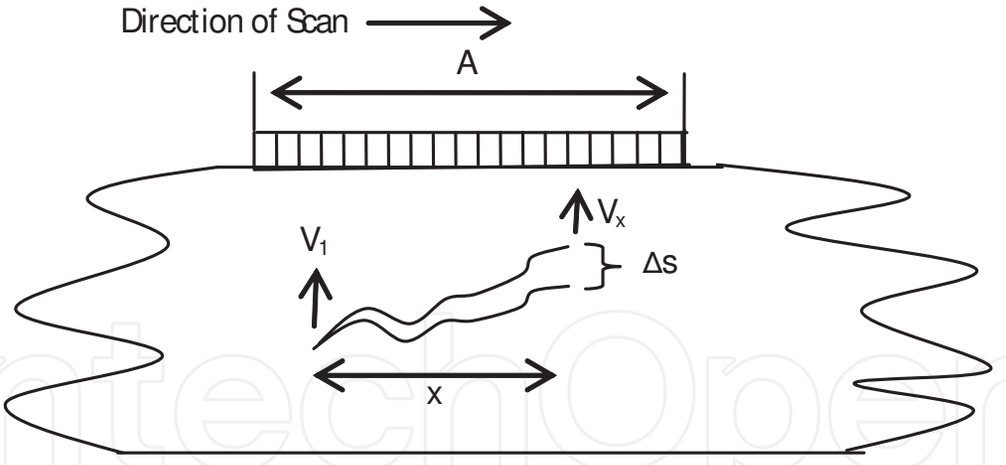

Figure 2. Formation of temporal artefacts

With reference to Figure 2, spatial distortion (Δs) could be written as:

$$\Delta s_{(x)} = \frac{x}{A} \times t_f \times v_x \quad (3)$$

where, v_X is the velocity of a point (x) on target.

http://dx.doi.org/10.5772/56378

The other limitation with a linear array scanner, as mentioned above, is the degradation of lateral resolution arising from the size of the aperture formed by the group of elements firing at any instant of time. The lateral resolution is limited by the beam width of the transducer or the group of elements. The diffraction limited beam width for a given transducer of aperture (D) could be expressed as:

$$\delta\theta = \frac{1.22\ \lambda}{D} \tag{4}$$

where, λ is the wavelength of sound in the medium. As can be clearly seen, for each scan line, D is determined by the number of elements within the group fired and this is clearly very much less than the total aperture size (A) of the array. Hence, the lateral resolution corresponding to that achievable with the fully available aperture is not realised.

2.2. Ideal properties of an imaging system

From the above discussion, it is clearly evident that two key properties of an ideal real-time ultrasonic imaging system is that it should be able to produce a complete image frame of the object volume from one insonifying pulse, while utilizing the full aperture available for each frame of the image. Additionally, an ideal system should produce focused images of the whole object field at the same instant of time irrespective of the distances of targets from the surface (Isochronicity) while maintaining accurate object-to-image spatial resemblance (image linearity). It is also clear that the existing technology utilising line-serial scanning cannot achieve these ideal properties and therefore alternative techniques may be needed to improve speed and high resolution capabilities beyond that feasible with conventional technology. This requires investigating non-conventional imaging modalities that can possess those capabilities, and the ways of overcoming limitations that may have precluded their use in practice. The next section presents some early developments that have some of the above key properties achieved through direct ultrasonic image reconstruction. Beyond academic interest, these techniques have not realised in large-scale use except in very specific applications due to other inherent problems.

3. Non-conventional methods

3.1. Direct ultrasonic imaging

Direct ultrasonic image visualization using alternative methods, such as ultrasonic holography, Bragg diffraction imaging etc. have been documented by many researchers in the past [12, 13, 14]. One such technique that has the above ideal properties is the Direct Ultrasonic Visualization of Defects (DUVD) system demonstrated by Hansted in the 1970's [12]. As schematically shown in Figure 3(a), this is a passive acousto-optical configuration which uses a pair of ultrasonic lenses with a common focus to form an ultrasonic image of the object field in a transparent medium from echoes received from a test object; much in the same way as an

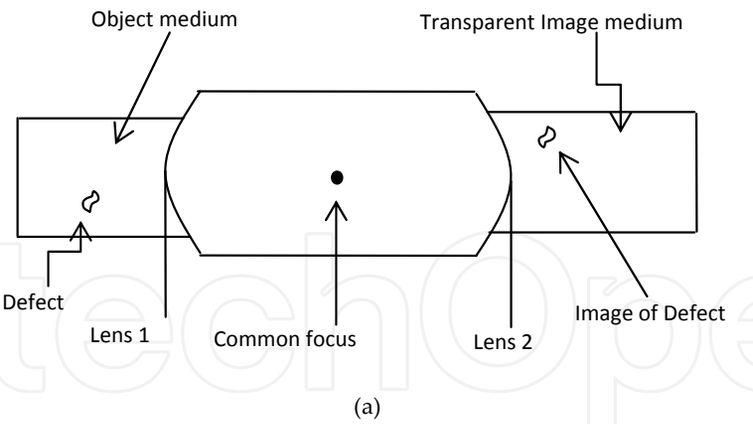

(a)

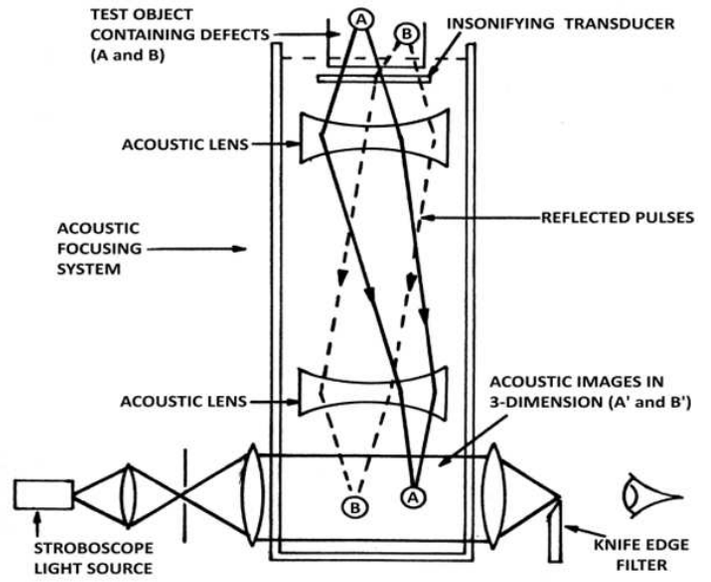

(b)

Figure 3. Direct Ultrasonic Imaging (DUVD) (a) DUVD Basic configuration; (b) A liquid coupled version of DUVD

optical lens producing an optical image. The insonifying transducer is physically bonded or intimately coupled via a liquid medium to the test object as part of Lens 1. Returned echoes are brought into focus by the acoustic lens arrangement in the image medium. The ultrasonic images thus produced is made visible by stroboscopic light which is synchronized to the transmitted insonifying ultrasound pulse, but with a fixed delay to allow the image to be formed and viewed at the point of best focus.

One of the DUVD realisations with liquid coupled lenses and a schlieren acoustooptical visualisation system developed by Hansted [12] is shown in Figure 3(b) above. It is interesting to note that the DUVD has many ideal features: It operates in Real-time; producing 3D images of the complete object field with every single insonifying pulse.

http://dx.doi.org/10.5772/56378

However, two main problems with the DUVD system shown above are: very low sensitivity and its design is such that the test objects virtually becomes part of the system; thus severely limiting flexibility as can be seen from the block diagram representation of the DUVD below (Figure 4).

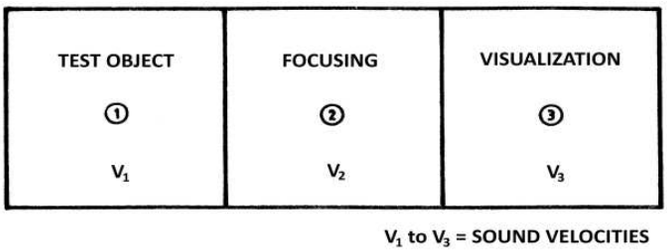

Figure 4. DUVD block schematic (Passive system). The insonifying transducer is bonded at the boundary between medium 1 & 2.

Further attempts to improve this approach have been reported by others in the late 1970's [13, 14]. But these were also passive systems and apart from theoretical interest the performance was practically inadequate.

3.2. A key development in the 1980's

3.2.1. Conceptual development

Because of the attractive features of direct ultrasonic imaging without the need for line serial scanning, a significant development was undertaken in the mid 1980's [15]. For initial feasibility studies, an active 2D version of the DUVD concept was considered. A major advancement was the introduction of amplification between a set of transmitting and receiving arrays of transducers; thereby solving the problems of low sensitivity and inflexibility inherent with the DUVD approach. This decouples the test object from the rest of the system as shown in Figure 5 below.

Since the system is now transformed from passive sonoptics to an active sampling and reconstruction technique, the design specifications were derived by detailed computer simulations and practical investigations to achieve satisfactory image quality. It should be emphasised that the requirements for image reconstruction for this system is very different to conventional imaging. It essentially involves image formation utilizing amplitude and phase of signals as represented by equation 5 and Figure 6 below.

$$P_{(x,\,y)} = \sum_{i=1}^{N} a_i \frac{exp^{-j(k r_i + \varnothing_i)}}{r_i} \tag{5}$$

where, p(x, y) represent the acoustic pressure at a point x, y in the image space as in Figure 6 below, a_i is the normalised signal amplitude, r_i is the distance to the point (x,y) from the i^{th} element, φ_i is the relative phase of the i^{th} element, and k is the wave number.

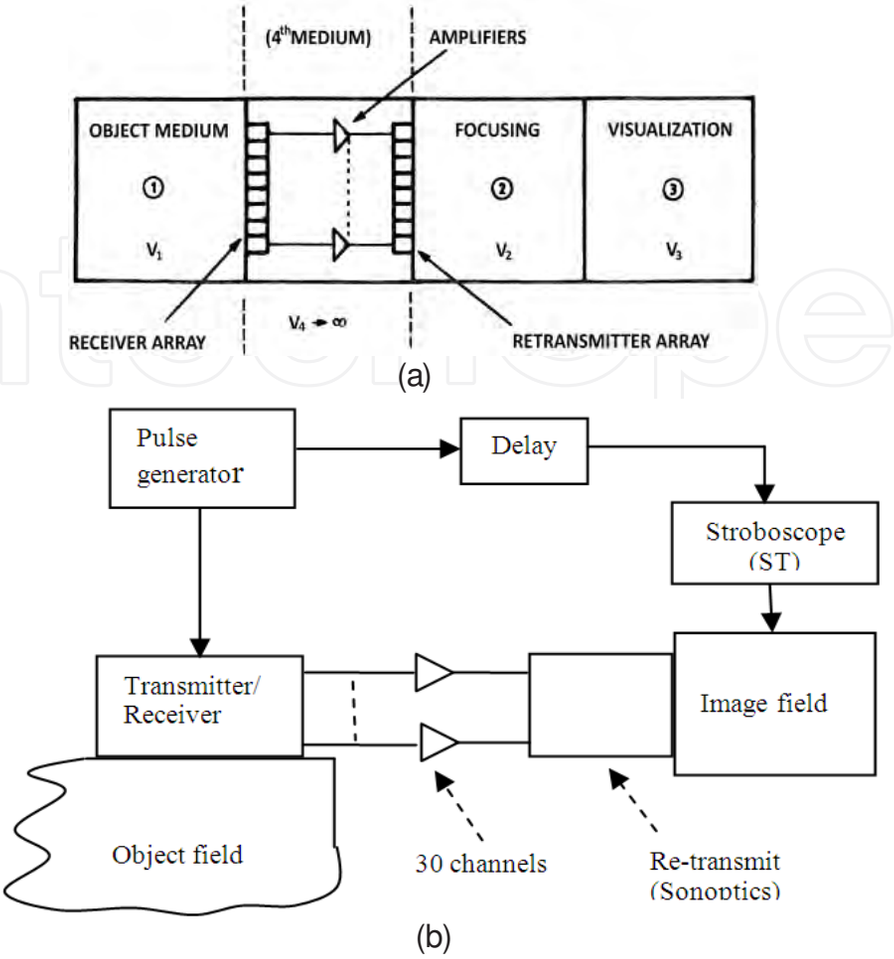

Figure 5. (a) – Active system block diagram with arrays (b) – Active system schematic block diagram

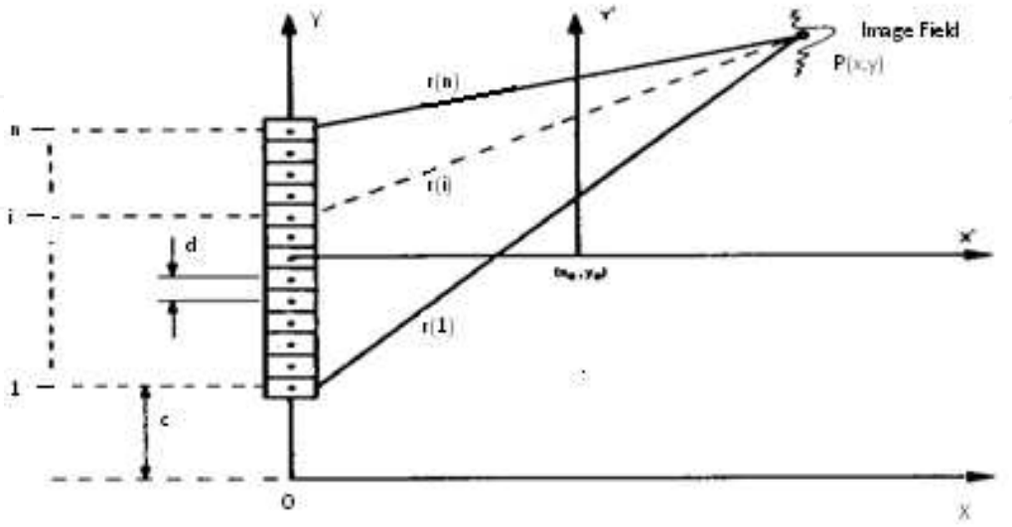

Figure 6.

http://dx.doi.org/10.5772/56378

Therefore in order to achieve good image quality, stringent control on the uniformity of the transducer elements in terms of their amplitudes and phase responses were essential requiring special fabrication techniques, since achieving close elemental uniformity in transducer arrays is a challenging task.

The details of the prototype design while achieving the ideal features described in section 4.1 above namely: linearity, isochronicity and maximum lateral resolution corresponding to the total acoustic aperture are presented in the Appendix.

3.2.2. First prototype system

For the feasibility study of the active direct imaging concept, a 2-D version of the 3-D DUVD sonoptics was chosen. However, it is important to note that as for the 3-D sonoptics, the same acoustooptical relationships could be maintained by using cylindrical lenses to give an image field similar to a B-scan. Because of the flexibility introduced by the sampling and retransmitting acoustic arrays, the operation of the lenses could be emulated by a number of different ways; e.g. by electronic focusing to represent both lenses, using solid cylindrical lenses, or by a combination of both. It should be emphasized that once the lens characteristics required are implemented, there is no further special requirement for dynamic focusing as the entire image field will be in focus at one instant of time requiring only one excitation pulse to produce the image of the whole object field.

After investigating different possibilities, the following configuration shown in Figure 7 below was used for the first prototype.

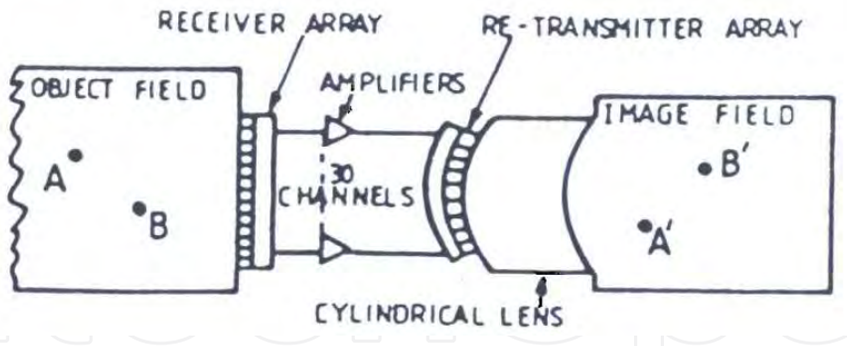

Figure 7. Active system configuration with conversion of DUVD sonoptics to maintain image linearity, Isochronicity and resolution.

Figure 8 below shows the construction of the retransmitting section of the system with retransmitting array, cylindrical lens and image medium. The design parameters were chosen to image a section of steel of depth up to 40 cm, which is well in excess of typical applications.

Figure 9 show the trolley-mounted 1st prototype system designed in accordance with the simplified block diagram shown in Figure 5. The optical assembly is equipped with an ultra-short stroboscopic light source [16] mounted on the right and a video camera for capturing

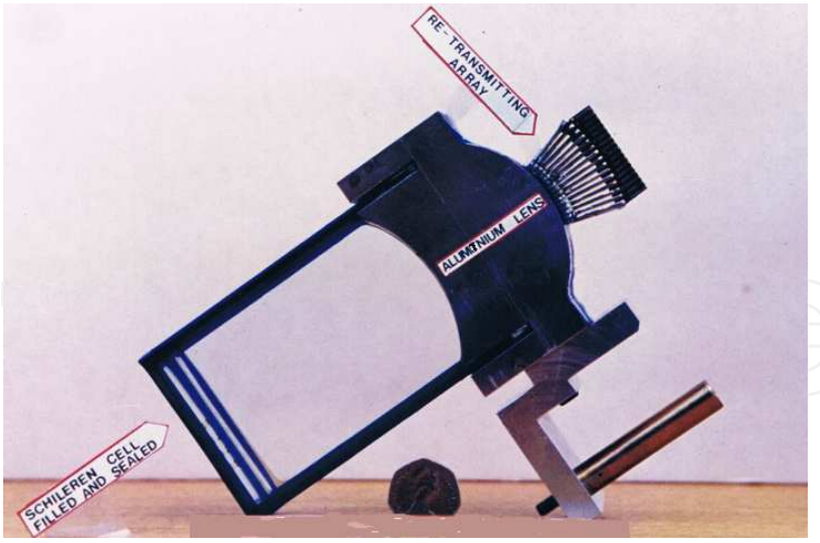

Figure 8. Sonoptical assembly including the imaging cell

images on the left along the optical axis. For experimentation, only 15 of the 30 available channels were used in this prototype.

Figure 9. The active acoustooptical imaging system (1st prototype)

http://dx.doi.org/10.5772/56378

3.2.3. System operation

When testing, the receiving probe array is coupled to the test object medium with a liquid couplant such as oil or jelly. The test object is insonified with a short pulse of ultrasound and the delay of the stroboscopic light source is set appropriately such that the acoustic images are optically frozen in time within the optical imaging medium (schlieren cell) at the instant of best focus.

The resulting optical image of the whole object field can be seen either by naked eye or can be captured with a video camera. Since the time required to form a complete image field is now only limited by the time of flight of the acoustic signals the frame rate could reach the theoretically possible maximum limits (e.g. in excess of 1000 frames per second).

3.2.4. Results from the first prototype

Image linearity and Isochronicity

Although the system was designed with 30 channels, only 15 were used because of the difficulty of making elements of the arrays with sufficiently close characteristics as required for this imaging topology. However, as can be seen from the images, they are exceptionally of high quality in terms of image clarity and resolution. Figure 10 shows a test block with side drilled holes and the resulting image, clearly demonstrating image linearity and isochronicity as expected from the system design.

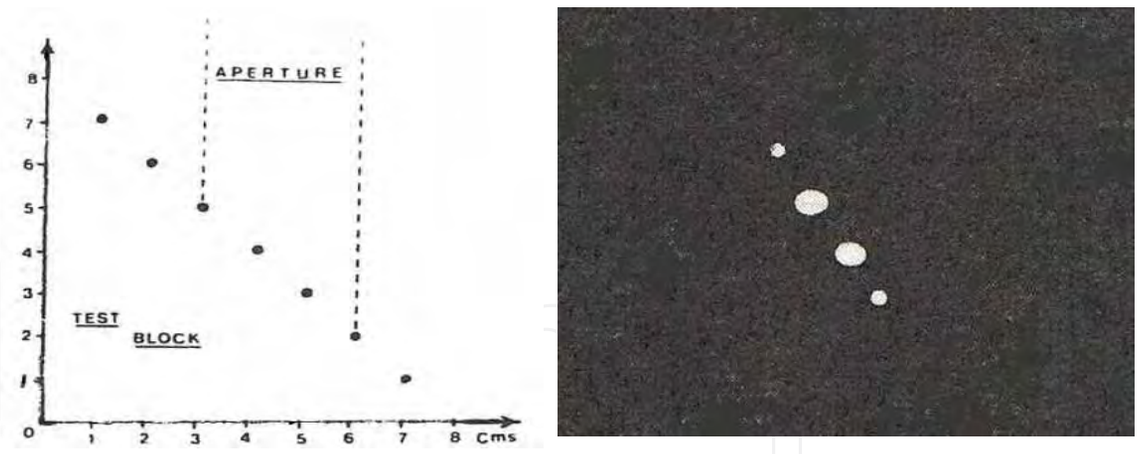

Figure 10. Images of 2mm side drilled holes.

Notice the axial magnification as depicted in equation 10 in appendix. The targets central to the array obviously have stronger return echoes, so they are somewhat saturated due to relatively low dynamic range of the channel amplifiers used. Figure 11 below show a test object, again with side drilled holes and the respective image with lateral and axial magnifications equalised. This image demonstrates exceptional image quality with object-to-image spatial relationship correctly maintained.

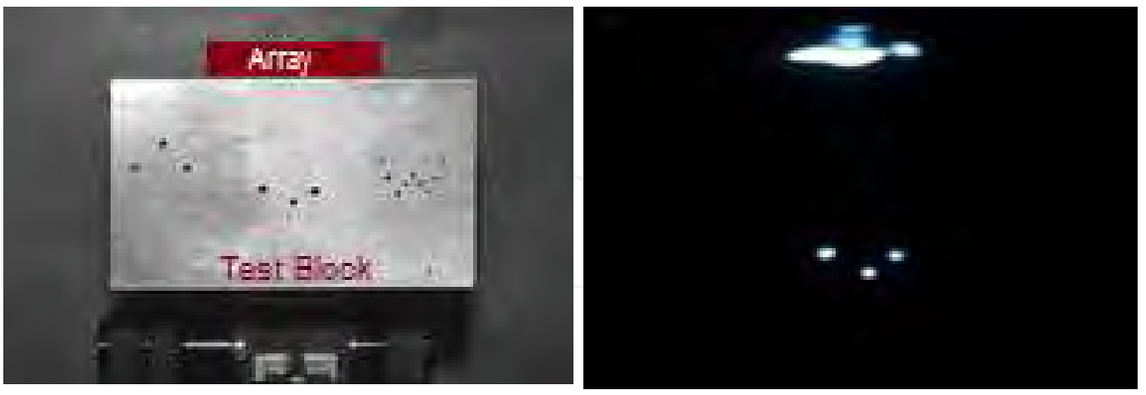

Figure 11. Imaging side-drilled holes in a test block

Figure 12 below shows an actual T-weld being tested with the prototype system and the image of a crack in the weld. This micro-crack was actually visible from the ground side surface of the test block.

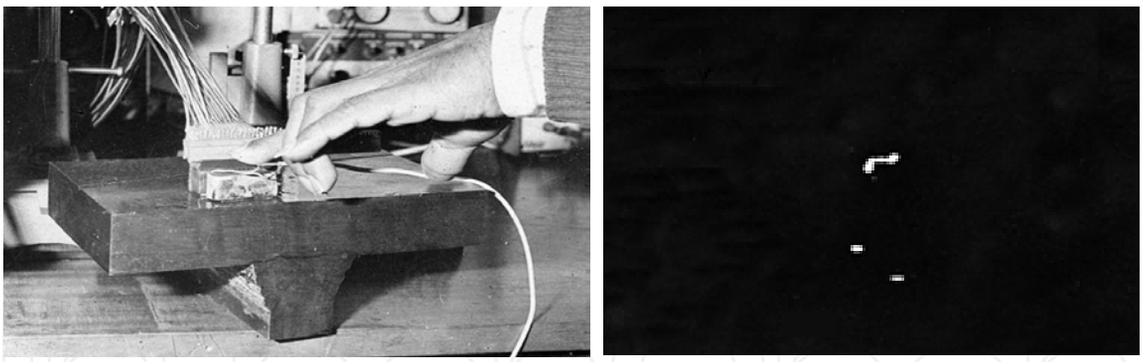

Figure 12. Image of a micro crack in a T-weld

3.2.5. Practical limitations of the first prototype

The results from the first prototype have clearly demonstrated the potential of direct ultrasonic imaging reaching performance close to theoretical limits. These include: maximum possible speed of imaging, maximum lateral resolution for the size of the arrays used, forming focused images of the whole object field covered by the transducer aperture.

However, there were still practical limitations. This system also had a small field of view approximately that covered laterally by the array aperture; in this case ~3 cm wide. This is too

http://dx.doi.org/10.5772/56378

narrow in practice since wider coverage requires moving the receiving array over the test surfaces, which are typically uneven. Since the image reconstruction is heavily dependent on the amplitude and phase information of the signals, unevenness influences the image quality to a greater extent than conventional imaging methods; although in ideal conditions, excellent results could be achieved as shown in the results section above.

4. Advancements in non-conventional methods — Development of a high-speed, computer-controlled hybrid scanner

From the performance of the acousto-optical imaging system shown in Figure 9, it was evident that to meet practical requirements and to advance the potential benefits, the following characteristics would be very desirable.

1. Ability to scan a test object for off-axis imaging, thus overcoming the limitation of small field of view.
2. Dynamic focusing along specified paths and sites to improve image quality.
3. Means of providing a degree of image enhancement.

The first property adds a much greater degree of freedom to test uneven surfaces from selected or prepared locations. The resulting images would be similar to a B-mode sector scan, but the imaging modality is such that it produces image zones for required sectors as opposed to individual line serial scanning, with just a few overlapping sectors enabling much higher frame rates to be achieved. Since there is no requirement for focusing in the image medium, as that is already taken care of by the sonoptical design, the scanning simply means that only the insonifying beam need to be steered to illuminate the object sector.

Since the image reconstruction is implemented with a sonoptical system designed with paraxial ray equations, when imaging a wide field like a sector, there is likely to be a significant degree of peripheral geometrical aberration in the image field. It should be possible to correct these dynamically, since for each image zone, implementation of an appropriately pre-calculated delay in the firing of the stroboscopic light source, channel gain/phase manipulation is possible.

Inclusion of the above properties is the basis of the development [17-19] described below. Figure 13 shows the basic block diagram of the hybrid prototype developed, incorporating scanning hardware (SCH) controlled by a microcomputer (PC). Dynamic control hardware (DCH) is intended to provide gain equalisation during off-axis imaging and time varying gain (TVG) to produce a uniform image field. Field Focus Control (FFC) ensures that the stroboscopic illumination is synchronised such that the image field is optically frozen at the instant of best focus. It is also intended to provide a degree of off-axis aberration correction with sector-dependent focusing delay control.

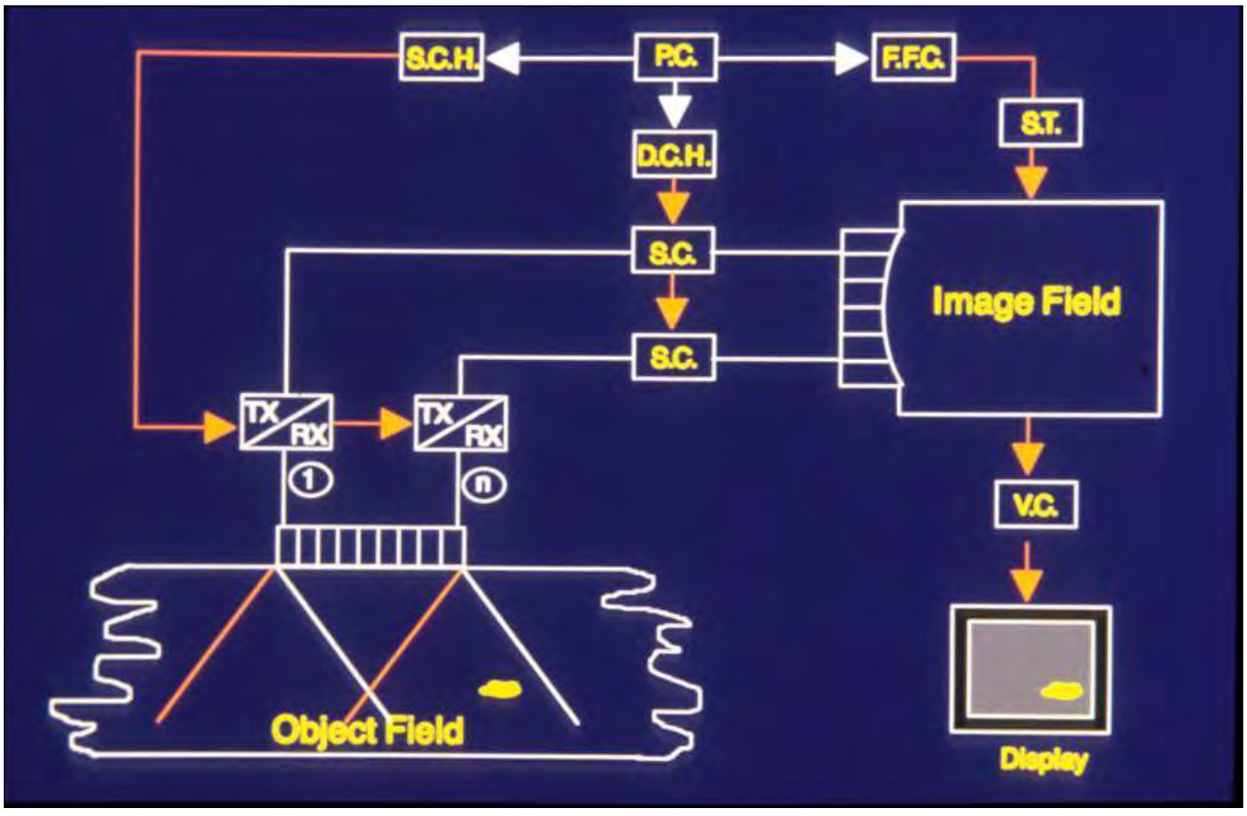

Figure 13. Basic block diagram of the hybrid scanner

4.1. Principle of operation

As mentioned previously, in contrast to conventional imaging, this system also operates on the basis of forming an ultrasonic map of the object field from received echoes inside a visible medium. Once an ultrasonic pulse illuminated the object medium, the acoustic signals intercepted by the receiving array is retransmitted into the image medium through the acoustic focusing system after conditioning and boosting signal power using signal conditioning hardware (SC). The re-transmitting section consists of an identical set of transducer array (except for the shape) to that of the receiving array, coupled to a specially designed ultrasonic focusing arrangement according to the requirements described in 8.1.1 (Appendix). Two important characteristics of this focusing lens design are that all the target echoes are brought into focus at the same instant of time irrespective of the target depth while maintaining image spatial linearity, so that a complete image frame is produced by just one insonifying pulse in real-time.

When the acoustic image field is at the time of best focus, an ultra-short stroboscopic light pulse of the order of a few nanoseconds is emitted, which produces a visible image. This can be viewed directly or captured by a video camera. Since the maximum repetition rate is now only determined by the time-of-flight of the sound pulse, the system achieves the highest speed of operation theoretically possible in ultrasonic imaging, eliminating the problem of temporal artefacts inherent with the existing systems.

http://dx.doi.org/10.5772/56378

Figure 14 shows a more detailed block diagram of the improved design with a possible use in testing of welds. Figure 15 shows the first prototype hybrid scanner developed.

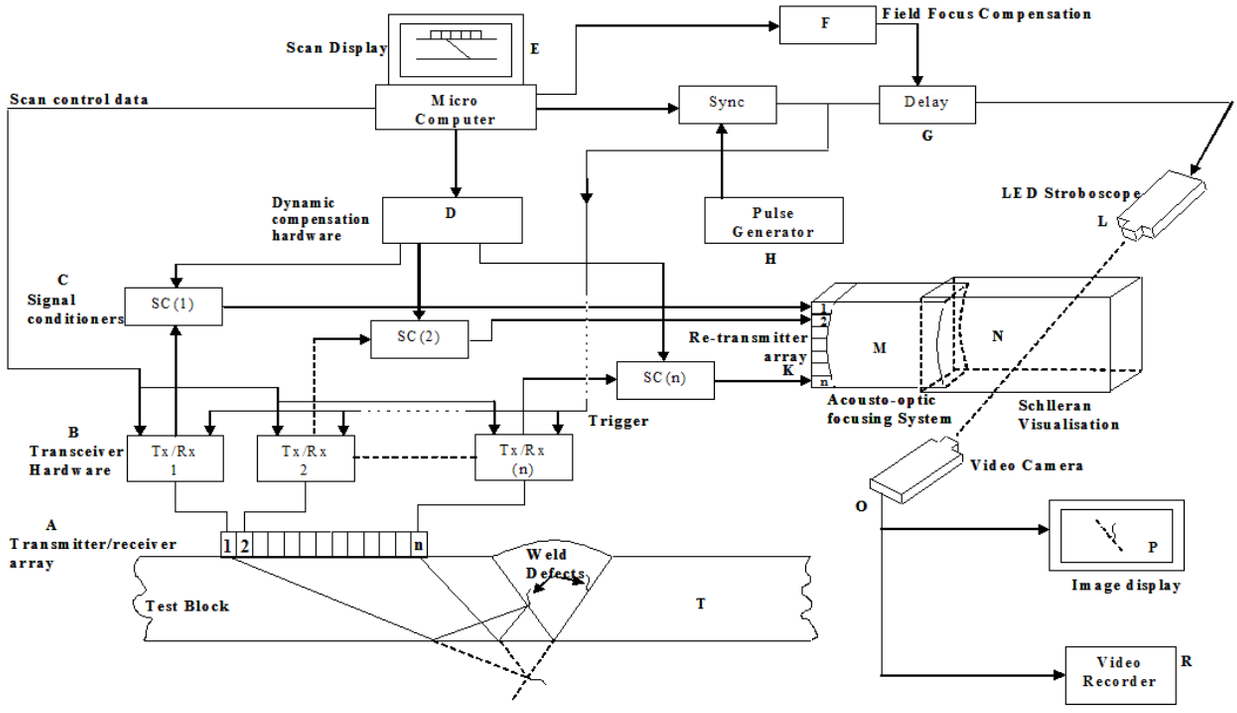

Figure 14. A hybrid imaging Topology with computer controlled scanning and acoustooptical image reconstruction (Expanded block diagram)

Figure 15. The first prototype of the hybrid scanner (GB2278443B)

Since the principle of acousto-optical imaging is very different to that of the conventional methods, some of the requirements of electronics and ultrasonic hardware is very different to that of the conventional systems in many ways. Since the received signals are converted back into ultrasound signals and retransmitted into an acoustic modulator to produce optical effects,

the technique relies on the preservation of amplitude and phase characteristics of the signals to a high degree. Also, adequate signal power is required to produce acousto-optical modulation in the image medium to make the acoustic map of the object field visible.

For the first hybrid prototype system, the excitation pulses generated were 2MHz single sinusoidal pulses of the order of 120Vpp as shown in Figure 16 below. These pulses were shaped to obtain the near-ideal response from the transducer elements.

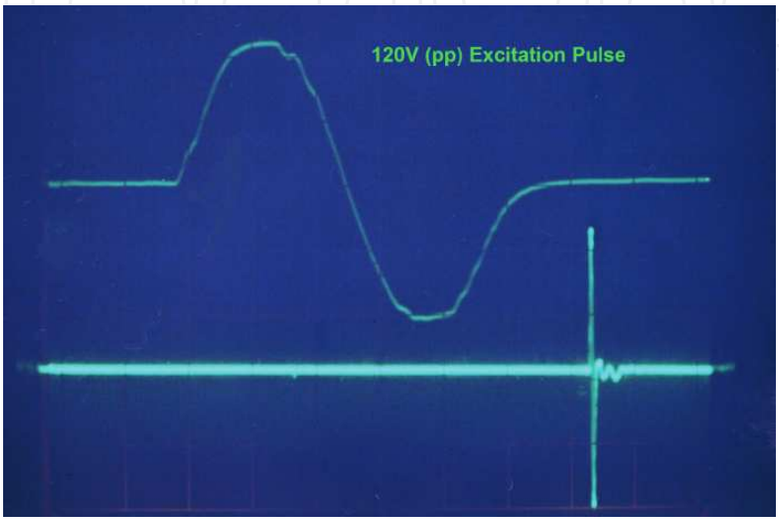

Figure 16. Single sinusoidal excitation pulse

The front-end receiving section of the hardware consists of wideband amplifiers (15 MHz) with a variable gain of up to 60dB. The output impedance is of the order of 50 Ohms with a maximum output swing capability of 120V pp. Input surge protection up to 1kV was provided with a very low recovery time to achieve minimal dead-zone. Although the above prototype scanner was equipped with 30 channels, only 8 channels were used for the feasibility study. This represented just 1.6 cm acoustic aperture. No dynamic compensation was used. However, the performance as can be seen from statically scanned images was still very good.

4.1.1. Operational modes

The system may be operated in the axial mode for very high-speed imaging or be used in the scanning mode to cover a wide field. In the coaxial mode, the system resembles in operation to that shown in Figure 10 -12, producing narrow-field linear array B-mode images covered by the aperture of the array. In the scanning mode the system is under the control of the computer and can be used to produce wide-field, high resolution B-mode sector scan images, or be programmed to scan along any specific areas of the target. In order to achieve field uniformity for off-axis imaging, scan-angle derived field-focus compensation (FFC) and dynamic compensation (DCH) may be applied. In the scanning mode, wideband insonifying pulses are beamed to target areas by phased array beam steering. However, when receiving the echoes from the targets, there is no requirement for beam forming at all, as the system

http://dx.doi.org/10.5772/56378

essentially behaving as an active, acousto-optical imaging device operating in real time. Therefore, even in the scanning mode, this allows very high temporal resolution to be achieved since one beam produces a complete image field or image zone. Furthermore, the whole of the effective aperture is utilized for each image frame and therefore diffraction-limited lateral resolution approaches the theoretical maximum.

If the scanning angles are small, the system could produce images without the need for any compensation. This is the simplest mode of scanning operation. For larger beam angles in the scanning mode, compensation to account for the reduction in sensitivity and field uniformity may be applied by the control of insonifying energy, receiver gain and scan derived electronic phase delays, which is an area for further development.

4.2. Results from the 1st hybrid scanner prototype

As mentioned above, although the prototype was equipped with 30 channels, the number of channels used for the feasibility study was just 8 with an effective aperture of only 1.6 cm (as marked on the receiving array in Figure 17a). This was because of a problem of some of the channels breaking into oscillations due to excessive capacitive feedback at the time of experiments. Nonetheless, it can be seen from Figure 17 that the images produced are still very good for the aperture used.

As mentioned above, in the coaxial mode, the system resembles in operation to that shown in Figure 10 to 12. The speed of imaging is very high, e.g. in a test block of steel 40 cm deep, a complete image is formed within 0.15ms and the frame rate can be as high as 1kHz or more. Estimation of resolution capabilities previously obtained using the coaxial system of Figure 9 showed that the images can be produced to within one wavelength resolution in the axial direction and about 1.5 wavelengths laterally at about 60mm below the surface of the test block; thus approaching theoretical limits.

In order to test the operation in the scanning mode; a test block with side drilled holes covering a wide sector was prepared as shown in Figure 17(a). Figure 17 (b), (c) & (d) shows the images when the insonifying beam was steered statically (i.e. in manually selected angles) to image the 3 holes in the left, two in the centre and the two on the right-hand side of the test block.

Dynamic scanning was also verified. However, since the scan sector required for the above test object was very large (~120^0) peripheral geometrical aberration was significant. When statically scanned, aberration can be controlled for each angle manually by selecting stroboscopic firing delays to achieve best focus. For smaller sectors (e.g. < 60^0) aberration was not a significant factor.

Although the prototype system was designed for NDT applications, attempts to image biological moving tissues, such as heart valves, revealed excellent temporal resolution as expected. However, since the transducer arrays used did not have the required element spacing characteristics and matching properties, and the sonoptics of the prototype was designed for industrial material, the prototype could not obviously produce true B-mode images for biological tissues although the potential for advancement in this area was clearly evident.

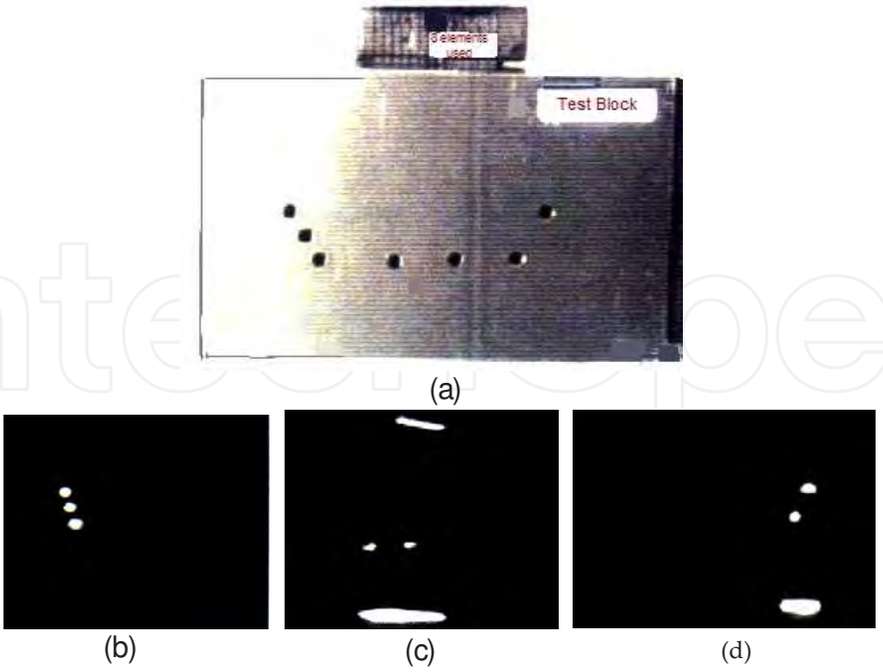

Figure 17. a) - Test Block. Statically scanned images of the test block

5. Discussion — Breaking through the speed barrier

In contrast to conventional line-serial computer based image reconstruction as used in existing systems, it has been demonstrated that the acousto-optical hybrid scanner has the potential to provide a number of important properties. These are:

- Ultimate speed of imaging as the image reconstruction is done using acousto-optical means thus *"Breaking through the speed barrier"* of the conventional line-serial imaging technology.
- In axial imaging mode, a complete image frame can be produced using a single ultrasonic pulse within its time of flight thus allowing ultimate imaging speed thus eliminating temporal artefacts when rapidly moving targets were imaged.
- In sector scanning mode image zones for each scan angle is produced allowing much higher frame-rates to be achieved, since very few scan angles are required as opposed to line serial scanning in conventional technology.
- A focused image of the whole object field is produced at the same instant of time without the need of any dynamic focusing as in the conventional technology.
- High lateral resolution, close to theoretical limits is achieved as the whole transducer aperture is used for each image frame.

As evident from the images, the signal-to-noise ratio (SNR) of the above prototype is very high. One of the reasons for this arises from the fact that true signals are coherent and the noise signals are not. Since the image reconstruction is based on amplitude and phase of signals, this

http://dx.doi.org/10.5772/56378

allows true signals from targets to be coherently re-constructed in the image medium while the noise and out of phase signals are being largely rejected as evident from Figure 18 below. However, just like all ultrasound equipment multiple reflections between closely spaced targets could still cause artefacts. Therefore, inclusion of selective insonification of the object medium as in item No. 2 above should enable the system to achieve even higher SNR while suppressing artefacts when imaging near-field targets.

Figure 18. Noise suppression

Another important factor as mentioned in section 2 for any imaging technique is the dynamic range. In this respect, one of the typical bottlenecks is the limited dynamic range of display equipment. The present development can provide a greater display dynamic range when images are viewed with the naked eye as the acousto-optical modulator can provide a higher display dynamic range than images captured by a camera and presented on a typical conventional VDU.

6. Conclusions

Conventional ultrasonic imaging systems have inherent limitations such as low speed leading to temporal artefacts and in some cases limited lateral resolution; these being the result of line-serial scanning, lengthy processing and other limitations arising from the particular techniques used. The extent to which the above deficiencies affect performance has been analytically investigated.

In this respect, it has been shown that an alternative hybrid approach to imaging using acousto-optical image reconstruction could give clear advantages; reaching theoretical limits of performance in speed and resolution unachievable with the existing methods. This is mainly due to the combination of electronic and sonoptical image reconstruction, avoiding line-serial scanning and lengthy processing required by the conventional systems. The hybrid system reaches almost ultimate speed and resolution in the coaxial imaging mode. In the B-scan mode,

it produces sector images formed by overlapping zones, but each zone requiring only one pulse to produce a complete zone image, thus gaining by far the highest speed of sector scanning compared to conventional methods.

Furthermore, the clarity and contrast of the images are high as the stroboscopic image mapping results in gating out many artefacts, problems due to reverberations and noise, to a high degree. Since the image reconstruction, by design, is based on coherent summation of signals in amplitude and phase corresponding to true targets satisfying the sonoptical focusing requirements, random noise gets suppressed without the need for further processing.

6.1. Future work

The typical results shown with the hybrid imaging system is applicable at present only to structural NDT for which it was designed. In order to produce true B-mode images for medical applications requires further work on the design of transducers and the sonoptical geometry to satisfy the conditions necessary for body tissue imaging, while accommodating the required dynamic range. In particular, it should be noted that the technique of image reconstruction is based on amplitude and phase integrity of signals; thus the inter-element uniformity of transducer elements and channels are crucial. In the case of medical imaging, the transducer element spacing is much smaller compared to NDT applications for any given frequency. For the above NDT system, the arrays were constructed using ordinary PZT transducer material. This is unlikely to be satisfactory in the case of medical transducers utilizing the above imaging techniques, since the requirements of transducer specifications are different and much tighter compared to conventional imaging to achieve good performance. Hence, transducers with piezo-composites or PVDF material may have to be developed for this application. Although the present system is designed to produce imaging in 2-D, extension of this technology to 3-D imaging in real-time is a distinct possibility which needs to be explored. This work and the development of dynamic compensation hardware will be taken forward in the next phase of development.

Appendix

Prototype design considerations

Since the active imaging system depicted in Figure 5 in section 4 above is required to produce a direct acoustic image which is made visible by synchronised stroboscopic light (Schlieren or other acoustooptical modulation technique), the design parameters for NDT applications were determined both by theoretical simulations and experimentation. For the construction of the transducer arrays, bearing in mind the tight requirements for elemental uniformity, number of parameters for a selected centre frequency of 2 MHz were determined which included [15]:

- Estimation of number of channels (30 for the initial design)
- Transducer element spacing (2 mm for the initial design)

http://dx.doi.org/10.5772/56378

- Element width-to-gap ratio
- Physical size, shape and transducer material

The primary aim was to obtain an idea of the sharpness of the images and the extent of artefacts that may be formed in a given image space. Since the transducer backings were conductive, maintaining a low level of electrical cross-coupling was required for the size of the backing thus the element gap spacing was kept around 0.3mm. For visualisation of the acoustic image formed in the modulating medium, the requirements for channel characteristics were then determined. These included practical determinations of number of parameters including:

- Typical and worst case input signal levels
- Output signal power required from each channel
- Phase linearity and bandwidth considerations
- Signal dynamic range
- Input and output impedances
- Element damping characteristics

Acoustooptical design considerations

As mentioned in section 4 above, as opposed to conventional image reconstruction, the passive DUVD system had some ideal properties for ultrasonic imaging namely, image linearity and isochronicity. Maintaining the same properties in the active system was therefore important. The requirement for image linearity as determined by Hansted [12] for the DUVD is given below.

Maintaining image linearity

Figure 19 shows the two-lens system of the DUVD.

Using paraxial ray analysis, it can be shown that in order to maintain image linearity throughout the image field, the only requirement is to make the focal point of the two acoustic lenses coincident. This however changes the lateral magnification as given in equation 10, but since this is a constant it does not affect linearity or image quality and can be easily compensated if necessary.

Maintaining isochronicity

As stated in section 4 above, iscochronicity means that when the test object is insonified with a short acoustic pulse, all the echoes from the different targets, irrespective of their special distribution within the object field, arrive simultaneously at their respective image points thus giving the system its ability to display the whole image at once.

The above capability is in stark contrast to the need for line serial scanning in conventional imaging, giving the system its speed - the highest theoretically possible speed of imaging as it

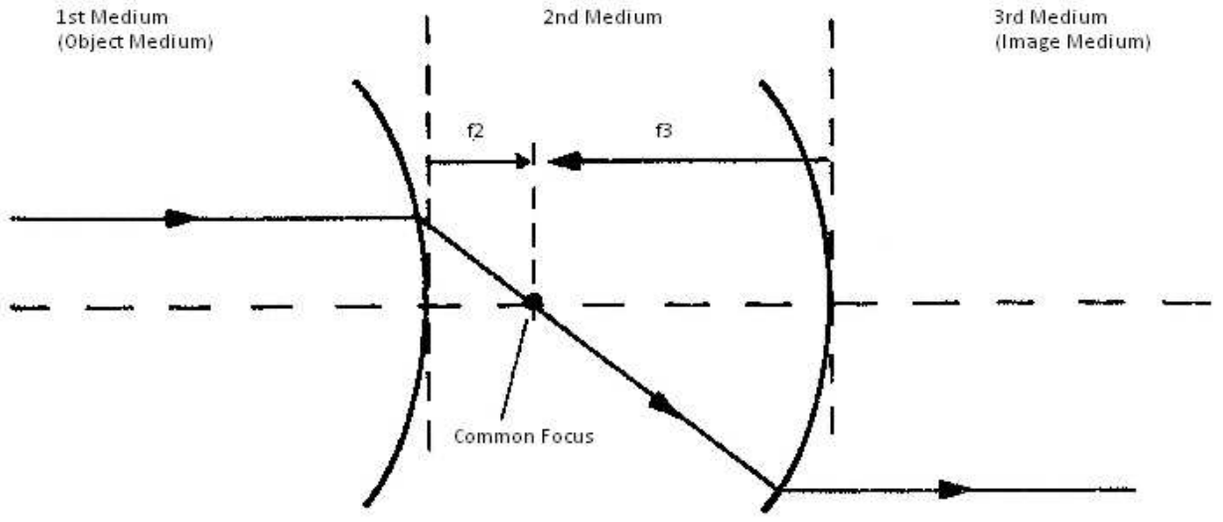

Figure 19. Maintaining image linearity

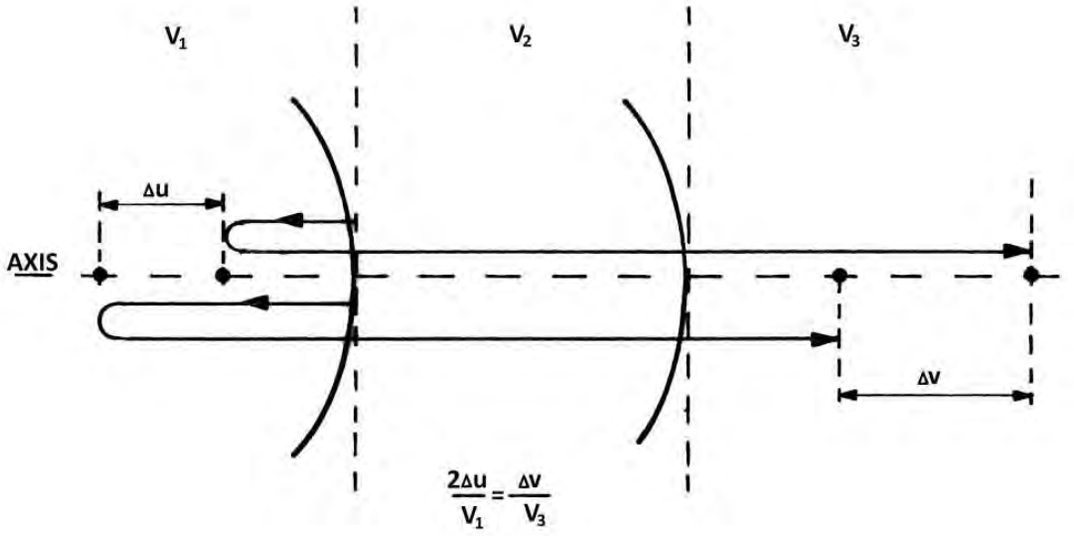

Figure 20. Requirements for maintaining Isochronicity

produces images with a single pulse practically within the time of flight of the pulse echoes in the object and image media. The conditions required for iscochronicity as determined by Hansted for his DUVD system with reference to Figure 20 is given below.

It can be clearly seen that the necessary and sufficient condition for the images of two objects in the object medium with velocity v_1 to be brought to focus at the same instant of time in the image medium with velocity v_2 could be given as:

http://dx.doi.org/10.5772/56378

$$\frac{2\Delta u}{V_1} = \frac{\Delta v}{V_3} \tag{6}$$

where, Δu is the axial separation of the objects in the object medium and Δv is the axial separation of the respective image points in the image medium. In terms of respective focal lengths in object and image media (f_1& f_4) the condition depicted in equation (6) is achieved for this lens combination with a common focus in the medium v_2 when f_1 & f_4 are related such that:

$$\frac{f_1}{f_4} = \frac{1}{\sqrt{2}} \tag{7}$$

Using paraxial ray analysis, it can also be shown that when satisfying the above necessary conditions, the maximum object distance (U_{max}) and maximum image distance (v_{max}) can be written as:

$$U_{\max} = \left(\frac{f_1 f_2}{f_3} \right) + f_1 \tag{8}$$

$$v_{\max} = \left(\frac{f_3 f_4}{f_2} \right) + f_4 \tag{9}$$

where, f_1 & f_2 are the focal lengths of the first lens defined by medium velocities v_1 v_2, and f_3 & f_4 are that determined by the 2nd acoustic lens.

Thus the necessary and sufficient conditions for linearity and Isochronicity for the acoustic imaging system are:

- The internal focal points must be coincident
- The external focal lengths must be related in accordance with that given in equation (7)

Using paraxial ray analysis taking also into account the conditions necessary for Isochronicity, it can be shown that there is however lateral image magnification (as mentioned above) such that:

$$M_A = \sqrt{2} M_L \tag{10}$$

Where, M_A and M_L are axial and lateral magnifications respectively. This does not affect image linearity and can be compensated if necessary.

Acknowledgements

Author wishes to express his sincere thanks to the School of Engineering of the Robert Gordon University, UK where much of the developmental work was carried out and to Mr Andrew Fairhead, ultrasound engineer of the Aberdeen Royal Infirmary, NHS Grampian, for his valuable comments and advice regarding medical imaging systems.

Author details

References

[1] http://inventors.about.com/od/sstartinventions/a/sonar_history.htm (Accessed 24th February 2013).

[2] http://www.ob-ultrasound.net/history1.html (Accessed 24th February 2013).

[3] http://www.ndt-ed.org/EducationResources/CommunityCollege/Ultrasonics/Introduction/history.htm (Accessed 1st Jan 2013).

[4] Three-dimensional imaging system: Olaf von Ramm and Stephen Smith, Duke University, USA, United States Patent – 4694434 http://www.freepatentsonline.com/4694434.html (Accessed 1st Jan 2013).

[5] Portable PC-based Ultrasound scanners, Imaging Tools, Telemed http://www.hospitalmanagement.net/contractors/imaging/telemed/ visited 1st Jan 2013.

[6] Zone Sonography, Zonare Medical systems, http://cdn.zonare.com/0d87056c5a4bae2587f9710a5d669d33.pdf (Accessed 24th February 2013).

[7] Coded Excitation: GE Healthcare, http://www.gehealthcare.com/usen/ultrasound/education/products/techcodex.html (Accessed 1st Jan 2013)

[8] Digitally Encoded Ultrasound: GE Healthcare, http://www.gehealthcare.com/usen/ultrasound/education/products/techedu.html (Accessed 1st Jan 2013)

[9] Research Corporation Technologies, *"Tissue Harmonic Imaging"*: http://rctech.com/resources/downloads/THI_Overview_9-06.pdf visited 1st Jan 2013.

[10] Ultrasound C-can camera: Acoustocam, http://www.reinforcedplastics.com/view/1180/ultrasound-camera-makes-internal-composite-damage-easy-to-find/ (Visited 2nd Jan. 2013).

http://dx.doi.org/10.5772/56378

[11] G.P.P. Gunarathne, "Ultrasonics Imaging, Invited Presentation at the World Congress of Engineering 2007, London, UK, July 2007.

[12] P.D. Hanstead: "*Three Dimentional Imaging of Ultrasound – Direct Ultrasonic Visualisation of Defects"*, Nature 239, 1972, pp 273-274.

[13] A.J. Hayman: *"Schlieren Visualisation of Ultrasonic Images"*, PhD Thesis, City University, London, 1977.

[14] Y. Bar-Cohen, B. Ben-Joseph and E. Harnick: *"Compact Sensitive Instrument for Direct Visualisation of Defects"*, Rev. Sci. Instruments, Vol.49, 1978, pp 1709–1911.

[15] G.P.P. Gunarathne and J Szilard:*"A Real-time High Frame Rate Ultrasonic Imaging System"*, IEEE Ultrasonics Symposium, San Francisco, USA, Conference Proceedings, 1985, pp 98-203.

[16] G.P.P. Gunarathne and J Szilard: *"A New stroboscope for Schileren and Photoelastic Visualisation of Ultrasound"*, Ultrasonics, July 1983, pp 188-190.

[17] G.P.P. Gunarathne: *"A new real-time Ultrasonic Imaging System"* IEE International Conference on Acoustic Sensing and Imaging, Conference Publication No. 369, pp93 – 98, March 1993.

[18] G.P.P. Gunarathne: "A Real-time, Hybrid Ultrasonic Display/Imaging System for Medical and Industrial Applications", United Kingdom Patent: GB2278443B, July1997.

[19] G.P.P. Gunarathne: "Real-time Ultrasonic Imaging and Advancements in Non- conventional Methods" ²MTC 2008 – IEEE International Instrumentation and Measurement Technology Conference, Victoria, Vancouver Island, Canada, May 12–15, 2008.

4

Advances in Breast Ultrasound

Heino Hille
Office for Obstetrics and Gynecology, Hamburg, Germany

1. Introduction

Breast ultrasound was introduced as a clinical method in breast imaging in the seventies of the 20th century (Jellins, 1971; Kobayashi, 1974). In the Anglo-Saxon countries breast ultrasound was employed mainly by radiologists, by gynecologists predominantly in Germany.

In the early period the indication for breast ultrasound was the differentiation between the cystic or solid nature of palpable lumps (Figs. 1, 2). To make this distinction is easier in ultrasound than in mammography. On this way ultrasound became an accepted method as an adjunct to mammography for further analysis of equivocal mammographic lesions.

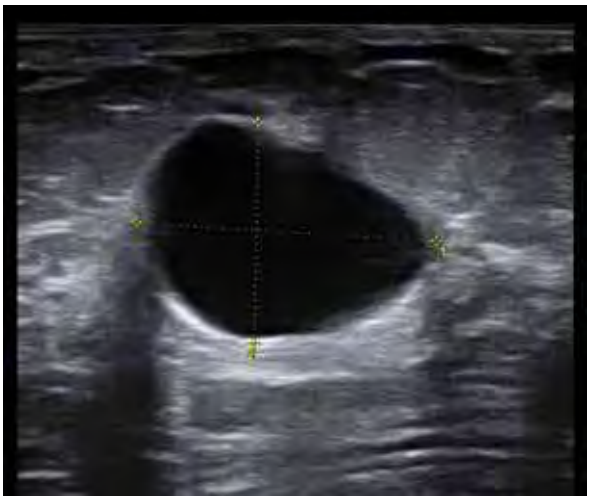

Fig. 1. Typical cyst: anechoic with distinct and smooth margins, benign

Though till now in guide lines of early detection of breast carcinoma indications for breast ultrasound are restricted in this sense, already in the eighties of the 20th century, the capability of breast ultrasound went far beyond this limits (Hackelöer et al., 1986). In contrast to mammography ultrasound is able to generate a detailed map of the anatomic structure of the breast. Because of this ability sonography is qualified to diagnose many benign and malign diseases of the breast by its own (Teboul & Halliwell, 1995).

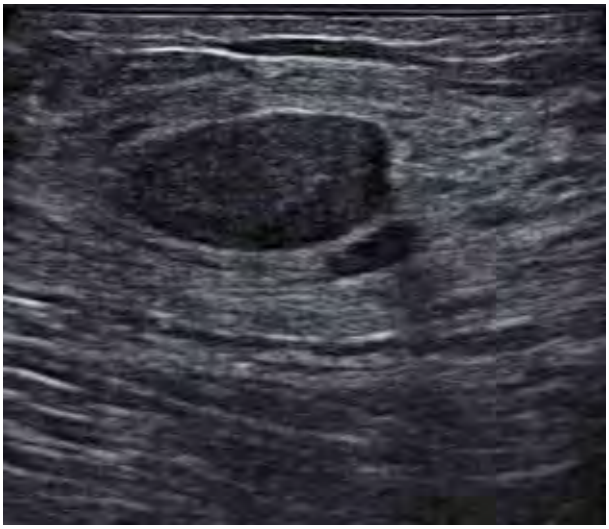

Fig. 2. Typical fibroadenoma: solid, isodens, distinct and smooth margins (pseudocapsule), benign

2. Contemporary principles of breast ultrasound

Breast ultrasound is a dynamic (live) examination, the diagnostic procedure is performed by scanning systematically the whole breast in perpendicular planes. Though not unusual in Anglo-Saxon countries, it´s not sufficient to make a diagnosis on the basis mainly of printed or frozen digital pictures like in mammography. It is necessary to scan both whole breasts in real time. Only in this way is it possible to get a true impression of the architecture of the individual breast. Only with this background structural and architectural distortions as well as differences in the architecture of both sides will be remarkable. To classify the margins of a lesion in detail the dynamic examination is basically as well.

During whole breast scanning there are several steps to absolve:

What kind of breast parenchyma exists in respect of density (that is the relation of glandular to fatty tissue), echogenicity, homogeneus or inhomogeneous structure?

Are there any distinct lesions or masses?

In case of a lesion: the sophisticated description of the lesion related to standardized terms with final submission in BI-RADS categories with recommendation which way to follow up, is mandatory (ACR, 2003; Madjar et al. 2006).

Are there non mass like structural distortions requesting further analysis or complementary imaging modalities?

Principles of the description and the classifying of a discovered lesion are described in known textbooks and publications of breast ultrasound (Madjar & Mendelson, 2008; Stavros, 2004).

Examples and illustrations of cases with *typical sonographic appearance*, see below (Fig. 3, 4, 5, 6).

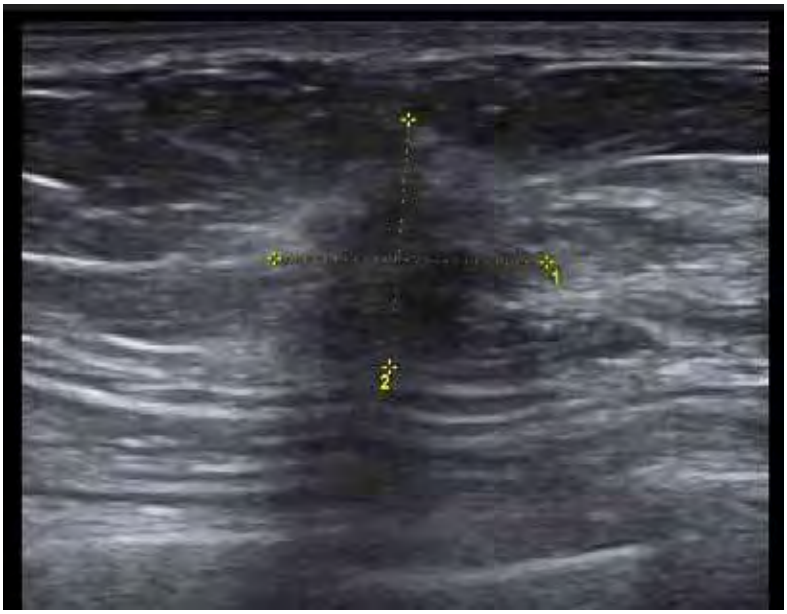

Fig. 3. Typical carcinoma: Architectural distortion, hypoechoic and echoinhomogeneous, margins ill-defined with echogenic halo, spiculae, acoustic shadow, vertical orientation

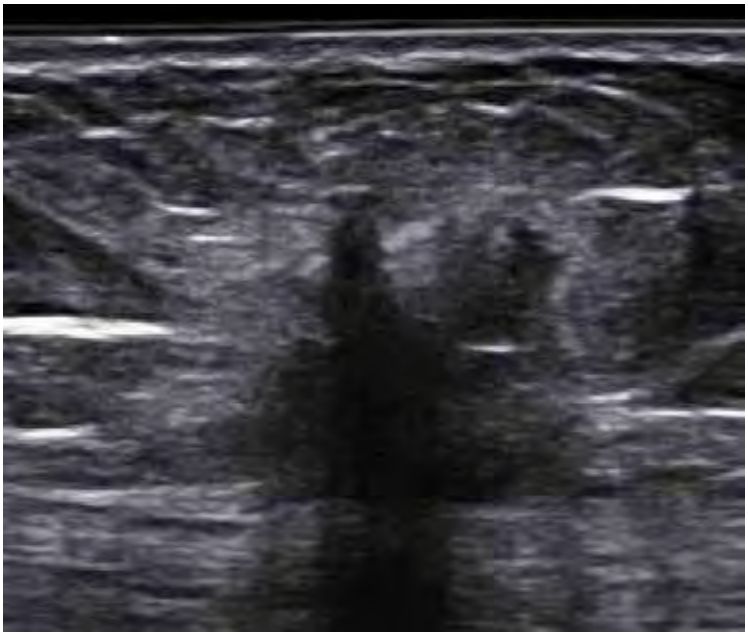

Fig. 4. Another carcinoma with typical architectural distortion, hypoechoic, acoustic shadow, desmoplastic reaction (echogenic halo)

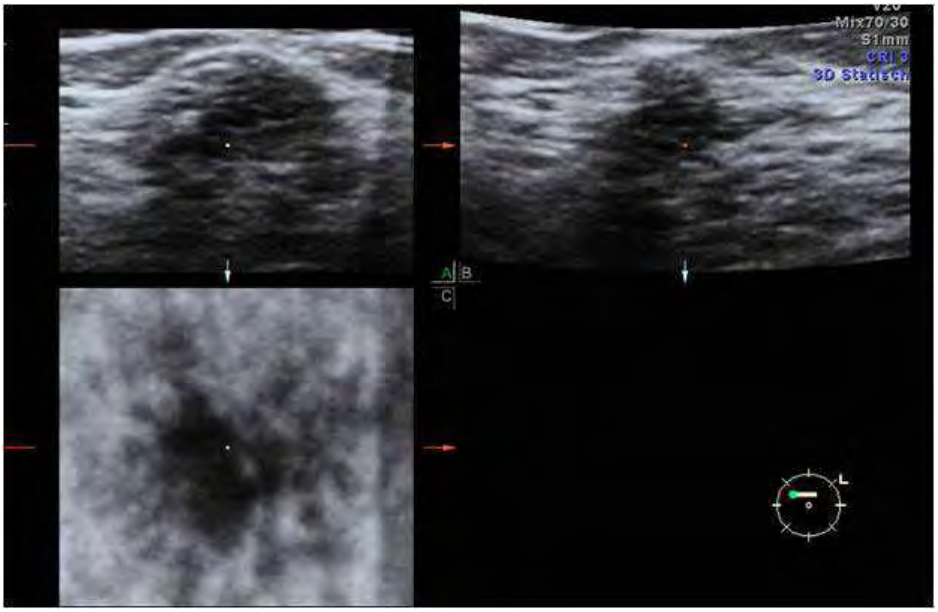

Fig. 5. Palpable lump: DCIS (ductal-in-situ-carcinoma): hypoechoic with indistinct margins, retraction pattern in the C-plane

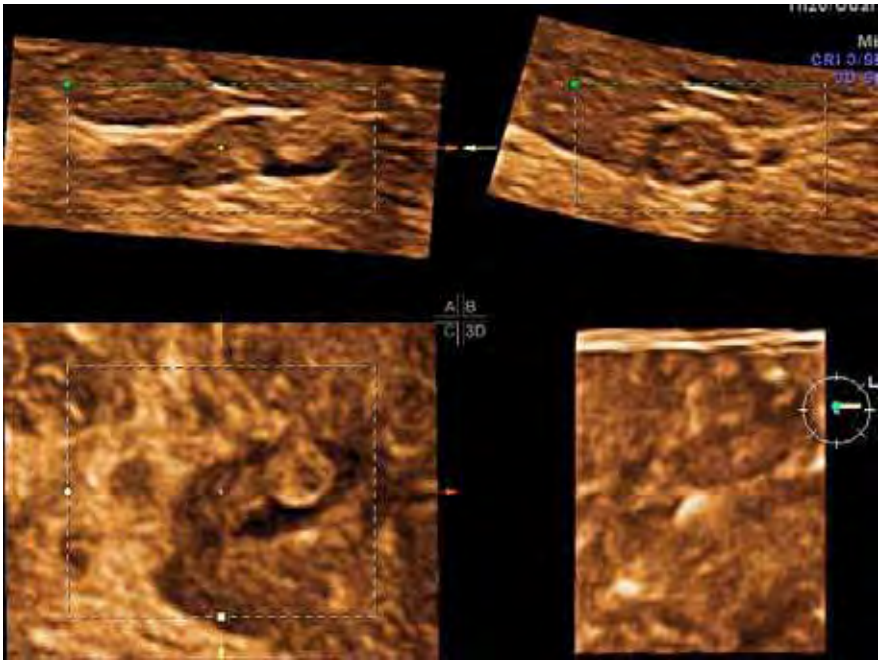

Fig. 6. Intraductal papilloma in 3-D technique: intraductal solid mass in a delated milkduct

3. New insights in breast ultrasound

To make the distinction between a benign and a malign or between a probably benign and a probably malign lesion, the differentiation of the margins and the echogenicity is essential. But with developing technology and experience some classical criteria like sound transmissing - shadowing versus enhancement - and the direction of growing - horizontal versus vertical - lose relevance. Enhancement is no longer a distinguishing marker for a benign lesion nor is this the horizontal growing pattern. By use of contemporary technology (Compound Scanning, Tissue Harmonic) enhancement can be observed in malign lesions as well and the growing pattern of ductal carcinomas often starts horizontal. Figs. 7, 8, 9 demonstrate not well known, but not rare characteristics of malign breast lesions.

With progress in resolution of the machines not smooth and not distinct circumscribed margins of fibroadenomas become more visible. Especially in the C-plane of the 3-D mode often fingerlike continuities are remarkable. That means that the finding of non smooth oval or round margins alone is no longer conclusive to submit this lesion to BI-RADS 4 (suspect) (Fig. 10, 11, 12).

On the other hand circumscribed margins are not rare – not only in special forms of carcinoma like medullary or mucinous carcinoma - but even in ductal carcinoma (Figs. 8, 15).

In this sense breast ultrasound with contemporary high definition ultrasound has become not easier, but more sophisticated.

Additional technical modules like color Doppler and 3-D therefore gain on relevance.

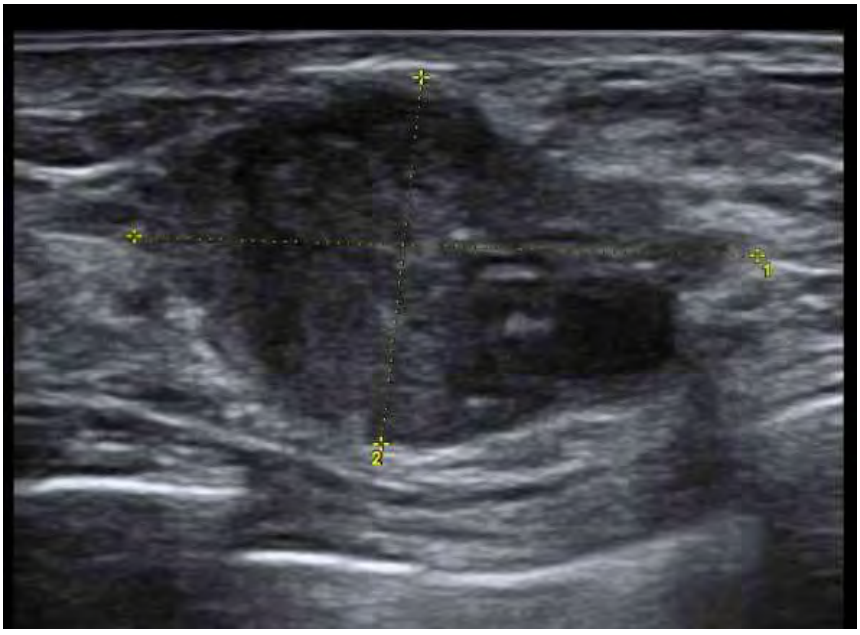

Fig. 7. A more horizontal orientation of a carcinoma, sound transmission attenuated only marginal, but predominantly enhanced

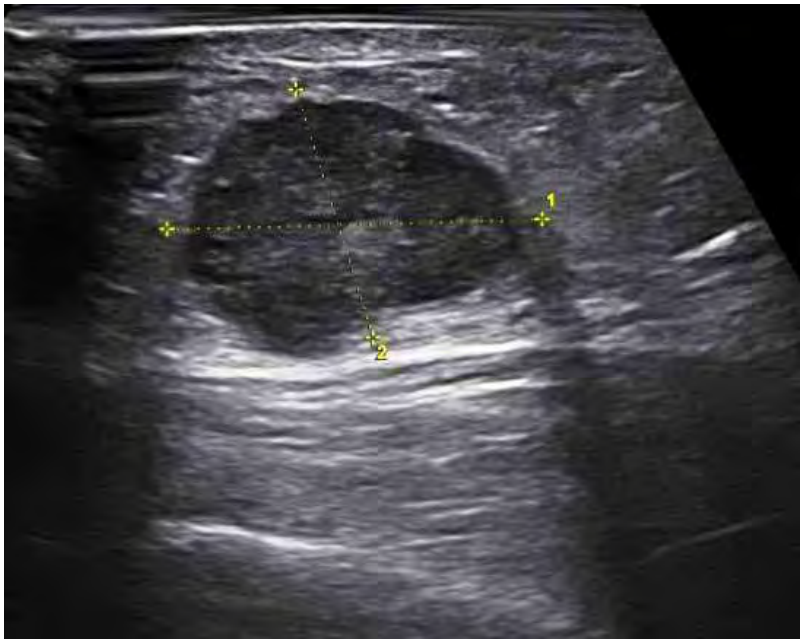

Fig. 8. Ductal carcinoma, smooth surrounded with sound - enhancement

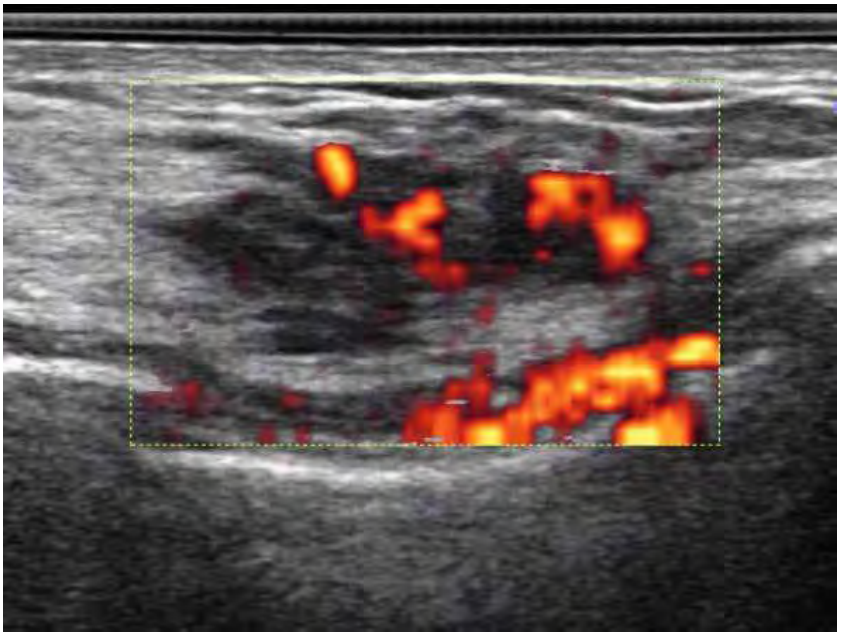

Fig. 9. DCIS: Horizontal growing pattern of a DCIS with microinvasion, clear vascularization in color Doppler

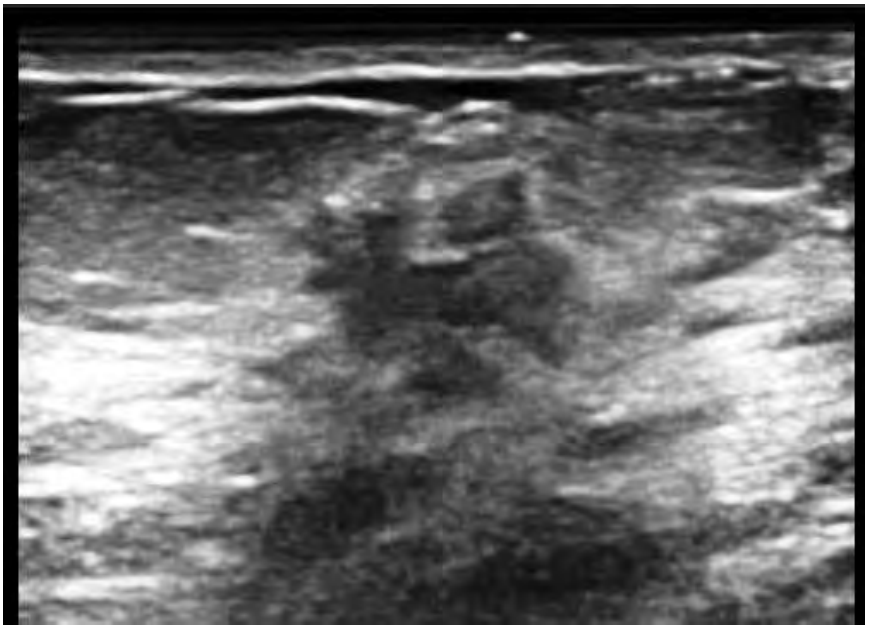

Fig. 10. Fibroadenoma: indistinct and not smooth margins (by this way not distinguishable from a carcinoma)

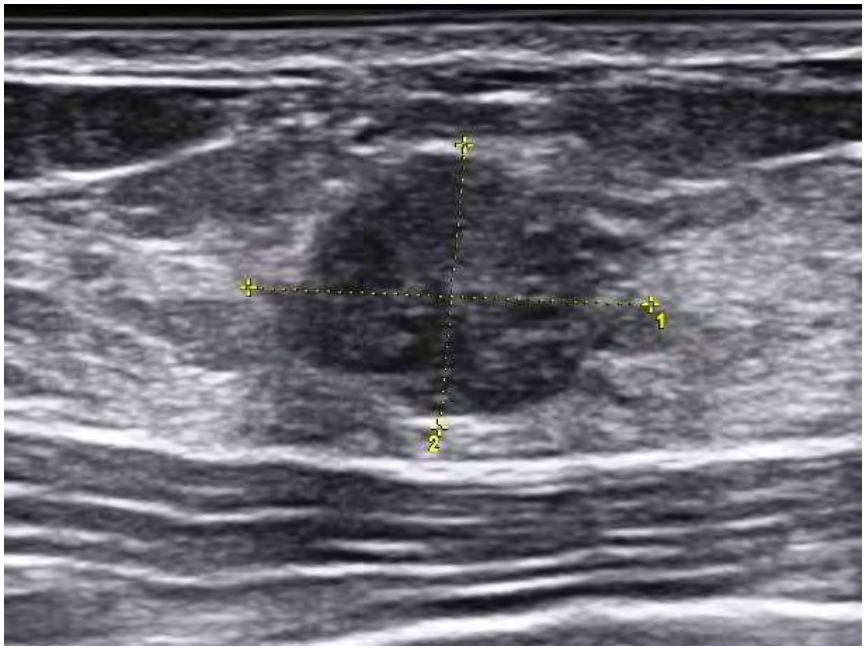

Fig. 11. Fibroadenoma: fingerlike continuities (not rare)

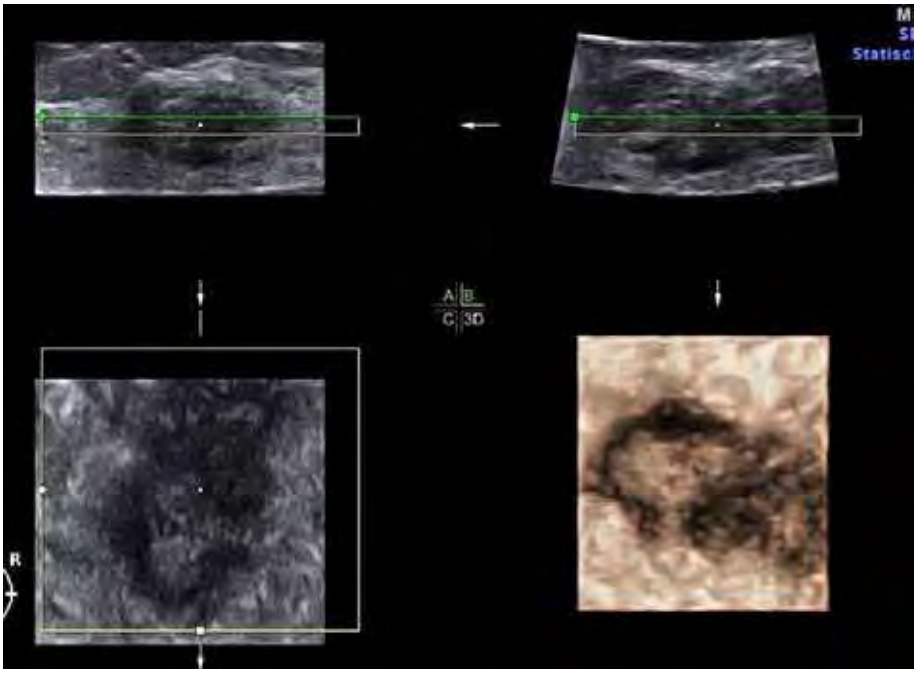

Fig. 12. The same lesion of Fig. 11 in 3-D mode

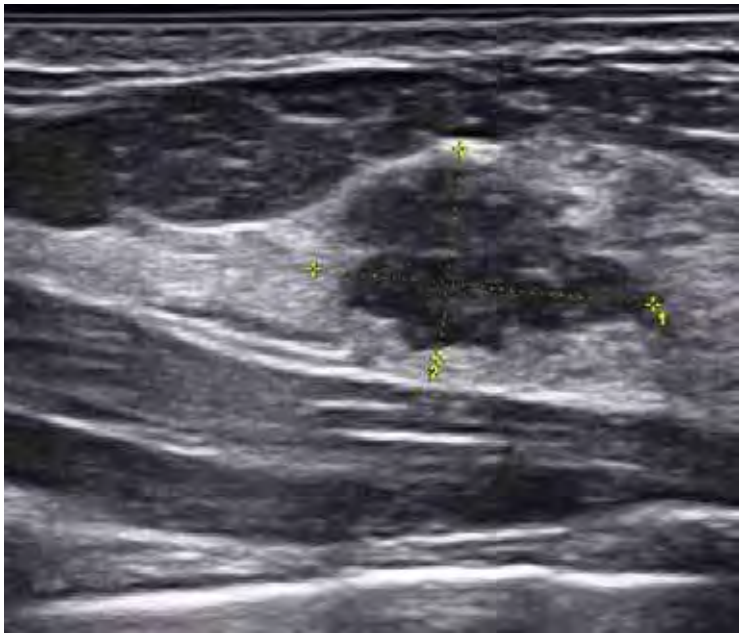

Fig. 13. Fibroadenoma with not smooth margins

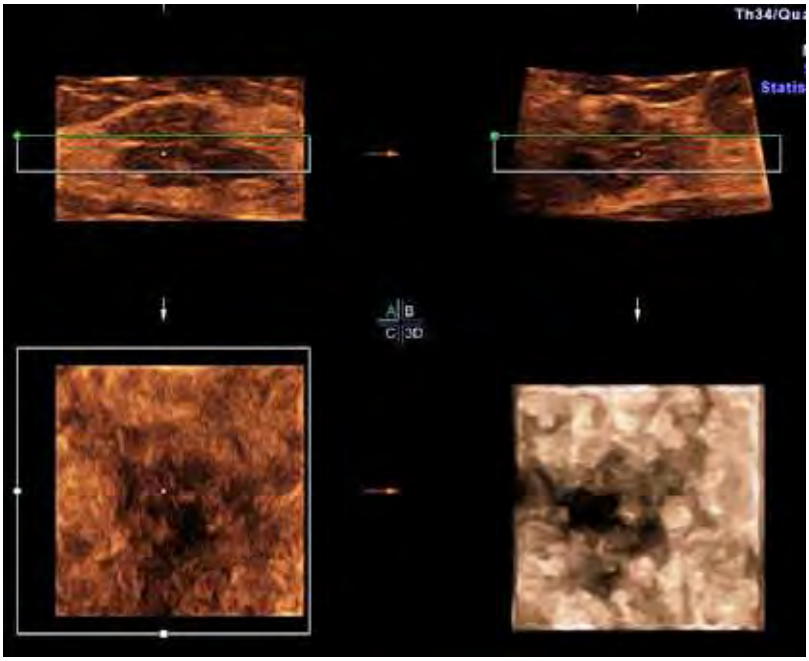

Fig. 14. Fibroadenoma of Figure 12 in 3-D mode with a canyon-like impression

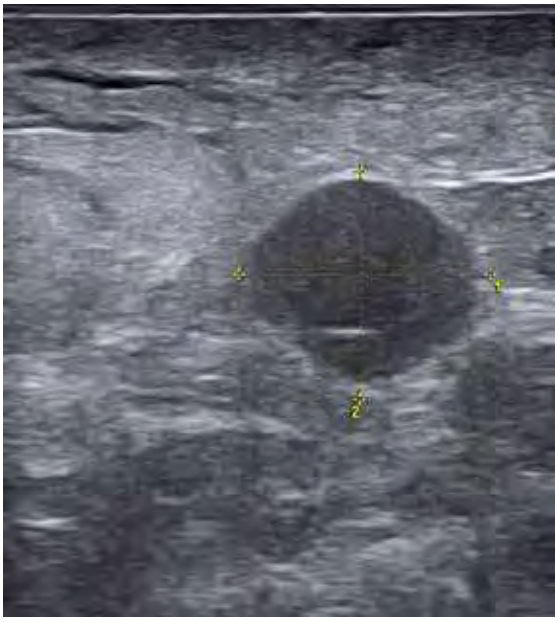

Fig. 15. Inflammatory, invasive ductal carcinoma with smooth and distinct margins, at first misinterpreted as mastitis

4. Color Doppler

Though color Doppler is not routinely used in all institutions performing breast ultrasound, in our view color Doppler is fundamental as an additional criterion in discriminating malign from benign lesions (Weismann, 2006). But as it is with other marker: the fact of a proven vascularity generates not for itself a definite submission to a suspect cluster. It is important to observe the type of vascularization: color signals running straight into the lesion are a hint of malignancy, whereas angiogenesis round the border of a lesion is not. Of course the degree of vascularization is relevant. Vascularization within the lesion stresses suspicion of malignancy, but is not a verification of malignancy. The missing of vascularization on the other hand is not a proof of benignancy (Figs. 16, 17).

The detection of significant vascularization within a lesion shifts an otherwise benign looking lesion from BI-RADS 3 (probably benign) to BI-RADS 4 (suspect), proposing it to core biopsy.

Quantitative spectral Doppler has not proven to be of relevance.

5. 3-D ultrasound

3-D technique, now available in breast ultrasound by different manufacturer, is a valuable tool to obtain a detailed impression of the margins and the surroundings of a lesion in a view from above (the so called C-plane). Necessary is a special probe with automated acquisition of different planes. The option of Volume Rendering strengthens the spacious impression of the lesion with its relationship to the neighborhood. By use of 3-D technique additional criteria for lesion submission could be applied. Pattern of retraction or compression in the near surroundings of a lesion are of importance. Star-like retraction

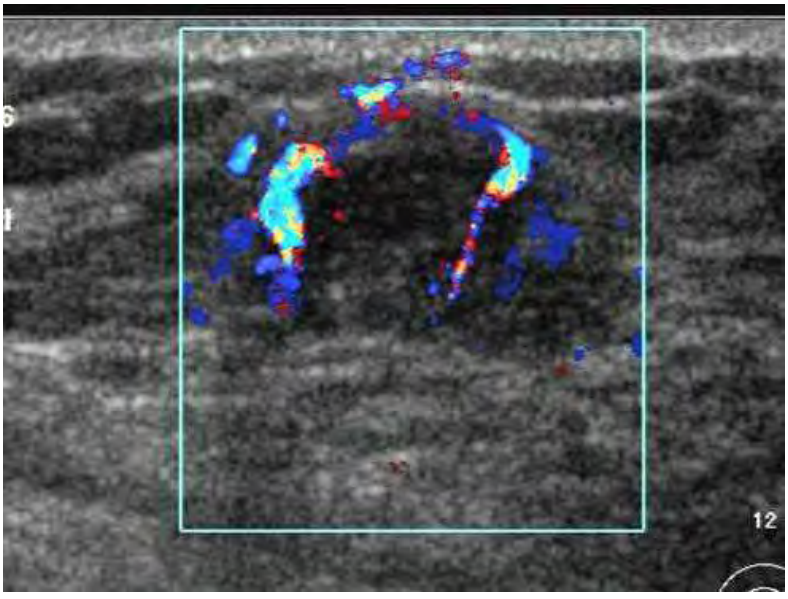

Fig. 16. DCIS (in pregnancy) with powerful vascularization

pattern is a hard marker for malignancy, whereas a compression pattern hints to benignancy (Fig. 19). With retraction pattern in the C-plane otherwise (in the A- and B-Plane) benign looking lesions are to subordinate to BI-RADS 4 (suspect) (Figs. 5, 17, 18).

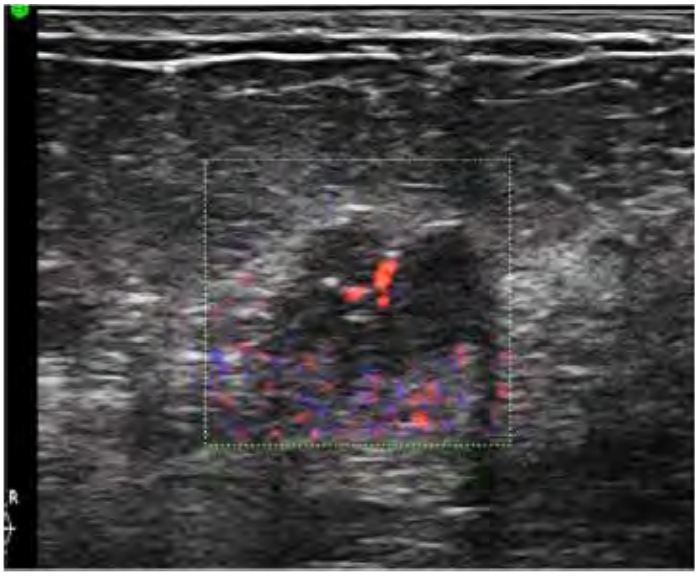

Fig. 17. Carcinoma: not easy detectable. Suspicion was strengthened by color Doppler

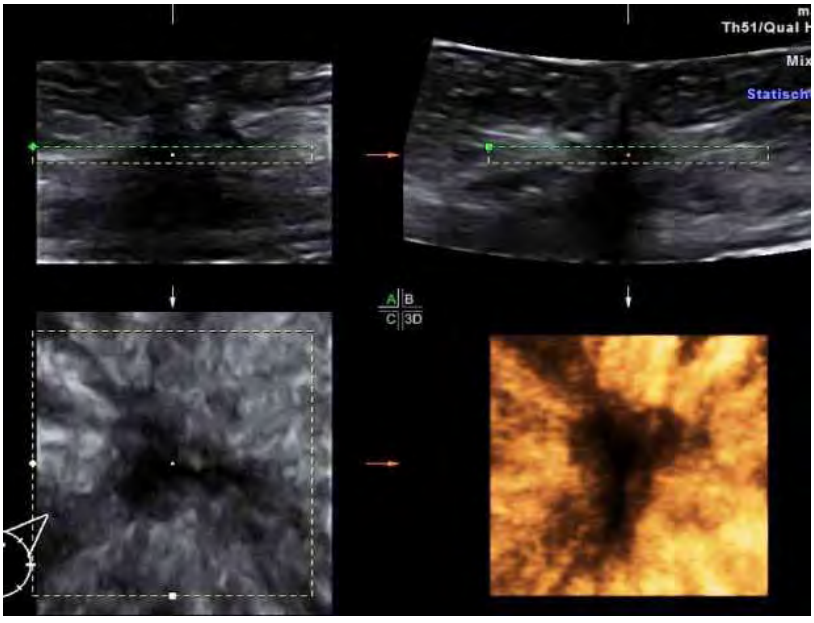

Fig. 18. Carcinoma of Fig. 17 in 3-D mode: suspicious retraction pattern

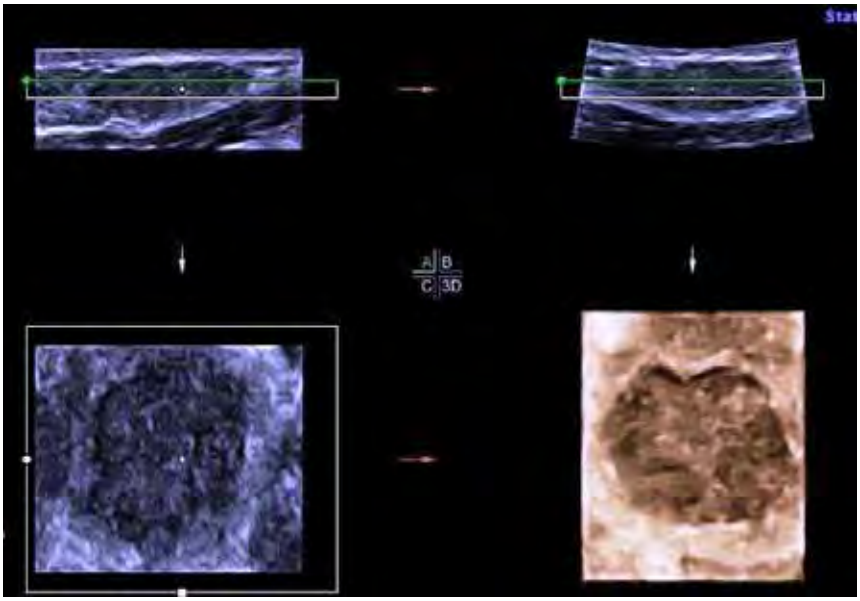

Fig. 19. Compression pattern of a benign fibroadenoma

However, carcinomas often may show indeterminate surrounding in the C-plane (not definite retraction phenomenon) as well. 3-D seems to be of similar value to color Doppler in differentiating masses further, detected previous in B-Mode (Weismann & Hergan, 2007).

The basic principle of sonographic diagnosis in breast ultrasound is to put all criteria in a synopsis or a mosaic, not to make a scarce diagnosis on one or two single signs.

6. Architectural distortion and structural disturbance

Architectural distortion is a term primary used in mammography and then became familiar in breast ultrasound too. In breast ultrasound it describes a well known hard marker for a malign lesion: the continuity of the glandular structure of the parenchyma is interrupted by an anechoic or hypoechoic irregular surrounded lesion (Figs. 3, 4).

What here is called "structural disturbance" is a far less obviously and more diffuse change in the echotexture of the gland of different extension. Echogenicity in local disturbances is somewhat more sonolucent, surroundings are not striking but poorly defined. It may correspond to a local discreet irregular course of the milk ducts. Such regions may represent only local mastopathic changes or preinvasive lesions like DCIS or so called "radial scars". In other cases even invasive carcinomas, i.e. triple negative (often mammographic occult) carcinomas may be present (Figs. 20, 21, 22, 23, 25).

To discover local "structural disturbances" whole breast scanning of each side is mandatory. It is necessary to take notice of the difference of a local disturbed region to the normal structure and echotexture of the individual breast and the difference to the other side. Specificity of breast ultrasound of such a lesion is not high, but this corresponds to the complexity of breast parenchyma in the sense of an extreme variable biological substrate.

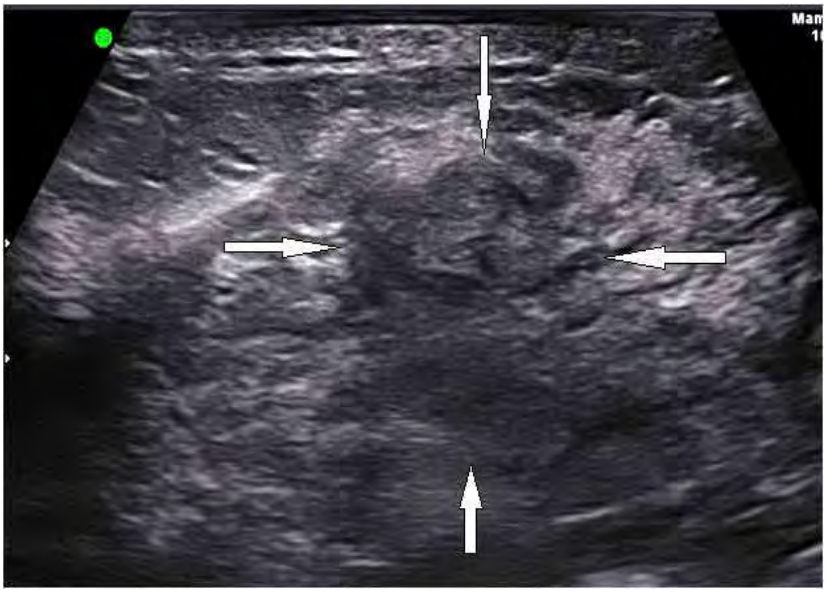

Fig. 20. Structural distortion: indistinct and ill defined, discreet sonolucent region in the center of the gland. The regular architecture of the gland-parenchyma is somewhat disturbed, but not disrupted: DCIS, in a dynamic examination better detectable than in a frozen picture

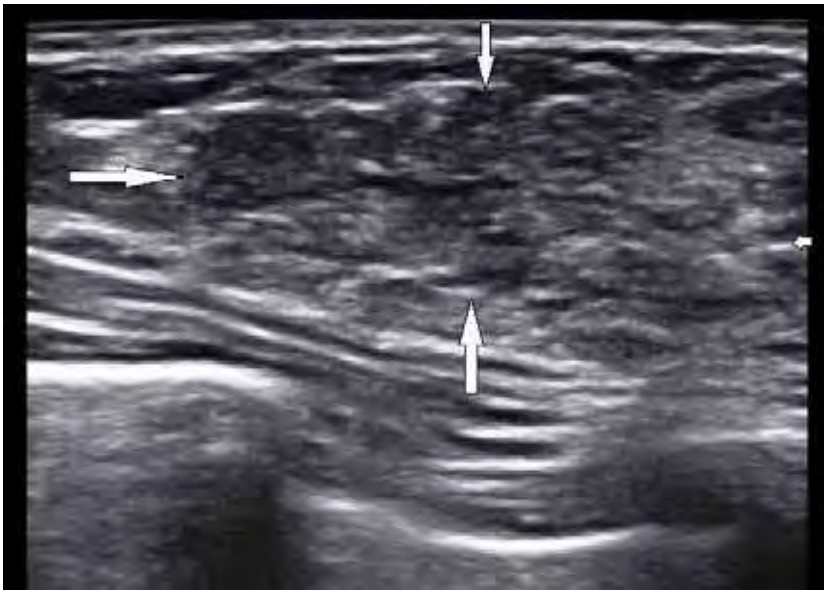

Fig. 21. DCIS in the outer upper region of the breast: not well defined extended region with lobulation and disturbed architecture

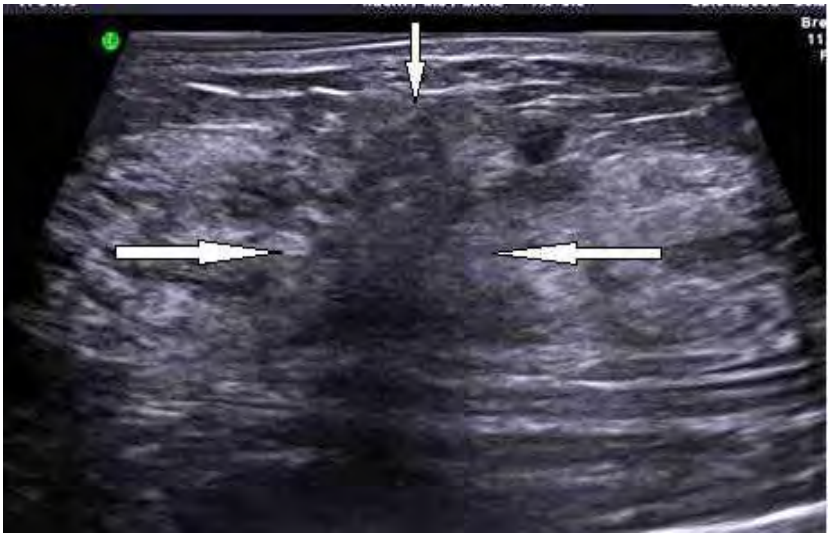

Fig. 22. A region with sonolucent structural disturbance

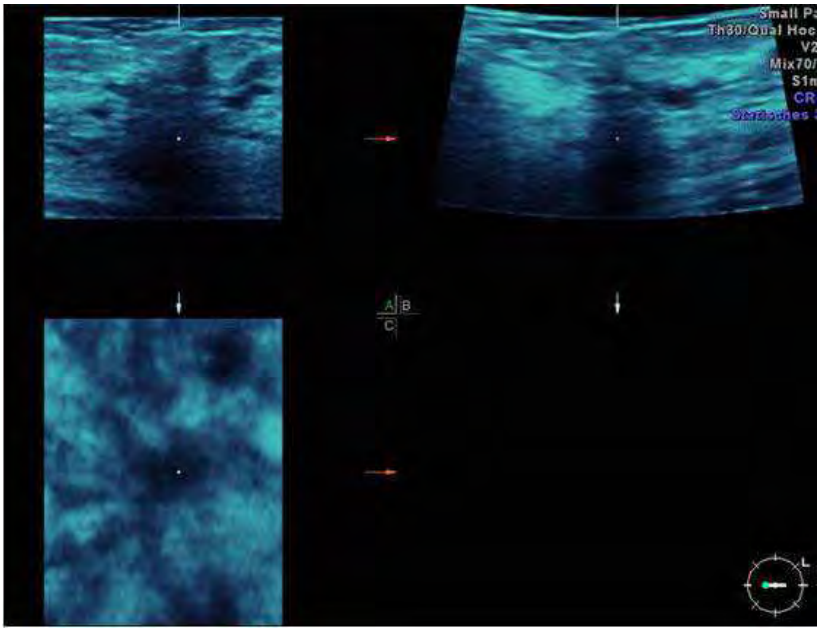

Fig. 23. Same lesion like Fig. 22: Suspicious retraction pattern in 3-D: "radial scar" with DCIS

Diagnosing and describing such local disturbances requires best technological equipment and some years of experience. However, this seems to be the most important field of progress in breast ultrasound: to become able to distinguish fine differences in the echotexture, not only to detect distinct striking masses.

It may be difficult and controversial to submit "structural disturbances" in BI-RADS 3 (probably benign) or 4 (suspect). At minimum such regions are to expose to complementary image modalities, i.e. mammography, perhaps MRI too and they are recommended for follow up. In more striking cases and high risk patients core biopsy should be preferred.

There is a need for further evaluation of the relevance of this type of ultrasound findings.

7. Ultrasound and DCIS (ductal carcinoma in situ)

In general ultrasound is thought to be not competent in detecting DCIS in comparison to mammography. That this is not true in some regards has been shown in the last decade. Breast ultrasound is especial important in detecting DCIS without microcalcifications. Today we do not know the real biological proportion of DCIS with and without microcalcifications (Hille et al., 2007).

The second entity is DCIS as a palpable lump, i.e. symptomatic DCIS. It could be shown that sonography is superior to mammography in detecting theses lesions (Yang et al., 2004), (Figs. 5, 16, 21).

Revealing "structural disturbances" seems to be of relevance to remove shortages of breast ultrasound in respect of diagnosing DCIS and to discover lesions that are otherwise, i.e. in mammography, occult (Figs. 9, 20, 22).

In a study evaluating the diagnostic competence of imaging methods in respect of breast carcinomas, which were operated, the sensitivity of sonography for DCIS was not far behind mammography (Berg et al., 2004)

Nevertheless, microcalcifications as a hint for DCIS is not reliable seen in ultrasound, when presenting without a mass (that means without sonolucent surroundings). This is the reason that - especially in a screening setting – sonography does not match mammography in diagnosing DCIS (Fig. 24).

8. Is breast ultrasound a screening tool?

The most controversial debate is going on about this topic. Most radiologists accept breast ultrasound mainly as an adjunct to mammography: mammography always first and then after - in cases of mammographical equivocal lesions or very dense breasts - ultrasound complementary. But that seems a traditional point of view and connected to specific interests. Ultrasound is time consuming, when performed by the physician in comparison to other modalities and is not well granted by insurances.

Under scientific and healthcare aspects the main point should be: What is the capacity of breast ultrasound in detecting early breast carcinoma in asymptomatic women? What we can say now: Breast ultrasound performed with high technology and in experienced hands at least has an equal, probably higher sensitivity for invasive carcinomas in comparison to mammography (Benson et al., 2004; Berg et al., 2008; Kolb et al., 2002) In respect to DCIS sensitivity is lower in published studies, but in this field there is evolvement, see above. Breast ultrasound can play an important role in detecting aggressive breast carcinoma not presenting microcalcifications like cases of "triple negative" types, often arising in younger women in dense breasts (Fig. 25). Recently investigations discovered that these cancers represent an important proportion of so called "interval cancers" in mammographic screening (Haakinson et al., 2010).

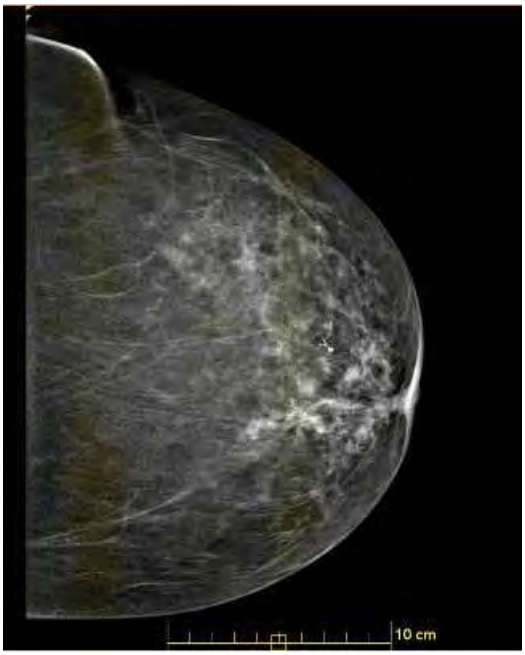

Fig. 24. Extended DCIS with microcalcifications in mammography, not visible in ultrasound

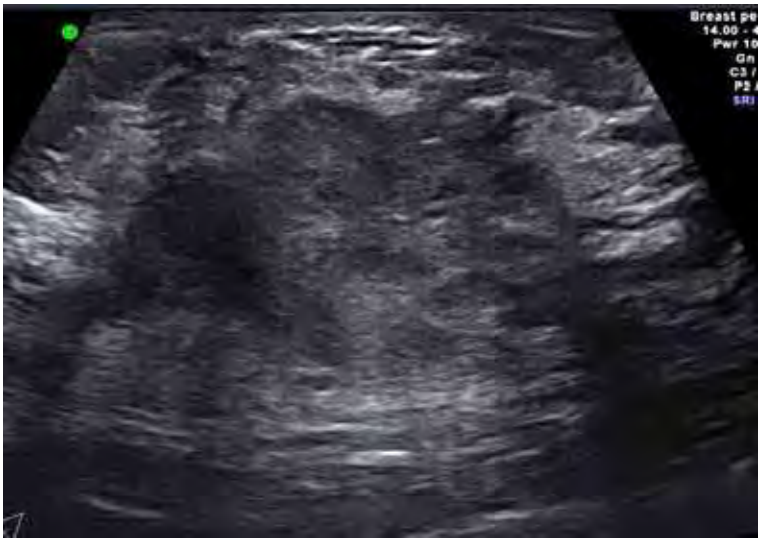

Fig. 25. "Triple-negative" carcinoma: extended, but not so obvious and with discreet structural changes

One important advantage of breast ultrasound is the absence of ionization. Sonography could be repeated without restriction.

Compared to mammography and MRI, ultrasound-machines are cheap. Special laboratories and assistants are not necessary.

But there are open questions and disadvantages of breast ultrasound. First, breast ultrasound is extremely dependant on the expertise of the physician and on the used technology. Second, handheld breast ultrasound does not produces an image document of the whole breast, that could be examined outside the laboratory. Therefore problems of quality control exist. New technologies of automated aquired 3-D volumes may remove these shortages in future. Third, there is a lack of randomizised trials comparing ultrasound versus other modalities.

Recently published studies demonstrate the feasibility of breast ultrasound as a preventive medical check-up in gynecological offices (Lenz, 2011; Madjar et al., 2010).

9. Areas of progress in breast ultrasound

9.1 Contrast- enhanced breast ultrasound

Contrast agents, intravenous applied, to improve sensitivity and specificity in breast ultrasound in detecting vascularization had been researched over a decade. Till now this - in sonography of the liver established – expanded procedure has not become a method of standard in breast ultrasound. The main reasons may be, that the procedure is more expensive and time consuming and is not suitable for breast-screening. A lesion which is to examine further with contrast agents is to detect in conventional B-Mode first. But there might be clinical indications for contrast agents instead of radioactive agents in future to test sentinel lymph nodes (Goldberg et al., 2011; Sever et al., 2011).

9.2 Elastography

At time manufacturer are equipping machines with elastography modules and some study groups are researching the potential role of this method. In conventional B-mode detected lesions were additionally examined in respect of the characteristics of stiffness. Different techniques, color coded or shear-wave techniques are used (Figs. 26a,b). Elastography is

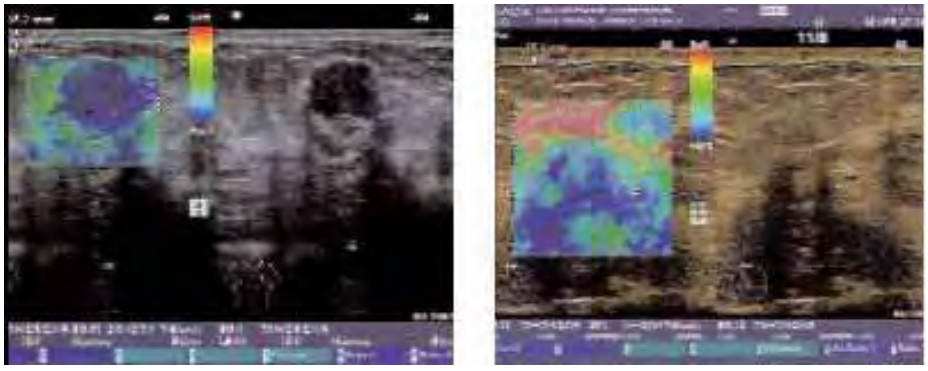

(a) (b)

Fig. 26. (a) (b) Elastography of carcinoma, coded in blue. (Figures by courtesy of R. Ohlinger, center of breast diseases, university of Greifswald, Germany)

extremely observer dependent in applying pressure by the handheld probe. Results are different and today it remains unclear, if specificity of breast ultrasound in discriminating benign from malign lesions can increase with elastography in a reliable way, so that invasive biopsies could be spared (Baldwin, 2011).

Fig. 27. Automated 3-D system (ABVS), figure with license by courtesy of SIEMENS AG

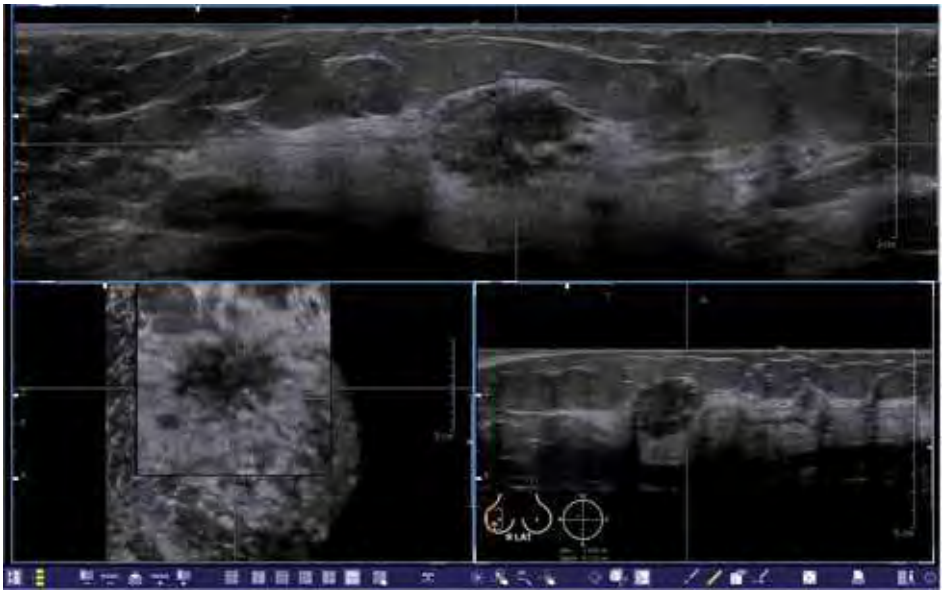

Fig. 28. Carcinoma in 3 planes bei ABVS, with license by courtesy of SIEMENS AG

9.3 Automated 3-D

Today a system is available, which acquires 3-D volumes of the whole breast (Fig. 27, 28). The resolution of the system is sufficient. The volume of the breast is acquired from different directions with a special probe by means of a large contact area. Than after the observer has to go through the whole volume to detect suspicious regions at the computer. The rendered C-Plane and the A- and B-plane could be presented in parallel on the screen. In future this step may be done by help of CAD (Computer Aided Detection). The acquisition itself could be done by assistant persons (sonographers).

Till now it is unclear, if an automated system can match traditional handheld breast ultrasound in accuracy performed by an expert and if the duration of the examination could be reduced. If suspect findings in the acquired volume are to check in handheld ultrasound afterwards, additional examination time would be required. There is a need for bigger trials (Chang et al., 2011; Moon et al., 2011)).

Advantages are the repeatability and the independence of the diagnostic procedure from patient´s presence. In aspects of a possible ultrasound screening this advantage may be helpful.

10. Conclusion

Breast ultrasound is a valuable tool for diagnosing breast carcinoma as well as benign diseases of the breast. Breast ultrasound could not only used as an adjunct to mammography and in symptomatic cases, but could probably used as a screening tool in asymptomatic women. Especially in women with dense breasts sonography will overcome mammography with a higher detection rate for invasive carcinomas.

Of special importance will be the capacity for detecting local "structural disturbances" as a hint for hidden malignancies.

Color Doppler and 3-D mode had proven to be of importance. Elastography has to demonstrate this in future.

A high technological standard and a very good experience of the examiner are prerequisites.

11. References

American College of Radiology (ACR) (2003). *ACR-BI-RADS® - Breast Imaging Reporting and Data System (BI-RADS™)*. Breast Imaging Atlas. 3rd ed. Reston (VA): ©America College of Radiology

Baldwin, P. (2011). Breast ultrasound elastography. *Radiologic Technology*, 82: 347M-365M

Benson S.R.; Blue J; Judd K.; et al. (2004) Ultrasound is now better than mammography in detection of invasive breast cancer. *Am JSurg,* 188: 381-385

Berg, W.A.; Gutierrez, L.; Ness Aiver, M.S.; Carter, W.B.; Bhargavan, M.; Lewis, R.S.; Ioffe, O.B. (2004). Diagnostic accuracy of mammography, clinical examination, US, and MR imaging in preoperative assessment of breast cancer. *Radiology,* 233: 830-849

Berg, W.A.; Blume, J.D.; Cormack, J.B. et al. (2008). Combined screening with ultrasound and mammography vs. mammography alone in women at elevated risk of breast cancer. *JAMA,* 299: 2151-2163

Chang, J., M.; Moon, W., K.; Cho, N.; Park, J., S.; Kim, S. J. (2011). Breast cancers initially detected by hand-held ultrasound: detection performance of radiologists using automated breast ultrasound data. *Acta Radiol,* 52: 8-14

Goldberg, B., B.; Merton, D., A.; Liu, J, B.; Forsberg, F.; Zhang, K.; Thakur, M.; Schulz, S.; Schanche, R.; Murphy, G.,F.; Waldman, S., A. (2011). Contrast-enhanced ultrasound imaging of sentinel lymph nodes after peritumal administration of Sonazoid in a melanoma tumor animal model. *JUltrasound Med,* 30: 441-453

Haakinson D., J; Stucky, C., C.; Dueck, A., C.; Gray, R. J; Wasif, N.; Apsey, H., A.; Pockaj, B. (2010). A significant number of women present with palpable breast cancer even with a normal mammogram within 1 year. *Am JSurg,* 200: 712-717

Hackelöer, B.J, Duda V. & Lauth G. (1986). *Ultraschall-Mammographie*. Springer, ISBN 3-540-16233-X, Berlin

Hille, H.; Vetter, M.; Hackelöer, B., J (2007). The Suitability of High-Resolution Ultrasound for the Detection of DCIS. *Ultraschall in Med,* 28: 307-312

Jellins, J; Kossof, G.; Buddee F.,W.; Reeve T., S. (1971). Ultrasonic visualization of the breast. *Med Journ of Australia,* 1: 305-307

Kobayashi, T. (1974). Clinical evaluation of Ultrasound techniques in breast tumors and malignant abdominal tumors. *Excerpta medica,* 191-198

Kolb, T.; M.; Lichy, J; Jeffrey, H. (2002). Comparison of the performance of screening mammography, physical examination, and breast ultrasound and evaluation of factors that influence them: An analysis of 27.825 patient evaluations. *Radiology,* 225: 165-175

Lenz, S. (2011). Breast ultrasound in office gynecology –Ten years of experience. *Ultraschall in Med,* 32: S3-S7

Madjar, H.; Ohlinger, R.; Mundinger, A.; Watermann, D.; Frenz, J. P.; Bader, W.; Schulz-Wendtland, R.; Degenhardt, F. (2006). BI-RADS-Analogue DEGUM Criteria for Findings in Breast Ultrasound - Consensus of the DEGUM Committee on Breast Ultrasound. *Ultraschall in Med* 27: 374-379

Madjar H., Mendelson E., B. (2008). *The practice of breast ultrasound*. 2nd revised edition. Thieme, ISBN 10-313124342, Stuttgart

Madjar, H.; Becker, S.; Doubek, K.; Horchler, T.; Mendoza, M.; Moisidis-Tesch, C.; Näther, B.; Niebling, K.; Pröls, U.; Schardt, A.-R.; Ulrich, S.; Zahn, U. (2010). Impact of Breast Ultrasound Screening in Gynecological Practice. *Ultraschall in Med,* 31: 289-295

Moon, W., K.; Shen, Y., W.; Huang, C., S.; Chiang, L., R.; Chang, R., F. (2011). Computer-aided diagnosis for the classification of breast masses in automated whole breast ultrasound images. *Ultrasound Med Biol,* 376: 539-548

Sever, A., R.; Mills, P.; Jones, S., E.; Cox, K.; Weeks, J; Fish, D.; Jones, P., A. (2011). Preoperative sentinel node identification with ultrasound using microbubbles in patients with breast cancer. *AJR,* 2: 251-256

Stavros A., T. (2004). *Breast ultrasound*. Lippincott, Williams & Wilkins. ISBN 0-397-51624-X, Philadelphia

Teboul, M.; Halliwell, M. (1995). *Atlas of ultrasound and ductal echography of the breast*. Blackwell, ISBN 0-632-03329-0, London

Weismann C. (2006). Role of colour Doppler ultrasound in breast imaging. *EJC Supplements,* 4:41-42

Weismann C., Hergan K. (2007). Current status of 3D/ 4D volume ultrasound of the breast. *Ultraschall in Med* 28: 273-282

Yang, W.T.; Tse, G.M.K. (2004). Sonographic, mammographic and histopathologic correlation of symptomatic ductal carcinoma in situ. *AJR,* 182: 101-110

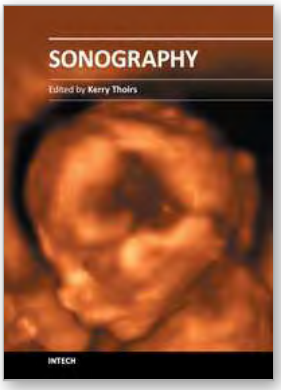

Sonography

Edited by Dr. Kerry Thoirs

ISBN 978-953-307-947-9
Hard cover, 346 pages
Publisher InTech
Published online 03, February, 2012
Published in print edition February, 2012

Medical sonography is a medical imaging modality used across many medical disciplines. Its use is growing, probably due to its relative low cost and easy accessibility. There are now many high quality ultrasound imaging systems available that are easily transportable, making it a diagnostic tool amenable for bedside and office scanning. This book includes applications of sonography that can be used across a number of medical disciplines including radiology, thoracic medicine, urology, rheumatology, obstetrics and fetal medicine and neurology. The book revisits established applications in medical sonography such as biliary, testicular and breast sonography and sonography in early pregnancy, and also outlines some interesting new and advanced applications of sonography.

How to reference

In order to correctly reference this scholarly work, feel free to copy and paste the following:

Heino Hille (2012). Advances in Breast Ultrasound, Sonography, Dr. Kerry Thoirs (Ed.), ISBN: 978-953-307-947-9, InTech, Available from: http://www.intechopen.com/books/sonography/advances-in-breast-ultrasound

INTECH
open science | open minds

InTech Europe
University Campus STeP Ri
Slavka Krautzeka 83/A
51000 Rijeka, Croatia
Phone: +385 (51) 770 447
Fax: +385 (51) 686 166
www.intechopen.com

InTech China
Unit 405, Office Block, Hotel Equatorial Shanghai
No.65, Yan An Road (West), Shanghai, 200040, China
中国上海市延安西路65号上海国际贵都大饭店办公楼405单元
Phone: +86-21-62489820
Fax: +86-21-62489821